

博士論文
Ph.D Dissertation

Superposition states in quantum optics: teleportation experiments, modeling theory, tomography algorithms

(非古典状態の量子テレポートーション実験の研究—
条件付き操作、理論モデル、トモグラフィアルゴリズム)

2013年01月

東京大学大学院	工学系研究科	物理工学専攻
The University of Tokyo	School of Engineering	Departement of Applied Physics

ベニキ ユーゴ
Benichi Hugo

Superposition states in quantum optics: teleportation experiments, modeling theory, tomography algorithms

(非古典状態の量子テレポーテーション実験の研究—条件付き操作、理論モデル、トモグラフィアルゴリズム)

Hugo Benichi

This manuscript is an updated version of the thesis submitted in fulfilment of the requirements for the Ph.D. degree at the University of Tokyo, School of Engineering, Department of Applied Physics. Date: Thursday 24 January 2013. Version number: 1.3.6.

Copyright © 2011, 2012, 2013 Hugo Benichi

Acknowledgments

The work presented in this manuscript was carried out at the Applied Physics department of the University of Tokyo, in the laboratory of Prof. Akira Furusawa. Starting from April 2009 and over the three years of doctor course I have spent at the Applied Physics department, I could start and complete my research project in a very fruitful research environment and in almost ideal working conditions. I am very grateful to the laboratory and to my supervisor for this wonderful research environment I had the chance to experience and be privileged with. I also would like to thank all the people of the laboratory, student, staff, and especially co-experimentalists, for their infinite help and support in many occasions, be it about research, daily life in Japan or administrative tasks.

Being a foreigner in Japan certainly has its challenges. Overall, moving from France to Japan I feel I had the chance to receive a very warm and hearty welcome and could integrate myself smoothly and find my place in this wonderful country, thanks to the help from the people of my laboratory, the great support from the staff of the University of Tokyo, and the international student community here. Especially, I would like to thank all my friends at the University of Tokyo, those who have already graduated and those who will still be studying after me, for interesting discussions about life in Japan, for cheering me up, for listening to my incessant rambling, and overall many good moments and memories. I am also very grateful to Japan and the Ministry of Education for giving me the financial support and opportunity to study three years at the University of Tokyo and obtain the doctoral degree in such favorable conditions.

I cannot close this section without looking back on the long road which brought me here as I think that getting the Ph.D title eventually plays out in more than three years. First and foremost, it is my family I want to thank, to whom I owe my education and personal values, my curiosity and taste for understanding my surroundings. I also thank my home country which gave me the rare opportunity to study at such wonderful schools and learn from so many knowledgeable and wise teachers and professors who gave me the willingness to succeed and pursue in scientific studies as far as I did until today. In that regard, my greatest thanks go especially to the professorial staff of the Physics department at Ecole Polytechnique and Ecole Normale Supérieure.

Contents

Acknowledgments	iv
Table of Contents	ix
List of Figures	xiii
List of Symbols	15
Introduction	17
1 Quantum Theory of Light	23
1.1 Quantum mechanics postulates	23
1.1.1 Hilbert space representation	23
1.1.2 Operators	24
1.1.3 Projective measurements	25
1.1.4 The density matrix and POVM measurements	25
1.1.5 Composite systems	26
1.2 Monomode quantum optics	27
1.2.1 Quantum description of light	27
1.2.2 Quadratures operators	28
1.2.3 Photon number states	29
1.2.4 Phase shifting	30
1.2.5 Coherent states	31
1.2.6 Squeezed states	32
1.2.7 Beam splitters	33
1.3 Phase space representations	36
1.3.1 The Wigner function	36
1.3.2 The characteristic function	40
1.3.3 Other phase-space representations	41
1.3.4 Linear absorption	42
1.3.5 Gaussian formalism	44
1.4 Multimode quantum optics	44
1.4.1 Time and frequency domains	45
1.4.2 Wave-packet states	46
1.4.3 Broadband squeezing	47
1.5 Detection of light	50
1.5.1 Intensity detection	50
1.5.2 Amplitude detection	51
1.5.3 Inefficient homodyne detection	54

1.5.4	Avalanche regime	57
2	Generation of non-Gaussian States	59
2.1	What is a non-Gaussian state	59
2.1.1	non-Gaussianity and non-classicality	60
2.1.2	Projection based conditional generation	61
2.1.3	Recent experimental history	62
2.2	Photon subtraction	63
2.2.1	Exact subtraction of m photons	65
2.2.2	Monomode click detection model and single photon subtraction	66
2.2.3	On/off detection	68
2.2.4	Multimode click detection model	69
2.3	Mode projection function	72
2.3.1	Multidimensional reduction mechanism	72
2.3.2	Selection of the Hilber space	73
2.3.3	Filtering cavities and electrical filtering	75
2.3.4	Instant of detection	78
2.4	Experimental generation	79
2.4.1	Experimental protocol	79
2.4.2	Optical setup	80
2.4.3	Control and automation	84
2.4.4	Measurement setup	86
2.4.5	Experimental results	88
2.4.6	Imperfection model	90
3	Quantum Tomography	95
3.1	Quantum state reconstruction	95
3.1.1	Inverse problem statement	96
3.1.2	The Radon transform	97
3.1.3	The density matrix picture	98
3.1.4	Direct measurement	99
3.2	Linear inversion	99
3.2.1	Inverse Radon transform	100
3.2.2	Polynomial series expansion	102
3.3	Variational principles for tomography	112
3.3.1	Variational reconstruction principle	112
3.3.2	Density matrix maximum likelihood reconstruction	115
3.3.3	Polynomial series maximum likelihood reconstruction	119
3.4	Faithfullness of reconstruction estimators	120
3.4.1	Error estimators for linear reconstruction method	120
3.4.2	Maximum likelihood and the Cramer-Rao inequality	124
3.4.3	Monte Carlo error simulation	125
3.4.4	Fidelity and distance to target state	128
4	Broadband Quantum Teleportation	133
4.1	Theory of continuous variable teleportation	133
4.1.1	Criterion of success	134
4.1.2	Heisenberg picture	135
4.1.3	Phase space picture	138
4.1.4	Noise model	139

4.1.5	Wave packet teleportation	142
4.2	Experimental setup and results	147
4.2.1	Experimental setup	148
4.2.2	Vacuum state teleportation, experimental results	153
4.2.3	non-Gaussian state teleportation, experimental results	155
4.2.4	Model of non-Gaussian state teleportation	156
4.3	Conditional quantum teleportation	160
4.3.1	Theory of conditional operation	161
4.3.2	Experimental Conditional Teleportation	172
4.3.3	Experimental results	175
Conclusion		183
4.4	Summary	183
A	FPGA digital program and circuitry	187
B	Control and automation setup	191
C	Control and drivers software interface	195
D	Optical setup	201
E	Conditional teleportation theory summary	203
Bibliography		206

List of Figures

1.1	Operators basis relation	29
1.2	Photon number states wave-functions	30
1.3	Coherent states photon number statistics	31
1.4	Squeezed vacuum states photon number statistics	32
1.5	Optical beam-splitter	33
1.6	Beam-splitter representation of optical losses	35
1.7	Examples of Gaussian Wigner functions	37
1.8	Examples of photon numbers Wigner functions	38
1.9	Effect of linear losses on the Wigner function	43
1.10	Optical parametric oscillator diagram	48
1.11	Homodyne measurement setup	52
2.1	Examples of Schroedinger's cat states Wigner functions	60
2.2	Electrical field of a small Schroedinger's cat state	64
2.3	Small Schroedinger's cat state and photon subtracted squeezed vacuum Wigner functions	64
2.4	Setup for the exact subtraction of m photons	65
2.5	Fidelities of the m photon subtraction protocol	67
2.6	Inline and offline single photon subtraction	67
2.7	Photon subtraction with on/off detector	68
2.8	Photon subtraction and wave-packet generation	70
2.9	Projection of the homodyne current	74
2.10	Modes transformation with filtering cavities	75
2.11	Calibration of the instant of photon detection	78
2.12	Small amplitude Schroedinger's cat states generation setup overview	79
2.13	Small amplitude Schroedinger's cat states generation setup details	80
2.14	Laser setup	81
2.15	AOM switching channel	82
2.16	Main characteristics of optical cavities for Schroedinger's cat state generation	82
2.17	Triggering channel and filtering cavities setup	83
2.18	Tomography process with alternate measurement and control phases	84
2.19	Time synchronization of the FPGA generated triggers	85
2.20	Laser beam power control overview	86
2.21	Homodyne current measurement overview	86
2.22	Marginal distribution of the electrical field, input state	89
2.23	Reconstructed Wigner functions, input state	89
2.24	Photon number distribution, input state	90
2.25	Input Wigner function negativity η dependancy	91
2.26	$W_{\text{in}}(0, 0) = 0$ as a function of η , s , and ϵ	92

3.1	Regularized integration kernel $K(x)$	97
3.2	Different transforms for different paths from p to W	101
3.3	Regularized integration kernel $K(x)$	102
3.4	Zernike polynomials in the unit circle	105
3.5	Chebysheff's polynomials of the second kind	106
3.6	Comparison between polynomial series tomography and filtered back-projection tomography, vacuum and single photon mixture	108
3.7	Comparison between polynomial series tomography and filtered back-projection tomography, thermal state	109
3.8	Increased radial resolution and stability of tomography, input state	110
3.9	Increased radial resolution and stability of tomography, output state	111
3.10	Effect of N and M on the convergence of polynomial series tomography, squeezed single photon state	112
3.11	Increased radial resolution and stability of tomography, Schroedinger's cat state	113
3.12	Convergence of iterative maximum likelihood with the iterative steps, residual matrice distance	117
3.13	Convergence of iterative maximum likelihood with the number J of experimental data points, Wigner functions	118
3.14	Convergence of iterative maximum likelihood with the number J of experimental data points, matrice distance	118
3.15	Estimation of $\sigma_W(0, 0)$	122
3.16	Effect of M on the convergence of $W'(0, 0)$ and the magnitude of $\sigma_{W'}(0, 0)$	123
3.17	Comparison between Monte Carlo simulation and direct estimation of $\sigma_W(0, 0)$	126
3.18	Illustration of the rejection sampling technique	127
3.19	Estimation of the distance between a target state and a reconstructed state for a thermal state	128
3.20	Estimation of the distance between a target state and a reconstructed state for a vacuum and single photon mixture	128
3.21	Estimation of the distance between a target state and a reconstructed state for a Schroedinger's cat state	129
3.22	Comparison of the reconstructed state mean distance to the target state, case 1	130
3.23	Comparison of the reconstructed state mean distance to the target state, case 1	132
4.1	Continuous variable teleportation protocol	134
4.2	Continuous variable teleportation protocol	136
4.3	2-mode EPR entangled state generation	137
4.4	Thermalization of the Wigner function of a teleported single photon state	139
4.5	Influence of noise on the effective EPR correlation level	141
4.6	Illustration of the teleportation of wave-packets in successive time slices	142
4.7	Experimental setup for broadband teleportation, overview	147
4.8	Experimental setup for broadband teleportation, details	149
4.9	2-mode EPR state experimental generation setup	150
4.10	Experimental squeezing and antisqueezing power traces	151
4.11	Experimental EPR correlation traces	152
4.12	Classical channel experimental setup	153
4.13	Optical delay line setup	153
4.14	[Vacuum broadband teleportation, output homodyne photocurrent power spectrum traces	153
4.15	Reconstructed Wigner functions, teleported vacuum state	154

4.16 Photon number distribution, teleported vacuum states	155
4.17 [Marginal distribution of the electrical field, input and output states	156
4.18 Reconstructed Wigner functions, output teleported state	156
4.19 Photon number distribution, input and output states	157
4.20 Quantum teleportation, input and output Wigner function	157
4.21 Wigner function negativity $W_{\text{in}}(0, 0)$ as a function of r , η and s	158
4.22 Negativity threshold as a function of r and η	158
4.23 Influence of ϵ and s on the negativity threshold $W_{\text{out}}(0, 0) = 0$	159
4.24 Conditional quantum teleportation, protocol overview	161
4.25 Conditional teleportation, acceptance zone in phase space	162
4.26 Probability of success of conditional teleportation, $ 1\rangle$ case	165
4.27 Improvement to $W(0, 0)$ with the probability of success of conditional teleportation, $ 1\rangle$ case	166
4.28 Probability of success of conditional teleportation, mixture of $ 1\rangle$ and $ 0\rangle$ case	167
4.29 Improvement to $W(0, 0)$ with the probability of success of conditional teleportation, mixture of $ 1\rangle$ and $ 0\rangle$ case	168
4.30 Improvement to $W(0, 0)$ with the probability of success of conditional teleportation with additional optical losses	170
4.31 Effect of extra anti-squeezing on the probability of success of conditional teleportation	171
4.32 Effect of extra anti-squeezing on the improvement to $W(0, 0)$ with conditional teleportation	172
4.33 Experimental setup for conditional teleportation, overview	173
4.34 Alice's homodyne detectors time calibration	174
4.35 Experimental probability of success of conditional teleportation	175
4.36 Effect of conditional teleportation on $W(0, 0)$, data sets #1 and #2	176
4.37 Effect of conditional teleportation on $W(0, 0)$, data sets #3 and #4	177
4.38 Effect of conditional teleportation on $W(0, 0)$, data sets #5 and #6	178
4.39 Effect of conditional teleportation on the Wigner function, data set #1	179
4.40 Effect of conditional teleportation on the Wigner function, data set #1	180
4.41 Effect of conditional teleportation on $W_{\text{out}}(0 L)$, model against experimental results	181
A.1 Triggers synchronisation FPGA circuit	187
A.2 Triggers generation FPGA circuit	188
A.3 Phase scanning signal generation FPGA circuit	189
A.4 Auxiliary FPGA circuit	190
A.5 APD edges counter FPGA circuit	190
B.1 External connection of FPGA generated signals	191
B.2 External trigger selector circuit	192
B.3 Laser beam intensity power control system	192
B.4 Homodyne photocurrent acquisition and measurement setup	193
C.1 Automation software general organization	196
C.2 Driver API interface architecture	197
C.3 Client/server architecture	198
C.4 Data transfer and copy architecture	199
D.1 Detailed schematic of the optical setup	202

List of Symbols

Symbol	Description
Variables and parameters	
x, q	position variable
p	momentum variable
$\alpha = (x + ip)/\sqrt{2}$	complex amplitude
t	time
ω, Ω	angular frequency and sideband angular frequency
s	squeezing power
r	EPR correlation power
η	loss coefficient
Operators	
\hat{x}, \hat{p}	position and momentum operators
\hat{a}, \hat{a}^\dagger	annihilation and creation operators
$\hat{\rho}$	density matrix
$\hat{D}(\alpha), \hat{D}_\alpha$	displacement operator
$\hat{S}(s), \hat{S}_s$	squeezing operator
$\hat{U}(\theta), \hat{U}_\theta$	phase-shifter operator
$\hat{B}(\theta), \hat{B}_\theta$	beam-splitter operation
Phase-space quasi-distributions	
$W(q, p), W_{q,p}, W(\alpha)$	Wigner function
$Q(q, p), Q_{q,p}, Q(\alpha)$	Husimi function
$P(q, p), P_{q,p}, P(\alpha)$	Glauber-P function
$\chi(u, v), \chi_{u,v}, \chi(\xi)$	Characteristic function
$\mathcal{R}, \mathcal{R}^{-1}$	Radon and inverse Radon transforms
Polynomial series and special functions	
$H_n(x)$	Hermite polynomials
$T_n(x), U_n(x)$	Chebyshev's polynomials, first and second kind
$Z_s^n(r, \phi) = R_s^n(r)e^{in\phi}$	complex Zernike polynomials
$J_n(r)$	Bessel's functions of the first kind
$\text{erf}(x)$	error function
Mathematical operations	
\circ, \star	1-dimensional convolution
$\circ\circ, \star\star$	2-dimensional convolution
$\text{tr}[\cdot]$	trace operation
\otimes	tensor product

Table 1: Recurrent mathematical symbols and notations.

Introduction

The field of Quantum Optics

Quantum optics could be defined as the study of the quantum properties of propagating waves of the electrical field. In other words, quantum optics is the description of light waves at the quantum level using quantum mechanics. Historically, the modern theory of quantum optics has been developed by Roy J. Glauber[115] in the sixties with his work on quantum coherence initiated to explain the Hanbury Brown-Twiss interferometer experiment and the photon bunching phenomena [11]. It was already known before that time that a quantum description of the electrical field was necessary to grasp the understanding of certain phenomena involving interaction between light and matter. Although the idea of the existence of particles of light appeared several times in the historical development of physics, the precise idea of quanta of light dates back to the beginning of the nineteenth century and to Planck[1] and Einstein's work[2]. As a matter of fact, the word "photon" itself was first proposed by Einstein to put a name on the concept of quanta of light. These ideas were later experimentally verified by Arthur Compton[6]. Despite these early development which also turned out to be the root of quantum mechanics itself and one of its first experimental hints, the modern theory of quantum optics was rather late to emerge. Before Glauber simplified the complex formalism of quantum field theory into a simpler theoretical framework for quantum optics, quantitative studies were only possible using the complete theory of quantum electrodynamics and radiation. Nowadays, we have gained a very good understanding of the quantum description of light, a question which for the most part is solved as far as fundamental sciences go.

Nevertheless quantum optics is nowadays a very active field of research. As it turns out, the electrical field is the most simple physical system for fundamental tests of quantum physics. The superposition principle, quantum entanglement, Bose-Einstein statistics, interferences; all essential properties of quantum mechanics can be observed and studied in quantum optics easily all the better thanks to the absence of direct photon-photon interactions. Experimental quantum optics was essentially started with the access to coherent light sources and Theodore H. Maiman's first ruby laser [13]. From the first pioneering laser systems of the sixties to current state-of-the-art experiments, experimental quantum optics has advanced steadily and passed several important milestones. In the sixties, seventies and eighties, the development of more powerful laser systems at new wavelengths allowed for the study of non-linear optics[14]. In the eighties, progress in the study and understanding of parametric-down conversion and four wave mixing phenomena led to the observation and demonstration of squeezed light and "two-photons coherent states", as squeezing was called at that time[24, 26, 27]. The availability of squeezed quantum states eventually paved the road to many quantum optics experiments, starting with the first Gaussian information processing experiments[51] and qubit experiments[42] of the late nineties. In the last ten years experimental quantum optics has been the testing ground of further experiments and fundamental tests of quantum mechanics, focusing on the generation, measurement, characterisation and manipulation of exotic or entangled quantum states of light. Inspired by the "gedenken experiment" of the founding fathers of quantum mechanics, these exotic quantum states of light

such as the elusive Schroedinger's cat state are now routinely produced in laboratories[100, 98, 127].

The rapid development of quantum optics was possible thanks to the rather unlikely combination of four ingredients: 1) lasers which produce very pure coherent light of all frequencies are now a mainstream technology, easy to produce, deploy and operate. 2) in the particular optical region of the electromagnetic spectrum, background light is virtually void of any black body radiations, so that a clean and quiet environment down to the level of the quantum vacuum can be easily obtained in the laboratory. 3) with electronics noise levels far below the optical shotnoise level, high energy conversion efficiency and linearity, silicon PIN photodiodes allow for easy measurements of the quantum state of light down to the quantum vacuum level. 4) easy passive manipulation of light through the index of refraction gives us a complete toolbox of so-called linear optical components which forms the backbone of most experimental setups: optical lenses, dielectric and Bragg mirrors, amplitude modulators, birefringent materials, waveguides.

Quantum Information Processing

Quantum mechanics calls for a different treatment of information processing than what Claude E. Shannon achieved with his classical theory of information[9]. With the swift development of computer technologies following the end of World War II and the invention of the transistor, it quickly appeared to physicists that quantum mechanics could certainly have a special status in information processing[20, 23]. Although the question is still open in computational complexity theory and although the exact relation between complexity classes associated with quantum computers like BQP (bounded error quantum polynomial time) and QMA (quantum analog of the deterministic complexity class NP or the probabilistic complexity class MA) and classical complexity classes is still unknown, it is firmly believed that quantum computers can genuinely solve a number of computational problems faster than classical computers . Some famous quantum algorithms like Shor's factoring algorithm[48] or Grover's search algorithm[44] are hints of this conjecture and of the advantage of quantum computers.

From the original idea of a quantum analogical computer by Feynman[20] and the experimental proof of violation of the Bell's inequalities[18] and therefore the genuine existence of quantum entanglement, the field of quantum information processing is now a major sub-field of quantum mechanics. Quantum information processing has now also become the major and most active research topic in the field of quantum optics. Of course, quantum information processing can be studied with several different physical systems, but light provides an especially adequate medium for the implementation of quantum communication and information algorithms, thanks to the absence of direct photon-photon interactions and the tendency of photons to stay undisturbed. In that respect, light waves have some genuine advantages for the practical applications and realization of quantum entanglement, quantum measurement and complex quantum information phenomena.

As a striking example of quantum communication protocols, teleportation was discovered early on in the development of the field of quantum information processing. With either qubit [Bennet83] and continuous variable flavors [39], experiments were soon to follow [42, 51]. Until now continuous variable teleportation has only been performed with the class of so-called Gaussian states [51, 130, 147, 168]. However, this alone is not sufficient for universal quantum computation where non-Gaussianity of some kind has been shown to be necessary: at least third order nonlinear operations are necessary for building a universal quantum computer[53], something Gaussian operations and Gaussian states alone cannot achieve. For instance photon-subtraction techniques which are based on discrete variable and qubit technology, can provide these useful non-linearities and are used to generate Schroedinger's cat states and other optical non-Gaussian states[43]. Schroedinger's cat states are of particular interest as they have been shown to be a use-

ful resource for fault-tolerant QIP[141]. Although such non-Gaussian non-classical states of light that would allow for such universal operations have been available experimentally for some time in the continuous variable regime [100, 98, 127], the major challenge of actually manipulating these states in some Gaussian protocol context beyond simple generation has remained mostly unaddressed. Therefore, it appears crucial to extend the well understood Gaussian continuous variable technology and linear optics with non-Gaussian states and non-Gaussian operations.

Subject of the thesis

The main subject of this thesis is the experimental study of the quantum teleportation process with as input states non-Gaussian quantum states of light approximating small amplitude Schroedinger's cat states. More precisely, we are interested in the experimental demonstration of the quantum teleportation of non-classical states of light up to the point where the output quantum state are still without ambiguity non-classical quantum states. This experiment is ambitious for it lies on top of two different frontiers of experimental quantum optics. On the one side we inherit from the long lineage of continuous variable Gaussian experiments and have built a quantum teleportation apparatus which transcends the sideband regime. On the other side we have used the photon subtraction protocol to generate in the laboratory these highly non-classical non-Gaussian states necessary for universal quantum information processing. In this thesis manuscript we report on how we have combined these two sets of technologies and how we could demonstrate successful Gaussian manipulation of non-classical non-Gaussian states by achieving experimental quantum teleportation of Schroedinger's cat states of light. Using the photon-subtraction protocol we generate quantum states approximating closely Schroedinger's cat states in a manner similar to [100, 98, 127]. To accommodate with the required time-resolving photon detection techniques and handle the wave-packet nature of these optical Schroedinger's cat states, we have developed a hybrid teleporter built with continuous-wave light yet able to directly operate in the time domain. For this purpose we have constructed a time-gated source of EPR correlations as well as a zero phase-dispersion classical channel. We were able to bring all the experimental parameters up to the quantum regime and performed successful quantum teleportation in the sense that both our input and output states are strongly non-classical quantum states of light. As a prototype of these new techniques in a fully quantum regime, this experiment constitutes a first step towards more advanced QIP protocols and future non-classical state manipulation experiments in quantum optics.

This thesis manuscript explains in details and reports on the results of the experiment described above, but also includes several related theoretical studies and analysis linked to this experimental work. Overall, these theoretical studies can be divided in three groups. First, there is the question of understanding precisely what we observe in the teleportation experiment. This requires a complete phase space model of input state, teleportation process, and output teleported state, taking into account in addition the relevant experimental parameters. The second point, which is to some extent related to the first, is to correctly understand the multimode properties of the input photon subtracted state and of the broadband teleporter apparatus to model the transient and time-domain nature of this experiment. The third point is about studies on the process of quantum tomography, which is a necessity for current state-of-the-art experiments in continuous variable quantum optics for characterization of unknown quantum states.

Content of the manuscript

The main content of this thesis manuscript is divided into four chapters. Additional material mostly related to experimental details can be found in the appendix sections.

- The first chapter is a summary and succinct presentation of the theory of quantum optics. It mostly focuses on the physics of a single quantum harmonic oscillator, which is reviewed in the Heisenberg picture, Schroedinger picture, and phase space formalism. It also introduces models for the main experimental measurement techniques available in quantum optics used in this thesis.
- The second chapter focuses exclusively on the single photon subtraction protocol, the tool of choice nowadays to generate small amplitude Schroedinger's cat states of light and other low photon number non-Gaussian states. It presents our experimental setup and results as well as a detailed analysis and quantum theoretical model for this family of photon subtracted states so important for the field of quantum information processing.
- The third chapter deals with the problem of quantum tomography and its practical numerical implementation. The core of the chapter is a demonstration and further study of one of the main results of this thesis, an algorithm for the reconstruction of the Wigner function using polynomial series decomposition and stable linear inversion. It is followed by a detailed analysis of the statistical error in tomography reconstruction algorithms, illustrated with Monte-Carlo simulations.
- The fourth and last chapter presents the main experimental results of this thesis: the experimental deterministic and conditional teleportation of Schroedinger's cat states of light. It includes a simple presentation of the elementary theory of teleportation, and an extended model of wave-packet teleportation. In addition, it gives a description of the experimental setup, presents experimental results and their analysis using the model mentioned above.

The reading order proposed by this manuscript chapters arrangement does not have to be strictly observed, as chapters 2, 3 and 4 are mostly independent, to the exception of experimental results of Chaps. 2 and 4. Chapter 1 is included in this manuscript mostly as a necessary reference for the good understanding of equations and mathematical derivations and the rigorous definition of operators and mathematical objects appearing in the following chapters. However, some paragraphs in chapter 1, most notably in Secs. 1.3 and 1.5 go beyond simple textbook material and are referenced at several latter points.

Academic Publications and Conferences

The results of this thesis have been published in several scientific journal publications. In chronological order, they are:

- N. Lee, H. Benichi, Y. Takeno, S. Takeda, J. Webbs, E. Hungtington, and A. Furusawa, "Quantum teleportation of nonclassical wave packets: An effective multimode theory", *Science* **332**, 330 (2011).
- H. Benichi, S. Takeda, N. Lee, and A. Furusawa, "Teleportation of Non-Classical Wave-Packets of light", *Phys. Rev. A* **84**, 012308 (2011).
- H. Benichi, and A. Furusawa, "Optical homodyne tomography with polynomial series expansion", *Phys. Rev. A* **84**, 032104 (2011).

The first of this article presents the main experimental results on Schroedinger's cat state teleportation, which is the subject of Chap. 4 for teleportation, and Chap. 2 for Schroedinger's cat state generation. The second article presents a detailed theoretical model of the experiment, with careful considerations of its broadband characteristics. This model can be found in Chap. 4, over Secs. 4.1

and 4.2.4. The last article presents a related work on quantum tomography and demonstrate a new reconstruction algorithm of the Wigner function, which is included in Chap.3. At the time of writing, another article reporting on the results of Gaussian conditional teleportation is in preparation. The work of this thesis has also been presented through posters and presentations at the following international and domestic conferences:

- ButsuriGakkai64, 64th fall meeting of the Japanese Society of Physics, Kumamoto University, Japan, Sep 2009 (presentation, 25pZF-2).
- QIT21, the 21st Quantum Information Technology Symposium, Tokyo, Japan, Nov 2009 (presentation).
- SPQT 2010, Quantum Measurement and Control workshop, Sydney, Australia, Feb 2010 (poster).
- ISPQT 2010, International symposium on Physics of Quantum Technology, Tokyo, Japan, Apr 2010 (poster, 8TH-01).
- QCMC 2010, Tenth International Conference on Quantum Communication, Measurement and Computation, Brisbane, Australia, Jul 2010 (poster, P3-10).
- FIRST 2010, Annual meeting of the FIRST project on quantum information processing, Atami, Japan, Dec 2010 (poster).
- CLEO 2011, Conference on Laser and Electro-Optics, Baltimore USA, May 2011 (presentation, JTUF4).

Finally, during the CLEO US 2011 conference, the work of this thesis has been awarded by the Optical Society of America (OSA) with the Theodore Maiman Outstanding Student Prize, first prize, including a \$3000 cash prize.

Chapter 1

Quantum Theory of Light

In this first chapter, we expose the basic theory of quantum optics and give to the reader all the necessary elements to understand the content of the subsequent chapters. In Sec.1.1, we present the postulates of quantum mechanics which are assumed and used through the thesis. In Sec.1.2, we introduce the standard textbook toolbox of monomode quantum optics. In Sec.1.3, we focus on the phase-space representation of quantum states of light which constitutes our representation of choice for the analysis of experimental results in Chaps.2, 3 and 4. In Sec.1.4, we extend our monomode toolbox with the more uncommon formulae of multimode quantum optics. Finally in Sec.1.5, we presents basic elements on the thoery of the detection of light and measurements in quantum optics as well as useful models for non-ideal imperfect detection devices.

1.1 Quantum mechanics postulates

The main axioms of quantum mechanics are by themselves already quite rich of consequences on the physics of quantum phenomena and quantum systems. Therefore, before looking at the specific details of quantum optics, it is important to precisely define these axioms. We start first with some basic elements on general quantum mechanics.

1.1.1 Hilbert space representation

Usually, the first postulate of quantum mechanics is the *postulate of description* which assumes the existence of a complete \mathbb{C} -vector space usually labeled \mathcal{H} and whose norm-unity vectors are assumed to be the possible *quantum states* of a given physical system. To any *pure* physical state corresponds a unity norm vector in \mathcal{H} , and any unity norm vector in \mathcal{H} describes a possible physical state of the syste and carries all information about it. Here, *pure* is a sementic term we will explain in Sec.1.1.4. This vector space \mathcal{H} is commonly called the *Hilbert space* of the system. \mathcal{H} can be finite or infinite dimensional. An element of \mathcal{H} is a vector which is usually written with the *ket* convention $|x\rangle \in \mathcal{H}$ introduced by Dirac. Linear forms on \mathcal{H} are written with the *bra* convention $\langle x| : \mathcal{H} \rightarrow \mathbb{C}$. The *bra / ket* notation is useful to express the inner product, or scalar product, on \mathcal{H}

$$(|x\rangle, |y\rangle) = \langle y|x \rangle \in \mathbb{C}, \quad (1.1.1)$$

which is also called a *bra-ket*. \mathcal{H} is a vector space and guarantees the validity of the *superposition principle*: quantum states written as sums of the form $|\psi\rangle \propto (|\alpha\rangle - |\alpha'\rangle)$ are valid physical states of the system, provided their norm is unity. This principle is at the heart of many phenomena in quantum physics and is of interest to us as we will see in Chap.2. Furthermore, \mathcal{H} is a complete space which guarantees the existence of infinitely many orthonormal basis. There can be countable

basis $\{|x_n\rangle\}_{n \in I}$ satisfying the scalar orthogonality relation

$$\langle x_n | x_m \rangle = \delta_n^m, \quad (1.1.2)$$

and uncountable basis $\{|x\rangle\}_{x \in \Lambda}$ satisfying the similar functional orthogonality relation

$$\langle x | x' \rangle = \delta(x - x'). \quad (1.1.3)$$

These two species of orthogonal basis are usually respectively called *discrete* and *continuous* basis in the context of quantum physics. Any quantum state $|\psi\rangle$ can be decomposed on $\{|x_n\rangle\}_{n \in I}$

$$|\psi\rangle = \sum_{n \in I} c_n |x_n\rangle, \text{ where } c_n = \langle x_n | \psi \rangle, \quad (1.1.4)$$

or on $\{|x\rangle\}_{x \in \Lambda}$

$$|\psi\rangle = \int_{\Lambda} dx c(x) |x\rangle, \text{ where } c(x) = \langle x | \psi \rangle, \quad (1.1.5)$$

Finally, \mathcal{H} is a vector space on \mathbb{C} , which postulates the existence of a *quantum phase* and the associated quantum interference phenomena. The quantum phase is most of time dynamical in nature and can be calculated with the Schroedinger's equation. It can also carry interactions in quantum field SU1 gauge theories, or results from cyclic adiabatic trajectories in phase space in which case it is called *geometric phase*[3].

1.1.2 Operators

Linear operators on \mathcal{H} , written $\hat{O} : \mathcal{H} \rightarrow \mathcal{H}$, describe how external interactions or the self dynamic of the physical system change a quantum state $|x\rangle$ into $|y\rangle = \hat{O}|x\rangle$. The identity operator is written $\hat{\mathbb{1}}$. If it exists, the inverse of \hat{U} is written \hat{U}^{-1} . \hat{U} is unitary if and only if $\hat{U}\hat{U}^{-1} = \hat{U}^{-1}\hat{U} = \hat{\mathbb{1}}$. With the bra-ket notation, the projector on $|x\rangle$ is easily written $\hat{P}_{|x\rangle} = |x\rangle\langle x|$. Any orthonormal basis $\{|x_n\rangle\}_n$ follows the closure relation

$$\hat{\mathbb{1}} = \sum_n \hat{P}_{|x_n\rangle} = \sum_n |x_n\rangle\langle x_n|, \quad (1.1.6)$$

where the identity is decomposed onto a complete sum of orthogonal projectors cutting the Hilbert space in as many subvector spaces. In finite dimensional Hilbert spaces, any operator \hat{A} can be expressed as a matrix in the orthonormal basis $\{|n\rangle\}$

$$\hat{A} = \sum_{n,m} A_{n,m} |n\rangle\langle m|, \text{ where } A_{n,m} = \langle n | \hat{A} | m \rangle. \quad (1.1.7)$$

This representation is still valid with discrete orthonormal basis in infinite-dimensional Hilbert spaces. The Hermitian adjoint of \hat{A} is written \hat{A}^\dagger . If and only if $\hat{A} = \hat{A}^\dagger$, \hat{A} is an Hermitian operator whose eigenvalues are real numbers. According to the spectral theorem, any Hermitian operator \hat{A} can be diagonalized on the basis of its eigenvectors $\{|y_n\rangle\}$ as a sum of projectors

$$\hat{A} = \sum_n \langle y_n | \hat{A} | y_n \rangle \hat{P}_{|y_n\rangle} = \sum_n a_n |y_n\rangle\langle y_n|, \quad (1.1.8)$$

where $a_n = \langle y_n | \hat{A} | y_n \rangle$ are the real valued eigenvalues of \hat{A} .

1.1.3 Projective measurements

The second postulate of quantum mechanics is the *measurement postulate*. In its weak version, it states that any measurable variable or property of the system can be represented as a Hermitian operator $\hat{A} = \hat{A}^\dagger$ whose eigenvalues a_n are the only possible outcome of any experimental measurement of this variable. The probability p_n of measuring $a_n = \langle y_n | \hat{A} | y_n \rangle$ when the system is in the state $|\psi\rangle$ is assumed to be

$$p_n = |\langle y_n | \psi \rangle|^2. \quad (1.1.9)$$

After the measurement of a_n happening with probability p_n , the state of the system is projected with probability 1 onto the corresponding eigenstate $|y_n\rangle$. The expectation value $\langle a \rangle$ of the variable represented by \hat{A} is therefore by definition

$$\langle a \rangle = \sum_n p_n a_n. \quad (1.1.10)$$

With Eq.(1.1.8), $\langle a \rangle$ is also

$$\langle a \rangle = \langle \psi | \hat{A} | \psi \rangle. \quad (1.1.11)$$

The variance Δa^2 of the measurement is simply $\langle a^2 \rangle - \langle a \rangle^2$ where $\langle a^2 \rangle = \langle \psi | \hat{A}^2 | \psi \rangle$. Such measurements are known as *projective* measurements and are a special case of the stronger version of the measurement postulate involving *Positive Operator-Valued Measures* (POVM).

1.1.4 The density matrix and POVM measurements

In practice it is usually impossible to define the precise quantum state of a physical system with a single ket $|x\rangle$. Rather, the system is in an unknown statistical mixture of several kets, a state fundamentally different from a superposition of the same kets. In this situation the state of the system is said to be *mixed* or *impure*. To describe this statistical mixture of different quantum states, we use the density matrix operator $\hat{\rho}$ which can be any positive semi-definite operator on \mathcal{H} . To describe a system which can be found in several states $\{|x_k\rangle\}_k$ with probabilities p_k , $\hat{\rho}$ is simply written as a weighted sum of projectors onto the respective vectors $|x_k\rangle$

$$\hat{\rho} = \sum_k p_k |x_k\rangle \langle x_k|. \quad (1.1.12)$$

Although written as a single sum, ρ is not in a diagonal form because nothing ensures that the vectors $\{|x_n\rangle\}$ are orthogonal. Therefore, the matrix representation of $\hat{\rho}$ in a discrete orthonormal basis $\{|n\rangle\}$ becomes

$$\hat{\rho} = \sum_{n,m} \rho_{n,m} |n\rangle \langle m|, \text{ where } \rho_{n,m} = \langle n | \hat{\rho} | m \rangle = \sum_k p_k (x_k^n) (x_k^m)^*, \quad (1.1.13)$$

with $x_k^n = \langle n | x_k \rangle$. Notice that $\hat{\rho}$ is non-negative and $\langle \psi | \hat{\rho} | \psi \rangle \geq 0$ for any ket $|\psi\rangle$, therefore, the set of all admissible density matrices is also the set of convex sums of projectors onto pure states. If our system is described by a density matrix $\hat{\rho}$, the average value $\langle a \rangle$ of the operator \hat{A} is now expressed as the weighted sum of $\langle x_k | \hat{A} | x_k \rangle$ with weights p_k

$$\langle a \rangle = \sum_k p_k \langle x_k | \hat{A} | x_k \rangle. \quad (1.1.14)$$

Using the closure relation, we can rewrite $\langle a \rangle$ as

$$\langle a \rangle = \sum_k \langle x_k | \left(\sum_m |m\rangle \langle m| \right) \hat{A} \left(\sum_n |n\rangle \langle n| \right) |x_k \rangle = \sum_{n,m} \rho_{n,m} A_{m,n}, \quad (1.1.15)$$

which can be equivalently and concisely written with the *trace operation*

$$\langle a \rangle = \text{tr}[\hat{\rho}\hat{A}] = \sum_n \langle n | (\hat{\rho}\hat{A}) | n \rangle. \quad (1.1.16)$$

In the same way that a density matrix describes a mixed state, POVMs describe mixed measurements, or non-projective measurements. A POVM is a set of operators $\hat{O}_n = \hat{M}_n \hat{M}_n^\dagger$ following the closure relation $\sum_n \hat{O}_n = \hat{\mathbb{1}}$, where $\{\hat{M}_n\}$ is any set of operators on \mathcal{H} . The decomposition $\hat{O}_n = \hat{M}_n \hat{M}_n^\dagger$ ensures the positivity of \hat{O}_n

$$\forall x \in \mathcal{H}, \langle x | \hat{O}_n | x \rangle \geq 0, \quad (1.1.17)$$

a necessary condition for real-valued measurement outcomes. After a POVM measurement with outcome \hat{O}_n , the system in the original state $\hat{\rho}$ is projected onto the new states $\hat{\rho}'$

$$\hat{\rho}' = \hat{M}_n \hat{\rho} \hat{M}_n^\dagger / \text{tr}[\hat{\rho} \hat{O}_n]. \quad (1.1.18)$$

With only very general assumptions on the mathematical structure of the Hilbert spaces describing the quantum reality of physical systems, it is actually possible not to assume, but to deduce the measurement postulate and the formalism of the density matrix. Such an approach is based on the Gleason theorem [12, 77], on which more details can be found for example in [165].

1.1.5 Composite systems

Complex experimental systems can often only be described using a composite representation involving several Hilbert spaces $\mathcal{H}_1, \mathcal{H}_2, \dots$ to take into account the physical reality of the laboratory. In this situation, the state of the system is described with a quantum state $|\psi\rangle$ which is an element of \mathcal{H} , the tensor product of all Hilbert spaces $\mathcal{H} = \mathcal{H}_1 \otimes \mathcal{H}_2 \otimes \dots$. If $\{|n\rangle_i\}_{n \in \mathbb{N}}$ is an orthonormal basis of \mathcal{H}_i , then the canonical basis of \mathcal{H} is

$$\{|n_1\rangle_1 \otimes |n_2\rangle_2 \otimes \dots\}_{n_1 \in \mathbb{N}, n_2 \in \mathbb{N}, \dots}, \quad \text{or} \quad \{|n_1, n_2, \dots\rangle\}_{n_1 \in \mathbb{N}, n_2 \in \mathbb{N}, \dots} \quad (1.1.19)$$

Although \mathcal{H} itself can be written as a direct tensor product of its subspaces, due to the superposition principle its elements may be non-factorizable themselves over these subspaces, such as for example

$$|\psi\rangle = \frac{1}{\sqrt{2}} (|0\rangle_1 |0\rangle_2 + |1\rangle_1 |1\rangle_2), \quad (1.1.20)$$

often written with the more simple notation $(|0,0\rangle + |1,1\rangle)/\sqrt{2}$. Such states are called entangled states because there is no valid representation of such non-local superposition states as products of separate states with their own individuality. Similarly, it is possible for density matrices to be non-factorizable entangled operators. In general, tracing out the degrees of liberty of one Hilbert space in a composite system leads to a representation of the latter state of the system with a mixed density matrix over the remaining reduced Hilbert space. For example if we trace $|\psi\rangle\langle\psi|$ on $\hat{\mathbb{1}}_2$ the identity operator of \mathcal{H}_2 , we obtain

$$\text{tr}_2 (|\psi\rangle\langle\psi|) = \frac{1}{2} (\langle 0|_2 |\psi\rangle\langle\psi|_0 |_2 + \langle 1|_2 |\psi\rangle\langle\psi|_1 |_2) = \frac{1}{2} (|0\rangle_1 \langle 0|_1 + |1\rangle_1 \langle 1|_1) \quad (1.1.21)$$

Entangled states and entanglement is at the heart of quantum information processing, both as a way to achieve computational tasks, and also as the central cause of decoherence mechanisms due to spurious entanglement with the exterior environment. It turns out that entanglement is a very complex phenomenon far from full understanding. For example, there are different ways a state can be entangled and there are different classes of entanglement, which depends, among other things, on the dimensionality of every sub-Hilbert spaces and the number of them. The classification of entanglement categories, especially for mixed states in infinite-dimensional Hilbert spaces, is still a work in progress.

1.2 Monomode quantum optics

In this section we review the usual theory of monomode quantum optics. Without trying to be comprehensive, we only review the relevant and necessary elements for the good understanding of the following chapters of this thesis. Further details about the full theory of quantum optics can be found in many dedicated textbooks, for example [46, 115, 69, 28, 60].

1.2.1 Quantum description of light

The description of light involves oscillating and propagating electrical \vec{E} and magnetic \vec{B} spatial vector fields, or in other words, electromagnetic waves. The dynamics of \vec{E} and \vec{B} which constitutes the physics of light is governed in classical physics by the famous Maxwell's equations. In the absence of electrical charges and currents, in the microscopic they take the form of the following differential equations

$$\begin{aligned}\vec{\nabla} \cdot \vec{E}(x, y, z, t) &= 0, & \vec{\nabla} \times \vec{E}(x, y, z, t) &= -\partial_t \vec{B}(x, y, z, t), \\ \vec{\nabla} \cdot \vec{B}(x, y, z, t) &= 0, & \vec{\nabla} \times \vec{B}(x, y, z, t) &= \frac{1}{c} \partial_t \vec{E}(x, y, z, t),\end{aligned}\tag{1.2.1}$$

where c is the speed of light in the medium, \times is the vector product and $\vec{\nabla} = (\partial_x, \partial_y, \partial_z)$. Quantum optics starts with the quantification of the Maxwell's equation. For a full description of the process of quantification of the electrical and magnetic fields, see [28, 69]. Here, we simply assume the validity of this process and present a shortcut to the result. For every independent mode l of frequency ω_l of the Maxwell's equations we associate a classical Hamiltonian functional H

$$H = \left(\sum_l \frac{1}{2m} p_l^2 + \frac{1}{2} m \omega_l^2 x_l^2 \right).\tag{1.2.2}$$

where x and p are the position and momentum variables. H describes the dynamic of a classical harmonic oscillator, a single mode of the Maxwell's equations, where a mode is a pair of (x, p) position and momentum variables whose dynamics is independent from the other modes. These modes naturally emerge in the spatio-temporal decomposition of the Maxwell's equation, for example with Fourier analysis. In this paragraph we can assume that these modes are plane waves, but other spatio-temporal decompositions are possible and strongly depend on the geometry of the system and its geometric limit conditions. The standard quantization procedure promotes the position and momentum variables by a pair of normalized non-commuting operators, themselves called the position and momentum operators or quadratures:

$$x_l \rightarrow \sqrt{\hbar/m\omega_l} \hat{x}_l, \text{ and } p_l \rightarrow \sqrt{\hbar m \omega_l} \hat{p}_l, \text{ with } [\hat{x}_l, \hat{p}_l] = i.\tag{1.2.3}$$

Looking at the original electrical field equation, we can understand the meaning of the mass parameter m as being

$$m = \epsilon_0 / L^3,\tag{1.2.4}$$

where ϵ_0 is the so-called *vacuum permittivity* and L^3 is the quantification volume of the mode being looked at in the decomposition of the Maxwell's equations. For example for a quantified harmonic oscillator inside a cavity L^3 is simply the total volume of the spatial mode inside the cavity. The lower the quantification volume is the higher the mass of the oscillator becomes, and therefore the larger the amplitude electrical field. This effective mass parameter illustrates how far the electrical field pendulum can swing. H becomes the Hamiltonian operator \hat{H} which describes the self evolution of light waves without any external interactions and is written

$$H \rightarrow \hat{H} = \sum_l \frac{\hbar \omega_l}{2} (\hat{p}_l^2 + \hat{x}_l^2).\tag{1.2.5}$$

Literary, quantum optics could be limited to the standard procedure of quantification of the Maxwell's equations and Eq.(1.2.5), but however, we are mainly interested in the consequences of this quantification. We notice that the quantum description of light is essentially equivalent to the physics of the quantum harmonic oscillator. This remains true in the multi-mode analysis of light in Sec.1.4 where we study collections of independent quantum harmonic oscillators. In the remaining of this section we focus on a single quantized mode of the electrical field and write $H = \hbar\omega (\hat{x}^2 + \hat{p}^2) / 2$. Finally, from now on we will use the unit system $\hbar = 1$.

1.2.2 Quadratures operators

We begin with the quadrature representation of the quantum harmonic oscillator. \hat{x} and \hat{p} are Hermitian operators and therefore they have two associated eigenvector basis $\{|x\rangle\}_{x \in \mathbb{R}}$ and $\{|p\rangle\}_{x \in \mathbb{R}}$. These basis are continuous and the eigenvectors relationship is written

$$\hat{x}|x\rangle = x|x\rangle, \text{ and } \hat{p}|p\rangle = p|p\rangle, \quad (1.2.6)$$

with $x \in \mathbb{R}$ and $p \in \mathbb{R}$. Both basis are orthonormal so that $\langle x'|x\rangle = \delta(x - x')$ and $\langle p'|p\rangle = \delta(p - p')$. They also satisfy the closure relations

$$\frac{1}{\sqrt{2\pi}} \int_{\mathbb{R}} dq |q\rangle \langle q| = \frac{1}{\sqrt{2\pi}} \int_{\mathbb{R}} dp |p\rangle \langle p| = \hat{\mathbb{1}}. \quad (1.2.7)$$

Although a position ket $|x\rangle$ or momentum ket $|p\rangle$ is not a physical, normalized and measurable state, the quadrature representation is particularly useful to write the wave-function of the quantum state $|\psi\rangle$ in the position or momentum domains with a single scalar product

$$\psi(q) = \langle q|\psi\rangle, \text{ and } \tilde{\psi}(p) = \langle p|\psi\rangle, \quad (1.2.8)$$

where $\psi(q)$ and $\tilde{\psi}(p)$ constitute a Fourier pair

$$\tilde{\psi}(p) = \frac{1}{\sqrt{2\pi}} \int_{\mathbb{R}} dq \psi(q) e^{-ipq}, \quad \text{and} \quad \psi(q) = \frac{1}{\sqrt{2\pi}} \int_{\mathbb{R}} dp \tilde{\psi}(p) e^{+ipq}. \quad (1.2.9)$$

Plane waves $\langle p|q\rangle = \exp[-ipq]/\sqrt{2\pi}$ are a special case of wave function from which we can deduce that both basis $\{|x\rangle\}$ and $\{|p\rangle\}$ are images of each-other through the same isometric Fourier transform

$$|q\rangle = \frac{1}{\sqrt{2\pi}} \int e^{-ipq} |p\rangle dp, \quad \text{and} \quad |p\rangle = \frac{1}{\sqrt{2\pi}} \int e^{+ipq} |q\rangle dq. \quad (1.2.10)$$

Finally, we can define translation operators in position or in momentum as follow. If we define the operator $\hat{T}_{\hat{x}}(\lambda) = e^{-i\lambda\hat{p}}$ and then express the commutator $[\hat{x}, \hat{T}_{\hat{x}}(\lambda)]$ with \hat{x} in the following form

$$\hat{x}\hat{T}_{\hat{x}}(\lambda)|0\rangle = \hat{T}_{\hat{x}}(\lambda)(\lambda + \hat{x})|0\rangle = \lambda\hat{T}_{\hat{x}}(\lambda)|0\rangle, \quad (1.2.11)$$

we deduce the translation in position relationship $\hat{T}_{\hat{x}}(q)|0\rangle_x = |q\rangle$ where $|0\rangle_x$ is the quantum state of position zero. In the same fashion if we define $\hat{T}_{\hat{p}}(\mu) = e^{+i\mu\hat{x}}$ we obtain the translation in momentum relationship $\hat{T}_{\hat{p}}(p)|0\rangle = e^{+ip\hat{x}}|0\rangle_p = |p\rangle$. These two operators are can be implemented experimentally almost perfectly using highly reflecting mirrors and auxiliary light beams and constitutes *half-displacement* operations.

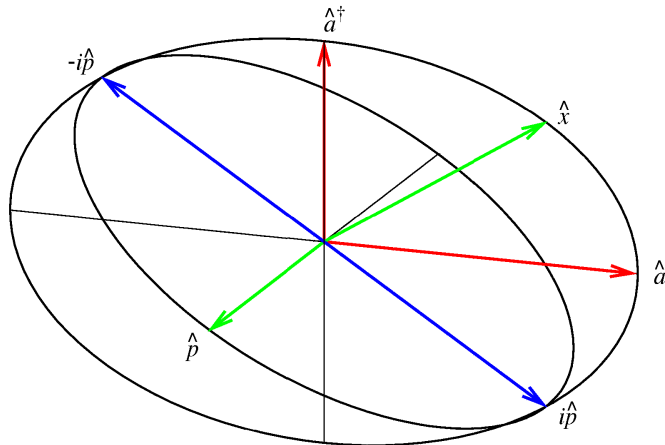


Figure 1.1: Relation between the (\hat{x}, \hat{p}) basis and the $(\hat{a}, \hat{a}^\dagger)$ basis. The complex multiplication by i is represented as a $\pi/2$ rotation around the \hat{x} axis.

1.2.3 Photon number states

If we introduce the operator \hat{a} and its Hermitian adjoint \hat{a}^\dagger , respectively called the *annihilation* and *creation* operators, by the relations

$$\hat{a} = (\hat{q} + i\hat{p}) / \sqrt{2}, \text{ and } \hat{a}^\dagger = (\hat{q} - i\hat{p}) / \sqrt{2}, \quad (1.2.12)$$

\hat{H} can be rewritten in the factorized form

$$\hat{H} = \hbar\omega \left(\hat{a}^\dagger \hat{a} + \frac{1}{2} \right) = \hbar\omega \left(\hat{n} + \frac{1}{2} \right). \quad (1.2.13)$$

The operator $\hat{n} = \hat{a}^\dagger \hat{a}$ is an Hermitian operator whose eigenvectors are written $|n\rangle$, with eigenvalues n .

$$\hat{a}^\dagger \hat{a} |n\rangle = \hat{n} |n\rangle = n |n\rangle \quad (1.2.14)$$

With the commutator relation $[\hat{a}, \hat{a}^\dagger] = 1$ it is possible to show that

$$\hat{a} |n\rangle = \sqrt{n} |n-1\rangle, \text{ and } \hat{a}^\dagger |n\rangle = \sqrt{n+1} |n+1\rangle, \quad (1.2.15)$$

from which we deduce that the admissible eigenvalues n are positive integer only, starting from 0. This integer spectrum is interpreted as the elementary particles of light, called photons, and \hat{n} is therefore called the *photon number* operator. For instance, $|3\rangle$ represents the state of exactly 3 energy quanta of light, while $|1\rangle$ is the state of exactly one quantum of light. $\{|n\rangle\}$ is called the photon basis, or the basis of photon number states. In quantum optics, it is the most commonly used representation for the density matrix $\hat{\rho}$. The eigenvector $|0\rangle$ of eigenvalue $\hat{n}|0\rangle = 0$ is called the *vacuum* state and also satisfies $\hat{a}|0\rangle = 0$. This translates into the differential equation $(q + \partial_q) \psi_0(q) = 0$, where $\psi_0(q) = \langle q|0\rangle$ and whose unique solution is

$$\psi_0(q) = \exp[-q^2/2]/\pi^{1/4}. \quad (1.2.16)$$

Any photon number state $|n\rangle$ can be written from the vacuum state $|0\rangle$ with successive iterations of the creation operator \hat{a}^\dagger

$$|n\rangle = \frac{(\hat{a}^\dagger)^n}{\sqrt{n!}} |0\rangle. \quad (1.2.17)$$

By turning the above relation into a differential equation with the correspondence rule $\hat{a}^\dagger \rightarrow q - \partial_q$, the wave-function $\psi_n(q) = \langle q|n\rangle$ of $|n\rangle$ can be expressed as

$$\psi_n(q) = H_n(q)\psi_0(q)/\sqrt{2^n n!}, \quad (1.2.18)$$

where H_n is the n^{th} order Hermite polynomial. The photon basis is also orthonormal and $\langle n|m\rangle = \delta_n^m$. It is complete and satisfies the closure relation $\sum_n |n\rangle\langle n| = \hat{1}$. Finally, the wave-functions $\psi_n(q)$ of the photon basis have the interesting property of being the eigenstates of the Fourier transform. Therefore for any n , ψ_n has the same algebraic expression in the position and momentum basis. In other words, photon number states give no information at all about the quadrature angle. Therefore, the photon number can be seen as the conjugate variable to \hat{n} , although this definition is mathematically fragile. Since the photon number states \hat{n} are also eigenstates of the Hamiltonian \hat{H} , it is natural that this symmetry is also found in the expression of \hat{H} in Eq.(1.2.5).

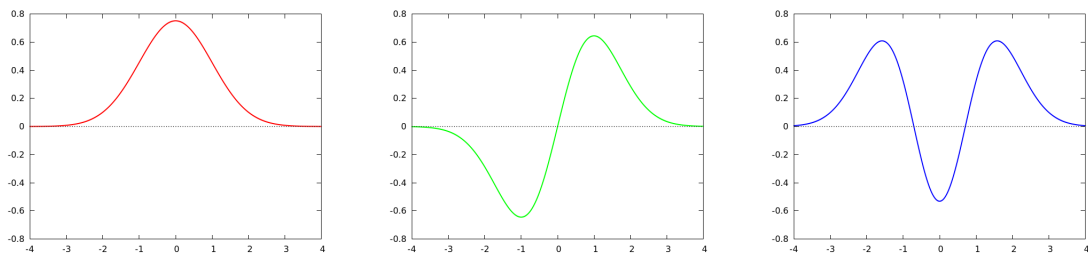


Figure 1.2: Examples of photon number state wave-functions in the position basis. Left: $|0\rangle$. Center: $|1\rangle$. Right: $|2\rangle$.

1.2.4 Phase shifting

The phase shifter operator \hat{U}_θ is defined by

$$\hat{U}_\theta = e^{-i\theta\hat{n}}, \quad (1.2.19)$$

with $\theta \in [0, 2\pi[$. Its action on \hat{a} is

$$\hat{U}_\theta^\dagger \hat{a} \hat{U}_\theta = \hat{a} e^{-i\theta}, \quad (1.2.20)$$

and can be calculated by deriving \hat{U}_θ with respect to θ and solving the differential equation $\partial_\theta \hat{U}_\theta^\dagger \hat{a} \hat{U}_\theta = i \hat{U}_\theta^\dagger [\hat{n}, \hat{a}] \hat{U}_\theta = -\hat{U}_\theta^\dagger \hat{a} \hat{U}_\theta$. In the position and momentum basis, the transformation becomes

$$\hat{x}_\theta = \hat{U}_\theta^\dagger \hat{x} \hat{U}_\theta = \cos \theta \hat{x} + \sin \theta \hat{p}, \quad \text{and} \quad \hat{p}_\theta = \hat{U}_\theta^\dagger \hat{p} \hat{U}_\theta = \cos \theta \hat{p} - \sin \theta \hat{x}. \quad (1.2.21)$$

The phase shifter operator is simply a rotation of the quadrature basis which can be used to define infinitely many quadrature operators basis $(\hat{x}_\theta, \hat{p}_\theta)$. It is important in the theory of optical homodyne tomography and appears in the expression of the Radon transform (see Sec. 3.1). For the case $\theta = \pi/2$, $\hat{U}_{\pi/2}$ is simply the Fourier operator which transforms \hat{x} to \hat{p} and \hat{p} to $-\hat{x}$. With the phase shifter operator, it is possible to extend the definition of the wave-function to any quadrature angle θ with the expression $\psi(q, \theta) = \langle q_\theta | \psi \rangle$ where $|q_\theta\rangle = \hat{U}_\theta^\dagger |q\rangle$. The relation between the original wave-function $\psi(q)$ in the position basis and the new wave-function in the rotated quadrature is given by a generalized angular Fourier transform. For the photon number state basis, this rotation simply takes the form of an additional phase factor

$$\psi_n(q, \theta) = H_n(q)\psi_0(q)e^{-in\theta}/\sqrt{2^n n!}. \quad (1.2.22)$$

1.2.5 Coherent states

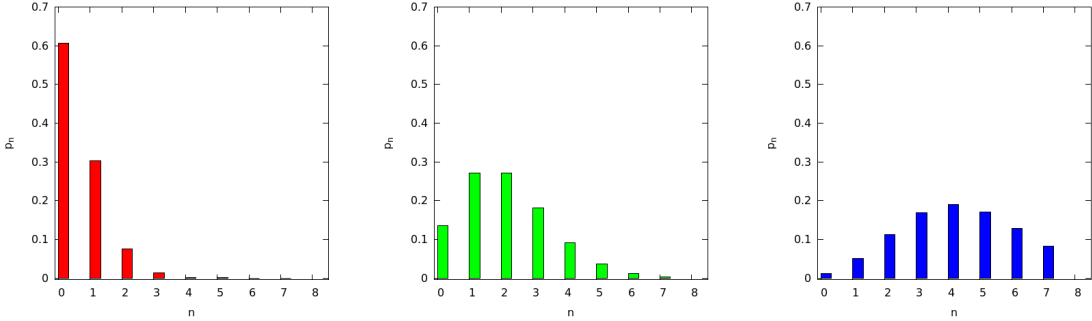


Figure 1.3: Example of photon number statistics for coherent states $|\alpha\rangle$. Left, $\alpha = 1$. Center, $\alpha = 2$. Right, $\alpha = 3$.

We introduce the unitary operator \hat{D}_α with the expression

$$\hat{D}_\alpha = e^{\alpha^* \hat{a} - \alpha \hat{a}^\dagger} = e^{ip_0 \hat{q} - iq_0 \hat{p}}, \quad (1.2.23)$$

where $\alpha = \frac{1}{\sqrt{2}}(q + ip)$ is any complex number. The Hermitian adjoint \hat{D}_α^\dagger of \hat{D}_α is $\hat{D}_{-\alpha}$. \hat{D}_α is called the *displacement* operator because its action on the annihilation operator \hat{a} is similar to a translation by the complex amplitude α

$$\hat{D}_\alpha^\dagger \hat{a} \hat{D}_\alpha = \hat{a} + \alpha. \quad (1.2.24)$$

Using the Baker-Hausdorff formula

$$e^{\hat{A} + \hat{B}} = e^{\hat{A}} e^{\hat{B}} e^{-[\hat{A}, \hat{B}]} = e^{\hat{B}} e^{\hat{A}} e^{[\hat{A}, \hat{B}]}, \quad (1.2.25)$$

we can decompose the displacement operator in the quadrature basis

$$\hat{D}_\alpha = e^{ip_0 q_0 / 2} e^{-iq_0 \hat{p}} e^{ip_0 \hat{q}} = e^{-ip_0 q_0 / 2} e^{ip_0 \hat{q}} e^{-iq_0 \hat{p}}, \quad (1.2.26)$$

which involves two separate translation operators on \hat{q} and \hat{p} . The effect of \hat{D}_α on \hat{x} and \hat{p} is therefore

$$\hat{D}_\alpha^\dagger \hat{q} \hat{D}_\alpha = \hat{q} + q, \quad \text{and} \quad \hat{D}_\alpha^\dagger \hat{p} \hat{D}_\alpha = \hat{p} + p. \quad (1.2.27)$$

Displacement operators can be concatenated in a vector-like fashion

$$\hat{D}_\alpha \hat{D}_\beta = \hat{D}_{\alpha+\beta} e^{i \text{Im}(\alpha \beta^*) / 2}. \quad (1.2.28)$$

We now define the set of coherent states $\{|\alpha\rangle\}_{\alpha \in \mathbb{C}}$ for any complex number α as the set of displaced vacuum states

$$|\alpha\rangle = \hat{D}_\alpha |0\rangle. \quad (1.2.29)$$

With Eq.(1.2.24), we deduce that coherent states are the eigenstates of the annihilation operator \hat{a}

$$\hat{a} |\alpha\rangle = \alpha |\alpha\rangle. \quad (1.2.30)$$

The wave-function $\psi_\alpha(x) = \langle x | \alpha \rangle$ of the coherent state of amplitude α can be derived from the vacuum state wave-function $\psi_0(x)$

$$\psi_\alpha(x) = \langle x | \hat{D}_\alpha | 0 \rangle = e^{ipx - ipq/2} \psi_0(x - q). \quad (1.2.31)$$

With Eq.(1.2.17), we deduce the photon number decomposition of $|\alpha\rangle$

$$|\alpha\rangle = e^{-|\alpha|^2/2} \sum_n \frac{\alpha^n}{\sqrt{n!}} |n\rangle. \quad (1.2.32)$$

We notice that the probability $p_\alpha(n)$ of measuring n photons in $|\alpha\rangle$ is equal to $|\alpha|^{2n} \exp(-|\alpha|^2)/n!$ and therefore follows a Poisson distribution. The average photon number $\langle n \rangle$ of $|\alpha\rangle$ is simply $|\alpha|^2$. This kind of Poissonian light statistics happens to describe very faithfully light emitted by laser sources. It is usually a safe approximation to model the light of a laser as a coherent state $|\alpha\rangle$ of intensity $\propto |\alpha|^2$. We deduce from the last equation the overlap formula of two coherent states $|\alpha\rangle$ and $|\alpha'\rangle$

$$\langle \alpha | \alpha' \rangle = \exp \left(-\frac{|\alpha|^2 + |\alpha'|^2}{2} + \alpha' \alpha^* \right). \quad (1.2.33)$$

We notice that coherent states are not strictly orthogonal. It turns out that the coherent state basis is over-complete and does not exactly follow the closure relation, but rather

$$\int d^2\alpha |\alpha\rangle \langle \alpha| = 2\pi. \quad (1.2.34)$$

The set of coherent states $\{|\alpha\rangle\}_{\alpha \in \mathbb{C}}$ has played an important historical role in the precise definition of the quantum theory of light by Glauber and others[115].

1.2.6 Squeezed states

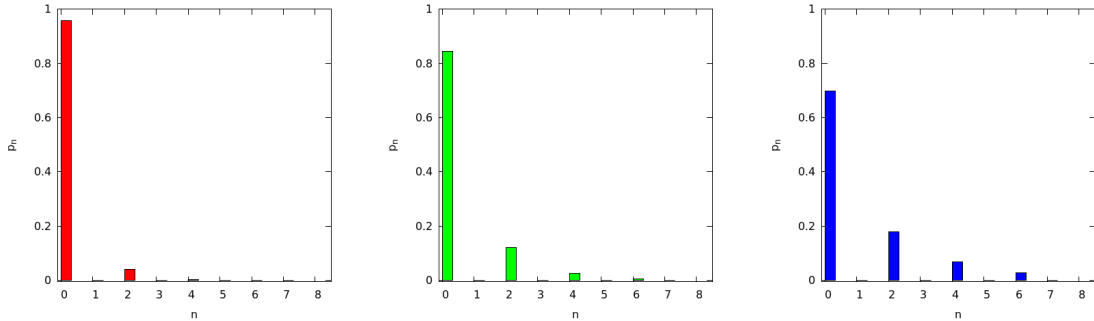


Figure 1.4: Example of photon number statistics for squeezed vacuum states $\hat{S}_s|0\rangle$. Left, $s = 0.3$. Center, $s = 0.6$ Right, $s = 0.9$.

We introduce the unitary *squeezing* operator \hat{S}_s , where $s \in \mathbb{R}$ is a real parameter, with the expression

$$\hat{S}_s = \exp \left[\frac{s}{2} ((\hat{a})^2 - (\hat{a}^\dagger)^2) \right]. \quad (1.2.35)$$

We notice that $\hat{S}_s^{-1} = \hat{S}_{-s}$. With its definition similar to the displacement operator \hat{D}_α , the squeezing operator is also called the *two-photon displacement* operator. Using the identity

$$e^{-\hat{B}} \hat{A} e^{\hat{B}} = \hat{A} + [\hat{B}, \hat{A}] + \frac{1}{2!} [\hat{B}, [\hat{B}, \hat{A}]] + \dots, \quad (1.2.36)$$

we deduce the effect of \hat{S}_s on \hat{a}

$$\hat{S}_s^\dagger \hat{a} \hat{S}_s = \cosh(s) \hat{a} - \sinh(s) \hat{a}^\dagger \quad (1.2.37)$$

and its characterization in the quadrature basis

$$\hat{S}_s^\dagger \hat{q} \hat{S}_s = e^{-s} \hat{q}, \quad \text{and} \quad \hat{S}_s^\dagger \hat{p} \hat{S}_s = e^{+s} \hat{p}. \quad (1.2.38)$$

The main property of the squeezing operator is to reduce the variance of one quadrature operator beyond the standard quantum noise level of the vacuum state, while the standard deviation of the orthogonal quadrature necessarily increases so that the Heisenberg inequalities are preserved

$$\langle 0 | \hat{S}_s^\dagger \hat{x}^2 \hat{S}_s | 0 \rangle = e^{-2s}/2, \quad \text{and} \quad \langle 0 | \hat{S}_s^\dagger \hat{p}^2 \hat{S}_s | 0 \rangle = e^{+2s}/2. \quad (1.2.39)$$

A state $\hat{S}_s | 0 \rangle$ is called a *squeezed vacuum* state. It is written in the photon basis

$$\hat{S}_s | 0 \rangle = (1 - \lambda^2)^{1/4} \sum_{n=0} \frac{\sqrt{(2n)!}}{n!} \left(\frac{\lambda}{2} \right)^n | 2n \rangle, \quad (1.2.40)$$

with $\lambda = \tanh(s)$. The mean photon number of a squeezed vacuum is $\langle \hat{n} \rangle = \sinh^2(s) \neq 0$. Such a squeezed quantum state can be produced with interaction Hamiltonian operators of the form $\propto (\hat{a})^2 - (\hat{a}^\dagger)^2$. Such hamiltonians can be engineered with non-linear optics, and for instance parametric-down conversion processes. The squeezed vacuum state is the primary resource of many quantum algorithms and circuits with applications to continuous variable quantum information processing. For instance, linear optics and ancilla squeezed vacuum states are the necessary and sufficient resources for Gaussian operations, such as teleportation or cluster state computation. Furthermore, we will see in Chap. 2 that squeezed vacuum states can also be used to generate non-Gaussian non-classical states by exploiting two-photons correlations present in squeezed vacuum states, and photon counting measurement operations.

1.2.7 Beam splitters

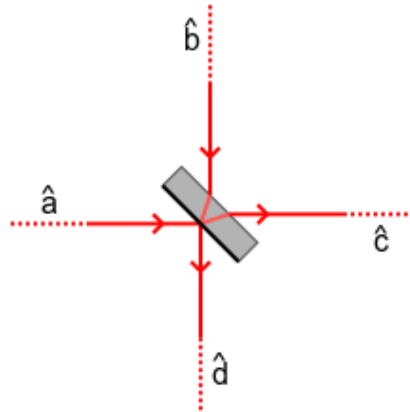


Figure 1.5: A beam-splitter with its input modes \hat{a}, \hat{b} and output modes \hat{c}, \hat{d} .

A beam-splitter is a 2 input ports 2 output ports passive device which stochastically splits incoming light on the input port and redistributes it towards the output port. It is a simple device, yet crucial for the field of quantum optics and the generation of quantum interferences with light. We consider two classical amplitudes E_1, E_2 at the input of a beam-splitter, whose two output electrical fields are E_3 and E_4 . The beam-splitter equations are written

$$E_3 = \cos \theta E_1 - \sin \theta E_2, \quad (1.2.41)$$

$$E_4 = \cos \theta E_2 + \sin \theta E_1, \quad (1.2.42)$$

where $\theta \in [0, 2\pi[$ is the amount at splitting of the beam-splitter. $\cos(\theta)$ and $\sin(\theta)$ are respectively the transmission and reflection coefficients T and R , in amplitude. The cosine/sine formulation automatically verifies the energy conservation rule $T^2 + R^2 = 1$. Eqs.(1.2.41) can also be put in the form of a matrix transformation

$$\begin{pmatrix} E_3 \\ E_4 \end{pmatrix} = B_\theta \begin{pmatrix} E_1 \\ E_2 \end{pmatrix}, \text{ with } B_\theta = \begin{pmatrix} \cos \theta & -\sin \theta \\ \sin \theta & \cos \theta \end{pmatrix}. \quad (1.2.43)$$

Since the quantization of the electrical field preserve the linear character of the Maxwell's equations, the effect of the beam-splitter on annihilation operators is written

$$\hat{c} = \cos \theta \hat{a} - \sin \theta \hat{b}, \quad (1.2.44)$$

$$\hat{d} = \cos \theta \hat{b} + \sin \theta \hat{a}, \quad (1.2.45)$$

where \hat{a} , \hat{b} , \hat{c} and \hat{d} are associated respectively to E_1 , E_2 , E_3 and E_4 . These two equations can also takes the same matrix form

$$\begin{pmatrix} \hat{c} \\ \hat{d} \end{pmatrix} = B_\theta \begin{pmatrix} \hat{a} \\ \hat{b} \end{pmatrix}. \quad (1.2.46)$$

which preserves commutators. We notice that B_θ is a unitary matrix and that $B_\theta^{-1} = B_\theta^T = B_{-\theta}$.

Heisenberg picture

We are looking for a unitary operator \hat{B}_θ which describes in the Heisenberg picture the beam-splitter input/output transformation of Eq.(1.2.44) in the following way

$$\hat{B}_\theta \begin{pmatrix} \hat{a} \\ \hat{b} \end{pmatrix} \hat{B}_\theta^\dagger = B_\theta \begin{pmatrix} \hat{a} \\ \hat{b} \end{pmatrix}. \quad (1.2.47)$$

As some other operators we saw in Secs.1.2.4, 1.2.5 and 1.2.6, \hat{B}_θ has a simple formulation as an exponential

$$\hat{B}_\theta = \exp \left[\theta \left(\hat{a}^\dagger \hat{b} - \hat{b}^\dagger \hat{a} \right) \right]. \quad (1.2.48)$$

When going through calculations with this specific expression of the beam-splitter operation, it is necessary to keep track of the current basis. In practice, it is necessary to know after every transformation if the current operators \hat{a} and \hat{b} represent the initial input modes or the output modes after the beam-splitter.

Schroedinger picture

In the Schroedinger picture, the action of \hat{B}_θ on the density matrix $\hat{\rho}$ is $\hat{\rho}' = \hat{B}_\theta^\dagger \hat{\rho} \hat{B}_\theta$ which translates in the photon basis to

$$\hat{B}_\theta^\dagger |n, m\rangle = \frac{1}{\sqrt{n!m!}} \hat{B}_\theta^\dagger a^{\dagger n} b^{\dagger m} \hat{B}_\theta |0, 0\rangle \quad (1.2.49)$$

with $\hat{B}_\theta^\dagger |0, 0\rangle = |0, 0\rangle$. The above expression can be decomposed into

$$\hat{B}_\theta^\dagger |n, m\rangle = \sum_{k=0}^n \sum_{l=0}^m B_\theta(n, m, k, l) |k+l, n+m-k-l\rangle \quad (1.2.50)$$

with the coefficients $B_\theta(n, m, k, l)$ given by

$$B_\theta(n, m, k, l) = (-1)^l \binom{n}{k} \binom{m}{l} \sqrt{\binom{n+m}{n} / \binom{n+m}{k+l}} (\cos \theta)^{m+k-l} (\sin \theta)^{n+l-k} \quad (1.2.51)$$

In the special case $m = 0$ where the second input port of the beam-splitter is in the vacuum state $|0\rangle$, Eq.(1.2.50) simplifies itself to

$$\hat{B}_\theta^\dagger |n, 0\rangle = \sum_{k=0}^n \sqrt{\binom{n}{k}} (\cos \theta)^k (\sin \theta)^{n-k} |k, n-k\rangle \quad (1.2.52)$$

which follows a binomial distribution. In other words, n photon at the input of a beam-splitter are randomly split to both output ports with probability $(\cos \theta)^2$, independently from each others. This is the stochastic nature of the beam-splitter splitting and quite naturally we understand that a beam-splitter can be thought of purely in term of classical physics, with the nuance that quantum coherence and quantum superposition are preserved because the beam-splitter splits amplitude and rather than intensity.

Model of linear losses

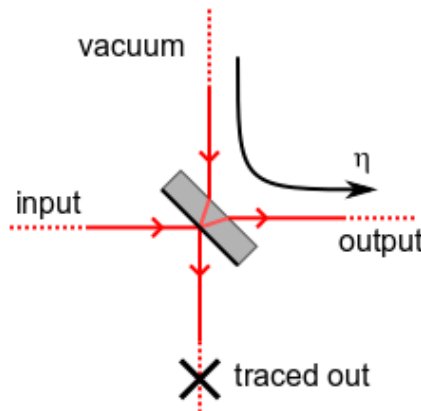


Figure 1.6: Representation of the beam-splitter model of linear amplitude losses.

In practice, quantum states of light generated in the laboratory suffer from experimental imperfections, and only a density matrix representation can faithfully describe such states. One of the main sources of imperfection is optical losses, random and uncorrelated absorption of light quanta. It happens that such optical losses can be easily modeled with the help of the beam-splitter formalism. The central idea of the model is to assume that losses are exactly proportional to the incoming amplitude of light. In other words, if a coherent state $|\alpha\rangle$ enters a system with an intensity transmission efficiency η , the output is the coherent state $|\sqrt{\eta}\alpha\rangle$. In the Heisenberg picture, this can be described by the transformation

$$\hat{a}' = \sqrt{\eta}\hat{a} + \sqrt{1-\eta}\hat{b}, \quad (1.2.53)$$

where \hat{b} is an auxiliary mode which carries away the energy taken from $|\sqrt{\eta}\alpha\rangle$. This relationship is exactly similar to Eqs.(1.2.44), provided $\cos \theta = \sqrt{\eta}$, and this model of amplitude dumping is

equivalent to the simple picture of a fictitious beam-splitter with a transmission coefficient $\sqrt{\eta}$. While the input quantum state suffers losses through the beam-splitter, the other input port of the beam-splitter is assumed to be $|0\rangle$. After the fictitious beam-splitter, the degrees of liberty introduced by the auxiliary mode are traced out. In the density matrix picture, if mode 1 is the input state $\hat{\rho}$, mode 2 is the auxiliary mode $|0\rangle\langle 0|$, the output state $\hat{\rho}'$ in mode 3 is expressed as

$$\hat{\rho}' = \text{tr}_4 \left[\hat{B}_\theta^\dagger \hat{\rho} \otimes |0\rangle_2 \langle 0|_2 \hat{B}_\theta \right]. \quad (1.2.54)$$

Eq.(1.2.52) can be used to conveniently detail this expression of $\hat{\rho}'$ in the photon basis. We notice that because the trace operation is partial only, we cannot change $\hat{B}_\theta^\dagger \hat{\rho} \otimes |0\rangle \langle 0| \hat{B}_\theta$ to $\hat{\rho} \otimes |0\rangle \langle 0|$ inside it with the circular trace formulae.

1.3 Phase space representations

We have seen in Sec.1.1 that the density matrix is most easily decomposed in the photon number basis. In this section instead of using a discrete representation of $\hat{\rho}$ we are interested in continuous representations $f(\alpha)$ of quantum states in phase space. Such continuous representations could for example look like $\int d^2\alpha f(\alpha) |\alpha\rangle\langle\alpha|$ and are known as *quasi-probability distributions* and it turns out there is infinitely many way to define such representations f . We will focus especially on the Wigner function which is the most convenient continuous representation to manipulate theoretically and to measure experimentally. A good reference for more details on the origin of most useful phase-space quasi-probability distributions and their relations to each other is [115]. [46] contains also an interesting summary of the most useful properties of the main phase-space distributions. More details about the Wigner function itself can be found in [69].

1.3.1 The Wigner function

The Wigner function was introduced by Wigner in [7] to describe corrections to classical thermodynamic equilibrium imposed by the early theory of quantum mechanics. The Wigner function is noted W and is uniquely defined from the density matrix $\hat{\rho}$ by the linear relation

$$W(q, p) = \frac{1}{2\pi} \int_{-\infty}^{+\infty} e^{ipx} \langle q - \frac{x}{2} | \hat{\rho} | q + \frac{x}{2} \rangle dx. \quad (1.3.1)$$

Here, q and p represent classical values of the phase space position and momentum variables. We will also sometime write $W(\alpha)$ with $\alpha = (q + ip)/\sqrt{2}$. The Wigner function has many interesting properties which make it a privileged tool of analysis in quantum optics. From its definition we notice that W is real and always definite. We will see in paragraph 1.3.1 that in addition, the Wigner function has a partial interpretation in term of probability distributions, which together with the two above properties, makes it the numerical representation of choice for quantum states. With Eq.(1.2.16) and the definition (1.3.1), we easily obtain the Wigner function $W_{|0\rangle}(q, p)$ of the vacuum state $|0\rangle$

$$W_{|0\rangle}(q, p) = e^{-q^2-p^2}/\pi. \quad (1.3.2)$$

$W_{|1\rangle}(q, p)$ is another Wigner function that we will use in Chap.2 and Chap.4

$$W_{|1\rangle}(q, p) = \frac{2}{\pi} (q^2 + p^2 - 1/2) e^{-q^2-p^2}. \quad (1.3.3)$$

Finally, the definition of Eq.(1.3.1) can be extended into a two-mode Wigner function $W_{1,2}(q_1, p_1, q_2, p_2)$ describing the sub-systems (\hat{q}_1, \hat{p}_1) and (\hat{q}_2, \hat{p}_2) . If the total density matrix $\hat{\rho}_{1,2}$ can be factorized into $\hat{\rho}_1 \otimes \hat{\rho}_2$, then $W_{1,2}(q_1, p_1, q_2, p_2)$ will also factorize into $W_1(q_1, p_1)W_2(q_2, p_2)$. In general such factorization is not possible and the Wigner function can also be used to account for entanglement.

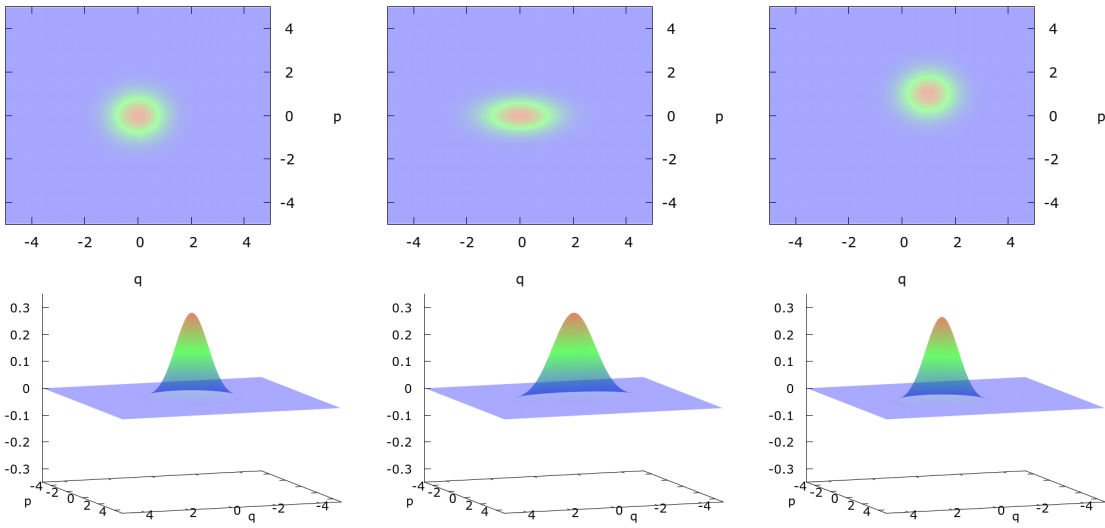


Figure 1.7: Examples of common Gaussian Wigner functions. Left: vacuum state $|0\rangle$. Center: squeezed vacuum state $\hat{S}_s|0\rangle$ with $s = 0.3$. Right: coherent state $|\alpha\rangle$ with $\alpha = (1 + i)/\sqrt{2}$.

Phase space transformations

Several unitary operators introduced in Sec. 1.2 have simple and interesting expressions in phase space with the Wigner function. If we displace the density matrix $\hat{\rho}$ whose Wigner function is $W(q, p)$ by $\alpha = (q_0 + ip_0)/\sqrt{2}$, then the Wigner function $W'(q, p)$ of $\hat{\rho}' = \hat{D}_\alpha \hat{\rho} \hat{D}_\alpha^\dagger$ is written

$$W'(q, p) = \frac{1}{2\pi} \int_{-\infty}^{+\infty} e^{ipx} \langle q - \frac{x}{2} | \hat{D}_\alpha \hat{\rho} \hat{D}_\alpha^\dagger | q + \frac{x}{2} \rangle dx \quad (1.3.4)$$

$$= \frac{1}{2\pi} \int_{-\infty}^{+\infty} e^{i(p-p_0)x} \langle (q - q_0) - \frac{x}{2} | \hat{\rho} | (q - q_0) + \frac{x}{2} \rangle dx. \quad (1.3.5)$$

The action of the displacement operator is a simple translation in phase space

$$W(x, p) \xrightarrow{\hat{D}_\alpha} W'(x, p) = W(x - x_0, p - p_0). \quad (1.3.6)$$

Therefore, the Wigner function W_α of the coherent state $|\alpha\rangle$ is simply $W_{|0\rangle}(q - q_0, p - p_0)$. In the same fashion, if we apply the squeezing operation $\hat{\rho} \rightarrow \hat{\rho}' = \hat{S}_s \hat{\rho} \hat{S}_s^\dagger$, then the Wigner function is transformed as

$$W(q, p) \xrightarrow{\hat{S}_s} W'(q, p) = W(e^{+s}q, e^{-s}p). \quad (1.3.7)$$

We immediately deduce the Wigner function $W_{\hat{S}_s|0\rangle}(q, p)$ of a squeezed vacuum as

$$W_{\hat{S}_s|0\rangle}(q, p) = W_{|0\rangle}(e^{+s}q, e^{-s}p) = \exp[-e^{+2s}x^2 - e^{-2s}p^2]/\pi. \quad (1.3.8)$$

The phase shifting operator \hat{U}_θ changes the Wigner function as

$$W(q, p) \xrightarrow{\hat{U}_\theta} W'(q, p) = W(\cos \theta q - \sin \theta p, \cos \theta p + \sin \theta q). \quad (1.3.9)$$

Finally, the beam splitter operator \hat{B}_θ will change the 2-mode Wigner function $W_{1,2}(q_1, p_1, q_2, p_2)$ into

$$W_{1,2}(q_1, p_1, q_2, p_2) \xrightarrow{\hat{B}_\theta} W'_{1,2}(q_1, p_1, q_2, p_2) = W_{1,2}(q'_1, p'_1, q'_2, p'_2). \quad (1.3.10)$$

with

$$\begin{pmatrix} q'_1 \\ -q'_2 \end{pmatrix} = B_\theta \begin{pmatrix} q_1 \\ q_2 \end{pmatrix}, \quad \text{and} \quad \begin{pmatrix} p'_1 \\ -p'_2 \end{pmatrix} = B_\theta \begin{pmatrix} p_1 \\ p_2 \end{pmatrix}. \quad (1.3.11)$$

Photon basis decomposition

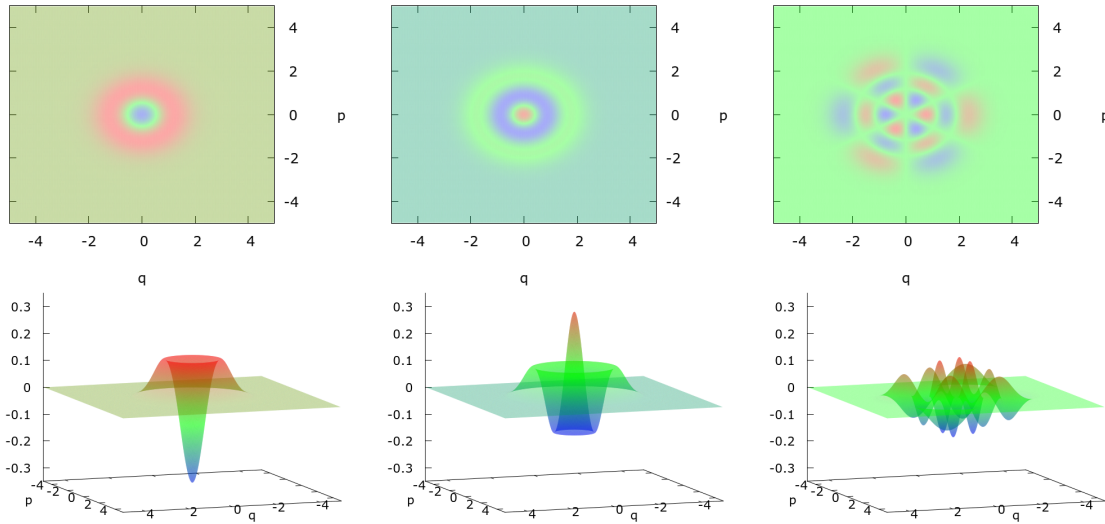


Figure 1.8: Examples of photon numbers Wigner functions. Left: $|1\rangle$. Center: $|2\rangle$. Right: real part of $|2\rangle\langle 5| + |5\rangle\langle 2|$.

If we write down the density matrix in the photon representation $\hat{\rho} = \sum_{n,m} \rho_{n,m} |n\rangle\langle m|$, thanks to the linearity of Eq.(1.3.1), we see that

$$W(q, p) = \sum_{n,m} \rho_{n,m} W_{n,m}(q, p), \quad (1.3.12)$$

where the functions $W_{n,m}(q, p)$, known as the Moyal functions of the harmonic oscillators [69], are defined as

$$W_{n,m}(q, p) = \frac{1}{2\pi} \int_{-\infty}^{+\infty} e^{ipx} \langle q - \frac{x}{2} | n \rangle \langle m | q + \frac{x}{2} \rangle dx, \quad (1.3.13)$$

and can be expressed for $n \geq m$ with the Laguerre polynomials $L_s^t(y)$ as

$$W_{n,m}(q, p) = (-1)^m \left(\sqrt{2}(q - ip) \right)^{n-m} \sqrt{m!/n!} L_m^{n-m} (2(q^2 + p^2)) W_{|0\rangle}(q, p), \quad (1.3.14)$$

with the symmetric expression for $m \geq n$. Because $|n\rangle\langle m|$ is not a physical state when $n \neq m$, $W_{n,m}(x, p)$ are complex functions, and we have the symmetry relation $W_{n,m}(q, p) = W_{m,n}^*(q, p)$. We notice that $W_{n,m}(0, 0) = (-1)^n \delta_n^m / \pi$, therefore we deduce the formula

$$W(0, 0) = \frac{1}{\pi} \sum_n (-1)^n \rho_{n,n}. \quad (1.3.15)$$

$W(0, 0)$ is usually called the *negativity* of the Wigner function. It is the central figure of merit for generation and teleportation of non-Gaussian states in Chaps.2 and 4 to evaluate the quality of experimental non-Gaussian states. In Chap.3, we will see how to evaluate the negativity $W(0, 0)$ with the process of quantum tomography.

Link with the marginal distribution

It is easy to show from the definition 1.3.1 of the Wigner function that

$$\int dp W(q, p) = \langle q | \hat{\rho} | q \rangle. \quad (1.3.16)$$

Furthermore we have seen in Eq.1.3.9 that the transformation $\hat{\rho}' = U_\theta \hat{\rho} U_\theta^\dagger$ changes the Wigner function to $W'(q, p) = W(q \cos \theta - p \sin \theta, p \cos \theta + q \sin \theta)$. Therefore, we also obtain after a $\pi/2$ rotation in phase space

$$\int dq W(q, p) = \langle p | \hat{\rho} | p \rangle. \quad (1.3.17)$$

Finally with further rotations, we can obtain the probability distribution of the position and momentum quadratures in any angular basis

$$\langle q | U_\theta \hat{\rho} U_\theta^\dagger | q \rangle = \int dp W(q \cos \theta - p \sin \theta, p \cos \theta + q \sin \theta). \quad (1.3.18)$$

The LHS of Eq.(1.3.18) is interpreted as the probability distribution of the position quadrature in the angular basis θ according to the measurement postulate. We explain in Sec.1.5 how this observable can be measured experimentally with a homodyne detector. The RHS of Eq.(1.3.18) is the Radon transform of the Wigner function. Eq.(1.3.18) is the central equation of Chap.3 and provides a way with optical homodyne detection to perform *quantum state tomography*, which is the reconstruction of an unknown quantum state's Wigner function $W(q, p)$ from angular resolved experimental measures of $\langle q | U_\theta \hat{\rho} U_\theta^\dagger | q \rangle$.

Correspondence rules

Since Eq.(1.3.1) defines a linear bijection between $\hat{\rho}$ and $W(q, p)$, any operation which can be described with the former density matrix can be described with the latter Wigner function. Here, we review the most useful links between the operator formalism and the Wigner function formalism. First of all, for any two operators \hat{A} and \hat{B} , we have the overlap formula

$$\text{tr} [\hat{A} \hat{B}] = 2\pi \int dq dp W^A(q, p) W^B(q, p), \quad (1.3.19)$$

where $W^A(q, p)$ is defined according to Eq.(1.3.1) with $\hat{\rho} \rightarrow \hat{A}$, whether A is Hermitian or not. More generally, a partial trace operation of $\hat{\rho}$ on mode (\hat{q}_i, \hat{p}_i) is expressed on W as an integration over \mathbb{R}^2 on the phase space variables (q_i, p_i) . A more general operator correspondence can be established between $\hat{\rho}$ and many phase-space representation of $\hat{\rho}$ [84]. We will only use these correspondence rules for the Wigner function $W(q, p)$

$$\begin{aligned} \hat{a} \hat{\rho} &\longrightarrow \left(\alpha + \frac{1}{2} \partial_{\alpha^*} \right) W(\alpha, \alpha^*), & \hat{\rho} \hat{a} &\longrightarrow \left(\alpha - \frac{1}{2} \partial_{\alpha^*} \right) W(\alpha, \alpha^*), \\ \hat{a}^\dagger \hat{\rho} &\longrightarrow \left(\alpha^* - \frac{1}{2} \partial_\alpha \right) W(\alpha, \alpha^*), & \hat{\rho} \hat{a}^\dagger &\longrightarrow \left(\alpha^* + \frac{1}{2} \partial_\alpha \right) W(\alpha, \alpha^*), \end{aligned} \quad (1.3.20)$$

with $\alpha = (q + ip)/\sqrt{2}$. Examples of the practical use of Eqs.(1.3.20) can be found in Secs.1.3.4.

Properties

We list in this paragraph the main properties of the Wigner function which are direct consequences of the definition (1.3.1). First, the Wigner function is a normed and bounded function

$$\int dqdpW(p, q) = 1, \text{ and } |W(q, p)| \leq 1/\pi. \quad (1.3.21)$$

From Eq.1.3.19 we deduce the expression of the mean value of an operator \hat{A} as

$$\langle \hat{A} \rangle = 2\pi \int dqdpW(q, p)W^A(q, p). \quad (1.3.22)$$

The expression of the inner product between two vectors $|\psi_1\rangle$ and $|\psi_2\rangle$ is

$$|\langle \psi_1 | \psi_2 \rangle|^2 = 2\pi \int dqdpW^1(q, p)W^2(q, p). \quad (1.3.23)$$

The purity of a quantum state is given by

$$\text{tr}[\hat{\rho}^2] = 2\pi \int dqdpW(q, p)^2. \quad (1.3.24)$$

It is interesting to notice that there is no widely accepted definition of the entropy based on the Wigner function. The von Neumann entropy $S = -\text{tr}[\hat{\rho} \ln \hat{\rho}]$ has no simple expression with $W(q, p)$. Other entropy measures can be defined directly with W , however, none of them seems to have better properties and prevail over the other for applications to the theory of quantum information processing. The consensus among theorists says that the absence of a simple canonical entropy measure for the Wigner function is a mathematical consequence of the infinite-dimensional nature of \mathcal{H} for continuous variable quantum systems such as the quantum harmonic oscillator.

1.3.2 The characteristic function

The two-dimensional Fourier transform $\chi(u, v)$ of the Wigner function $W(x, p)$ defined by

$$\chi(u, v) = \int \int dx dp W(x, p) e^{-ivx + iup}, \quad (1.3.25)$$

is called the *characteristic* function. The inverse transform is given by

$$W(x, p) = \frac{1}{4\pi^2} \int \int du dv \chi(u, v) e^{+ivx - iup}. \quad (1.3.26)$$

With this particular choice of Fourier norm and sign, $\chi(u, v)$ is equal to the Weyl function, which is defined as the mean value of the displacement operator \hat{D}_α^\dagger with $\alpha = (u + iv)/\sqrt{2}$

$$\chi(u, v) = \langle \hat{D}_\alpha^\dagger \rangle = \text{tr} [\hat{\rho} e^{-iv\hat{q} + iup\hat{p}}]. \quad (1.3.27)$$

The inverse transform of Eq.(1.3.27) is called the Weyl's expansion of the density matrix and is written

$$\hat{\rho} = \int d^2\alpha \hat{D}_\alpha^\dagger \chi(\alpha). \quad (1.3.28)$$

As we will see in Chap.3, the Weyl function has important properties for quantum tomography. Also, Eqs.(1.3.25) and (1.3.28) together with the definition of the Wigner function in Eq.(1.3.1) close the loop of quantum states representations.

1.3.3 Other phase-space representations

The next two most common phase-space representations of $\hat{\rho}$ after the Wigner function are the Husimi $Q(\alpha)$ and Glauber $P(\alpha)$ representations, with $\alpha \in \mathbb{C}$. The Husimi $Q(\alpha)$ function is a true probability distribution defined as

$$Q(\alpha) = \langle \alpha | \hat{\rho} | \alpha \rangle, \quad (1.3.29)$$

with $|\alpha\rangle$ a coherent state of amplitude α . $Q(\alpha)$ can be directly measured with a joint homodyne measurement of \hat{x} and \hat{p} [46]. The Glauber $P(\alpha)$ function is the counterpart of $Q(\alpha)$ in the sense that it describes $\hat{\rho}$ in the coherent state basis $\{|\alpha\rangle\}$ while $Q(\alpha)$ describes measurements of $\hat{\rho}$ in the same basis. $P(\alpha)$ is defined as the distribution which verifies

$$\hat{\rho} = \int d^2\alpha P(\alpha) |\alpha\rangle\langle\alpha|. \quad (1.3.30)$$

$P(\alpha)$ is not always a regular function and it exists mathematically only if it is permitted to be a sufficiently singular generalized function. Therefore, it is much harder to manipulate and impossible to measure in the general case. Q and P can be used to express respectively anti-normally and normally ordered products of creation and destruction operators

$$\langle (\hat{a})^n (\hat{a}^\dagger)^m \rangle = \int d^2\alpha Q(\alpha) \alpha^n (\alpha^*)^m, \quad (1.3.31)$$

$$\langle (\hat{a}^\dagger)^m (\hat{a})^n \rangle = \int d^2\alpha P(\alpha) \alpha^n (\alpha^*)^m. \quad (1.3.32)$$

We will not directly use Q or P in the following chapters, however, it is interesting to emphasize the connection between W , Q and P , which is especially useful to understand the effect of Gaussian decoherence processes such as amplitude dumping or teleportation on fragile non-Gaussian states (as in Sec.1.3.4 for instance). Similar to Eq.(1.3.25), we define χ_Q and χ_P the 2-dimensional Fourier transforms of Q and P by

$$\chi_Q(\lambda) = \int d^2\alpha Q(\alpha) e^{\lambda^* \alpha - \lambda \alpha^*}, \quad \text{and} \quad \chi_P(\lambda) = \int d^2\alpha P(\alpha) e^{\lambda^* \alpha - \lambda \alpha^*}. \quad (1.3.33)$$

Also similar to Eq.(1.3.27), χ_Q and χ_P can be expressed as expectation values of products of $\exp[-i\alpha\hat{a}^\dagger]$ and $\exp[-i\alpha^*\hat{a}]$ terms:

$$\chi_Q(\lambda) = \langle \exp[-i\alpha^*\hat{a}] \exp[-i\alpha\hat{a}^\dagger] \rangle, \quad \text{and} \quad \chi_P(\lambda) = \langle \exp[-i\alpha\hat{a}^\dagger] \exp[-i\alpha^*\hat{a}] \rangle. \quad (1.3.34)$$

With the Baker-Hausdorff formula of Eq.(1.2.25), it is easy to relate the three characteristic functions χ , χ_Q and χ_P of Eqs.(1.3.27) and (1.3.34) together. If we define a generalized characteristic function $\chi_g(u, v, s)$ parametrized by a real number s taken in $[-1, +1]$ by

$$\chi_g(u, v, s) = \chi(u, v) e^{s(u^2 + v^2)/4}, \quad (1.3.35)$$

we observe that

$$\chi_g(\lambda, -1) = \chi_Q(\lambda), \quad \chi_g(\lambda, 0) = \chi(\lambda), \quad \text{and} \quad \chi_g(\lambda, +1) = \chi_P(\lambda). \quad (1.3.36)$$

Taking the Fourier transform of Eq.(1.3.35), we obtain the definition of a generalized Wigner function $W_g(q, p, s)$, where $W_g(q, p, s)$ can be expressed from $W_g(q, p, s')$ for $s \leq s'$ with the convolution

$$W_g(q, p, s) = \frac{1}{\pi(s - s')} \int \int dq' dp' W_g(q', p', s') e^{((q - q')^2 + (p - p')^2)/(s - s')} \quad (1.3.37)$$

We immediately notice that the previously introduced phase-space representations W , Q and P are only special cases of this new generalized Wigner function $W(q, p, s)$:

$$Q(q, p) = W_g(q, p, -1) \quad W(q, p) = W_g(q, p, 0) \quad P(q, p) = W_g(q, p, +1) \quad (1.3.38)$$

We also notice in the case $s' = 0$ and $-1 \leq s \leq 0$ that Eq.(1.3.37) can be seen as a convolution of the original Wigner function W with a normalized 2-dimensional Gaussian G_σ of standard deviation σ

$$W_g(q, p, s) = W(q, p) \circ G_\sigma = W_g(q', p', -2\sigma^2), \quad (1.3.39)$$

with $\sigma = \sqrt{|s|/2}$. If we remember that Q is a true probability distribution and that therefore $Q(\alpha) \geq 0$ for all α , then for any negative Wigner function W , a convolution of W with a Gaussian of standard deviation σ larger than $1/\sqrt{2}$ will always lead to a positive Wigner function according to Eq.(1.3.39). In other words, if we say that a non-classical quantum state has necessary a negative Wigner function, that state can suffer at most losses equivalent to a Gaussian convolution with $\sigma \leq 1/\sqrt{2}$ and still keep a negative Wigner function. This is only a necessary criteria and there exists Wigner functions of mixed states whose negativity will disappear before the $1/\sqrt{2}$ threshold. In Chap.4, we apply Eq.(1.3.39) to the teleportation protocol to prove the $3dB$ threshold on non-classical states teleportation.

1.3.4 Linear absorption

Phase-space formulation

In the quantum models we develop in Chaps.2 and 4 for the experimental generated and teleported quantum states, we recurrently use the model of beam-splitters losses introduced in Sec.1.2.7. Here, we show how to adapt Eq.(1.2.54) to the Wigner formalism. First, if $\hat{\rho}$ and $\hat{\rho}'$ are the density matrices of the quantum state respectively before and after losses, using Eq.(1.3.30) we define the Glauber functions $P(\alpha)$ and $P'(\alpha)$ of these two density matrices by

$$\hat{\rho} = \int d^2\alpha P(\alpha)|\alpha\rangle\langle\alpha|, \quad \text{and} \quad \hat{\rho}' = \int d^2\alpha P'(\alpha)|\alpha\rangle\langle\alpha|. \quad (1.3.40)$$

As in Sec.1.2.7, we only assume that the model of linear amplitude dumping is equivalent to the transformation $|\alpha\rangle \rightarrow |\sqrt{\eta}\alpha\rangle$. Therefore, $\hat{\rho}'$ can be expressed with $P(\alpha)$ as

$$\hat{\rho}' = \int d^2\alpha P(\alpha)|\sqrt{\eta}\alpha\rangle\langle\sqrt{\eta}\alpha|, \quad (1.3.41)$$

and a straightforward change of variable proves that $P'(\alpha) = P(\alpha/\sqrt{\eta})/\eta$. Equivalently, we can write this relation with the generalized characteristic and Wigner functions as

$$\chi'_g(u, v, +1) = \chi_g(\sqrt{\eta}q, \sqrt{\eta}p, +1), \quad (1.3.42)$$

$$W'_g(q, p, +1) = \frac{1}{\eta}W_g(q/\sqrt{\eta}, p/\sqrt{\eta}, +1). \quad (1.3.43)$$

Applying Eq.(1.3.35) on both sides of Eq.(1.3.42), we obtain

$$\chi'_g(u, v, 0) = \chi_g(\sqrt{\eta}q, \sqrt{\eta}p, 1 - 1/\eta). \quad (1.3.44)$$

Coming back to the generalized Wigner formalism, Eq.(1.3.44) becomes

$$W'_g(u, v, 0) = \frac{1}{\eta}W_g(q/\sqrt{\eta}, p/\sqrt{\eta}, 1 - 1/\eta), \quad (1.3.45)$$

which translates with Eq.(1.3.37) into the convolution

$$W'(q, p) = \frac{1}{\eta} \frac{1}{2\pi\lambda^2} \int \int dq' dp' W(q', p') e^{-((q/\sqrt{\eta}-q')^2+(p/\sqrt{\eta}-p')^2)/2\lambda^2}, \quad (1.3.46)$$

with $\lambda = \sqrt{(1-\eta)/2\eta}$. In summary, the beam-splitter model of linear amplitude dumping has for the Wigner function the equivalent formula

$$W(q, p) \xrightarrow{\text{losses}} W'(q, p) = \frac{1}{\eta} (W \circ G_\lambda) \left(\frac{q}{\sqrt{\eta}}, \frac{p}{\sqrt{\eta}} \right). \quad (1.3.47)$$

Omitting the rescaling of phase space, if we apply Eq.(1.3.39) to this model, we find that the strongest amplitude losses η a non-classical state can suffer and still be a non-classical state, in the sense of negativity of the Wigner function, is given by

$$\lambda = \sqrt{(1-\eta)/2\eta} \leq 1/\sqrt{2}, \quad (1.3.48)$$

which gives $\eta \geq 1/2$. Finally, it can be easily proven with Eq.(1.3.46) that two linear amplitude dumping process in a row with amplitude losses coefficients η_1 and η_2 are equivalent to a single process with coefficient $\eta' = \eta_1\eta_2$.

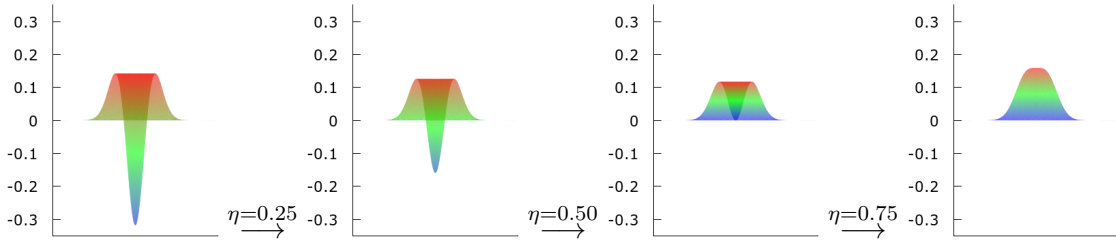


Figure 1.9: Attenuation of the Wigner function of a single photon state through a beam-splitter. From left to right, η equals successively 0, 0.25, 0.5 and finally 0.75.

Master equation

We now have two expressions, one in the photon number basis and one in phase-space, of the same linear amplitude dumping model. To put things in perspective, it is interesting to link Eq.(1.3.47) with the equivalent master equation formulation on $\hat{\rho}$, as was done for example in [110]. First we prove that Eq.(1.3.47) is equivalent to a differential equation. Let's introduce a fictitious time variable t and write $W(q, p) = W(q, p; t_0 = 0)$, $W'(q, p) = W(q, p; t_1 = t)$. We assume that the linear amplitude dumping is equivalent to a continuous dumping process between $t_0 = 0$ and $t_1 = t$ and write $\sqrt{\eta} \rightarrow \sqrt{\eta(t)} = \exp[-\gamma t]$ with γ a decay rate constant in Hertz. Eq.(1.3.46) is rewritten

$$W(q, p; t) = \frac{1}{\pi(1 - e^{-2\kappa t})} \int \int dq' dp' W(q, p; 0) \exp \left[-\frac{(q - e^{-\kappa t} q')^2 + (p - e^{-\kappa t} p')^2}{1 - e^{-2\kappa t}} \right]. \quad (1.3.49)$$

If we calculate the total time derivative $dW(q, p; t)/dt$ and partial spatial derivatives $\partial_q(W(q, p; t))$ and $\partial_p(W(q, p; t))$, we notice that the ersatz of Eq.(1.3.49) satisfies the differential equation

$$\frac{d}{dt} W(x, p; t) = \gamma \left(\partial_x x + \partial_p p + \frac{1}{4}(\partial_x)^2 + \frac{1}{4}(\partial_p)^2 \right) W(x, p; t). \quad (1.3.50)$$

With the correspondence rules of Eqs.(1.3.20), we immediately obtain the following master equation for $\hat{\rho}$

$$\frac{d}{dt}\hat{\rho}(t) = \gamma \left(2\hat{a}\hat{\rho}\hat{a}^\dagger - \hat{a}^\dagger\hat{a}\hat{\rho} - \hat{\rho}\hat{a}^\dagger\hat{a} \right), \quad (1.3.51)$$

written in the Linblad form as

$$\frac{d}{dt}\hat{\rho}(t) = L[\hat{\rho}(t)] \quad \text{with} \quad L[\hat{\rho}] = \gamma \left([\hat{a}, \hat{\rho}\hat{a}^\dagger] - [\hat{a}^\dagger, \hat{a}\hat{\rho}] \right). \quad (1.3.52)$$

This is the most simple possible form of the Linblad formulation of the master equation. As is explained in Chap.4, this model is not equivalent to the damped quantum harmonic oscillator connected to a heat bath at temperature $T \neq 0$. Rather, the master equation (1.3.51) describes a density matrix which will always relax back to the vacuum state $|0\rangle\langle 0|$ as we can notice when solving Eq.(1.3.51) for $d\hat{\rho}/dt = 0$. It therefore describes a perfect relaxation to the ground state of the oscillator at $T = 0$.

1.3.5 Gaussian formalism

Many usual states of quantum optics, such as coherent and squeezed states, have exactly Gaussian shaped Wigner functions and can therefore be described with very few parameters: namely $\langle \hat{q}^2 \rangle$, $\langle \hat{p}^2 \rangle$ and $\langle \hat{q}\hat{p} \rangle$. It is possible to have a systematic description of these states through their Gaussian correlation matrix Γ defined by

$$\Gamma = \frac{1}{2} \begin{pmatrix} \langle \hat{q}^2 \rangle & \langle \hat{q}\hat{p} \rangle \\ \langle \hat{q}\hat{p} \rangle & \langle \hat{p}^2 \rangle \end{pmatrix}. \quad (1.3.53)$$

The Wigner function of such states can be written using Γ only

$$W(q, p) = \frac{1}{\pi^d \det(\Gamma)} \exp \left[-\vec{\Phi}^T \Gamma^{-1} \vec{\Phi} \right], \quad \text{with } \vec{\Phi} = \begin{pmatrix} q \\ p \end{pmatrix}. \quad (1.3.54)$$

with $d = 1$ for a 1-mode Wigner function. Eqs.(1.3.53) and (1.3.54) can be extended to composite systems of more than 1 mode, with $\vec{\Phi} = (q_1, p_1, q_2, p_2, \dots)$ and $\Gamma = \langle \vec{\Phi} \cdot \vec{\Phi}^T \rangle$ and d equal to the number of modes involved. As expected, the Gaussian formalism is extremely useful to express in a compact way Gaussian operations on Gaussian states. In Sec.4.3 of Chap.4, we use the Gaussian formalism to conveniently express the 2-mode EPR correlations shared between Alice and Bob in the theory of the conditional teleportation protocol.

1.4 Multimode quantum optics

The monomode description of quantum optics we have seen in Sec.1.2 is implicitly based on the study of a single quantum harmonic oscillator. Although the physics of monomode quantum optics is already rich and usually enough to understand the core mechanism of many quantum phenomena, it is almost always irrelevant to actual experimental setups. Indeed, a pure monomode description assumes at the very least stationary light beams in every respect. Furthermore, a monomode description also ignores the complex spectral properties of detection devices or non-linear optical crystals. In this section, we expand the monomode picture of Sec.1.2 to a multimode quantum description of light. An interesting reference on the subject and one of the only textbook with a detailed study of multimode quantum optics is [60].

1.4.1 Time and frequency domains

By necessity, any multimode analysis has to be conducted in the Heisenberg picture. We start our multimode analysis in this paragraph with the introduction of annihilation and creation operators at different times and frequencies, in the Heisenberg picture.

Annihilation and creation operators

The quantum representation of time-dependent light beam with non-trivial spectral properties requires to extend the annihilation \hat{a} and creation \hat{a}^\dagger operators to every plane wave of frequency ω

$$\hat{a} \longrightarrow \hat{a}(\omega) = \hat{a}_\omega, \quad \text{and} \quad \hat{a}^\dagger \longrightarrow \hat{a}^\dagger(\omega) = \hat{a}_\omega^\dagger, \quad (1.4.1)$$

Implicitly, for every frequency mode ω , there is an associated Hamiltonian operator $\hat{H}_\omega = \omega(\hat{a}_\omega^\dagger \hat{a}_\omega + 1/2)$. Since all these Hamiltonians are independent quantum modes, the commutators between $\hat{a}(\omega)$ and $\hat{a}^\dagger(\omega')$ are

$$[\hat{a}(\omega), \hat{a}^\dagger(\omega')] = \delta(\omega - \omega'). \quad (1.4.2)$$

We define $\hat{a}(t)$ and $\hat{a}^\dagger(t)$ in the time domain with the Fourier transform pairs

$$\hat{a}(t) = \frac{1}{\sqrt{2\pi}} \int d\omega \hat{a}(\omega) e^{-i\omega t}, \quad (1.4.3)$$

$$\hat{a}(\omega) = \frac{1}{\sqrt{2\pi}} \int dt \hat{a}(t) e^{+i\omega t}. \quad (1.4.4)$$

The commutator in the time domain is $[\hat{a}(t), \hat{a}^\dagger(t')] = \delta(t - t')$. We want to emphasize that these different basis in the time or frequency domains only correspond to different decomposition of the Maxwell's equations in Eqs.(1.2.1). Therefore, the multimode character of light is not in any way a quantum property of it, but only a consequence of the dynamics of the Maxwell's equations. In other words, the multimode description of light in quantum optics is simply a choice of a specific point of view and a specific temporal basis to decompose the physical system under study. In the next section, we see how we can adopt a wave-packets description for multimode quantum optics, an approach fruitful to model the non-classical non-Gaussian states generated with photon subtraction in Chaps. 2 and 4. In most cases we are interested in a narrow band of frequency $[-\Delta\omega, +\Delta\omega]$ around the laser central carrier frequency ω_0 . In this situation we will often use sideband mode operators at frequency Ω , written in capital letters \hat{A} and \hat{A}^\dagger and defined as

$$\hat{A}_\Omega = \hat{a}_{\omega_0+\Omega}, \quad \text{and} \quad \hat{A}_t = \hat{a}_t e^{i\omega_0 t}. \quad (1.4.5)$$

Photon number and energy

We write down the total photon number operator over the frequency band $[-\Delta\omega, +\Delta\omega]$ as

$$\hat{n} = \int_{\omega_0-\Delta\omega}^{\omega_0+\Delta\omega} d\omega \hat{a}^\dagger(\omega) \hat{a}(\omega). \quad (1.4.6)$$

The total energy E is written

$$E = \int_{\omega_0-\Delta\omega}^{\omega_0+\Delta\omega} d\omega \omega \hat{a}^\dagger(\omega) \hat{a}(\omega), \quad (1.4.7)$$

with $\hbar = 1$. Usually, we can assume the narrow band approximation $2\Delta\omega \ll \omega_0$ to be valid and factorise the ω factor outside of the integral in Eq.(1.4.7), which yields for the instantaneous energy $E(t)$ at time t the simple expression $E(t) \propto \hat{n}(t) = \hat{a}^\dagger(t) \hat{a}(t)$, a relation we use in Sec. 1.5.2 to model a broadband homodyne detector.

1.4.2 Wave-packet states

We define a quantum mode $(\hat{a}_f, \hat{a}_f^\dagger)$ through the transformation

$$\hat{a}_f = \int d\omega \tilde{f}^*(\omega) \hat{a}(\omega) = \int dt f(t)^* \hat{a}(t), \quad (1.4.8)$$

$$\hat{a}_f^\dagger = \int d\omega \tilde{f}(\omega) \hat{a}^\dagger(\omega) = \int dt f(t) \hat{a}^\dagger(t). \quad (1.4.9)$$

where $\tilde{f}(\omega)$ is the Fourier transform of $f(t)$ and where $f(t)$ verifies $\int |f(t)|^2 dt = 1$ so that $[\hat{a}_f, \hat{a}_f^\dagger] = 1$. The commutator of \hat{a}_ω with \hat{a}_f^\dagger is given by

$$[\hat{a}(\omega), (\hat{a}_f^\dagger)^n] = n \tilde{f}(\omega) (\hat{a}_f^\dagger)^{n-1}. \quad (1.4.10)$$

The quantum mode defined by $f(t)$ can be effectively regarded as a wave-packet quantum mode unless $f(t)$ is simply the wave-function of a plane wave: $\exp[-i\omega t]$. Such a mode is adequate to describe pulses of light where the classical electrical field exactly follows $f(t)$. If we define $(\hat{A}_f, \hat{A}_f^\dagger)$ with the sideband operators $(\hat{A}_\Omega, \hat{A}_\Omega^\dagger)$, then $f(t)$ is the envelop of the classical electrical field quickly oscillating at the laser central carrier frequency ω_0 . Instead of using the time or frequency domains, it is actually possible to define a basis of such wave-packet quantum modes to describe all multimode properties of light. We introduce a set of functions $\{f_n(t)\}$ and define for every n a quantum mode \hat{a}_n by

$$\hat{a}_n = \int dt f_n(t) \hat{a}(t). \quad (1.4.11)$$

To ensure that $[\hat{a}_n, \hat{a}_m^\dagger] = \delta_n^m$ and obtain a valid multimode decomposition of the Maxwell's equations, the set of functions $\{f_n(t)\}$ needs only to verify $\int dt f_n(t) f_m^*(t) = \delta_n^m$ for every n and m . In other words, any set of orthonormal functions $\{f_n(t)\}$ can be used to define a set of independent wave-packet quantum modes describing as many independent quantum harmonic oscillators. The reverse transform of Eq.(1.4.11) is simply

$$\hat{a}(t) = \sum_n f_n^*(t) \hat{a}_n, \quad (1.4.12)$$

which allows to decompose a time domain or frequency domain expression onto a wave-packet modes basis. The closure relation $\sum_n f_n^*(t) f_n(t') = \delta(t - t')$ allows to easily go from Eq.(1.4.11) to Eq.(1.4.12).

One photon pulse

A one photon pulse of light with an electrical field described by $f(t)$ is simply written $|1\rangle_f = \hat{a}_f^\dagger |0\rangle$. In the frequency domain for example, it can really be thought of as a weighted superposition of single photon states over different frequencies

$$|1\rangle_f = \int_{-\infty}^{+\infty} d\omega f(\omega) (\hat{a}^\dagger(\omega) |0\rangle). \quad (1.4.13)$$

This is in practice the most faithful way to describe a freely propagating single photon quantum state of light in most experiments, where $f(\omega)$ would account for the spectral characteristics of the particle.

Coherent pulse

It is also possible to define a generalized coherent state $|\alpha\rangle_f$, where α is any complex number, as

$$|\alpha\rangle_f = \exp \left[\alpha \hat{a}_f^\dagger - \alpha^* \hat{a}_f \right]. \quad (1.4.14)$$

$|\alpha\rangle_f$ is an eigenstate of \hat{a}_f with eigenvalue α . It is also an eigenstate of $\hat{a}(t)$ or $\hat{a}(\omega)$ with the slightly different eigenvalue relations

$$\hat{a}(\omega)|\alpha\rangle = \alpha \tilde{f}(\omega)|\alpha_f\rangle, \quad \text{and} \quad \hat{a}(t)|\alpha\rangle = \alpha f(t)|\alpha_f\rangle. \quad (1.4.15)$$

Two photons pulse

Although we can define photon number states $|2\rangle_f, |3\rangle_f, \dots$ in a way similar to Eq.(1.4.13), a two photons pulse can show more complex spectral properties as well as entanglement between different spectral components. It is valid in general to write any two-photon state $|1+1\rangle$ in the form

$$|1+1\rangle = \frac{1}{\sqrt{2}} \int_{-\infty}^{+\infty} d\omega \int_{-\infty}^{+\infty} d\omega' g(\omega, \omega') \hat{a}^\dagger(\omega) \hat{a}^\dagger(\omega') |0\rangle, \quad (1.4.16)$$

with the only necessary restrictions that $\int d\omega \int d\omega' |g(\omega, \omega')|^2 = 1$ for normalization and that $g(\omega, \omega') = g(\omega', \omega)$ for bosonic commutation. To convince ourselves that $|1+1\rangle$ contains 2 photons, we compute $\langle 1+1 | \hat{n} | 1+1 \rangle$ where \hat{n} is given by Eq.(1.4.6) and obtain 2. Only if $g(\omega, \omega') = f(\omega)f(\omega')$ would we have the 2 photons number state $|2\rangle_f$ in the wave-packet $f(t)$. In the most general case, $g(\omega, \omega')$ describes frequency correlations between these two photons, and unless $g(\omega, \omega')$ can be factorized between both frequency variables, these photons are indeed entangled in their spectral components. Similar to Eq.(1.4.16), we can also define a two-photon pulses in two different spatial modes \hat{a} and \hat{b} by

$$|1_a, 1_b\rangle = \frac{1}{\sqrt{2}} \int_{-\infty}^{+\infty} d\omega \int_{-\infty}^{+\infty} d\omega' h(\omega, \omega') \hat{a}^\dagger(\omega) \hat{b}^\dagger(\omega') |0\rangle. \quad (1.4.17)$$

Here, the symmetry of $h(\omega, \omega')$ is not required and only $\int d\omega \int d\omega' |h(\omega, \omega')|^2 = 1$ is necessary.

1.4.3 Broadband squeezing

While Eq.(1.4.16) is useful to describe broadband squeezed vacuum states generated from the central degenerate mode of an optical parametric oscillator (OPO), Eq.(1.4.17) is useful do describe correlated photons generate by an OPO in symmetric resonant modes. To understand the multimode properties of the photon subtraction protocol, we are interested in Eq.(1.4.16) which we use in this section to define a broadband squeezing operator.

The first squeezing experiments were conducted both in the pulsed and the continuous regimes in the mid and late eighties [24, 26, 27]. In the continuous wave regime where it is difficult to obtain strong non-linear effects with low amplitude electrical field, OPOs play a central role for the generation of high purity squeezed quantum states. Although continuous wave regime setups are typically more complex than pulsed setups, these OPOs can indeed achieve higher level of squeezing and squeezed quantum states with higher purity[103, 126, 146]. For example, 12.7 dB is currently the highest level of squeezing seen experimentally, made with a monolithic cavity configuration based on a periodically poled potassium titanyl phosphate (PPKTP) crystal as reported in [157].

It is shown in [157] how this strongly squeezed light has been experimentally used to improve the noise floor of a Sagnac interferometer. It was noted early on that squeezed light emitted from

OPOs had complex spectral properties[22]. These spectral properties have been studied by many, both theoretically[22, 31, 34, 61, 78, 95, 106] and experimentally [74, 131]. We will not derive and get into the full details of the OPO theory, as it has been amply treated before. Instead, we only summarize the most important results and, more importantly, write the exact multimode squeezing operator we will use in Chap.2.

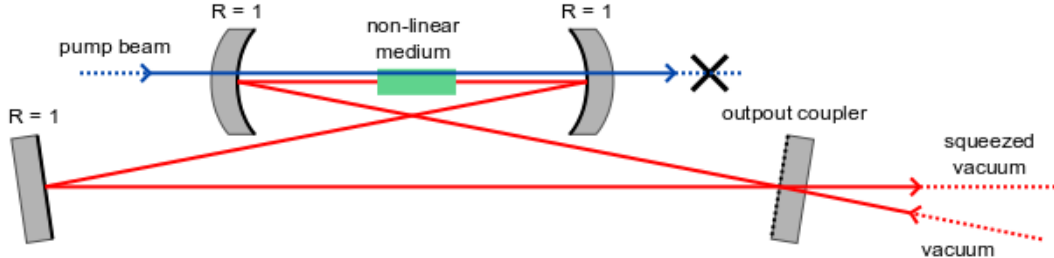


Figure 1.10: Typical bow-tie cavity based optical parametric oscillator.

Time and frequency correlation functions

With a careful model of the non-linear interaction Hamiltonian describing the parametric-down conversion process inside the non-linear crystal, and the consideration of the cavity around this crystal, it is possible to derive mean correlation functions in the output field annihilation and creation operators over the frequency or time variables [22, 31, 34]. For the degenerate central mode of an OPO, we have

$$\langle \hat{a}(t)\hat{a}(t') \rangle = \frac{\lambda^2 - \mu^2}{4} \left(\frac{e^{-\mu|t-t'|}}{2\mu} + \frac{e^{-\lambda|t-t'|}}{2\lambda} \right), \quad (1.4.18)$$

$$\langle \hat{a}^\dagger(t)\hat{a}(t') \rangle = \frac{\lambda^2 - \mu^2}{4} \left(\frac{e^{-\mu|t-t'|}}{2\mu} - \frac{e^{-\lambda|t-t'|}}{2\lambda} \right), \quad (1.4.19)$$

where $\lambda = \gamma/2 + \epsilon$ and $\mu = \gamma/2 - \epsilon$, with γ the cavity decay rate, including losses, and ϵ the non-linear gain in the crystal. For a non-degenerate OPO with two output modes \hat{a}_+ and \hat{a}_- , we have

$$\langle \hat{a}_\pm(t)\hat{a}_{\mp}(t') \rangle = \frac{\lambda^2 - \mu^2}{4} \left(\frac{e^{-\mu|t-t'|}}{2\mu} + \frac{e^{-\lambda|t-t'|}}{2\lambda} \right), \quad (1.4.20)$$

$$\langle \hat{a}_\pm^\dagger(t)\hat{a}_\pm(t') \rangle = \frac{\lambda^2 - \mu^2}{4} \left(\frac{e^{-\mu|t-t'|}}{2\mu} - \frac{e^{-\lambda|t-t'|}}{2\lambda} \right). \quad (1.4.21)$$

\hat{a}_+ and \hat{a}_- can be either two symmetric resonant modes around the central resonant mode of the OPO, or the two polarization central resonant modes of a type II OPO.

Broadband squeezing operator

In practice, Eqs.(1.4.18) and (1.4.20) are not sufficient for our purpose. We would rather know the expression of a multimode squeezed vacuum state with the help of an appropriately defined broadband squeezing operator. By combining the definition of the monomode squeezing operator

$\hat{S}_s = \exp[s((\hat{a})^2 - (\hat{a}^\dagger)^2)/2]$ in Eq.(1.2.35) and the expression of the two photons pulse state in Eq.(1.4.16), we can obtain such an operator with the substitution

$$\frac{s}{2}\hat{a}^2 \longrightarrow \int d\Omega d\Omega' \frac{g(\omega_0 + \Omega, \omega_0 - \Omega')}{2} \hat{a}(\omega_0 + \Omega)\hat{a}(\omega_0 - \Omega'), \quad (1.4.22)$$

where ω_0 is the laser carrier frequency and where $g(\omega_0 + \Omega, \omega_0 - \Omega')$ contains all the spectral properties of the parametric down conversion process in this particular OPO configuration. Since the OPO is pumped at $2\omega_0$ and the parametric-down conversion process conserves energy, $g(\omega_0 + \Omega, \omega_0 - \Omega')$ can be assumed to have the form $\zeta(\Omega)\delta(\Omega - \Omega')$ or $\zeta_\Omega\delta(\Omega - \Omega')$ with the sideband symmetry relation $\zeta_{+\Omega} = \zeta_{-\Omega}$. We obtain a simplified expression of the broadband squeezing operator as

$$\hat{S} = \exp \left[\int d\Omega \frac{\zeta_\Omega}{2} \left(\hat{A}_{+\Omega}\hat{A}_{-\Omega} - \hat{A}_{+\Omega}^\dagger\hat{A}_{-\Omega}^\dagger \right) \right], \quad (1.4.23)$$

with the sideband notation $\hat{A}_\Omega = \hat{a}(\omega_0 + \Omega)$. With the development rule of Eq.(1.2.36), we can write the effect of \hat{S} on sideband modes \hat{A}_Ω as the following Bogoliubov transformation

$$\hat{S}^\dagger \hat{A}_\Omega \hat{S} = \cosh(\zeta_\Omega) \hat{A}_\Omega - \sinh(\zeta_\Omega) \hat{A}_{-\Omega}^\dagger, \quad (1.4.24)$$

where the mixing of upper $+\Omega$ and lower $-\Omega$ frequency sidebands is readily apparent. With Eq.(1.4.24) we calculate the expression of the frequencies mean correlation functions as

$$\langle \hat{A}_\Omega^\dagger \hat{A}_{\Omega'} \rangle = (\sinh \zeta_\Omega)^2 \delta(\Omega - \Omega'), \quad (1.4.25)$$

$$\langle \hat{A}_\Omega \hat{A}_{\Omega'} \rangle = -\sinh(\zeta_\Omega) \cosh(\zeta_\Omega) \delta(\Omega + \Omega'). \quad (1.4.26)$$

By identification of Eqs.(1.4.18) and (1.4.25), we can relate the spectral correlation function ζ_Ω to the relevant OPO parameters γ and ϵ .

How different this new multimode squeezing operator is from the monomode formulation of Eq.(1.2.35)? To investigate this question we define a basis of wave-packets mode $\{\hat{A}_n\}$ using the set of real, symmetric and orthonormal functions $\{\phi_n(\omega)\}$ in the same way as in Eq.(1.4.11)

$$\hat{A}_n = \int d\Omega \phi_n(\Omega) \hat{A}_\Omega, \quad (1.4.27)$$

$$\hat{A}_\Omega = \sum_n \phi_n(\Omega) \hat{A}_n. \quad (1.4.28)$$

$$(1.4.29)$$

If $\zeta_\Omega = s$ happens to be a constant function, \hat{S} will be written

$$\hat{S} \stackrel{\zeta_\Omega=s}{=} \exp \left[\frac{s}{2} \sum_n \left((\hat{A}_n)^2 - (\hat{A}_n^\dagger)^2 \right) \right] = \bigotimes_n \exp \left[\frac{s}{2} \left((\hat{A}_n)^2 - (\hat{A}_n^\dagger)^2 \right) \right]. \quad (1.4.30)$$

Which is simply a factorized product of independent squeezing operators acting on different wave-packet modes. In this situation, monomode of multimode squeezing operators are the same. However, this is only a limit case or approximation at best, at least because the bandwidth of spectral correlations needs to be cut at some upper frequency point. In the general case, for any function ζ , \hat{S} can be written

$$\hat{S} = \exp \left[\frac{1}{2} \vec{A} \cdot \bar{\zeta} \cdot \vec{A} - \frac{1}{2} \vec{A}^\dagger \cdot \bar{\zeta} \cdot \vec{A}^\dagger \right], \quad (1.4.31)$$

where $\hat{\vec{A}}$ is the operator vector $(\hat{A}_0, \hat{A}_1, \dots)$ and $\bar{\zeta}$ is a matrix whose elements $(\bar{\zeta})_{n,m}$ are

$$(\bar{\zeta})_{n,m} = \int d\Omega \zeta_\Omega \phi_n(\Omega) \phi_m(\Omega). \quad (1.4.32)$$

The off-diagonal elements of the matrix $\bar{\zeta}$ describe the entanglement between the different wave-packet modes caused by the spectral correlation function ζ_Ω . With actual experimental parameters of typical OPOs in the weak pumping regime, these off-diagonal terms turn out to be only a fraction of the corresponding diagonal elements. In other words, they are almost invisible in measurements and irrelevant for numerical applications. Actual numerical applications can be found in [155] and [122, 121].

Eqs.(1.4.23) and (1.4.24) contain all the multimode behavior we need to correctly describe experimentally generated photon-subtracted squeezed vacuum states in Chap.2. Rather than introducing new tools, in this section we have explained how to combine the existing tools of Sec.1.2 in way a relevant for our purpose. From now on, the multimode description of light is essentially a matter of applying the definitions of this section with care and in the good spatio-temporal basis.

1.5 Detection of light

The possibility to build homodyne detectors able to resolve the power of the quantum shotnoise is a blessing for the field of quantum optics. These detectors can have signal to noise ratio of tens of decibels with off-the-shelves components such as PIN photodiodes and operational amplifiers. Without easy detection of light and the availability of low-noise electronics ICs and components, quantum optics would certainly not have known such a rapid experimental development. The microscopic details of light absorption by matter is a complex affair, but these complex phenomenon can be tamed to engineer physical detection devices with nice properties that can be described by simple and efficient models. The development of novel detection technologies is today an active field of research, with applications in major industries, such as imaging and video technologies, communication and information networks, solar energy, ... Until now the PIN photodiode has always been the bread and butter of light detection in quantum optics experiments, and is main focus our attention in this section. Some new technologies have recently made their appearance in laboratories with interesting non-linear properties for applications in quantum optics [152]. Currently the most promising technologies are certainly supra-conducting transition edge sensors[50, 65, 140] and super-conducting nanowire single-photon detectors[135, 148].

In this section, we focus on the description of light detection and review the PIN silicon photodiode both in its linear and avalanche regimes. In our description, we show how to include detection losses, electronic noise, and multimode properties of light detection.

1.5.1 Intensity detection

Intensity detection relies on the direct absorption of light by matter. At the quantum level, an intensity detector will only be able to measure $\hat{n} = \hat{a}^\dagger \hat{a}$ or some derivative of \hat{n} , but will not be able to measure linear combination of \hat{a} and \hat{a}^\dagger . The previously mentioned supra-conducting detectors have been shown to have photon number resolving properties, and be able to distinguish between different photon number states of light, therefore partially achieving the measurement operator $|n\rangle\langle n|$. Because of thermal agitation, PIN photodiodes are not at that level of precision, but offer other advantages in term of linearity, bandwidth, recovery time, and ease of utilisation.

Photodiodes

From an electrical point of view, the photodiode is simply a diode in parallel with a current source i called the *photocurrent*, where i is proportional to the incoming light intensity. A PIN photodiode is nothing else than a simple PIN diode, made with a P-N semiconductor junction and an additional "I" semiconductor layer in the middle, with silicon and gallium arsenide as the two main semiconductor technologies. The I layer acts as a pool of charge carriers and accepts carriers from the P and N layers until a threshold is reached and current starts to flow through the junction. This I layer drastically enhances the linearity of the photocurrent with incoming light. The photodiode effect is simply a consequence of the photoelectric effect where incoming photons are converted to charge carriers. PIN photodiodes are blessed with many desirable characteristics. First of all, being made of silicon for infrared light detection, they are quite inexpensive. In the infrared and near-infrared, they can be engineered to reach very high level of light conversion efficiency, a parameter also called quantum efficiency, with devices achieving near unit efficiency. Their detection bandwidth can reach the gigahertz range, usually at the expense of quantum efficiency, although 99% efficient diodes can be run in the range of tens of megahertz with ease. Their intrinsic dark current or dark noise, the electrical current generated at room temperature by a photodiode in the absence of incoming light, can be under 1 nA for silicon devices.

Linear regime

In the linear regime, PIN photodiodes are usually connected with a reverse voltage biasing across electrodes. The voltage bias reduces the capacity of the semiconductor layers, therefore increasing the bandwidth dramatically. The bias also induces some additional dark noise, usually in negligible amount. Thanks to the PIN architecture, the photocurrent i shows a linear response to the incoming light intensity \hat{n} on a dynamic scale of tens of magnitude order. At the quantum level, we can introduce \hat{i} the photocurrent operator which is assumed to be written

$$\hat{i} = g \sum_k \hat{a}_k^\dagger \hat{a}_k, \quad (1.5.1)$$

where g is the gain of the photodiode and k refers to all incident spatial modes illuminating the photodiode active area. In this scenario the classical variable photocurrent i is simply a random variable with a probability distribution $p(i)$ equal to

$$p(i) = \text{tr} \left[\hat{i} \hat{\rho} \right]. \quad (1.5.2)$$

1.5.2 Amplitude detection

With current technology, direct amplitude detection of an electrical field oscillating as fast as light is not possible. No electronics circuits can keep with optical frequencies at a sufficiently large bandwidth, although progress in nanotechnologies might allow for such devices in the future. Amplitude detection of light has to be achieved with indirect means, through interferences with light oscillating as fast or faster than the light beam to be measured. In pulse light experiments there is a variety of different interferometric measurement techniques for characterisation of ultra short pulses of light. In the continuous wave regime homodyne measurement is the main interferometric measurement.

Homodyne measurement

An homodyne detector is made of a beam splitter and two photodiodes. The incoming light mode is mixed on the beam-splitter with a *local oscillator* beam, which is a strong laser beam in a

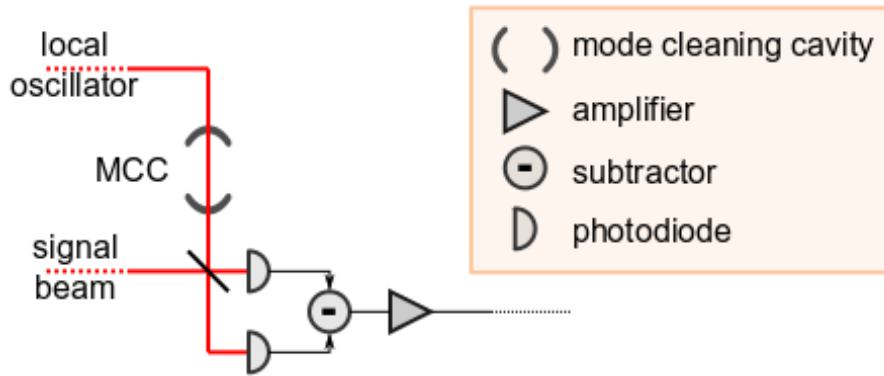


Figure 1.11: Setup for optical homodyne measurement. The mode cleaning cavity helps to enhance the overlap between the spatial modes of the signal and local oscillator.

coherent state $|\alpha\rangle$. Both output modes are measured separately by the two photodiodes, and the two photocurrents are then subtracted. The homodyne detector operator \hat{D} can be written in the output modes after the beam-splitter as

$$\hat{D} = g \left(\hat{d}^\dagger \hat{d} - \hat{c}^\dagger \hat{c} \right), \quad (1.5.3)$$

where g is the photodiode conversion gain. We rewrite \hat{D} in the input modes and obtain

$$\hat{D} = grt \left(\hat{a}^\dagger \hat{b} + \hat{a} \hat{b}^\dagger \right), \quad (1.5.4)$$

with r and t the amplitude reflection and transmission coefficients of the beam splitter. For a balanced homodyne detector, rt is maximal and is equal to $1/2$. The local oscillator is a strong laser beam in a coherent state $|\alpha\rangle$. We project mode \hat{b} onto the coherent state $|\alpha\rangle = |\rho e^{i\theta}\rangle$ and define the homodyne current operator $\hat{i} = \langle \alpha | \hat{D} | \alpha \rangle$ which reads

$$\hat{i} = grt\rho (\cos \theta \hat{x} + \sin \theta \hat{p}). \quad (1.5.5)$$

We notice that by controlling the relative phase θ of the local oscillator relatively to the incoming signal mode, the homodyne current \hat{i} can be adjusted to measure any angle in the quadrature basis. The intensity ρ^2 of the local oscillator can be adjusted to obtain a stronger photocurrent and a higher signal to noise ratio, within the limit of saturation of the photodiode semiconductor layers.

Detection of broadband light

If we want to measure light over a broad spectrum of frequencies, we need to consider the photocurrent operator at every point of time $\hat{i} \rightarrow \hat{i}(t)$. Typically we measure $\hat{i}(t)$ over some interval Δt and look at the Fourier transform of the time series $i(t)$ to analyse the frequency spectrum and look into the broadband properties of the electrical field. The expression of the homodyne detector operator of the previous paragraph is still valid as long as we consider \hat{D} for every time instant t .

$$\hat{D}(t) = grt \left(\hat{a}_t \hat{b}_t^\dagger + \hat{a}_t^\dagger \hat{b}_t \right). \quad (1.5.6)$$

We assume the inverse of the laser line-width to be smaller than any other time constant involved in the detection. Therefore, the projection of \hat{b} onto $|\alpha\rangle\langle\alpha|$ at time t simply adds a rapidly oscillating

complex phase whose power is averaged by the semiconductor layers inside the photodiodes and by the external electrical circuit. We expand the signal mode $\hat{a}(t)$ onto an orthonormal basis of wave-packet modes $\{f_n(t)\}$ and obtain for the multimode detector operator $\hat{D}(t)$

$$\hat{D}(t) = grt \sum_n f_n(t) \left(\hat{A}_n \hat{b}_t^\dagger + \hat{A}_n^\dagger \hat{b}_t \right), \quad (1.5.7)$$

and for the homodyne current

$$\hat{i}(t) = grt\rho \sum_n f_n(t) \left(\cos \theta \hat{X}_n + \sin \theta \hat{P}_n \right), \quad (1.5.8)$$

with \hat{X}_n and \hat{P}_n the wave-packet quadratures operators associated to the modes \hat{A}_n . We notice that the homodyne detector probes many different wave-packet modes at the same time in the same measurement. The photocurrent operators is indeed a sum of the different quadrature operators of all these modes, all measured at the same relative phase θ . From now on we assume $\theta = 0$ for simplicity. If we call $|y\rangle_n$ the eigenvector of the quadrature operator \hat{X}_n with eigenvalue y , then the eigenvectors of \hat{i} are

$$\bigotimes_m |y_m\rangle = |\vec{y}\rangle, \quad (1.5.9)$$

with eigenvalues

$$\sum_n f_n(t) y_n. \quad (1.5.10)$$

where $|\vec{y}\rangle$ is defined as $\bigotimes_m |Y_m\rangle$. We define the two additional vectors $\vec{f}(t) = (f_0(t), f_1(t), \dots)$ and $\vec{y} = (y_1, y_2, \dots)$ which we use to express the above eigenvector relation as

$$\hat{i}(t)|\vec{y}\rangle = (\vec{f} \cdot \vec{y}) |\vec{y}\rangle \quad (1.5.11)$$

In short, for every time series measurement of $\hat{i}(t)$ over an interval Δt , an eigenvalue \vec{y} is randomly observed with the underlying probability distribution $\langle \vec{y} | \hat{\rho} | \vec{y} \rangle$. Therefore the shotnoise normalized homodyne current $U(t)$ is a random process written

$$U(t) = (\vec{f} \cdot \vec{Y}) = \sum_n f_n(t) Y_n. \quad (1.5.12)$$

where the Y_n are random variables associated with the quadrature operators \hat{X}_n . The joint probability distribution of the Y_n exactly reads

$$p(Y_0 = y_0, Y_1 = y_1, \dots) = \langle y_0, y_1, \dots | \hat{\rho} | y_0, y_1, \dots \rangle. \quad (1.5.13)$$

The marginal distribution $p_n(y)$ of every Y_n is given by

$$p_n(y) = p(Y_n = y) = \langle y | \text{tr} [\hat{\rho}]_{m \neq n} | y \rangle. \quad (1.5.14)$$

If there is no entanglement between the different modes, every Y_n is an independent random variable and it is sufficient to only know the marginal distributions $p_n(y)$ for every Y_n . We see that with projections of the homodyne current $\int dt f_k(t) U(t)$ onto the different wave-packet modes, thanks to the orthogonality of the wave-packet basis $\{f_n(t)\}$, a smart analysis of the photocurrent time series can retrieve and separate every single mode. Furthermore, by combining the different projections $\int dt f_k(t) U(t)$ and looking at 2-modes correlation functions, it is also possible to retrieve entanglement between the different wave-packet modes.

1.5.3 Inneficient homodyne detection

There is no such things as a perfect measurement. In this section we investigate the effect of optical losses, imperfect homodyne visibility, imperfect photodiode conversion efficiency, and electronic noise on the process of homodyne measurement. Since the homodyne measurement is a Gaussian measurement, all these sources of imperfections can be modeled with the linear amplitude dumping model of Sec.1.3.4. Therefore, we prove for all these case their equivalence to the beam-splitter model of lineal amplitude losses.

Optical losses and finite quantum efficiency

The effect of any optical losses on the signal mode before the homodyne beam splitter has already been covered in Sec.1.3.4. Losses on the local oscillator beam only reduces its amplitude $|\alpha|^2$. We assume the presence of two beam-splitters with amplitude transmission coefficients $\sqrt{\eta}$ in front of the photodiodes. If we call \hat{e}, \hat{f} the auxiliary modes in the vacuum states mixed in at these additional beam-splitters, and \hat{c}', \hat{d}' the output modes incoming into the photodiodes, we can write the effect of these beam-splitters as

$$(\hat{d}^\dagger \hat{d}' - \hat{c}^\dagger \hat{c}') = \eta (\hat{d}^\dagger \hat{d} - \hat{c}^\dagger \hat{c}) + (1-\eta) (\hat{f}^\dagger \hat{f} - \hat{e}^\dagger \hat{e}) + \sqrt{\eta(1-\eta)} (\hat{c}^\dagger \hat{e} + \hat{e}^\dagger \hat{c} + \hat{d}^\dagger \hat{f} + \hat{f}^\dagger \hat{d}). \quad (1.5.15)$$

The first term of the RHS of Eq. is the expression of the homodyne detector operator \hat{D} from Eq.(1.5.3) without losses. The second term of the RHS of Eq.(1.5.15) has no contribution to the final photocurrent after modes \hat{e} and \hat{f} are projected onto the vacuum state. The third term of the RHS of Eq.(1.5.15) can be rewritten as

$$\frac{\sqrt{\eta(1-\eta)}}{2} (\hat{b}^\dagger (\hat{e} + \hat{f}) + \hat{b} (\hat{e}^\dagger + \hat{f}^\dagger)), \quad (1.5.16)$$

neglecting terms in \hat{a} . Keeping only the contributing terms of Eq.(1.5.15), the imperfect detector operator \hat{D}_η can be written as

$$\hat{D}_\eta \propto \sqrt{\eta} (\hat{b}^\dagger \hat{a} + \hat{a}^\dagger \hat{b}) + \frac{\sqrt{1-\eta}}{2} (\hat{b}^\dagger (\hat{e} + \hat{f}) + \hat{b} (\hat{e}^\dagger + \hat{f}^\dagger)) \quad (1.5.17)$$

$$\propto \hat{b}^\dagger \left(\sqrt{\eta} \hat{a} + \frac{\sqrt{1-\eta}}{2} (\hat{e} + \hat{f}) \right) + \hat{b} \left(\sqrt{\eta} \hat{a}^\dagger + \frac{\sqrt{1-\eta}}{2} (\hat{e}^\dagger + \hat{f}^\dagger) \right). \quad (1.5.18)$$

The effect of these beam splitters is equivalent to a single beam-splitter with amplitude transmission coefficient $\sqrt{\eta}$ placed on the signal beam before the homodyne detector. In essence, we have only shown that the additional beam-splitters can be commuted out of the homodyne detection into a single beam-splitter on the signal beam. Eq.(1.5.18) formally proves that any optical losses inside the homodyne detector can be described with the model of linear amplitude dumping of Sec.1.3.4 and a single transmission efficiency coefficient.

Imperfect quantum efficiency

The effect of imperfect quantum efficiency of photodiodes is exactly similar to optical losses in front of the photodiodes. This effect can be modeled in the same way as in the previous paragraph, and accounted for with a single parameter.

Imperfect spatial overlap

In the homodyne measurement technique, the local oscillator defines which spatial mode is being measured. In effect, only the photon flux of the signal beam in the exact same overlapping mode as the local oscillator is measured by the homodyne detector. In other words, an imperfect mode matching or imperfect overlap between the local oscillator and signal beams leads to a loss of information through the photons of the signal beam not interfering with the local oscillator. As with the previous loss mechanisms, a situation of imperfect spatial overlap can be fully described by the same linear amplitude dumping model with a single efficiency coefficient usually called the homodyne detector *visibility*. Details about the analysis of this effect can be found for example in [46].

Electronic noise

Finally we study the effect of additional electrical noise in the homodyne detector circuitry. A similar analysis can be found in [109]. We assume that we use homodyne detection to record the statistics of an unknown quantum state and use the homodyne current to perform tomographic reconstruction of the Wigner function (see Chap.3 for details). The homodyne current random variable i is crippled by an unknown Gaussian noise that cannot be distinguished from the information of the quantum state. We know from Eq.(1.3.18) that the Wigner function is linked to the probability distribution of the photocurrent by the Radon transform:

$$p(x, \theta) = \mathcal{R}(W) = \iint_{\mathbb{R}^2} W(q, p) \delta(x - q \cos \theta - p \sin \theta) dq dp, \quad (1.5.19)$$

$$= \int_{-\infty}^{+\infty} W(x \cos \theta - p \sin \theta, x \sin \theta + p \cos \theta) dp. \quad (1.5.20)$$

The difficulty of the analysis is to understand how a pure classical source of noise affects the purity of the quantum state being measured. In our analysis we will use the four following results:

1. If a random variable X has a distribution $p(X = x) = p_X(x)$ then the random variable aX has for distribution

$$p(aX = x) = \frac{1}{a} p(X = x/a). \quad (1.5.21)$$

In the case of a Gaussian distribution $G_\sigma(x)$ of standard deviation σ , we obtain the distribution $G_{a\sigma}(x)$.

2. If X and Y are two independent random variables with distribution $p_X(x) = p(X = x)$ and $p_Y(y) = p(Y = y)$, then the random variables $Z = X + Y$ has for distribution

$$p_Z(z) = p_{X+Y}(z) = (p_X \circ p_Y)(z). \quad (1.5.22)$$

In the case of two Gaussian distributions of standard deviations σ and σ' we obtain a Gaussian distribution of standard deviation $\sqrt{\sigma^2 + \sigma'^2}$.

3. If W_X and W_Y are two Wigner functions whose Radon transforms are the marginal distributions p_X and p_Y , then the Wigner function $W_Z = W_X \circ \circ W_Y$ has for Radon transform $p_X \circ p_Y$, where $\circ \circ$ denotes a 2-dimensional convolution:

$$\mathcal{R}(W_X \circ \circ W_Y)(x, \theta) = (\mathcal{R}(W_X) \circ \mathcal{R}(W_Y))(x, \theta). \quad (1.5.23)$$

4. If $p(x, \theta)$ is the Radon transform of $W(q, p)$, then the Radon transform of $W(q/a, p/a)$ is $ap(x/a, \theta)$:

$$\frac{1}{a} \mathcal{R}(W(q/a, p/a))(x, \theta) = \mathcal{R}(W(q, p))(x/a, \theta). \quad (1.5.24)$$

Armed with this four lemmes, we assume that the raw homodyne current U is the sum of two independent random variables X and Y

$$U = g(X + Y), \quad (1.5.25)$$

with g the detection gain. X is distributed according to $p(x, \theta)$ the distribution of the original quantum state we want to measure. Y is an additional Gaussian noise of standard deviation $\sigma = \epsilon/\sqrt{2}$. Now let's assume that we calibrate the homodyne detection with a measure of the variance of the vacuum state $|0\rangle$. Because this calibration also includes the electronic noise, the homodyne current is now the random variable V

$$V = g(X_0 + Y), \quad (1.5.26)$$

with X_0 having for distribution a Gaussian of standard deviation $1/\sqrt{2}$. From above results 1) and 2), V will be a Gaussian of standard deviation $\sigma_V = g\sqrt{1+\epsilon^2}/\sqrt{2}$. We now renormalize U to the measured vacuum noise standard deviation $\sqrt{2}\sigma_V$ and obtain

$$U \rightarrow U' = \frac{1}{\sqrt{2}\sigma_V} U = \frac{1}{\sqrt{(1+\epsilon^2)}}(X + Y). \quad (1.5.27)$$

According to results 1) and 2), the probability distribution of U' is

$$p(U' = x) = \sqrt{1+\epsilon^2} \left(p_X \circ G_{\epsilon/\sqrt{2}} \right) (\sqrt{1+\epsilon^2}x), \quad (1.5.28)$$

whose Wigner function $W_{U'}$ can be expressed with results 3) and 4) as

$$W_{U'}(q, p) = (1+\epsilon^2) \left(W_x \circ G_{\epsilon/\sqrt{2}} \right) (\sqrt{1+\epsilon^2}q, \sqrt{1+\epsilon^2}p). \quad (1.5.29)$$

If we now define $\eta = 1/(1+\epsilon^2)$, we obtain

$$W_{U'}(q, p) = \frac{1}{\eta} (W_x \circ G_\lambda)(q/\sqrt{\eta}, p/\sqrt{\eta}), \quad (1.5.30)$$

with $\lambda = \sqrt{(1-\eta)/2\eta}$. This results is exactly equivalent to the beam-splitter model of linear losses in Eq.(1.3.47) of Sec.1.3.4. In the case that U is normalized at the raw shotnoise standard deviation of X_0 , according to results 3) we can achieve the tomography reconstruction of the Wigner function W defined by

$$W(q, p) = (W_x \circ G_\sigma)(q, p). \quad (1.5.31)$$

This formula is exactly the outcome of unity gain teleportation (see Chap.4 for details). In both cases, the electronic noise from the homodyne circuit adds a Gaussian filtering process to the reconstructed Wigner function and decreases the quality of the tomographic reconstruction. Although this analysis appears to be unnecessary and somewhat redundant with the results of Eqs.(1.5.15) and (1.5.18), it can easily be applied to broadband photocurrent operators and random variables of Eqs.(1.5.8) and (1.5.12) in the multimode regime. As is shown in Chap.2, this property is crucial to understand practical experimental handling of a noisy broadband photocurrent where, for example, the effect of electrical high pass filter needs to be accounted for precisely.

1.5.4 Avalanche regime

A photodiode operated in the avalanche regime is simply reverse biased with a much stronger voltage. In this regime, the voltage bias is large enough so that the internal gain inside the semiconductor triggers an avalanche of charge carriers for every photoelectric conversion event. In practice the avalanche is amplified to be large enough for a visible current spike to appear and be detected by some external circuit. After the detection of a current spike, the external circuit pulls off immediately the reverse voltage bias and waits for the avalanche carriers to dissipate. Once the diode is quiet enough and ready for the next avalanche, the external circuit rearms the reverse voltage bias. This trigger pulling and rearming mechanism implies a recovery time during which the photodiode is blind to any incoming light. This recovery time also limits the maximum rate of detection events per second.

In the avalanche regime, the photodiode acts as a Geiger counter able to detect individual photons at precise time. This behavior is crucial for the generation of non-classical non-Gaussian states of light as explained in Chap.2. At the quantum level, avalanche photodiodes are effectively sensible to single quanta of light. They can be used to detect single photons and therefore are the perfect non-linear detector for many experiments in quantum optics, both in the qubit and continuous variable regimes. There are several ways to model the measurement operator describing the action of the avalanche photodiode, all of them being equivalent in the case of a very weak incoming light flux.

Click detector

The click detector model assumes that the action of the avalanche photodiode is equivalent to \hat{a} . The measurement is written

$$\hat{\rho} \rightarrow \hat{\rho}' = \hat{a}\hat{\rho}\hat{a}^\dagger / \text{tr} [\hat{a}\hat{\rho}\hat{a}^\dagger]. \quad (1.5.32)$$

Since the photodiode absorbs the light, the degrees of liberty of the incoming mode of light are traced out, and the formulation of Eq.(1.5.32) is only relevant if $\hat{\rho}$ is a multimode density matrix. More precisely, Eq.(1.5.32) should reads

$$\hat{\rho}_{1,2} \rightarrow \hat{\rho}'_1 = \text{tr}_2 (\hat{a}_2 \hat{\rho}_{1,2} \hat{a}_2^\dagger) / \text{tr}_{1,2} (\hat{a}_2 \hat{\rho}_{1,2} \hat{a}_2^\dagger). \quad (1.5.33)$$

There are slight differences between Eqs.(1.5.32) and (1.5.33) that are illustrated in Sec.2.2.2. With the correspondence rules of Eqs.(1.3.20), the click detector model on the 2-modes Wigner function $W_{1,2}(q, p, q', p')$ is written as

$$W'_2(q, p) \propto \int \int dq' dp' \left((q' + \partial_{q'})^2 + (p' + \partial_{p'})^2 \right) W_{1,2}(q, p, q', p'), \quad (1.5.34)$$

where (q', p') is the mode measured by the photodiode. This is the most simple model to describe an avalanche photodiode. It hides many operational details, yet it is surprisingly efficient to understand the physics of photon subtracted states. The click detector model works especially well when photon number states higher than $|1\rangle$ are rare at the photodiode.

On/Off detector

Since an avalanche photodiode cannot discriminate between a one photon avalanche or a two photons avalanche, it is necessary to include detection events beyond $|1\rangle$. The on/off detector models assume that the avalanche photodiode can trigger an avalanche on any quantum states

which is not the vacuum state. The measurement operator model is thus a 2 operators POVM model, with $\hat{\Pi}_{\text{off}}$ describing no incoming light

$$\hat{\Pi}_{\text{off}} = |0\rangle\langle 0|, \quad (1.5.35)$$

and $\hat{\Pi}_{\text{on}}$ describing any incoming light

$$\hat{\Pi}_{\text{on}} = \sum_{n \geq 1} |n\rangle\langle n| = \hat{\mathbb{1}} - \hat{\Pi}_{\text{off}}. \quad (1.5.36)$$

This model easily translates in the Wigner function formalism into

$$W'(q, p) = 2\pi \int \int dq' dp' W_{\text{det}}(q', p') W(q, p, q', p'), \quad (1.5.37)$$

where W is the 2-modes Wigner function before detection and W_{det} is the Wigner operator of $\hat{\Pi}_{\text{on}}$ given by

$$W_{\text{det}}(q, p) = \frac{1}{\pi} \left(\frac{1}{2} - e^{-q^2-p^2} \right). \quad (1.5.38)$$

There are significant differences between the click detector and on/off detector models only when higher photon number events are common enough. In this regime, the quantum efficiency of the photodiode becomes more and more important for the precise accounting of photon number events detection probabilities.

Number resolving detector

The photon number resolving detector is an ideal model far from the reality of the avalanche photodiode. It is however interesting to consider it for the theory of photon subtraction. The ideal photon number detector is described by the set $\{\hat{\Pi}_n\}$ of projectors onto number states

$$\hat{\Pi}_n = |n\rangle\langle n|. \quad (1.5.39)$$

By combining the on/off detector model of Eq.(1.5.36) with the photon number projectors of Eq.(1.5.39), it is possible to develop a POVM model which describes very well physical avalanche photodiode detectors[104]. For n incoming photons, the photodiode will fire an avalanche if it absorbs one or more photon. Therefore the probability p_n of an avalanche is 1 minus the probability of no photon absorption. If η is the quantum efficiency of the photodiode, p_n is $1 - (1 - \eta)^n$. $\hat{\Pi}_{\text{on}}$ can be then rewritten

$$\hat{\Pi}_{\text{on}} = \sum_{n \geq 1} (1 - (1 - \eta)^n) |n\rangle\langle n|, \quad (1.5.40)$$

with $\hat{\Pi}_{\text{off}} = \hat{\mathbb{1}} - \hat{\Pi}_{\text{on}}$.

Chapter 2

Generation of non-Gaussian States

In this chapter, we expose our research on the experimental generation and measurement of non-Gaussian non-classical states. In Sec.2.1, we first give the precise definition and the meaning of the expression *non-Gaussian non-classical states*. We also explain why this family of quantum states is important for universal quantum information processing and give a succinct list of related experiments. In Sec.2.2, we explain in details the photon subtraction protocol which is at the moment the most popular scheme in quantum optics to generate these non-Gaussian states. We also show how to model precisely and efficiently this protocol in the context of the multimode continuous wave regime. In Sec.2.3, we show how an inherently multimode photon subtracted state can yet be measured as a singlemode state. We explain how this multidimensional reduction process happens implicitly in the homodyne measurement through the choice of a mode projection function. In Sec.2.4, we details our experimental setup for the generation and measurement of these non-Gaussian non-classical quantum states of light. Also, we present experimental results and show how they fit with a simple theoretical model of the expected Wigner function, taking into account the relevant experimental parameters.

2.1 What is a non-Gaussian state

In 1935, to illustrate what he thought was an unphysical artifact of the young theory of quantum mechanics, Schroedinger proposed his famous thought experiment of a cat in a macroscopic superposition of dead and alive states. Nowadays, one of the consensus definitions in quantum optics of a Schrödinger's cat state $|\text{cat}\rangle$ is the superposition of two quasi-classical coherent states of opposite amplitudes

$$|\text{cat}_{\alpha,\phi}\rangle \propto |+\alpha\rangle + e^{i\phi}|-\alpha\rangle. \quad (2.1.1)$$

When $\phi = 0$, $|\text{cat}_{\alpha,\phi}\rangle$ is also called an *even* cat state, or an *odd* cat state when $\phi = \pi$, $|\text{cat}_\phi\rangle$. This terminology refers to the photon number basis expansion of Eq.(2.1.1)

$$|\text{cat}_{\alpha,\phi}\rangle \propto e^{-|\alpha|^2/2} \sum_n (1 + e^{i\phi+in\pi}) \frac{\alpha^n}{\sqrt{n!}} |n\rangle, \quad (2.1.2)$$

where the term $(1 + e^{i\phi+in\pi})$ selects only the photon number components $|2p\rangle$ or $|2p+1\rangle$ when ϕ is respectively equal to 0 or π .

Besides being a well-known and popular curiosity of quantum physics, Schrödinger's cat states are actually useful for quantum information processing. It has been shown that non-linearity is a necessity to achieve universal quantum information processing [53], something that Schrödinger's cat states can indeed provide[79, 141]. More precisely, it is impossible to truly benefit from quantum mechanics for computational or communication tasks beyond the classical limit only with

Gaussian resources and without using either non-Gaussian states such as for example Schroedinger's cat states or non-linear detectors. In any case, mastering the generation of such non-classical states is an absolute requirement for the steady development of the field of quantum information processing. Producing high fidelity $|{\text{cat}}\rangle$ states of even moderate amplitude is a tremendous challenge. Although the generation of high photon number $|\alpha|^2$ Schroedinger's cat states is still at a very early experimental stage, proof of principle experiments exist for several different physical systems (see Sec.2.1.3). In essence, the objective of non-Gaussian state generation protocols is to produce ersatz of Schroedinger's cat states in a reasonable and feasible way. We explain in Sec.2.2 how the photon subtraction protocol achieves this objective.

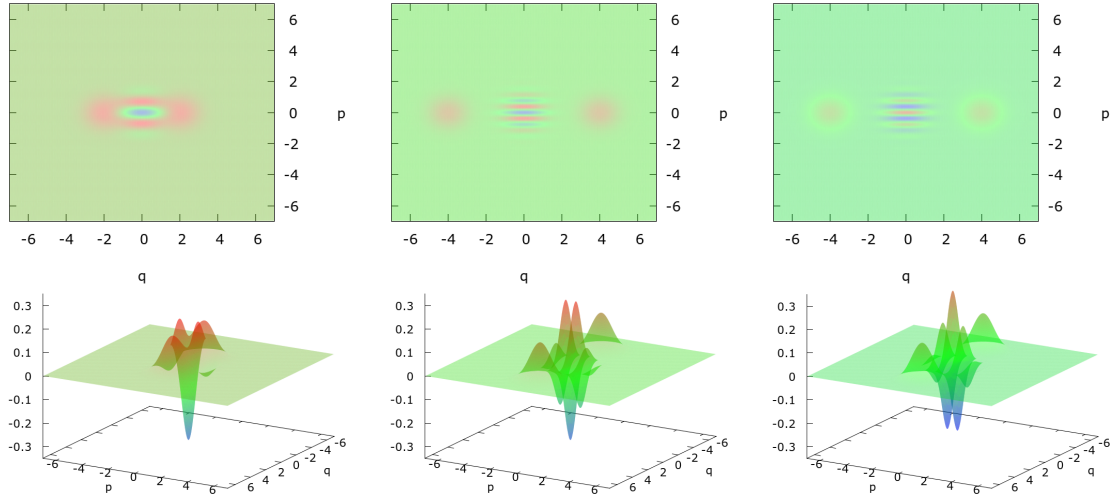


Figure 2.1: Examples of Schroedinger's cat states $| + \alpha\rangle + e^{i\phi}| - \alpha\rangle$ Wigner functions. Left: $\alpha = 2, \phi = \pi$. Center: $\alpha = 4, \phi = \pi$. Right: $\alpha = 4, \phi = 0$.

2.1.1 non-Gaussianity and non-classicality

The question of defining what non-classicality exactly means and what non-classical states exactly are leads to delicate discussions. In the current state of knowledge, it is still an open question, and essentially a matter of references. In the context of infinite dimensional Hilbert spaces, there are two broadly accepted criteria to distinguish a non-classical state from a classical state of light.

The first criterion is based on the possible interpretation of the Wigner function as a true probability distribution. For this school of thought, a classical state is defined as a state which has a positive Wigner function for every coordinate of phase-space, and is therefore interpretable as a probability distribution. Any state which has a negative Wigner function can be thought of as a true quantum state without any classical representation or classical counterpart. It was proven in [15] that being Gaussian is a sufficient condition for any density matrix $\hat{\rho}$ to have a positive Wigner function. The set of Gaussian states is exactly the set of displaced and squeezed vacuum states, which are written as

$$\hat{\rho}_{\text{Gaussian}} = \hat{D}_\alpha \hat{U}_\theta \hat{S}_s |0\rangle\langle 0| \hat{S}_s^\dagger \hat{U}_\theta^\dagger \hat{D}_\alpha^\dagger, \quad (2.1.3)$$

for any complex α , any real s , and any real θ . With pure states, the Gaussian criteria is necessary and sufficient for the Wigner function to be positive. Reciprocally, any non-Gaussian pure state has a negative Wigner function. With mixed states, a non-Gaussian state does not have necessarily a negative Wigner function. However, in practice the amalgam between non-classical states, in the sense of the negativity of the Wigner function, and non-Gaussian states is often made when

talking about mixed states. Of course, different Wigner functions can show different magnitude of negativity, which can be quantified in a precise way[85]. A consequence of [15] is that any finite superposition state is automatically a non-classical state with a negative Wigner function. The Schroedinger's cat states are the perfect example of this. The criteria we adopt and use in this manuscript to distinguish non-classical from classical states is the presence of negativity in the Wigner function. This is why we speak of Schroedinger's cat states, superposition states, non-classical states and non-Gaussian states in an equivalent manner, although strictly speaking this is an abuse of terminology. Experimentally, we want to generate quantum states with negative Wigner functions, we want to manipulate this states in a non-trivial manner, and we want to preserve quantum states with negative Wigner functions after they have been manipulated.

The other widely accepted criteria to distinguish classical and non-classical states is based on the comparison of the photon statistics to a Poisson distribution[63]. With this criteria, a quantum non-classical state has a sub-Poisson photon number statistics. In phase-space, this translates into a Wigner function with a Gaussian envelop with a variance smaller than the vacuum state Gaussian $\exp[-q^2 - p^2]$ along one quadrature at least. For example a squeezed state $\hat{S}_s|0\rangle$ with $s \neq 0$ is considered as a quantum state, although its Wigner function is positive. Stated more precisely, a quantum state of light has no classical counterpart or interpretation if its characteristic function χ has a slower decay than the vacuum state. As a consequence, this implies that the Glauber P distribution is not a regular function immediately representable with numbers.

These two criteria raises the question of compatibility. Although a Schroedinger's cat state and thermal state can be safely said to be respectively a quantum state and a thermal state in both contexts, there exist states for which the two criteria do not agree. The squeezed state is the best examples: it is a pure Gaussian state, yet it can be used to produce entangled non-classical states. For quantum optics with continuous variables and infinite dimensional Hilbert spaces, this question of state hierarchy has no definite answer. It is conjectured that a sufficient and necessary universal criterion to distinguish classical from quantum states does not exist in this context. In other word, inside the set of all physical density matrices, the frontier of the subset of non-classical states cannot be properly defined due to the complexity of the Hilber space. In practice, it is important to remember the interpretation of the criterion one uses to classify states. For example, with the criteria of negativity of the Wigner function, a squeezed state could be said to be a classical state in the sense that in a situation where only squeezed states and other Gaussian states, linear optics components, and homodyne detectors are used, any measurable quantity can be purely interpreted and predicted in term of classical probabilities. This would require only using the Wigner function, with the added condition that the purity of the Wigner function $\int |W|^2$ is bounded by 1. To truly unveil the non-classical character of a squeezed state, it is necessary to look directly at its photon distribution or at photons correlations.

2.1.2 Projection based conditional generation

In the laboratory, it is nowadays relatively easy to produce any kind of Gaussian state. But genuinely obtaining a non-Gaussian state requires at least a third order Hamiltonian with terms such as $\hat{a}^\dagger \hat{a}^\dagger \hat{a}^\dagger$. For optics the Kerr effect is an example of such a third order Hamiltonian. It is possible to engineer systems with these non-linear interactions that directly creates non-Gaussian states in a deterministic way. However, these protocols all turns out to be extremely difficult to realize experimentally. Especially, the recurrent difficulties are: the extremely weak third order non-linear interaction coefficients; the sensibility to decoherence of non-Gaussian states. The other way to produce non-Gaussian states revolves around the use of non-Gaussian detectors. In this family of schemes, the non-Gaussian state generation happens through a projection operation of an initial Gaussian resource state with a conditional non-Gaussian measurement. The non-Gaussian mea-

surement projects the Gaussian state onto one element of its basis of non-Gaussian POVMs or eigenstates. In the Wigner function formalism, this mechanism is written very simply with the partial overlap formula

$$W'(x, p) = \int \int dx' dp' W_1(x, p, x', p') W_{\text{det}}(x', p') / N, \quad (2.1.4)$$

where W_1 is the initial Gaussian resource, W_{det} is the action of the detector, and W' is the Wigner function onto which W_1 was conditionally projected. In the density matrix formalism this translates into

$$\hat{\rho}_{12} \rightarrow \hat{\rho}_1 = \text{tr}_2 (\hat{O}_2 \hat{\rho}_{12}) / \text{tr}_{12} (\hat{O}_2 \hat{\rho}_{12}), \quad (2.1.5)$$

with \hat{O}_2 describing the action of the detector associated with W_{det} . Via the integral operation induced by the measurement if the non-linear detector is projective enough, that is if W_{det} is negative enough, then so is W' . Such a process is sometimes called *degaussification*[89]. Incidentally the study of non-linear detectors as quantum detectors with negative Wigner functions W_{det} is an approach which has received recently quite a lot of attention[165].

For the actual experimental generation of non-Gaussian non-classical states, this second method is incomparably more fruitful in the field of optics. It is also very successful with atomic and condensed matter systems. In optics, the most commonly available non-linear detector is the avalanche photodiode on which is based the photon subtraction protocols that we explain in more details in Sec.2.2. Recently, with the rising interest and possible applications of non-Gaussian states to quantum information processing, the development of novel non-linear detectors for light is quite an active research area [152].

2.1.3 Recent experimental history

Most of the current experimental demonstrations and generations of non-Gaussian states in optics are derived from the photon subtraction protocol proposed by Dakna *et al*[43]. However, the idea of using conditional protocols to achieve deGaussification of Gaussian resources states traces back to former work[32, 33, 37]. The first experimental demonstration of the photon subtraction protocol was achieved in 2004 by Wenger *et al*[89] in the pulsed regime. However, the negativity of the conditional states could not be directly observed with the available overall detection efficiency. Soon after this pioneering step, several groups achieved the generation of non-classical states of light with the same photon subtraction protocol, in the pulsed regime[100] and the continuous wave regime[98, 127]. Very recently, novel true photon number resolving detectors have been applied to the photon subtraction protocol to directly generate large amplitude Schroedinger's cat states[159].

From these early experiments, the photon subtraction protocol has been used as a base on which more complex protocols and setups have been proposed and demonstrated. Some interesting variations include conditional non-Gaussian and Gaussian measurements to produce Schroedinger's cat states of larder amplitude from high enough photon number states [123]. By combining single photon subtraction events at different times, it was shown that larger Schroedinger's cat states can be generated[144, 143]. With smart use of beam-splitters and interferences, it is also possible to generate non-local superposition states[120, 154] similar to NooN states. Similar in nature to the photon subtraction protocol, it is possible to generate photon number states with conditional measurements at high purity levels[68, 108, 99, 107, 119, 122, 121]. In addition the photon subtraction protocol can be used for other purposes: entanglement distillation [124, 162], noiseless amplifiers[158, 164, 163], and related protocols on non-Gaussian states purification[105]. With additional displacement operations and ancillary coherent states, it is also possible to engineer more complex non-Gaussian non-classical states[94, 151].

With access to non-linear detectors, linear passive devices and laser beams, light appears as the medium of choice for the demonstration and implementation of these non-Gaussian states generation protocols. In the recent years, another kind of physical system has seen a rapid development of similar conditional experimental protocols for the generation of non-Gaussian states. Cavity Quantum Electro-Dynamics (CQED) in the strong coupling regime [88, 145] between a cavity field and an external qubit or atomic system offers the perfect testing grounds and implementation basis for such conditional generation protocols[117, 116, 133, 136]. While the cavity system is almost always a micro-wave cavity, which tends to heavily favor the strong coupling regime, qubits systems may be quite different, ranging from giant Rydberg atoms to SQUID flux qubits. Thanks to the strong coupling regime, these systems are able to show very strong non-linearity and are able to produce a variety of non-Gaussian states[134, 137, 169]. Currently the Schroedinger's cat states with the largest amplitude are made with these setups[134]. Also, a quantum state inside the cavity being a bound state, these systems are perfect for the demonstration of many quantum effects about measurement reversibility and irreversibility[139], Zeno and anti-Zeno effects[132, 161], or quantum feedback effects[150].

2.2 Photon subtraction

The photon subtraction protocol closely approximates a Schroedinger's cat target state $|\text{cat}_{\alpha,\phi}\rangle$ with successive applications of the annihilation operator \hat{a} onto a squeezed vacuum state $\hat{S}_s|0\rangle$. To understand the mechanism of this protocol, let's look at an interesting eigenvalue equation we can derive for the $|\text{cat}_{\alpha,\phi}\rangle$ state. According to the definition of Eq.(2.1.1), the actions of \hat{a} and \hat{a}^2 onto $|\text{cat}_{\alpha,\phi}\rangle$ is

$$\hat{a}|\text{cat}_{\alpha,\phi}\rangle = \alpha|\text{cat}_{\alpha,\phi+\pi}\rangle, \quad (2.2.1)$$

$$\hat{a}^2|\text{cat}_{\alpha,\phi}\rangle = \alpha^2|\text{cat}_{\alpha,\phi}\rangle. \quad (2.2.2)$$

Since $|\text{cat}_{\alpha,\phi}\rangle$ states are stable with \hat{a} , successive applications of the annihilation operator onto some appropriate ancillary states may eventually yield an approximation very close to a Schroedinger's cat state. This is the central idea behind the protocol.

In the most simple case of $|\alpha|^2 = 1$, there is a strong similitude between an odd Schroedinger's cat state $|\text{cat}_{1,\pi}\rangle$ on the one hand, and a squeezed photon state on the other hand. (The electrical field of both states are plotted in Fig.2.5. With simple algebra we can rewrite the state $\hat{S}_s|1\rangle$ as, omitting normalization factors

$$\hat{S}_s|1\rangle \longrightarrow \hat{S}_s\hat{a}^\dagger|0\rangle \longrightarrow \hat{a}\hat{S}_s|0\rangle. \quad (2.2.3)$$

In this last expression, the role of the annihilation operator appears clearly. Furthermore, if we recall Eq.(1.2.40), we see that a squeezed state $\hat{S}_s|0\rangle$ has only even photon number components $|2p\rangle$. Therefore, a squeezed photon state $\hat{S}_s|1\rangle$, or equivalently a photon subtracted squeezed vacuum state $\hat{a}\hat{S}_s|0\rangle$, only has odd photon number components $|2p+1\rangle$, which can be written

$$\hat{a}\hat{S}_s|0\rangle = S_1(s)|1\rangle + S_3(s)|3\rangle + \dots \quad (2.2.4)$$

As we have seen with Eq.(2.1.2), an odd Schroedinger's cat state $|\text{cat}_{\alpha,\pi}\rangle$ also only has odd photon number components

$$|\text{cat}_{\alpha,\pi}\rangle = C_1(\alpha)|1\rangle + C_3(\alpha)|3\rangle + \dots \quad (2.2.5)$$

By matching the coefficients $S_n(s)$ and $C_n(\alpha)$ for all ranks n , it is possible to approximate a Schroedinger's cat state. As it turns out, this similitude also holds for larger amplitude α , provided a sufficient number m of successive photon subtractions \hat{a}^m onto an appropriately squeezed vacuum state[43].

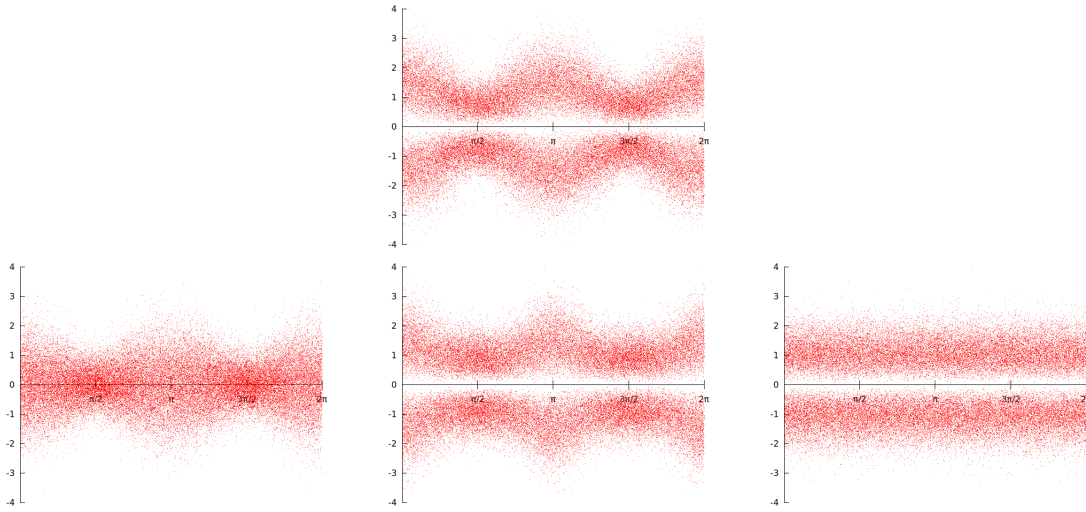


Figure 2.2: Electrical field of a small Schroedinger's cat state and similitude with a squeezed photon state. Top center, $|+\alpha\rangle - |-\alpha\rangle$ with $\alpha = 1$. Bottom left: $\hat{S}_s|0\rangle$ with $s = 0$. Bottom center: $\hat{S}_s|1\rangle$ with $s = 0.3$. Bottom right: $|1\rangle$.

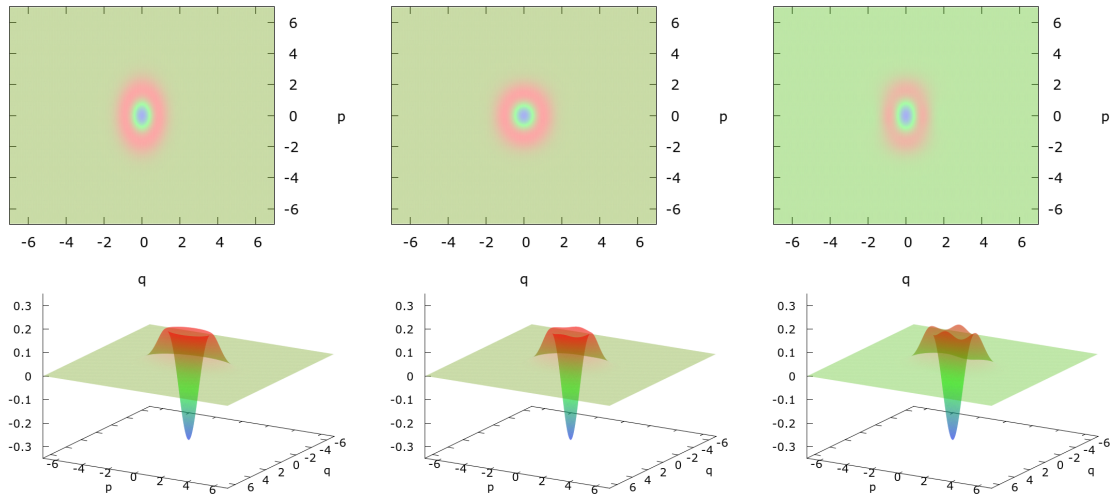


Figure 2.3: Small Schroedinger's cat state and photon subtracted squeezed vacuum Wigner functions Left: $\hat{a}\hat{S}_s|0\rangle$ with $s = 0.3$ Center: $|+\alpha\rangle - |-\alpha\rangle$ with $\alpha = 1/\sqrt{2}$. Right: $|+\alpha\rangle - |-\alpha\rangle$ with $\alpha = 1$.

There exist quite a number of different models for the photon-subtraction protocol, monomode[43, 97, 103, 86] and multimode[102, 144]. The main differences between these models are in the assumptions made about the nature of the photon subtraction phenomenon, or in other words which measurement model should be used to describe actual non-linear photon detectors. It is interesting to note that no matter how precisely the models take into account the realistic detection of individual photons, all are asymptotically equivalent. Experimentally, the asymptotic regime means a small amount of squeezing s , and a low rate of detection for the non-linear detector. In this regime, the asymptotic state is found to be precisely $\hat{a}\hat{S}_s|0\rangle$. Also, this regime yields experimentally the highest quality non-Gaussian non-classical states. This is the asymptotic regime which is the most

relevant to us and on which we focus in this chapter. We review the two major models of photon subtraction in Secs. 2.2.1 and 2.2.3. In Sec. 2.2.2, we show a slight declination of the model of Sec. 2.2.1 that we then adapt in Sec. 2.2.4 to a multimode description of the squeezed light and photon detection. In Sec. 2.3, we use this multimode model to understand in a rigorous way the mode projection process and measurement properties of multimode photon-subtracted states in the continuous wave regime.

2.2.1 Exact subtraction of m photons

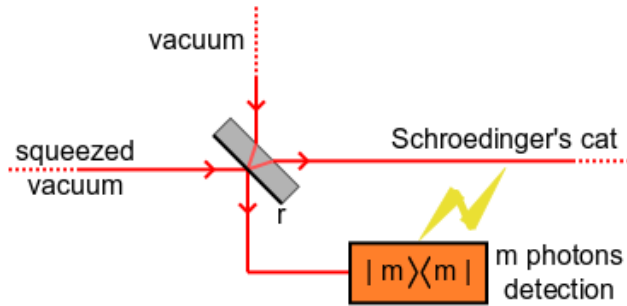


Figure 2.4: Setup for the exact subtraction of m photons.

The model presented here is the original conditional protocol derived and demonstrated in [43], in the case of a perfect photon number detector. The protocol starts with an ancillary squeezed vacuum state $\hat{S}_s|0\rangle$ in mode \hat{a} . This squeezed vacuum is split on a beam-splitter of amplitude reflection and transmission coefficients r and t with $r^2 + t^2 = 1$, and whose action is represented by the operator \hat{B} . The other input mode \hat{b} is in the vacuum state. Mode \hat{c} , the transmitted part of mode \hat{a} , is called the *signal* mode or signal channel. Mode \hat{d} , the reflected part of mode \hat{a} , is called the *trigger* channel or trigger mode. In the trigger channel, an m photon subtraction event is equivalent to the projection of the state $\hat{B}^\dagger \hat{S}_s|0,0\rangle$ onto the state $|m\rangle\langle m|$ on mode \hat{d} . Therefore, the output state $|\psi_{\text{sig}}(m, s)\rangle$ in mode \hat{c} for m subtracted photons can be expressed as

$$\hat{\rho}_{\text{sig}}(m, s) = \text{tr}_{\hat{d}} \left(|m\rangle\langle m| \hat{B}^\dagger \hat{S}_s |0,0\rangle\langle 0,0| \hat{S}_s^\dagger \hat{B} \right), \quad (2.2.6)$$

$$|\psi_{\text{sig}}(m, s)\rangle = \langle m | \hat{B}^\dagger \hat{S}_s | 0,0 \rangle. \quad (2.2.7)$$

Introducing a closure relation on mode \hat{a} , we rewrite $|\psi_{\text{sig}}(m, s)\rangle$ as

$$|\psi_{\text{sig}}(m, s)\rangle = \sum_{n=0}^{\infty} \langle n | \hat{S}_s | 0 \rangle \langle m | \hat{B}^\dagger | n, 0 \rangle = \sum_{n=0}^{\infty} \sum_{k=0}^n \langle n | \hat{S}_s | 0 \rangle B_k^n \delta_{n-k}^m | k \rangle, \quad (2.2.8)$$

where we have used Eq.(1.2.52) to change $\hat{B}^\dagger |n, 0\rangle$ into $\sum_k^n B_k^n |k, n-k\rangle$ with the binomial coefficients $B_k^n = \sqrt{n! / k! (n-k)!} t^k r^{n-k}$. We invert the sums on n and k and apply the change of variable $n \rightarrow n+k$ so that the right expression of Eq.(2.2.8) becomes

$$|\psi_{\text{sig}}(m, s)\rangle = \sum_{k=0}^{\infty} \langle k+m | \hat{S}_s | 0 \rangle B_k^{k+m} | k \rangle. \quad (2.2.9)$$

We immediately notice that the term $\langle k+m | \hat{S}_s | 0 \rangle$ requires that $k+m$ be an even number, a property we can explicitly enforce with the phase factor $\phi(l) = (1 + \exp[i l \pi]) / 2$. We define the

set of coefficients $\{\psi_k(m, s)\}_k$ by $|\psi_{\text{sig}}(m, s)\rangle = \sum_k \psi_k(m, s) \phi(m+k)|k\rangle$, which reads

$$\psi_k(m, s) = r^k t^m \sqrt{(1 - \lambda^2)^{1/2} (\lambda/2)^{k+m} / k! m!} \frac{(k+m)!}{((k+m)/2)!}, \quad (2.2.10)$$

with $\lambda = \tanh(s)$. $|\psi(m, s)\rangle$ can now be written onto a basis of two orthogonal states $|\psi_+(m, s)\rangle$ and $|\psi_-(m, s)\rangle$ according to the parity of m :

$$|\psi_{\text{sig}}(m, s)\rangle = \phi(m)|\psi_+(m, s)\rangle + \phi(m+1)|\psi_-(m, s)\rangle, \quad (2.2.11)$$

with the following definitions of $|\psi_+(m, s)\rangle$ and $|\psi_-(m, s)\rangle$

$$|\psi_+(m, s)\rangle = \sum_k \psi_{2k}(m, s) |2k\rangle, \quad (2.2.12)$$

$$|\psi_-(m, s)\rangle = \sum_k \psi_{2k+1}(m, s) |2k+1\rangle. \quad (2.2.13)$$

We recognize in the states $|\psi_+(m, s)\rangle$ and $|\psi_-(m, s)\rangle$ the ersatz of an even and an odd Schroedinger's cat states. If we define the exact normalized even and odd Schroedinger's cat target states by

$$|\text{cat}_+(\alpha)\rangle = \frac{\exp[|\alpha|^2/2]}{2 \cosh |\alpha|^2} \left(\sum_{k=0}^{\infty} \frac{\alpha^{2k}}{\sqrt{2k!}} |2k\rangle \right), \quad (2.2.14)$$

$$|\text{cat}_-(\alpha)\rangle = \frac{\exp[|\alpha|^2/2]}{2 \sinh |\alpha|^2} \left(\sum_{k=0}^{\infty} \frac{\alpha^{2k+1}}{\sqrt{2k+1!}} |2k+1\rangle \right), \quad (2.2.15)$$

we can compute the fidelity figures $F_{\pm}(m, s, \alpha) = |\langle \text{cat}_{\pm}(\alpha) | \psi_{\pm}(m, s) \rangle|^2$ to evaluate the faithfulness of the subtraction protocol with the target Schroedinger's cat states. These fidelity figures have rather complex expression in the general case[86, 90]. For $m = 1$ and a single photon subtraction, the fidelity $F_-(1, s, \alpha)$ is calculated to be[86]

$$F_-(1, s, \alpha) = \frac{|\alpha|^2 e^{-|\alpha|^2 \tanh(s)}}{\sinh |\alpha|^2 \cosh^3 s}. \quad (2.2.16)$$

We notice that the ersatz states $|\psi_+(m, s)\rangle$ and $|\psi_-(m, s)\rangle$ are always pure states. This is a consequence of the perfectly projective detection model used in [43]. With non-projective measurements or multimode models, this property is not verified anymore.

2.2.2 Monomode click detection model and single photon subtraction

It is interesting to treat the situation of the previous paragraph in the more simple case $m = 1$. In this case, starting from Eq.(2.2.6) our conditional density matrix simply reads

$$\hat{\rho}_{\text{sig}}(1, s) = \text{tr}_{\hat{d}} \left(|1\rangle \langle 1| \hat{B}^\dagger \hat{S}_s |0, 0\rangle \langle 0, 0| \hat{S}_s^\dagger \hat{B} \right), \quad (2.2.17)$$

$$= \langle 0 | \hat{d} \hat{B}^\dagger \hat{S}_s |0, 0\rangle \langle 0, 0| \hat{S}_s^\dagger \hat{B} \hat{d}^\dagger |0\rangle. \quad (2.2.18)$$

Omitting normalization factors, we can write the output conditional state before the projection onto $|0\rangle \langle 0|$ as

$$\hat{d} \hat{B}^\dagger \hat{S}_s |0, 0\rangle = \hat{B}^\dagger \left(\hat{B} \hat{d} \hat{B}^\dagger \right) \hat{S}_s |0, 0\rangle = \hat{B}^\dagger \hat{a} \hat{S}_s |0, 0\rangle = \hat{B}^\dagger \hat{S}_s |1, 0\rangle. \quad (2.2.19)$$

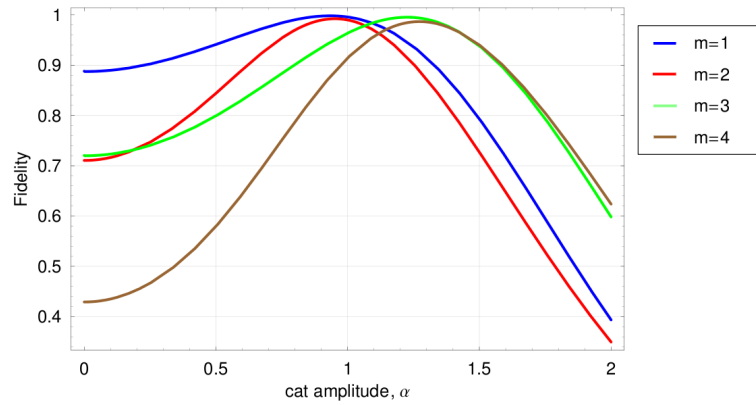


Figure 2.5: Evolution with the value of the target Schrödinger's cat state amplitude α the fidelities of the m photon subtraction protocol for different m number.

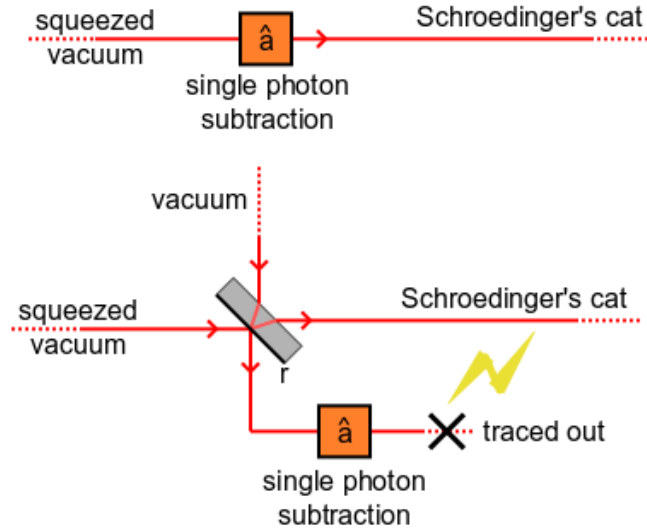


Figure 2.6: Top: inline subtraction of a single photon. Bottom: offline subtraction of a single photon with the auxiliary beam-splitter.

Adding the hypothesis $r \ll 1$, which means that $\hat{B} \approx \hat{\mathbb{1}}$, we are actually looking at the asymptotic regime of the single photon subtraction, since Eq.(2.2.18) rewrite itself into

$$\langle 0 | \hat{d}^\dagger \hat{B} \hat{S}_s | 0, 0 \rangle \rightarrow \hat{a} \hat{S}_s | 0 \rangle, \quad (2.2.20)$$

whose Wigner function is

$$W(q, p) = W_{|1\rangle}(e^{+s}q, e^{-s}p) = \frac{2}{\pi} \left(e^{2s}q^2 + e^{-2s}p^2 - \frac{1}{2} \right) e^{-e^{+2s}q^2 - e^{-2s}p^2}. \quad (2.2.21)$$

This exactly follows the click APD model of Eq.(1.5.32) directly applied on mode \hat{a} .

However experimentally this picture is too simple and forgets to take into account the effect of the beam-splitter. We now precisely apply the click APD model of Eq.(1.5.32), this time on mode \hat{d} and additionally we trace out the degrees of liberty of mode \hat{d} . We obtain the conditionally

heralded density matrix

$$\rho_{\text{sig}}(1, s) = \text{tr}_d \left(\hat{B}^\dagger \hat{S}_s |0, 0\rangle\langle 0, 0| \hat{S}_s^\dagger \hat{B} \hat{d}^\dagger \right). \quad (2.2.22)$$

In comparison to Eq.(2.2.17), the projection onto $|0\rangle\langle 0|$ has disappeared. Applying the transformation of Eq.(2.2.19), we obtain

$$\rho_{\text{sig}}(1, s) = \text{tr}_d \left(\hat{B}^\dagger \hat{S}_s |1, 0\rangle\langle 1, 0| \hat{S}_s^\dagger \hat{B} \right). \quad (2.2.23)$$

Looking at Eq.(2.2.22), we observe that the beam-splitter adds direct losses on the conditional state, following the model of linear losses of Sec.1.2.7. This is a consequence of the approximation of the photon subtraction operation with an auxiliary trigger channel and it illustrates clearly the difference between the perfect projection model of Sec.2.2.1 or the online click APD model results of Eq.(2.2.20), and the trigger channel assisted photon subtraction. Especially, the output state is not a pure state anymore. In [97], it is proven with the correspondence rules of Eqs.(1.3.20) that Eq.(2.2.23) yields in phase-space the Wigner function

$$W'(q, p) \propto \int dq' dp' ((2q' + \partial_{q'})^2 + (2p' + \partial_{p'})^2) W(q, p, q', p'), \quad (2.2.24)$$

in the asymptotic regime $\hat{B} \approx \hat{\mathbb{1}}$ where $W(q, p, q', p')$ is the 2-mode Gaussian Wigner function of the beam-splitter squeezed vacuum state (see the next paragraph for details). Intuitively, we understand that these beam-splitter losses should be kept at the lowest minimum, that is, $r \ll 1$. To fall back on the prediction of Eq.(2.2.23) we can simply add beam-splitter losses with a Gaussian convolution on $W'(q, p)$. Therefore, in this asymptotic regime, it is valid to first think of $\hat{\rho}_{\text{sig}}$ as the pure state $\hat{S}_s |1\rangle$, and only latter to account for the non-zero r coefficient and apply the effect of \hat{B}^\dagger as optical losses, following the model of amplitude linear losses. This approach facilitates the development of an efficient multimode model for the continuous wave regime, as is shown in Sec.2.2.4.

2.2.3 On/off detection

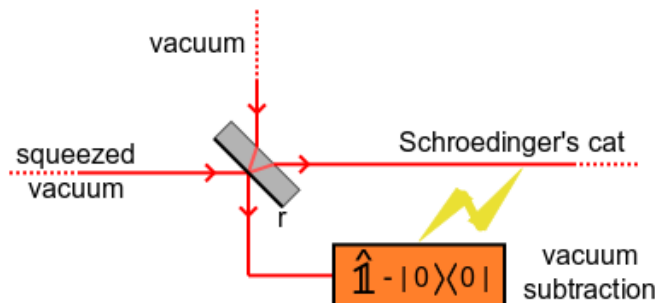


Figure 2.7: Setup for photon subtraction with on/off detector

It can be a concern that the detector considered in Sec.2.2.1 is a perfect photon number detector. Even when $m = 1$, this detector will remove the higher photons number event. A more realistic model of detector is the on/off detector which can only be triggered to yield a detection event by a state which is not the vacuum state. As we saw with Eq.(1.5.36), the action of this detection is $\hat{\Pi}_{\text{on}} = \hat{\mathbb{1}} - |0\rangle\langle 0|$. A more precise model which take into account the inefficiency of photo

detection is written $\hat{\Pi}_{\text{on}} = \sum_{k=1}^{\infty} p_k |k\rangle\langle k|$, where p_k is the probability for the APD to detect the state $|k\rangle$ [104]. Instead of $|m\rangle\langle m|$, we apply the former detection operator onto $\hat{B}^\dagger \hat{S}_s |0, 0\rangle$. It is however easier to use the Wigner function formalism of Eq.(1.5.37) given the fact that before detection, the state $\hat{B}^\dagger \hat{S}_s |0, 0\rangle$ is a Gaussian state and can therefore be described with the correlation matrix Γ introduced in Sec.1.3.5 and written in our case as

$$\Gamma = \begin{pmatrix} a & e & \\ b & f & \\ e & c & \\ f & d & \end{pmatrix}. \quad (2.2.25)$$

To compute the matrix elements we first express the correlation matrix Γ_0 of $\hat{S}_s |0, 0\rangle$ before the beam-splitter

$$\Gamma_0 = \begin{pmatrix} \Gamma_{\hat{S}_s |0\rangle} & \\ & \Gamma_{|0\rangle} \end{pmatrix}, \quad \text{with } \Gamma_{\hat{S}_s |0\rangle} = \frac{1}{2} \begin{pmatrix} e^{-r} & \\ & e^{+r} \end{pmatrix} \quad \text{and } \Gamma_{|0\rangle} = \frac{1}{2} \begin{pmatrix} 1 & \\ & 1 \end{pmatrix}, \quad (2.2.26)$$

in 2×2 block form. The beam splitter action results in the correlation matrix $\Gamma = B^T \Gamma_0 B$ with B in the form of Eq.(1.2.43) using $\cos \theta = t$ and $\sin \theta = r$. Γ is then written in block form as

$$\Gamma = \begin{pmatrix} t^2 \Gamma_{\hat{S}_s |0\rangle} + r^2 \Gamma_{|0\rangle} & rt (\Gamma_{|0\rangle} - \Gamma_{\hat{S}_s |0\rangle}) \\ rt (\Gamma_{|0\rangle} - \Gamma_{\hat{S}_s |0\rangle}) & t^2 \Gamma_{|0\rangle} + r^2 \Gamma_{\hat{S}_s |0\rangle} \end{pmatrix}. \quad (2.2.27)$$

where each block matrix is a diagonal 2×2 matrix which satisfies the form requirement of Eq.(2.2.25)[155]. We can therefore express the coefficients a, b, c, d, e and f from r, t and s . Using the expression in phase-space of $\hat{\Pi}_{\text{on}}$ from Eq.(1.5.38), the Wigner function W' after detection expressed as

$$W'(q, p) = 2\pi \int \int dq' dp' W_{\text{det}}(q', p') W(q, p, q', p'), \quad (2.2.28)$$

is written[142]

$$W'(q, p) = \frac{1}{\pi \sqrt{ab}} e^{-q^2/a - p^2/b} - \frac{1}{\pi \sqrt{\nu \mu}} e^{-(1-c)q^2/\nu - (1+d)p^2/\mu}, \quad (2.2.29)$$

with ν and μ given by

$$\nu = a(1+c) - e^2 \text{ and } \mu = b(1+d) - f^2. \quad (2.2.30)$$

This Gaussian formalism is very efficient to predict the Wigner function of the conditional state. The action of the different models of non-linear detectors are especially clear in this picture. However because it is directly applied in the Schrodinger picture the Gaussian formalism says nothing about the mode of the density matrix itself. Despite this it can be used to develop a multimode model of photon subtraction at the price of more complex and careful derivations[142].

2.2.4 Multimode click detection model

It was noted early in the theoretical development of models of photon subtraction models that in the continuous wave regime, the output conditional state would have complex multimode properties [102, 97]. As is shown in Sec.2.3, for such a state to be measured with monomode tomography, it is necessary experimentally to use a mode projection function to filter the homodyne electrical current[98, 127] according to the multimode properties of the conditional state[142, 155]. To the notable exception of [102], most multimode models of photon subtraction are built around the Gaussian formalism on top of the monomode basis of Sec.2.2.3.

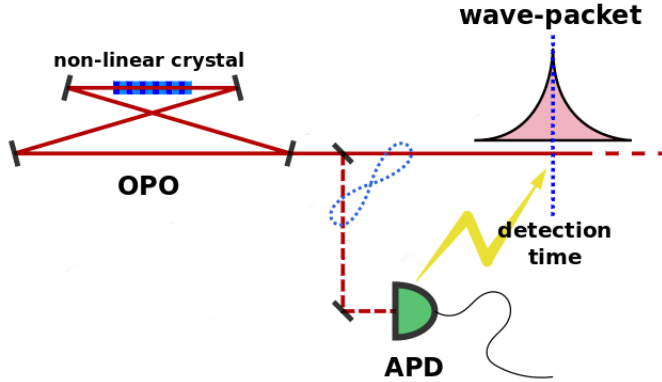


Figure 2.8: Illustration of the photon subtraction protocol multimode properties in the time domain.

In this paragraph we exhibit an alternate model of multimode photon subtraction inspired by similar calculations found in [155]. This model constitutes the basis on which in Sec.2.3 we show how to analyse the multimode nature of the non-classical light we generate experimentally in the continuous wave regime. For simplicity we use the same model of single click detection as in [97] and Sec.2.2.2. Compared to the monomode discussion of the previous paragraphs, we need to take a few additional phenomena into account to describe the multimode nature of the photon subtraction process. Firstly, as is explained in Sec.1.4.3 the squeezed vacuum state generated by a continuous wave OPO has a certain bandwidth that we cannot ignore. This induces complex spectrum correlations at different frequencies between the signal and trigger channels. We change the monomode squeezing operator used before to the broadband OPO squeezing operator of Eq.(1.4.23).

$$\exp \left[\frac{r}{2} \left(\hat{a}^2 - \hat{a}^\dagger \hat{a} \right) \right] |0\rangle \rightarrow \exp \left[\int d\Omega \frac{\zeta_\Omega}{2} \left(\hat{A}_{+\Omega} \hat{A}_{-\Omega} - \hat{A}_{+\Omega}^\dagger \hat{A}_{-\Omega}^\dagger \right) \right] |0\rangle, \quad (2.2.31)$$

where $\hat{A}_\Omega = \hat{a}(\omega_0 + \Omega)$. Secondly, the avalanche photodiode is not able to detect a single frequency but rather has a very wide bandwidth of detection. We model this by defining the photodiode detection mode \hat{a}_{det} by

$$\hat{a}_{\text{det}}(t_c) = \int dt f_{\text{det}}(t - t_c) \hat{a}(t), \quad (2.2.32)$$

where t_c is the instant the APD detects a photon, and f_{det} describes the detection bandwidth of the APD. As is explained in [97], the exact shape of f_{det} does not matter in the typical conditions of continuous wave experiments. Indeed, if we consider the time resolution of the detector to be much smaller than any other time constant, we can simply model its action by the annihilation operator taken at t_c the time of the detection click. In practice the shape does not have any relevance and we can assume $f_{\text{det}}(t) = \delta(t - t_c)$. In other words, in this regime we would not be able to actually measure f_{det} if we would try to. In consequence, the click detection model in the multimode case can be thought of as a projection onto the state $|1\rangle_{f_{\text{det}}} = \hat{a}^\dagger(t_c)|0\rangle$. Finally, our model of multimode input state is

$$|\psi_{\text{sig}}\rangle = \hat{a}(t_c) \hat{S}_\zeta |0\rangle = \hat{a}(t_c) \exp \left[\int d\Omega \frac{\zeta_\Omega}{2} \left(\hat{A}_\Omega \hat{A}_{-\Omega} - \hat{A}_\Omega^\dagger \hat{A}_{-\Omega}^\dagger \right) \right] |0\rangle. \quad (2.2.33)$$

As we have seen in Sec.2.2.2, we do not need to take into account the effect of the beam-splitter and the ancillary mode directly in Eq.(2.2.33), but rather we will simply add optical losses at

some latter point once we derive the theoretical target state. This approach is still valid in the multimode regime thanks to the very good uniform spectral properties of beam-splitters found in the laboratory. We first work out a transformation of Eq.(2.2.33) similar to the one shown in Eq.(2.2.20). Although the commutation of \hat{a} and \hat{S}_s is trivial in the monomode case, it is more delicate in the multimode case. We express $\hat{a}(t_c)$ into the frequency domain

$$\hat{a}(t_c)\hat{S}_\zeta|0\rangle = \frac{1}{\sqrt{2\pi}} \int d\omega e^{-i\omega t_c} \hat{a}(\omega)\hat{S}_\zeta|0\rangle = \frac{e^{-i\omega_0 t_c}}{\sqrt{2\pi}} \int d\Omega e^{-i\Omega t_c} \hat{A}_\Omega \hat{S}_\zeta|0\rangle, \quad (2.2.34)$$

and inserting the factor $\hat{S}_\zeta \hat{S}_\zeta^\dagger$ before using the Bogoliubov transformation of Eq.(1.4.24), we obtain

$$\hat{a}(t_c)\hat{S}_\zeta|0\rangle = -\frac{e^{-i\omega_0 t_c}}{\sqrt{2\pi}} \hat{S}_\zeta \int d\Omega e^{-i\Omega t_c} \sinh(\zeta_\Omega) \hat{A}_{-\Omega}^\dagger|0\rangle. \quad (2.2.35)$$

If we define $f(t)$ the Fourier transform of $\sinh(\zeta_\Omega)$ by

$$\sinh(\zeta_\Omega) = \int e^{i\Omega t'} f(t') dt', \quad (2.2.36)$$

we can rewrite Eq.(2.2.35) in the time domain as

$$\hat{a}(t_c)\hat{S}_\zeta|0\rangle = -\hat{S}_\zeta \int dt' e^{-i\omega_0 t'} f(t') \hat{a}^\dagger(t_c - t')|0\rangle. \quad (2.2.37)$$

By definning the sideband function $f_{\text{sig}}(t)$ as

$$f_{\text{sig}}^*(t) = e^{-i\omega_0 t} f(t), \quad (2.2.38)$$

we obtain the compact expression

$$|\psi_{\text{sig}}\rangle = \hat{a}(t_c)\hat{S}_\zeta|0\rangle = -\hat{S}_\zeta (f_{\text{sig}} \circ \hat{a})^\dagger(t_c)|0\rangle, \quad (2.2.39)$$

where $f_{\text{sig}} \circ \hat{a}(t)$ is equal to $\int dt' f_{\text{sig}}(t-t')\hat{a}(t')$. If we calibrate the time origin at $t_c = 0$, it is possible to define the wave-packet mode \hat{A}_{sig} by

$$\hat{A}_{\text{sig}} = - \int dt f_{\text{sig}}(-t) \hat{a}(t). \quad (2.2.40)$$

and obtain an expression very similar to $\hat{a}\hat{S}|0\rangle$ in the monomode case

$$|\psi_{\text{sig}}\rangle = \hat{a}(t_c = 0)\hat{S}_\zeta|0\rangle = \hat{S}_\zeta \hat{A}_{\text{sig}}^\dagger|0\rangle. \quad (2.2.41)$$

It is important to notice that this last expression does not contain any approximation at that point except for the simplified choice of the APD mode function $f_{\text{det}}(t) = \delta(t)$ and the click detector model. As we have seen in Sec.1.4.3, if we define a basis of orthonormal function $\{\phi_n\}$ starting from the above wave-packet function $\phi_0(t) = f_{\text{sig}}(t)$, \hat{S}_ζ may or may not be considered to be factorisable over this basis. In the latter case, the state $\hat{a}(t_c)\hat{S}_\zeta|0\rangle$ is intrinsically a multimode entangled state which any monomode expression of can only be an approximation. This is the central question of the following section, in which we show to which extent a monomode approximation of Eq.(2.2.41) is relevant.

2.3 Mode projection function

A multimode model of the photon subtraction protocol is only a starting point to understand the experimental consequences in the continuous wave regime of the multimode properties of these conditional states. The question we have to answer is to predict the behavior of the homodyne detector photocurrent and understand its properties, in order to perform optimal quantum tomography. It is important to notice that this is an experimental requirement in order to make the tomography process easier. In principle, nothing forbids to perform the tomography on a full wave-packet basis $\{\phi_n(t)\}$ to obtain a complete multidimensional density matrix. Such a method has the advantage of directly probing any entanglement which might exist in the multimode photon subtracted state. However, numerically this approach fails even with a small number of modes. Essentially the information a multimode density matrix can contain is huge to the point that it quickly becomes intractable as the number of modes increases. Therefore, the only viable experimental approach is the monomode tomography of the conditional state, and for instance, the reconstruction of its Wigner function.

The model of Sec.2.2.4 based on the density matrix and operator formalism is especially relevant for this task. In contrary to this, the more popular approach based on the Gaussian correlation matrix is harder to use in order to understand how to precisely handle the homodyne current. In these Gaussian models, first of all the Gaussian correlation matrix $\Gamma(\omega, \omega')$ before the action of the non-linear photon detector is written with two frequencies field operator terms such as $\langle \hat{a}(\omega) \hat{a}(\omega') \rangle$. Then the correlation matrix is integrated with a trigger and mode functions, which yields a 2-mode correlation matrix $\Gamma(\omega, \omega') \rightarrow \Gamma = \int d\omega \int d\omega' f_{\text{trig}}(\omega) f_{\text{sig}}(\omega') \Gamma(\omega, \omega')$. At that point the multimode reduction has already happened, and any insight into the properties of the homodyne current is lost. Finally the action of the non-linear detector is applied onto the reduced 2-modes trigger and signal Gaussian state. A first disadvantage is that the action of the filtering cavities on the trigger channel is hard to include correctly. Even harder to precisely include inside the model is the effect of any classical manipulation of the homodyne current. The purpose of this section is to address this problem in a rigorous fashion.

2.3.1 Multidimensional reduction mechanism

We base our analysis on Eq.(2.2.39). We assume the existence of an orthonormal basis of wavefunction $\{\phi_n(t)\}_n$ with associated modes $\hat{a}_n = \int dt \phi_n(t) \hat{a}(t)$ on which the broadband squeezing operator is factorisable into $\hat{S}_\zeta = \bigotimes_n \hat{S}_n$. Also, we calibrate the origin of time to the instant of the detection click $t_c = 0$. Finally, we decompose the mode function $f_{\text{sig}}(t)$ of Eq.(2.2.38) onto the basis $\{\phi_n(t)\}_n$ by $f_{\text{sig}}(t) = \sum_n f_n \phi_n(t)$. The conditional quantum state $|\psi_{\text{sig}}\rangle$ then becomes

$$|\psi_{\text{sig}}\rangle = S_\zeta \left(\sum_n f_n |1\rangle_n \right). \quad (2.3.1)$$

If we choose our mode projection function to be $\phi_0(t)$, we trace out all the degrees of liberty of the other modes $n \geq 1$ and define the projected density matrix $\hat{\rho}_0$ as

$$\hat{\rho}_0 = \text{tr} [\hat{\rho}_{\text{sig}}]_{k \geq 1} = \sum_{n,m} f_n f_m^* \text{tr} [S_\zeta |1\rangle_n \langle 1|_m S_\zeta^\dagger]_{k \geq 1}. \quad (2.3.2)$$

We write down $\hat{S}_\zeta = \bigotimes_i \hat{S}_i$ and extract \hat{S}_0 from the trace operation to obtain

$$\hat{\rho}_0 = \sum_{n,m} f_n f_m^* \hat{S}_0 \text{tr} \left[\left(\prod_{i \geq 1} \hat{S}_i \right) |1\rangle_n \langle 1|_m \left(\prod_{j \geq 1} \hat{S}_j^\dagger \right) \right]_{k \geq 1} \hat{S}_0^\dagger. \quad (2.3.3)$$

The trace operation happens on all modes except $k = 0$, which matches the action of the operator $(\prod_{i \geq 1} \hat{S}_i)$, therefore we can use the circularity of the trace operation and simplify the previous expression to

$$\hat{\rho}_0 = \sum_{n,m} f_n f_m^* \hat{S}_0 \text{tr} [|1\rangle_n \langle 1|_m]_{k \geq 1} \hat{S}_0^\dagger. \quad (2.3.4)$$

Finally, the trace operation cancels out all the terms $n \neq m$ and conserves on mode ϕ_0 a single $|1\rangle\langle 1|$ term when $n = m = 0$, and otherwise $|0\rangle\langle 0|$ when $n = m \geq 1$. The projected density matrix then reads

$$\hat{\rho}_0 = |f_0|^2 \hat{S}_0 |1\rangle\langle 1| \hat{S}_0^\dagger + \sum_{n \geq 1} |f_n|^2 \hat{S}_0 |0\rangle\langle 0| \hat{S}_0^\dagger. \quad (2.3.5)$$

We formally obtain the expression of $\hat{\rho}_0$ as a mixture of a squeezed single photon state and a squeezed vacuum, to the extent of how much f_{sig} overlap with ϕ_0 . This shows how the multimode reduction of $|\psi\rangle$ naturally leads to a mixture of a squeezed photon and a squeezed vacuum. Of course, we notice that if $f_{\text{sig}} = \phi_0(t)$, $\hat{\rho}_0$ is exactly a squeezed single photon state. This derivation contains only one approximation: the factorization of the squeezing operator. As is explained in Sec.1.4.3, for small pump intensity this approximation works perfectly well. Together with the weak beam-splitter losses induced by the subtraction triggering channel, these two conditions constitute the low intensity pump regime, which as we have seen in Sec.2.2.2 is asymptotically equivalent to the state $\hat{S}_s |0\rangle$. For higher pump intensity, the monomode reduction picture presented here collapses, as the state is inherently a multimode entangled state. This property can be checked and asserted rigorously with the Schmidt decomposition of the density matrix[4]. This entanglement is a property of the squeezing operator only. However, non-projective models of APD can also induce similar multimode entanglement properties.

2.3.2 Selection of the Hilber space

The reduction mechanism of the previous paragraph clearly shows how a multimode state can be eventually partially approximated in a pure monomode fashion. Experimentally there is one question that the previous paragraph does not answer to. In practice of course, the physicist does not directly trace out the higher order modes. Rather, this phenomenon happens implicitly when the physicist analyses the photocurrent time series coming from the homodyne detector. In this paragraph we show how this phenomenon takes place while manipulating not quantum but classical quantities. This also shows why in practice the choice of the wave-packet basis $\{\phi_n(t)\}_n$ in order to perfectly match $f_{\text{sig}}(t)$ may be far from trivial.

Our analysis relies on two previously introduced elements. The first one is the broadband expression of the homodyne current of Sec.1.5.2. The second one is the multimode expression of $\hat{\rho}_0$ onto the basis $\{\phi_n(t)\}$. First of all we write down $|\psi_{\text{sig}}\rangle$ in its density matrix form, assuming the separability of squeezing $\hat{S}_\zeta = \bigotimes_n \hat{S}_n$, and also $f_{\text{sig}}(t) = \phi_0(t)$.

$$\hat{\rho}_0 = \left(\hat{S}_0 |1\rangle\langle 1| \hat{S}_0^\dagger \right) \bigotimes_{n \geq 1} \left(\hat{S}_n |0\rangle\langle 0| \hat{S}_n^\dagger \right). \quad (2.3.6)$$

We know from Sec.1.5.2 that the broadband homodyne current random variable $U(t)$ will be written on the basis $\{\phi_n(t)\}$ as

$$U(t) = \sum_n \phi_n(t) Y_n = \left(\vec{\phi}(t) \cdot \vec{Y} \right), \quad (2.3.7)$$

with $\vec{\phi}(t) = (\phi_0(t), \phi_1(t), \dots)$, and the probability distribution of the random variable Y_n given by

$$p(Y_0 = y) = |\langle y | \hat{S}_0 | 1 \rangle|^2, \quad (2.3.8)$$

$$p(Y_n = y) = |\langle y | \hat{S}_n | 0 \rangle|^2, \text{ for } n \geq 1. \quad (2.3.9)$$

We now apply the projection operation of the homodyne current $U(t)$ onto the wave-packet mode defined by the function $\bar{f}(t)$

$$Q = \int dt \bar{f}^*(t) U(t) = \left(\left(\int dt \bar{f}^*(t) \vec{\phi}(t) \right) \cdot \vec{Y} \right). \quad (2.3.10)$$

$\bar{f}(t)$ is the physicist chosen mode projection function which is used to filter the homodyne photocurrent and achieves the multimode reduction mechanism. It is therefore a variable of the detection model that we would like to determine optimally. Q is a random variable that we would ultimately want to be distributed according to Y_0 , therefore, we want the total overlap between \bar{f} and $\phi_0(t)$ to be 1. In other words we want $\bar{f}(t) = \phi_0(t)$. In this case $\int dt \bar{f}^*(t) \vec{\phi}(t)$ reduces to $(1, 0, \dots)$ and indeed $Q = Y_0$. If the overlap is not perfect, according to Sec. 1.5.3, the tomography of the variable Q is harmed by electronic noise equivalent to beam-splitter losses $\eta = 1/(1 + \epsilon^2)$ where ϵ is the total amplitude of added noise, in shotnoise level unit. In this case, let's assume that $\bar{f}(t)$ decomposes itself onto the basis $\{\phi_n(t)\}$ into

$$\bar{f}(t) = \sum_n \bar{f}_n \phi_n(t). \quad (2.3.11)$$

Then the non-pure projected homodyne current Q' becomes

$$Q' = \bar{f}_0^* Y_0 + \sum_{n \geq 1} \bar{f}_n^* Y_n. \quad (2.3.12)$$

To obtain the expression ϵ , we simply need to estimate the total variance of the term $\sum_{n \geq 1} \bar{f}_n^* Y_n$.

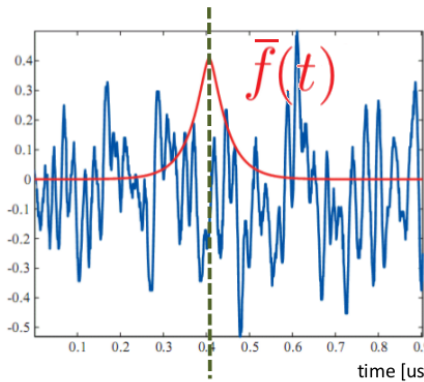


Figure 2.9: Projection of the homodyne current with $\bar{f}(t)$.

If the amount of squeezing is not null, the random variables Y_n have different amount of noise for different phases. To obtain a good estimate of the effect, we can take the average over all phases θ . Reintroducing the phase dependence of Q' , we write

$$Q'(\theta) = \bar{f}_0^* Y_0(\theta) + \sum_{n \geq 1} \bar{f}_n^* Y_n(\theta). \quad (2.3.13)$$

The expression of the quadrature operator \hat{x}_θ at angle θ is $\cos \theta \hat{x} + \sin \theta \hat{p}$, and therefore, the average amount of noise over $[0, 2\pi]$ of Y_n for any n is

$$\langle x_\theta^2 \rangle = \frac{1}{2\pi} \int_0^{2\pi} d\theta (\cos^2 \theta e^{-s_n} + \sin^2 \theta + \sin 2\theta e^{+s_n}), = \cosh(2s) \quad (2.3.14)$$

where s_n is the amount of squeezing for the wave-packet mode n . Applying the results of Sec.1.5.3, we obtain for the equivalent amount of noise ϵ the expression

$$\epsilon = \frac{1}{\bar{f}_0^*} \left(\sum_{n \geq 1} \bar{f}_n^* \cosh(2s_n) \right)^{1/2}. \quad (2.3.15)$$

for a final amount of losses η equal to

$$\eta = 1 / \left(1 + \sum_{n \geq 1} \cosh(2s_n) (\bar{f}_n^* / \bar{f}_0^*) \right). \quad (2.3.16)$$

Although this derivation may seem more complicated than the results it proves, it takes all its purpose once we apply it to a more complex situation where for example the homodyne electrical current is altered.

2.3.3 Filtering cavities and electrical filtering

The discussion of the previous paragraph may seem to go much beyond what is necessary to justify the choice of the mode projection function $\bar{f}(t)$. But until now we have ignored two experimental complications. The first effect to take into account is the action of the filtering cavities placed on the trigger channel and used to cancel out any photons found in the non-degenerate modes of the OPO. It can be precisely accounted for directly in the expression of $\hat{\rho}_{\text{sig}}$. The second effect is the action of electrical filters on the homodyne current, such as for example the finite bandwidth of the homodyne detector, and possibly high-pass filters used to cut additional low frequency noise hampering the homodyne current. Such filtering of the electrical current can be included into the expression of the homodyne current random variable $U(t)$.

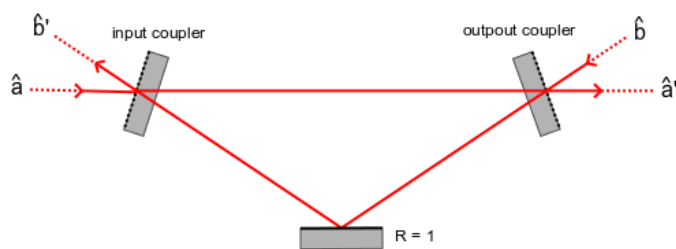


Figure 2.10: Modes transformation with filtering cavities

We can model the effect of cavities as passive optical devices described by their transmission and reflection transfer function $h_t(t)$ and $h_r(t)$ with the mode transformation

$$\hat{a}'(t) = \int dt h_t(t - t') \hat{a}(t) + \int dt h_r(t - t') \hat{b}(t) = (h_t \circ \hat{a})(t) + (h_r \circ \hat{b})(t), \quad (2.3.17)$$

where \hat{b} is the auxilliary mode necessary for commutation relations to hold on mode \hat{a}' , which also requires that

$$\delta(t) = \int dt' (h_t(t+t')h_t^*(t') + h_r(t+t')h_r^*(t')) . \quad (2.3.18)$$

To respect causality $h_t(t)$ and $h_r(t)$ need to be identically zero when $t \leq 0$. The effect of a standard Fabry-Perot cavity is a decaying exponential filtering similar in every respect to a combination of low-pass and high-pass filters:

$$h_t(t) = ke^{-kt}u(t) \longleftrightarrow h_t(\omega) = k/(k+i\omega), \quad (2.3.19)$$

$$h_r(t) = \delta(t) - ke^{-kt}u(t) \longleftrightarrow h_r(\omega) = i\omega/(k+i\omega), \quad (2.3.20)$$

with $u(t)$ the Heaviside function. Notice that $h_t(t) + h_r(t) = \delta(t)$ ensure the preservation of commutation relations and conservation of energy. To take into account the effect of the filtering channel in our multimode model, we simply have to chain in the effect of every individual cavities in series with successive convolution of their transfer functions. We call $h_{\text{cav}}(t)$ the resulting total transfer function. Instead of directly applying the operator $\hat{a}(t_c)$ onto $\hat{S}_\zeta|0\rangle$ as advocated in Sec.2.2.4, we change \hat{a}_{det} of Eq.(2.2.32) into

$$\hat{a}_{\text{det}}(t - t_c) = (\hat{a}_{\text{det}} \circ h_{\text{cav}})(t - t_c) + \hat{a}_{\text{vac}}, \quad (2.3.21)$$

where \hat{a}_{vac} is an auxilliary mode introduced by the reflection ports of the different filtering cavities, and which can be assumed to be in the vacuum state. The presence of the \hat{a}_{vac} term has no influence on the final expression of the density matrix since the APD automatically discards this vacuum term. Thanks to the linearity of the convolution transformation of Eq.(2.3.17), the derivation of Eq.(2.2.39) in Sec.2.2.4 stays valid, with the only added modification

$$f_{\text{sig}}(t) \longrightarrow f'_{\text{sig}}(t) = (f_{\text{sig}} \circ h_{\text{cav}})(t). \quad (2.3.22)$$

There is an additional difficulty in this case because $h_{\text{vac}}(t)$ cannot be a symmetric function. When the time origin t_c is calibrated at 0, we obtain the expression

$$|\psi_{\text{sig}}(0)\rangle = -\hat{S}_\zeta \left(\int dt f'_{\text{sig}}(-t) \hat{a}^\dagger(t) \right) |0\rangle. \quad (2.3.23)$$

With this change applied to $\hat{\rho}_{\text{sig}}$, the discussion of the previous section is also valid, except that $\bar{f}(t)$ has to take into account this filter. This happens with the choice of the wave-packet mode basis: the original basis $\{\phi_n(t)\}_n$ is changed into $\{\phi'_n(t)\}_n$, starting from the filtered wave-packet function $\phi'_0(t) = (f_{\text{sig}} \circ h_{\text{cav}})(t)$. Notice that by successive application of either transmitting or reflecting filtering cavities, it is possible to engineer any final output mode function f'_{sig} on the signal side, with the restriction of course that we are starting from the original function f_{sig} .

We also want to take into account the effect of an electrical filter applied on the homodyne current $U(t)$. The filter is described by its electrical transfer function $h_{\text{elec}}(t)$ and the filtered homodyne current $U'(t)$ is written from Eq.(2.3.7)

$$U'(t) = (h_{\text{elec}} \circ U)(t) = \int dt' h_{\text{elec}}(t-t') \left(\sum_n \phi_n(t') Y_n \right). \quad (2.3.24)$$

Using the same wave-packet basis $\{\phi_n(t)\}_n$, we decompose $h_{\text{elec}}(t)$ into

$$h_{\text{elec}}(t) = \sum_m h_m \phi_m(t), \quad (2.3.25)$$

and $U'(t)$ becomes

$$U'(t) = \sum_{n,m} h_m Y_n (\phi_n(t) \circ \phi_m(t)). \quad (2.3.26)$$

Using the same vector notation as before, we introduce the vector $\vec{h} = (h_0, h_1, \dots)$ and the cross-convolution matrix $C^\phi(t)$ of the basis $\{\phi_n(t)\}_n$ by the relation

$$(C^\phi(t))_{n,m} = \int dt' \phi_n(t') \phi_m(t-t'), \quad (2.3.27)$$

to obtain a compact formulation of Eq.(2.3.26)

$$U'(t) = \vec{h} \cdot C^\phi(t) \cdot \vec{Y}. \quad (2.3.28)$$

As before, we project the filtered homodyne current onto a specific mode with the mode projection function $\bar{f}(t)$, and obtain for Q' the expression

$$Q' = \vec{h} \cdot \left(\int dt \bar{f}^*(t) C^\phi(t) \right) \cdot \vec{Y} \quad (2.3.29)$$

Ideally we would like to obtain a filtered cross-convolution matrix C^ϕ void of terms which would bring Y_n terms other than Y_0 into the expression of Q' . In the frequency domain, the expression of Q' is written

$$Q' = \int d\omega \bar{f}^*(\omega) h_{\text{elec}}(\omega) \left(\sum_n \phi_n(\omega) Y_n \right). \quad (2.3.30)$$

To maximize the purity of the random variable Q' , we therefore want to chose the function \bar{f} which satisfies

$$\int d\omega \bar{f}^*(\omega) h_{\text{elec}}(\omega) \phi_0(\omega) = 1. \quad (2.3.31)$$

To compensate for the electrical filter we then simply have to choose

$$\bar{f}(\omega) = \phi_0^*(\omega) / h_{\text{elec}}^*(\omega) = f_{\text{sig}}(\omega) / h_{\text{elec}}^*(\omega), \quad (2.3.32)$$

assuming that $f_{\text{sig}}(t)$ is symmetric. Taking also into account the effect of the filtering cavities, the final expression of $\bar{f}(\omega)$ is

$$\bar{f}(\omega) = \phi_0^*(\omega) h_{\text{cav}}^*(\omega) / h_{\text{elec}}^*(\omega) = f_{\text{sig}}(\omega) h_{\text{cav}}^*(\omega) / h_{\text{elec}}^*(\omega). \quad (2.3.33)$$

This is the most complete expression of \bar{f} , taking into account all major phenomena which can affect the multimode properties of our photon subtracted state. However, there might still be some small differences between the predicted \bar{f} and the optimal mode projection function for a given set of experimental homodyne photocurrent time series. Among the experimental imperfections we did not take into account, there are possible light leakages in the cavities of the trigger channel or mode mismatch which may change the effective shape of h_{cav} . Also, a true homodyne detector shows realistically some noise which contaminates $U(t)$ to some extent. If this noise is not flat, but rather has a particular spectrum, it might be beneficial to remove it though the choice of the mode projection function \bar{f} . Using techniques of optimal filtering, this can be achieved in a rigorous and systematic way. Finally, it might be physically impossible to exactly cancel h_{elec} , especially if h_{elec} completely cuts a given frequency region which would therefore requires an infinite gain for total compensation. This happens when h_{elec} describes for example a high-pass or notch filter. Note that if the role of the electrical filter was in the first place to remove additional noise, the exact compensation of h_{elec} in \bar{f} is ultimately detrimental. Experimentally, a good method is to look manually for the best mode projection function starting from the predicted \bar{f} , although in reasonable experimental scenarios, this best \bar{f} function matches closely the predicted expression of Eq.(2.3.33).

2.3.4 Instant of detection

In the previous paragraph, we have assumed that the origin of time at the homodyne detector to be exactly at $t_c = 0$ the instant of photon detection at the APD. In the laboratory it is not possible to calibrate an absolute time reference so that the homodyne current is recorded at $t_c = 0$. Therefore, we need a method to calibrate the time reference between the homodyne detector and the APD. The technique we use is to look over an ensemble of different photocurrent time series from the homodyne detector and search for a spike in the point-wise ensemble variance of these series. If the time jitter of the detection event in this ensemble is negligible we can observe the precise time of arrival of the squeezed photon. This method works because the variance of the quadrature operator is larger for a single photon state than for a vacuum state. In this paragraph we demonstrate rigorously this point.

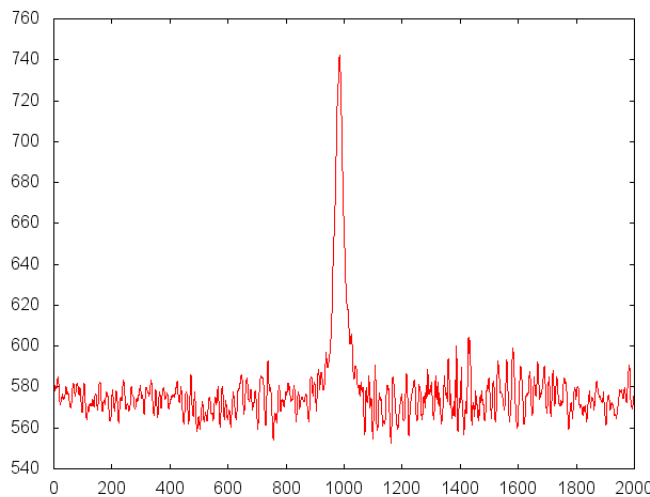


Figure 2.11: Experimental point-wise average of $\langle U^2 \rangle(t - \Delta t)$ the homodyne photocurrent, for a set of 20000 times series of 2000 data points. Horizontal axis, time series point(nanosecond scale, $2 \mu s$ length frames). Vertical axis, arbitrary unit of power. The signature of the photon-subtracted suqeezed vacuum state is clearly visible above the background shotnoise level.

We assume that there is a constant time difference Δt between the instant of detection of a photon by the APD and origin of time when recording the homodyne current. $U(t - \Delta t)$ being the raw homodyne current random process, we know from Sec.2.3.2 that

$$U(t - \Delta t) = \sum_n \phi_n(t - \Delta t) Y_n. \quad (2.3.34)$$

We want to calculate $\langle U^2 \rangle(t - \Delta t)$ the ensemble average at every time. Since all Y_n are assumed to be independant random variables, we obtain

$$\langle U^2 \rangle(t - \Delta t) = \sum_n \phi_n^2(t - \Delta t) \langle Y_n^2 \rangle, \quad (2.3.35)$$

where $\langle Y_0^2 \rangle$ is the power of a squeezed photon

$$\langle Y_0^2 \rangle = \langle 1 | \hat{S}^\dagger X^2 \hat{S} | 1 \rangle = \frac{3}{2} e^{-2s_0}, \quad (2.3.36)$$

and for all $n \neq 0$, $\langle Y_n^2 \rangle$ is the power of the squeezed vacuum $\exp[-2s_n]/2$. As in the Sec.2.3.2, we average $\langle Y_n^2 \rangle$ over all phase angles θ to take into account the squeezing and antisqueezing effect. This can be done by adding a factor $\cosh(2s_n)$ to all terms $\langle Y_n^2 \rangle$. The ensemble average is then expressed as

$$\langle U^2 \rangle(t - \Delta t) = \frac{1}{2} \left(3 \cosh(2s_0) \phi_0^2(t - \Delta t) + \sum_{n \geq 1} \cosh(2s_n) \phi_n^2(t - \Delta t) \right). \quad (2.3.37)$$

With sufficiently homogeneous squeezing parameters s_n , the second term of Eq.(2.3.37) yields a flat noise floor above which $\phi_0^2(t - \Delta t)$ clearly stands. Experimentally, we only need to numerically compute $\langle U^2 \rangle(t - \Delta t)$ for a big enough ensemble and observe the $\phi_0^2(t - \Delta t)$ shape appears in the averaging process. With a simple fit of $\phi_0^2(t - \Delta t)$, we can calibrate the origin of time at the homodyne current for the precise application of the mode function projection function $\bar{f}(t - \Delta t)$. Although this method could be used to deduce the optimal shape of the mode projection function \bar{f} , in practice the time series of the photocurrent $U(t)$ usually show too much noise for this method to be precise.

2.4 Experimental generation

2.4.1 Experimental protocol

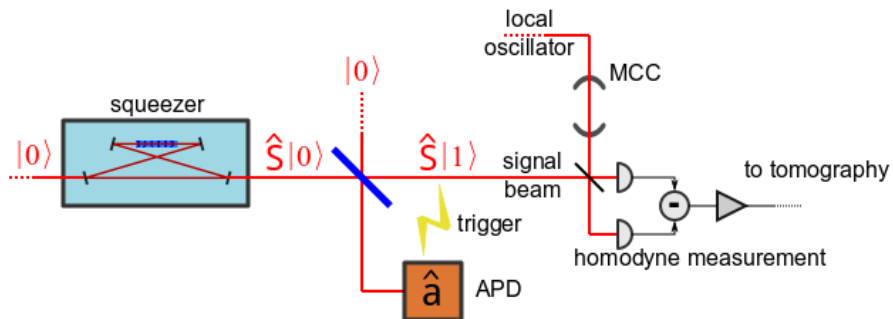


Figure 2.12: Overview of the experimental setup for generation of small amplitude Schrödinger's cat states.

It is straightforward to implement the photon subtraction protocol of [43] into an experimental setup for the case $m = 1$ as it requires only four parts: the squeezed vacuum resource, the triggering channel, the non-linear detector, and the homodyne detector. The optical setup of our experiment is presented and explained in the next section 2.4.2. Sec.2.4.3 presents how the control and automation of the experiment is achieved, with many more information on the digital circuitry found in the Appendixes A and B. In Sec.2.4.4, measurement process are shown with additional details in Appendix C. The general experimental protocol for generation and measurement of a photon subtracted squeezed vacuum state follows this order:

- Pre-alignment: all auxiliary locking beams and probe beams, OPO pumping beam.
- Triggering channel: alignment and mode-matching between filtering cavities and the probe beam, alignment of the APD fiber coupler, confirmation of dark count rate and total event count rate.

- Homodyne detector: alignment of the visibility.
 - Final alignment of the OPO pumping beam and locking of the system.
 - Pre-calibration of the time reference, confirmation of the presence of the heralded squeezed photon state with a measure of $\langle U^2 \rangle(t)$.
 - Optical homodyne tomographic measurement of the Wigner function, with calibration of the shotnoise level before and after.

Experimental results obtained with this protocol are shown in Sec.2.4.5 and fitted to a simple model in Sec.2.4.6. In general, our experimental setup is similar to the setups described in [127] and [167].

2.4.2 Optical setup

The optical setup is shown in Fig.2.13. Appendix D contains a full schematic of the experimental table and of the optical setup, which includes the setup for Schroedinger's cat states generation. More factual experimental details about the optical setup can be found in [156] and [166]. In addition, [166] sports detailed technical drawings of some of the different optical and mechanical elements.

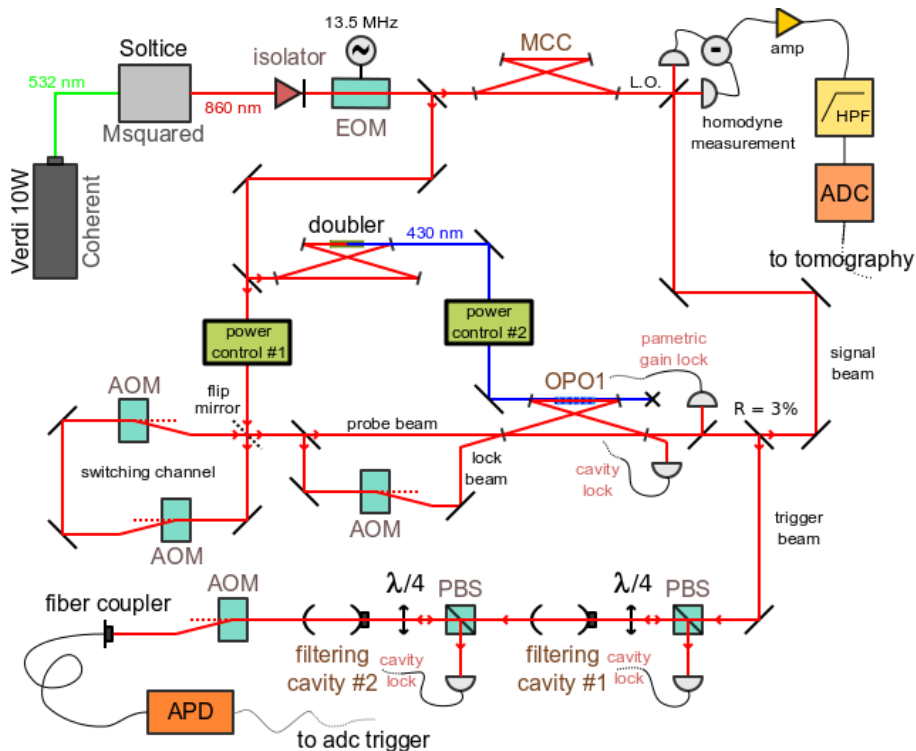


Figure 2.13: Details of the experimental setup for generation of small amplitude Schroedinger's cat states.

Laser light

We use a continuous-wave titanium-sapphire laser at 860 nm (SolsTiS-SRX, M Squared Lasers, Verdi 10 W pump, Coherent) delivering a round, zero-order Gaussian TEM beam of total intensity

1.9 W. This setup has evolved from a titanium-sapphire laser MBR unit from Coherent pumped by a 18 W Verdi laser, also from Coherent[156]. It offers more intensity stability, less amplitude noise, more ease of utilisation and more reliability. About 1 W of this main laser beam is used to pump a second-harmonic generation cavity with a KNbO₃ crystal for pumping the OPO. This cavity is a bow-tie cavity, locked and frequency stabilized with a sideband transmission scheme based on the Pound-Drever-Hall locking technique[21]. The output of second-harmonic generation cavity is typically between 300 and 350 mW of blue light at 430 nm in the round zero-order Gaussian TEM spatial mode.

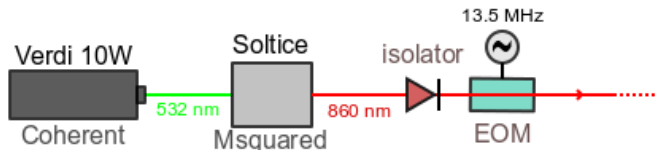


Figure 2.14: Diagram of the laser setup used in the experiment. The 13.5 MHz frequency modulation signal is used for locking feedback loops of the doubler cavity, the mode cleaning cavity and the three OPO cavities.

AOM switches

Acousto-optical modulators (AOM) are used in the setup as light switches. An AOM diffracts incoming light with sound-waves usually in the radio-frequency range. It is build around a crystal where a standing sound wave is generated with two electrodes from an electrical oscillating signal. The sound wave induces a spatial modulation of the index of refraction inside the crystal, which then induces a Brillouin scattering phenomenon on the incoming light. At the particles level, this effect can be understood as a four-wave mixing between phonons and photons. Due to energy conservation, a scattered photon is also shifted in frequency. AOMs can be used as frequency shifters, or also as amplitude modulators by changing the voltage of the electrical signal. The scattering effect can be used to engineer fast light switches, as fast as the inverse of the amplitude modulation bandwidth, typically around 20 MHz. At the current state of technologies, an AOM based switch is orders of magnitude faster than MEMs based optical switches.

Three AOMs are used in a single pass configuration for two optical switches in the optical setup. The first switch uses 2 AOMs with a positive frequency shift and then an identical negative frequency shift for switching light at the laser carrier frequency. Since the RF frequency source is identical for both shifts, any running phase between the RF source and the laser is automatically cancelled by the opposite shifts configuration. The second switch uses only 1 AOM in front of the non-linear avalanche photodiode detector for protecting it from intense laser fields. Since the APD has a very broad range of detection and is "frequency blind", the frequency shift does not need to be compensated. AOMs are powered with RF electrical signals in the 1W to 2W range, with a single stage amplification using high power high bandwidth amplifiers from Minicircuits, ZHL series[177].

OPO

We use for the photon subtraction protocol a weakly squeezed vacuum state $\hat{S}|0\rangle$ generated with an Optical Parametric Oscillator (OPO). It is a standard type I OPO operated below threshold, with a bow-tie cavity built around a periodically poled potassium titanyl phosphate KTiOPO₄ crystal (PPKTP). The finesse of the cavity is 48 for a Full-Width-at-Half-Maximum of 12.3 MHz. PPKTP

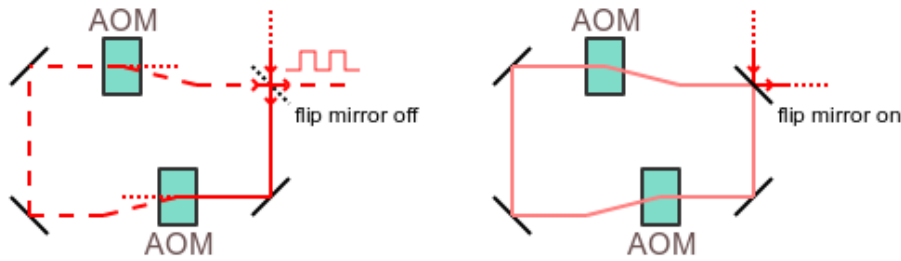


Figure 2.15: AOM switching channel. On the left, the flip mirror is off and the output beam is alternatively switched on and off by the two AOMs. On the right, the flip mirror is on and the output beam is simply reflected towards the OPO.

crystals are very useful non-linear optical medium for generation of squeezing, thanks to their high second order non-linear coefficients and low "blue-light induced red absorption" (BLIRA) effect [103, 126]. The locking and frequency stabilisation of this OPO cavity is based on a transmission sideband locking scheme[21]. The OPO is typically pumped with 15 mW of 430 nm light, for a measured squeezing parameter $s = 0.28 \pm 0.02$ (details of the calibration of s are in Sec.2.4.5). Total intra-cavity losses with the pump beam injected are 0.0033 ± 0.0005 .

Triggering channel

cavity	geometry	l	T	FWHM	FSR	finesse
OPO1	bow-tie	500 mm	0.125	12.3 MHz	590 MHz	48
filtering #1	FB	0.88 mm	$\approx 1-0.9982$	110 MHz	169.4 GHz	1540
filtering #2	FB	2.55 mm	$\approx 1-0.9982$	36 MHz	58.7 GHz	1630

Figure 2.16: Main characteristics of the optical cavities used for Schroedinger's cat state generation.

A small fraction of the squeezed vacuum state produced by the OPO is tapped on a beam-splitter(intensity reflection coefficient $R = 3\%$) and guided into an Avalanche Photo Diode (APD, Perkin-Elmer). Two Fabry-Perot cavities (FWHM: 110 and 36 MHz, finesse: 1540 and 1630) allow for the degenerate central mode of the OPO only to reach the APD. The two cavities are frequency stabilized and locked with the tilt locking scheme. In this scheme, the input beam is very slightly misaligned on one transverse axis so that, for example, the TEM 01 mode of the cavity is also coupled to the input beam. Inside the cavity, the TEM 00 and 01 modes interfere spatially together in proportion to the cavity detuning relatively to the TEM 00 mode[54]. The reflected beam from the cavity carries information on this detuning which can be detected and made into an error signal with either a split photodiodes or either two separate photodiodes.

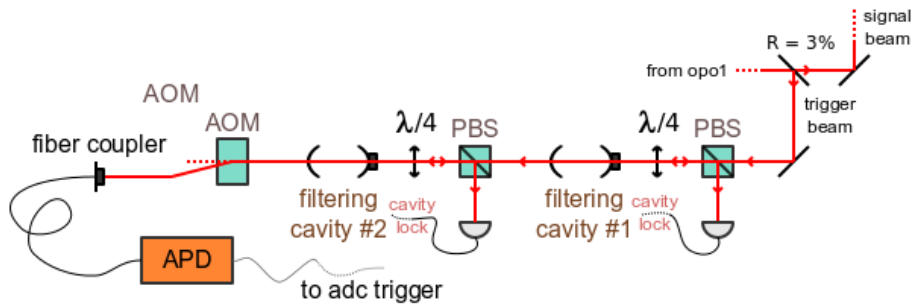


Figure 2.17: Diagram of the triggering channel and setup of the filtering cavities.

Single photon counting

The non-linear photon detector we use is an Avalanche PhotoDiode (APD) whose general behavior is described in Sec.1.5.4. The APD is a SPCM-AQRH-14 model made by Perkin-Helmer[180], where SPCM stands for Single Photon Counting Module, with a certified maximum dark count rate of 100 events per second. The maximum count rate before saturation is 25 million. The dead time or recovery time is 32 ns, and pulse width is 15 ns. The quantum efficiency at 860 nm is approximately $45\% \pm 5\%$.

Homodyne detection

The homodyne measurements is performed in a balanced configuration with a 50/50 beam-splitter. For better spatial mode-matching the local oscillator beam is filtered in a separate empty bow-tie cavity with the same geometry as the OPO cavity. Once aligned, the visibility is as high as 99%. The detector circuitry itself is built according to the transimpedance design[56] and employ a pair of silicon pin photodiodes with a 99% quantum efficiency (Hamamatsu, special order diode). The bandwidth of the detectors is above 20 MHz and large enough for the measurement of $f_{\text{sig}}(\omega)$ and of all frequency components of the non-Gaussian state. The local oscillator power is set at 10 mW before the beam-splitter to avoid saturation of the photodiodes yet to obtain a high electrical signal-to-noise ratio.

Parameters optimization

With a 15 mW pump beam and a $R = 3\%$ intensity pick-up on the signal beam, the photon detection rate at the APD is in the 9000 ± 500 events per second range after all losses on the trigger channel. The effective dark count, which is the sum of the intrinsic dark count of the APD plus additional scattered photons from the environment, is around 120 ± 20 events per second, for an event-to-dark-counts ratio of 66 ± 6 . The modal purity parameter Ξ [89] in these conditions is about 0.98.

Experimentally there is a trade-off between the modal purity Ξ and the purity of the squeezing generated by the OPO. When the pump intensity is weaker (small s values), the squeezing is purer but the number of parametric down converted photon pairs is smaller, therefore the event rate falls compared to the total dark count and the modal purity decreases. When the pump intensity is stronger (higher s values), the squeezing is less pure, which eventually results in losses on the conditional heralded state $\hat{\rho}_{\text{sig}}$, but the modal purity is higher, therefore the conditionally generated state is statistically purer. Furthermore the value of R also directly affects the amount of photons send to the triggering channel, at the expense of counterpart losses on the signal beam, as shown in Sec.2.2.2. In addition higher R and s parameters invalidates the hypothesis of negligible higher

photon number states events beyond $|0\rangle$ and $|1\rangle$ in the trigger channel, and besides effective losses on \hat{p}_{sig} , the conditional signal state starts to show complex multimode properties. Theoretically, the smallest possible R and s the conditional state of the highest quality we can observe. Due to the modal purity trade-off, this is not the case in the laboratory, and the optimal value for s , and to some extent for R too, has to be found by trials and errors, as it strongly depends on the total transmission efficiency of the triggering channel.

In the winter of 2008, the event rate was in the 6000 events per second range, for a pump beam intensity of 35mW . The total dark count was around 250 events per second. With these parameters the measured negativity of the Wigner function was at best -0.091 , for a purity around 0.52, a value much insufficient for teleportation with a reasonable amount of EPR correlations. After improvements to the triggering channel transmission efficiency, namely filtering cavities alignment and locking point, switching AOM coupling efficiency and fiber coupling alignment, the current value of the $\Xi = 0.98$ could be achieved with only 15 mW of pump intensity. Following this improvement in the triggering channel by 350%, the experimental values of negativity also improved and $W(0,0)$ was measured around -0.15 in the summer of 2009, then later around -0.17 in the summer of 2010 after further improvements to the measurement system.

2.4.3 Control and automation

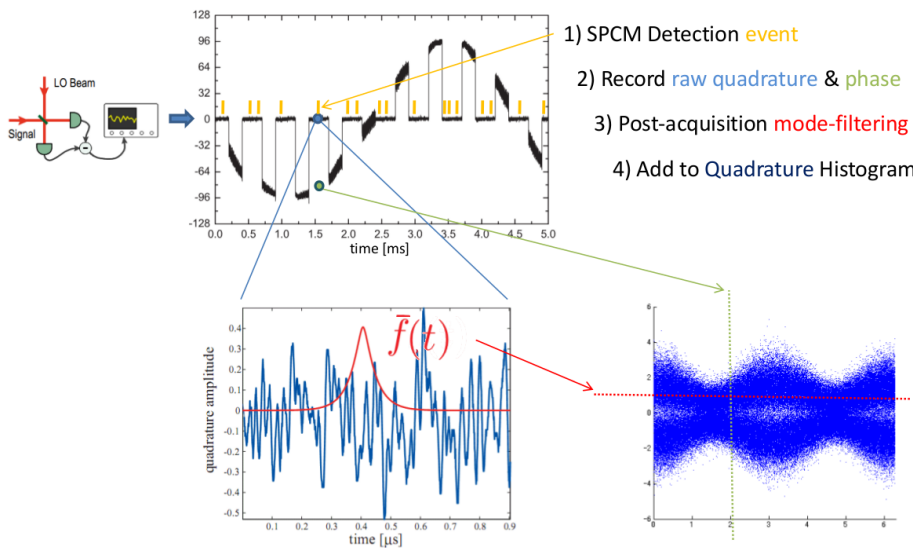


Figure 2.18: Overview of the homodyne tomography process with alternate measurement and control phases.

Because the APD heralded non-Gaussian states are delocalized over a broad range of frequencies as we have seen in Secs. 2.2 and 2.3, it is impossible to use a locking scheme based on frequency sideband modulation directly without irreversibly harming the fragile non-Gaussian states. It would be possible, however difficult, to have modulated sidebands for locking at some higher frequencies outside of the spectrum of the non-Gaussian states. Instead of supporting phase control and noiseless measurement at the same time, we perform time-gated operations where the setup is alternatively in a control phase and in a measurement phase.

In the measurement phase, there is no probe beams and every locking circuit is set on hold, applying a constant feedback value to every PieZoelectric Transducer (PZT) which stops moving anymore beyond their own inertia. In this phase the AOM switch in the triggering channel is

activated and the APD is receiving incoming light from the setup. At the end of the triggering channel, detection events from the APD triggers individually the measurement and record of times series of the homodyne current on the signal channel. These time series are then saved for latter analysis.

In the control phase, the APD AOM switch is turned off and the APD is off-coupled from the setup. Turning on the AOM switching channel described above, a weak coherent beam is injected into the OPO and propagates along the trigger and signal channels. It is used to lock the OPO and filtering cavities. The relative phase between the probe beam on the signal channel and the local oscillator is not locked but rather continuously scanned with a PZT to measure time series of the homodyne detector homogeneously over $[0, 2\pi]$. At the end of the control phase, the voltage level of the error signal of every feedback loop circuit is sampled and holded by a dedicated integrated circuit for the duration of the next measurement phase.

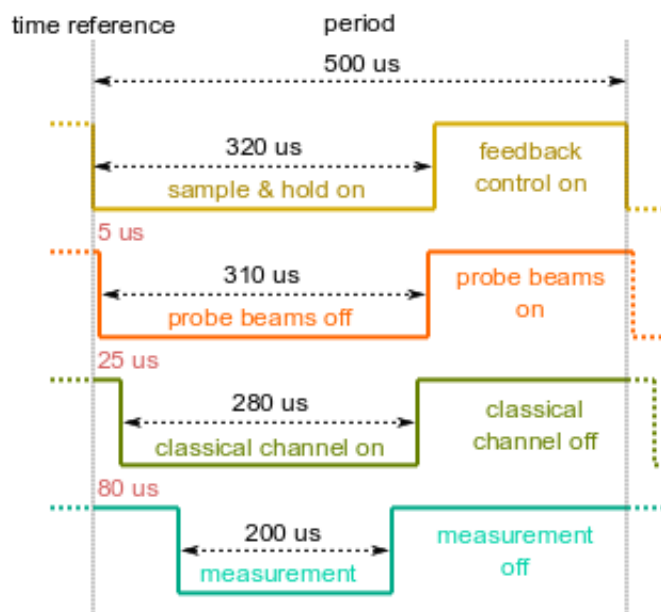


Figure 2.19: Time synchronization of the FPGA generated triggers.

The switching between these two phase happens at a frequency of 2 KHz, with a 3/5 duty cycle biased towards the locking phase. The different triggers logic signals are generated by an FPGA chip running at 40 MHz (National Instruments PXI-7833[175]). This FPGA synchronizes together the triggers signals to activate the 3 AOM switches, to activate the sample & hold circuitry of the feedback loop, and to gate the APD triggers to the measurement electronics. There are user programmable delays between the different triggers so that the exact duty cycles and reference time of every trigger can be adjusted precisely up to a precision of one 40ns FPGA clock cycle. The FPGA also generates the voltage ramp signal to continuously and slowly scan the phase of the local oscillator relatively to the signal. A full scan happens in 5 seconds. To compensate for the slightly non-linear answer of the PZT to a voltage ramp, the FPGA voltage signal has a configurable squared order component. Finally, the FPGA is also used to generate fake photon detection events to trigger the measurement devices when measuring the shotnoise power of the vacuum state. This function is also used when measuring the power spectrum of input and output teleported vacuum states. More details about the analogical electronics circuit used in the feedback loop can be found in [156, 166]. Details about the digital programming of the FPGA can be found in Appendix A.

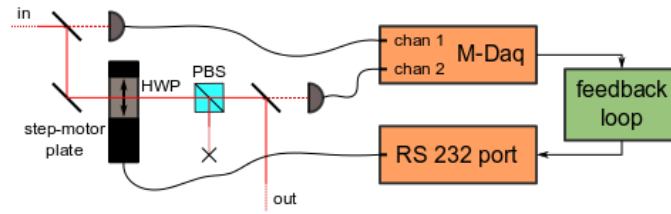


Figure 2.20: Overview of the laser beam power control setup.

Finally, two digital power control feedback loops control the intensity of the laser beams over a large period of time. These feedback control loops are built around a step motor plate rotator[182] on which a half-wave plate if fixed. The laser beam goes through the half-wave plate and then through a polarization beam-splitter (PBS). Two single photodiode placed before and after the PBS and recorded by a low-speed ADC (National Instruments PXI-6251[174]) are used to monitor the transmitted power. The plate can be rotated to adjust the power of the beam to a chosen locking point. The first loop is used to stabilize the power of probe beams, locking beams and local oscillator beams, while the second loop is used on the output beam of the second harmonic generation cavity to stabilize the pumping powers of the different OPOs. More details about this system can be found in Appendix B.

2.4.4 Measurement setup

The homodyne photocurrent to be analyzed for quantum tomography is measured by an analog to digital converter (National Instruments, PXI-5152, sampling rate 1 GHz, 8 bits resolution [176]). To retrieve the non-Gaussian statistics of the state the AD converter is triggered by the clicks of the APD and records 500 data points for every trigger. These 500 points together constitute a single quadrature measurement calculated using the projection mode function \bar{f} in the time domain assumed to be $\exp[-\gamma|t|]$ where γ is the bandwidth of OPO1. At 1 GHz sampling, one data frame is therefore 500 ns long and large enough to capture a full wave-packet of non-Gaussian light. One set of measurements for a complete tomography is made of 200000 quadrature measurements with a uniformly distributed phase angle θ and recorded in approximately 90 seconds. More details about the setup can be found in Appendix B.

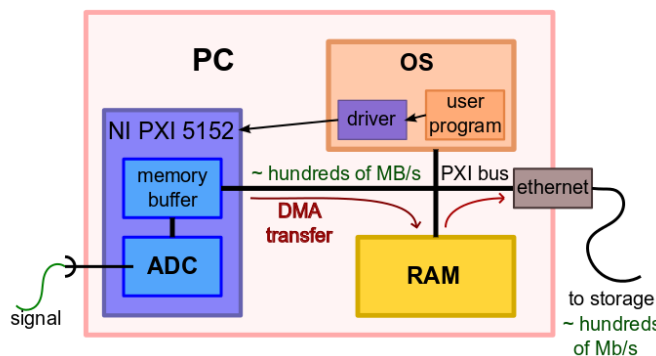


Figure 2.21: Overview of the homodyne current measurement setup.

The homodyne photocurrent needs to be recorded at a sampling rate high enough for all the

frequency components of the photon subtracted state to be measured. According to the Nyquist-Shannon sampling theorem and the experimental parameters of our setup, this requires a measurement bandwidth of 50 MHz, including a safe margin of security to avoid aliasing. In practice we use a 20 times faster sampling rate of 1 GHz for two simple reasons. First, with a sampling rate of 1 GHz the exact instant of the APD trigger is more precisely defined than with a lower sampling rate. In other words when adjusting the exact time origin of the mode projection function $\bar{f}(t - \Delta t)$ we obtain more precision in the estimation of Δt . Second, for cost efficiency as it is not possible to engineer an ADC faster than a few hundreds of MHz with at the same time a vertical precision better than 12 bits at a reasonable cost. There is an implicit trade-off between these two properties and roughly speaking the vertical precision / sampling rate product is constant, all other technologies and parameters being equal. Although the product is constant, the cost is usually lower for a high speed low precision ADC than for a low speed high precision ADC. While a 8 bits vertical precision may seem low, in practice since we eventually only use the photocurrent time series to integrate it with the mode projection function \bar{f} , we benefit directly from the higher number of total sampled points in this 1 GHz oversampling regime. For example, averaging 256 samples at a given bit precision yields a single number with 4 additional bits of precision. In our case, we gain 2 bits of precision with a 20 times faster sampling rate, while at the same time being more cost effective, and having a better precision for the exact calibration of t_c .

The second difficulty is to achieve a measurement data throughput high enough to handle the maximum amount of mean raw data the experiment can produce. With roughly 8000 events per seconds, 500 1-bytes data point per events, two channels to record, and in total data sets of 100000 to 200000 events, the system has to cope with approximately 7 Mb of data per second for a total of 95 Mb. For less sensibility to drifts, other instabilities, and quicker feedback from experimental results, we want to acquire this amount of data in the shortest possible time. In Chap.4, conditional teleportation requires a two times faster data rate, and a three times higher total amount of data. Although it seems a small enough number for modern computers to handle, a bad design of the acquisition and measurement chain will not be able to reach this level of performance. Besides this data rate problem, the main and central difficulty lies in the fact that it is not possible to use a linear flow of control for the automation procedure, because the measurement triggers from the APD randomly happen and are therefore not synchronized with anything else. A linear flow of control would have first to wait for random triggers to happen first and be able to instantly transfer the measurement data from the ADC buffer to the computer. This design can work for a low event rate, but it simply fails in our regime at higher data rates. At around 8000 events per second, such a system would have to treat every events in about one tenth of a microsecond to reach maximum performances. To work around these limitations, and build a truly scalable system as we would like to have for the latter experiments on conditional teleportation, we need to have the following properties:

- **A concurrent flow of control:** it is necessary to be able to handle events independently from data transfer, and therefore a linear flow of control is almost impossible to design. Since the ADC can be configured to record data in parallel of the CPU activity and allows for DMA copy (direct memory access), it is natural to use a multithreaded architecture for this purpose.
- **Nanosecond synchronicity:** the exact calibration of t_c is crucial for a good projection of the homodyne photocurrent. Therefore we need to eliminate any time jitter between the APD and the ADC triggers.
- **Sufficient data throughput:** we need to read out the data in the ADC buffer memory at least faster, on average, than the recording speed. This is possible with a good ADC card that allows direct memory access and has a fast front buffer clearance and copy time.

- **Server/client architecture:** we need to use separate processes for on the one hand the measurement session and acquisition of one data set, and on the other hand the interface and control of long running modules like FPGA triggers and the laser beam intensity power control module.

Appendix C contains the detailed architecture of the software control programs which allow to meet these design guidelines. In its grand lines, the program is built around separate modules programmed in the Ruby language[181]. Every module has a specific function, for example driver interfacing with one piece of hardware. The FPGA and intensity power control are run continuously on a separate process, while for every measurement sessions, a measurement process is run independently. This process loads the necessary modules for the measurement, configures the different hardware devices, starts the acquisition, saves the data to the hard-drive, and then terminates.

2.4.5 Experimental results

Wigner functions reconstructed through quantum homodyne tomography are the main experimental results of this section. We are interested by the Wigner function $W_{\text{in}}(q, p)$ of the quantum states generated by our experimentally setup and want to know if it is in agreement and fidel to the photon subtraction protocol. the "in" label refers to the fact that this quantum is used as the input state for the broadband teleportation experiment presented in Chap.4. Especially, we want to know if the Wigner function shows some negativity and with which magnitude. More in depth details about the process of quantum tomography and the possible Wigner function reconstruction algorithms are presented in Chap.3.

Quantum tomography

The measurement and homodyne time series analysis process explained in the previous sections produce a set of independently and identically distributed quadrature values at homogeneously distributed phase angle, plotted in Fig.2.22. Using this set of quadrature points $\{x_i, \theta_i\}_i$, we reconstruct either the density matrix $\hat{\rho}_{\text{in}}$ of the quantum state with the maximum-likelihood iteration algorithm[45, 87] or the Wigner function $W_{\text{in}}(q, p)$ with the inverse Radon transform[5]. Using Eq.(1.3.13) and the Moyal functions of the harmonic oscillator we can easily pass from $\hat{\rho}$ to $W_{\text{in}}(q, p)$ and vice-versa. For both reconstruction techniques, the algorithms are applied without any compensation for imperfection or prior knowledge of the quantum state. For the maximum-likelihood iteration algorithm, we use a photon number basis up to $|15\rangle$, with 40 iterations, which is sufficient for the convergence error to fall inside the tomography statistical error. For the inverse Radon transform, we use the polynomial series decomposition technique demonstrated in Chap.3, with the parameter $L = 10.0$ (reconstruction disk radius), $M = 40$ (radial reconstruction order) and $N = 8$ (angular reconstruction order). Wigner functions reconstructed with both techniques are presented in Fig.2.23. Also, using the reconstructed density matrix, we plot the photon number distribution of the quantum state in Fig.2.24. Further figures and number derived below are calculated using the Wigner function reconstructed with the maximum likelihood iteration algorithm.

The marginal distributions exhibit the characteristic eye shape of photon-subtracted squeezed states, with a clear lack of detection events around the origin for any phase. Although necessary, this feature alone is not sufficient to confirm the presence of negativity in the Wigner function. The reconstructed input Wigner functions in Fig.2.23 shows the two positive Gaussian functions of $|+\alpha\rangle$ and $|-\alpha\rangle$ together with a central negative dip ($W(0, 0) = -0.171 \pm 0.003$) caused by the interferences of the $|+\alpha\rangle$ and $|-\alpha\rangle$ superposition. The purity of the state is found to be 0.62 ± 0.01 . The experimental state has an average photon number $\langle \hat{n} \rangle$ equal to 1.22 ± 0.01 . Both

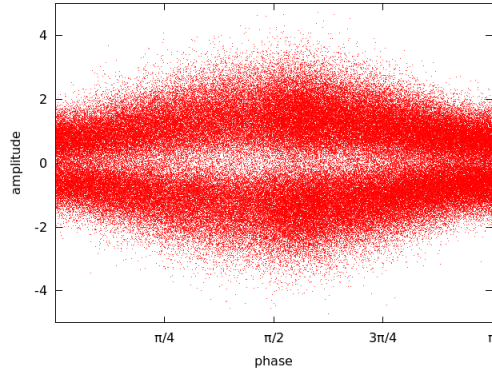


Figure 2.22: Marginal distribution of the electrical field of the experimentally generated photon subtracted squeezed vacuum state. All points together constitute the set of independently and identically distributed quadrature values $\{x_i, \theta_i\}_i$ obtained through angular resolved optical homodyne measurement.

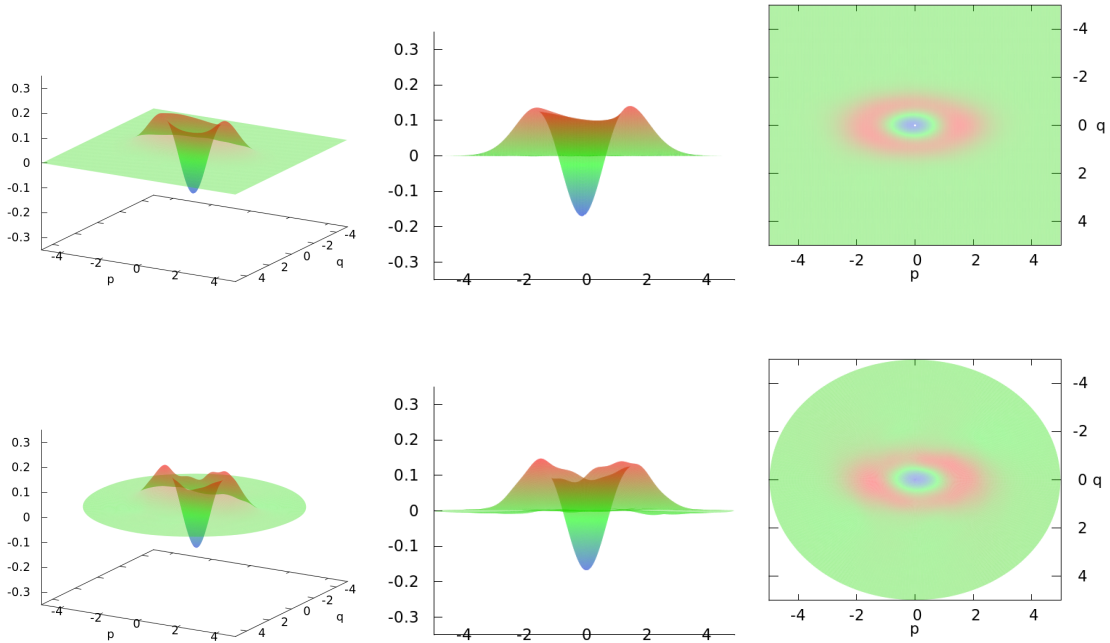


Figure 2.23: Reconstructed Wigner functions of the experimentally generated photon subtracted squeezed vacuum state. Top row, with the maximum likelihood iteration algorithm. Bottom row, with the polynomial series decomposition inverse Radon transform algorithm.

tomography techniques give numbers matching and in agreement, to the extent of the tomography reconstruction error.

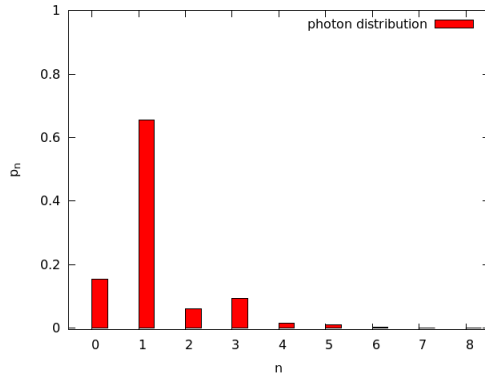


Figure 2.24: Photon number distribution of the experimentally generated photon subtracted squeezed vacuum state.

Schroedinger's cat state fidelity

To calculate the Schroedinger's cat state fidelity $F_{\text{cat}} = \langle \text{cat}_{\alpha,\pi} | \hat{\rho}_{\text{in}} | \text{cat}_{\alpha,\pi} \rangle$ we express the scalar product in phase space as

$$F_{\text{cat}} = 2\pi \int_{-\infty}^{+\infty} dq \int_{-\infty}^{+\infty} dp W_{\text{cat}}(q, p) W_{\text{in}}(q, p). \quad (2.4.1)$$

Our target Schroedinger's cat state is the odd-cat state $(| +\alpha \rangle - | -\alpha \rangle)/\sqrt{N}$ where N is a normalization factor expressed as $2(1 - \exp[-2\alpha^2])$ and α is a real number. Its Wigner function W_{cat} is given as

$$W_{\text{cat}}(q, p) = \frac{2}{N} e^{-q^2-p^2} \left(e^{-2\alpha^2} \cosh(2\sqrt{2}\alpha q) - \cos(2\sqrt{2}\alpha p) \right). \quad (2.4.2)$$

To estimate the fidelity to the nearest odd-cat state, using our reconstructed density matrix $\hat{\rho}_{\text{in}}$ and the above expression of W_{cat} we evaluate numerically the above integral and look for its maximum value over the free parameter α . We calculate that the fidelity F_{cat} is as high as 0.750 ± 0.005 for the input Wigner function W_{in} with the nearest Schroedinger's cat having an amplitude equal to $|\alpha_{\text{in}}|^2 = 0.98$.

2.4.6 Imperfection model

As is inevitable, the experimentally measured and reconstructed Wigner functions of our photon subtracted squeezed vacuum state shown in Fig.2.23 are not perfect. The negativity $W_{\text{in}}(0, 0)$ for instance does not reach the theoretical minimal value $-1/\pi$. The degradation of the central negative dip and the full shape of W_{in} can be fully understood with a phase-space model of input state. Fortunately we have already prepared all the necessary elements to easily develop this model here. We saw in Sec.2.2 that the various single-mode and multi-mode models for the subtraction protocol are equivalent in the limit of small s and R parameters and all predict for the heralded photon-subtracted squeezed vacuum $\hat{a} \hat{S}_s |0\rangle$. The Wigner function W_{ref} of this reference state is written

$$W_{\text{ref}}(q, p) = 2(e^{2s}q^2 + e^{-2s}p^2 - 1/2)G_{1/\sqrt{2}}(e^s q, e^{-s} p), \quad (2.4.3)$$

and has a maximal central negativity of $W_{\text{ref}}(0, 0) = -1/\pi$. From now on we focus on the value of the Wigner function at the origin of phase space as the figure of merit for our experimental input state. Equation (2.4.3) is, of course, of little interest since an actual experimental input state

is virtually always a mixed state and a more realistic model of input is required. The experimental input state shown in Fig.2.23 happens to fit well a simple loss model where the experimental Wigner function W_{in} can be modeled from W_{ref} the reference state, by applying beam-splitter losses $1 - \eta$ equivalent in phase space to the operation

$$W_{\text{in}}(x, p) = \frac{1}{\eta} (W_{\text{ref}} \circ G_\lambda) \left(\frac{x}{\sqrt{\eta}}, \frac{p}{\sqrt{\eta}} \right), \quad (2.4.4)$$

with $\lambda = \sqrt{\frac{1-\eta}{2\eta}}$ (see Sec.1.3.4). By using the previous algebraic expression (2.4.3) of W_{ref} together with the transformation (2.4.4), we can obtain the exact expression of W_{in} with any mathematical software. We rather are interested in the central negativity given by

$$W_{\text{in}}(0, 0) = (1 - 2\eta)/\pi (1 + 4\eta(1 - \eta)\text{sh}^2(s))^{3/2}, \quad (2.4.5)$$

where the negativity threshold $W_{\text{in}}(0, 0) = 0$ depends only on η : $\eta \geq 0.5$ implies $W_{\text{in}}(0, 0) \leq 0$. Looking at Fig.2.25, we notice that the negativity quickly disappear with increasing losses, a process which is amplified by the amount of squeezing. Until now, our model of reference state has

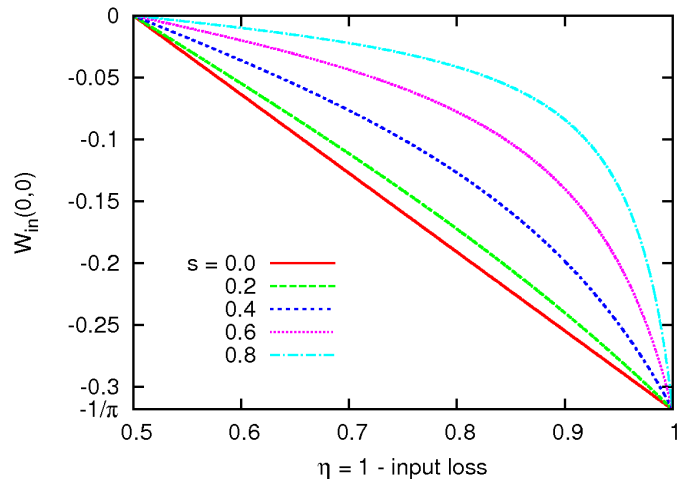


Figure 2.25: Input Wigner function negativity $W_{\text{in}}(0, 0)$ as a function of η for different values of the squeezing parameter s .

assumed a pure state with an initial density matrix $\hat{\rho}_{\text{ref}}$ of the form

$$\hat{\rho}_{\text{ref}} = \hat{a} \hat{S}_s |0\rangle\langle 0| \hat{S}_{-s} \hat{a}^\dagger. \quad (2.4.6)$$

However, to be more faithful to experimentally produced squeezed photon states, rather than an ideal photon resolving detector, we should consider the unideal projection properties of the Geiger silicon Avalanche PhotoDiode (APDs) experimentally used to produce photon subtracted states. Essentially two mixing mechanisms are at work. First, the on/off character of the APD makes it only able to detect the presence of photons without resolving the actual number of them. This leads quite naturally to a Positive Operator Valued Measure (POVM) solution to model the APD measurement, as was done in [103]. However, the effect is rather marginal if we restrict ourselves to small squeezing s and small tapping fraction R and we actually neglects photon components higher than $n = 1$ in the trigger channel. Second, the laboratory APD is also characterized by a dark count rate, which will produce false heralding events and induce some statistical mixing of

the target state. When such a false event occurs, no projection happens on the signal mode as no photon is subtracted and the signal mode density matrix is just $\hat{\rho}_{\text{false}} = \hat{S}_s|0\rangle\langle 0|\hat{S}_s^\dagger$ corresponding to the OPO output squeezed vacuum. We introduce a parameter ϵ that reflects this statistical mixing and write the new reference density matrix $\hat{\rho}'_{\text{ref}}$ as

$$\hat{\rho}'_{\text{ref}} = (1 - \epsilon)\hat{\rho}_{\text{ref}} + \epsilon\hat{\rho}_{\text{false}}, \quad (2.4.7)$$

where ϵ is related to the modal purity parameter Ξ introduced in [89] by $1 - \epsilon = \Xi$. With $\epsilon \neq 0$, the value of $W_{\text{ref}}(0, 0)$ is not optimal anymore, but becomes

$$W_{\text{ref}}(0, 0) \rightarrow (1 - \epsilon).W_{\text{ref}}(0, 0) + \epsilon.W^{\text{false}}(0, 0) = (2\epsilon - 1)/\pi. \quad (2.4.8)$$

Correcting for the effect of Eq. (2.4.7) in the input negativity expression of Eq.(2.4.5) is straightforward as the beam-splitter loss model of Eq.(2.4.4) is linear with W_{ref} and we write

$$W^{\text{in}}(0, 0) \rightarrow (1 - \epsilon)W^{\text{in}}(0, 0) + \frac{\epsilon}{\eta}(W_{\text{false}} \circ G_\lambda)(0, 0). \quad (2.4.9)$$

We finally find for the corrected input negativity the new expression

$$W_{\text{in}}(0, 0) \rightarrow W_{\text{in}}(0, 0) + 2\epsilon\eta \frac{1 + 2(1 - \eta)\text{sh}^2(s)}{\pi (1 + 4\eta(1 - \eta)\text{sh}^2(s))^{3/2}}, \quad (2.4.10)$$

The input state negativity threshold $W_{\text{in}}(0, 0) = 0$ now gives the following relation between η and ϵ

$$\epsilon = (2\eta - 1)/2\eta (1 + 2(1 - \eta)\text{sh}^2(s)). \quad (2.4.11)$$

For nonzero ϵ , the input threshold becomes dependent on the squeezing parameter s (see Fig.2.26). The first step to test the validity of our results is to check that the input state model we have

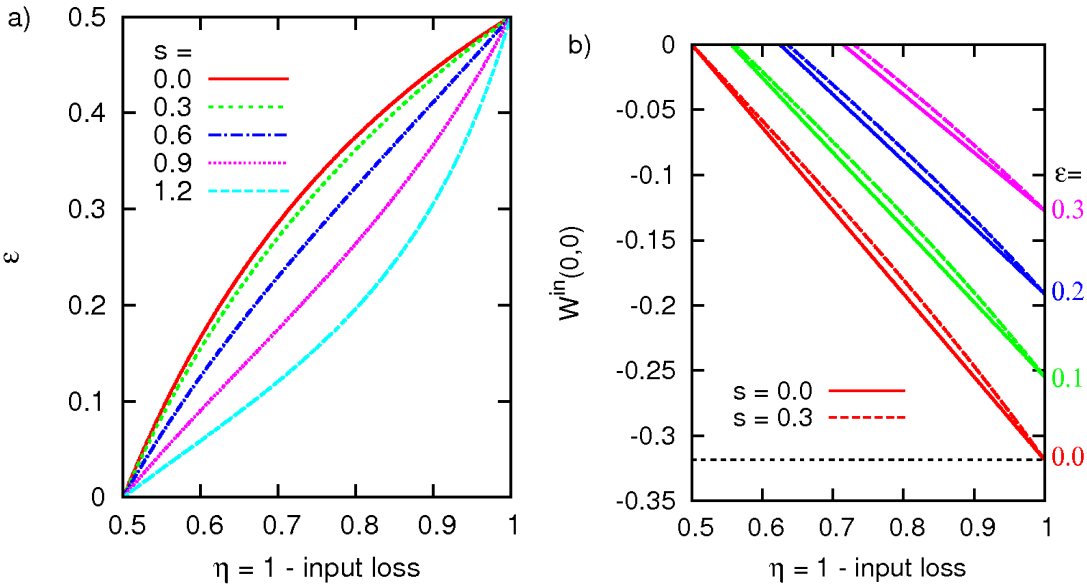


Figure 2.26: (a) Input negativity threshold $W_{\text{in}}(0, 0) = 0$ as a function of η , s , and ϵ . (b) Input negativity $W_{\text{in}}(0, 0)$ as a function of η for different values of s and ϵ .

developed for experimentally generated photon subtracted squeezed vacuum states works well

with the experimental input states of Fig.2.23. For that we need to estimate three parameters: the squeezing parameter s , the loss parameter $1 - \eta$, and the APD dark noise parameter ϵ . A direct measure of the APD dark noise and event counts gives for ϵ a value of 0.013. With the help of quantum tomography of the input squeezed vacuum state $\hat{S}_s|0\rangle$ the squeezing parameter s is estimated to be 0.28. This tomography is done using the wave-packet function f_s as a filter of the measured homodyne currents and without conditioning on the APD triggers. This means that s is actually an effective squeezing parameter in the sense of Eq.(4.1.46) (see Sec.4.1.5 in Chap.4), taking into account the bandwidth of the OPO used to generate the state $\hat{S}_s|0\rangle$. Furthermore, notice that the value of s to be used in the model has to be compensated for losses and other experimental imperfection if s is estimated from reconstructed Wigner functions of the squeezed vacuum state produced by OPO1. Finally, to estimate the value of η , we use the equation (2.4.10) with the value of $W_{\text{in}}(0, 0)$ obtained from a quantum tomography of the input state and obtain $\eta = 0.80$. With these three parameters known we can numerically simulate W_{in} using our model and compare it to the reconstructed Wigner function with the overlap formula,

$$O(W_a, W_b) = 2\pi \int \int dx dp W_a(x, p) W_b(x, p). \quad (2.4.12)$$

However, this formula does not work so straightforwardly in our case: if W_a and W_b are mixed states and even though $W_a = W_b$, the overlap given by formula (2.4.12) will not be 1 but rather the purity of W_a . We therefore use a modified version of the above formula with a renormalization factor taking into account the purity of both quantum states:

$$O'(W_a, W_b) = \frac{O(W_a, W_b)}{(O(W_a, W_a)O(W_b, W_b))^{1/2}}. \quad (2.4.13)$$

With this modified overlap formula (2.4.13) we calculate an overlap of 0.987 between our model and the reconstructed state. The L2 Euclidian distance $d(W_a, W_b)$ defined by

$$d(W_a, W_b) = \left(\int \int dx dp |W_a(x, p) - W_b(x, p)|^2 \right)^{1/2}, \quad (2.4.14)$$

between the two states is found to be 0.05. Finally one could also choose to maximize O' rather than fitting the value of $W_{\text{in}}(0, 0)$ to estimate η . However, because this approach can lead to a value of $W_{\text{in}}(0, 0)$ significantly different from the experimentally measured value, we chose to directly fit $W_{\text{in}}(0, 0)$ instead.

Overall, the fitting results based on Eq.(2.4.10) are numerically in good agreement with the experimental results of Fig.2.23. Our model uses a set of only three parameters and even though more complex models for photon subtracted squeezed vacuum states exist, we found it was not necessary to use them. This confirms the validity of our initial assumption to only consider the small R , small s regime. Finally we end this chapter with an estimate of the loss budget for our Schroedinger's cat state generation setup. Experimentally we have found for the parameter η a value equal to 0.8. This parameter is actually a compound of the effect of different loss mechanisms happening on top of each other. We can write η as

$$\eta = \eta_p \eta_B \eta_{\text{opt}} \eta_{\text{homodyne}} \eta_{\text{det}} \eta_{\text{proj}} \quad (2.4.15)$$

where η_p the purity of the initial squeezed vacuum state is around 0.87, η_B the transmission of the subtraction beam-splitter is 0.97, η_{opt} the propagation losses are around 0.99, η_{homodyne} the homodyne detector visibility is 0.99, η_{det} the efficiency of the photodiode and the homodyne detector is 0.98 and η_{proj} is the information loss induced by the single-mode projection mechanism and is approximately 0.98. Overall, this compound estimation of η yields a value of 0.81 in good agreement with the model estimate. We notice that the purity of the initial squeezed vacuum state is by far the most important parameter for high quality non-Gaussian state generation in the laboratory.

Chapter 3

Quantum Tomography

We present in this chapter results on optical homodyne tomography and quantum state reconstruction. In Sec.3.1, we first introduce the two main experimental techniques for tomography: inverse reconstruction algorithms based on Gaussian measurements; and direct sampling of the Wigner function with non-linear measurements. We focus afterwards on the former category of reconstruction techniques. In Sec.3.2, we present the linear quantum state reconstruction techniques based on the inverse Radon transform. In addition to the usual filtered back-projection algorithm, we demonstrate a novel method for optical homodyne tomography based on polynomial series expansion of the Wigner function and the marginal distribution. We show that this technique solves most technical difficulties encountered with kernel deconvolution based methods and reconstructs overall better and smoother Wigner functions. In Sec.3.3, we present reconstruction techniques based on variational principles, focusing on the maximum-likelihood principle, and applied to the iterative reconstruction of the density matrix. In Sec.3.4, we look in more details at errors produced by the different reconstruction algorithms. For linear techniques, we derive and give estimators of the reconstruction errors for both the filtered back-projection algorithm and the polynomials series decomposition algorithm. We demonstrate that the later shows improvement in noise handling properties and resilience to statistical errors.

3.1 Quantum state reconstruction

In quantum mechanics it is not possible to directly observe an unknown quantum state $|\psi\rangle$ in a single measurement. In order to obtain full knowledge about $|\psi\rangle$ it is necessary to accumulate measurement statistics of observables, such as position \hat{x} or momentum \hat{p} , on many different bases. In quantum optics, this statistical measurement can be achieved by angle resolved homodyne measurement of the operator $\hat{x}_\theta = \hat{x} \cos \theta + \hat{p} \sin \theta$ to acquire statistics of the squared modulus of the wave function $|\langle x_\theta | \psi \rangle|^2$ (see Sec.1.5.2 or also [46]). Instead of the quantum state $|\psi\rangle$, one is rather usually interested in reconstructing the more general density matrix $\hat{\rho}$ of the system. In this case, the probability of measuring a value x for the quadrature \hat{x}_θ at angle θ is simply given by

$$p(x, \theta) = \text{tr} [\hat{\rho} |x_\theta\rangle \langle x_\theta|] = \langle x | U_\theta \hat{\rho} U_\theta^\dagger | x \rangle. \quad (3.1.1)$$

Fully equivalent to $\hat{\rho}$, it is also possible to reconstruct the Wigner function $W(q, p)$ from $|\langle x_\theta | \psi \rangle|^2$. However, the reconstruction of $\hat{\rho}$ or $W(q, p)$ is not immediate and requires the reconstruction of the complex phase of the quantum system from the angle resolved measurements. With the measurement of $|\langle x_\theta | \psi \rangle|^2$, these two operations together are referred to as quantum homodyne tomography or optical homodyne tomography [36].

While some tomography algorithms reconstruct the former density matrix, others reconstruct the latter Wigner function. Independently, tomography algorithms can be roughly classified into

two categories. Historically the first to be proposed and used for optical homodyne tomography, linear methods exploit and inverse the linear relationship between the experimentally measurable quantity $|\langle x_\theta | \psi \rangle|$ on the one hand and $\hat{\rho}$ or $W(q, p)$ on the other hand. Among them, the filtered back-projection algorithm [30, 36] based on the inverse Radon transform [5] is the most commonly used. Similar in nature, there also exist methods based on quantum state sampling of individual components of the density matrix $\hat{\rho}$ with "pattern" sample functions [40, 41]. The linear methods, however, suffer in general from technical difficulties associated with the numerical deconvolution necessary to perform the linear inversion of the Radon transform (see Sec.3.2 for details). In addition, they usually do not guarantee the physicality of the reconstructed state, that is the positivity of $\hat{\rho}$. Finally they also usually perform more weakly against statistical noise and show numerical instabilities for higher frequency components and fine details of the reconstructed objects. In Sec.3.2.2, we show that these difficulties are essentially technical and can be solved with a better approach to the inverse Radon transform. Variational methods, such as the maximum entropy [72] and maximum likelihood [45] algorithms, were latter applied to optical homodyne tomography to address some of these problems. These second category of methods can be designed to enforce the physicality of the reconstructed state and are usually more resilient to statistical errors. Since the reconstructed states are not defined constructively, an approximation procedure, typically iterative, is used to achieve the reconstruction in practice [87]. Sec.3.2 focuses on linear methods while variational methods are the subject of Sec.3.3.

3.1.1 Inverse problem statement

Because measures in quantum mechanics can only be interpreted as random processes, quantum tomography is in essence a statistical problem. The task at hand is to numerically reconstruct an unknown quantum state $\hat{\rho}_0$ with some experimentally measured data set. In practical terms, the experimental data set results from the repeated measure $\langle \hat{O} \rangle$ of a chosen observable operator \hat{O} taken on the unknown underlying state $\hat{\rho}_0$. As far as experiments go it is never possible to actually obtain direct information about the underlying state $\hat{\rho}_0$. What quantum tomography can only achieve is to give a statistical estimate, not of the unknown underlying state $\hat{\rho}_0$, but of $\hat{\rho}_{\text{exp}}$ the experimentally accessible state in the measurement process. For instance in such a statistical reconstruction process, one cannot tell between any external statistical source of noise and the underlying quantum state $\hat{\rho}_0$. In other words, any attempt to infer information on $\hat{\rho}_0$ from the measurement of $\hat{\rho}_{\text{exp}}$ is equivalent to a biased measurement. This problem is further made complex by the fact that only one averaged measurement $\langle \hat{O} \rangle$ is not enough in any case to obtain without ambiguity a full and complete description of an unknown quantum state, whatever is the tomography algorithm.

We now rigorously state the problem of quantum tomography. Before adding quantum mechanics into the mix we first describe the random measurement process itself and say that with a repeated experimental procedure, we have obtained an experimental set of J data points $\{\vec{x}_i\}_{i \leq J}$ where every event \vec{x}_i is assumed to be a vector. Our assumption is that the experiment outcome can be fully described by a mathematical object S , which can be either a scalar, a vector, a matrix, or even a function. The probability to observe the experimental data set $\{\vec{x}_i\}_{i \leq J}$ only depends on S and can be therefore written as the conditional probability

$$P(\{\vec{x}_i\}_{i \leq J} | S). \quad (3.1.2)$$

We want to produce a numerical estimate of S , which takes the form of an estimator functional \check{S} taking for input the experimental data set $\{\vec{x}_i\}_i$. S and \check{S} are related by the relation

$$\check{S}(\{\vec{x}_i\}) = S + b + \epsilon, \quad (3.1.3)$$

where b and ϵ are estimation errors. b is the bias of \check{S} and quantifies systematic errors in the estimator. ϵ is a random error which quantifies statistical errors due to the finite size of the experimental

data set $\{\vec{x}_i\}_i$. If S is a scalar or vector-like object we can usually assume that components of ϵ are normally distributed. For most linear algorithms and some variational algorithms, it is possible to obtain a direct expression of the estimator \check{S} which can be used to directly calculate an estimate of S given an experimental data set $\{\vec{x}_i\}$. Sometimes a direct expression is not derivable and the estimate has to be approximated with some procedure, typically in an iterative fashion.

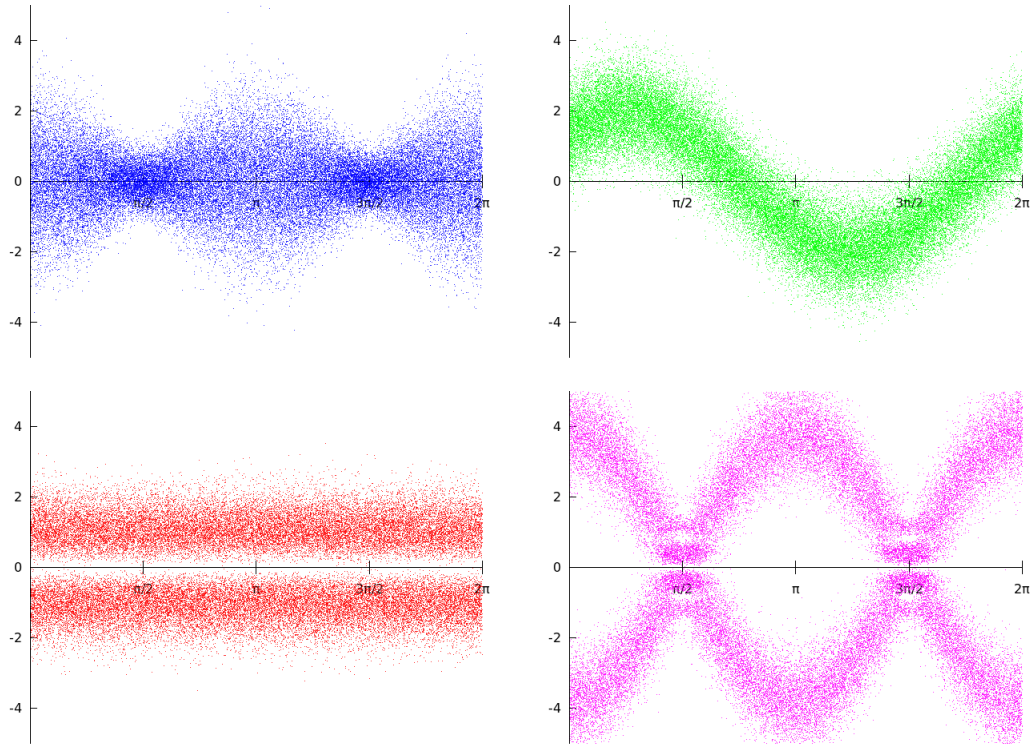


Figure 3.1: Example of the marginal distribution of the electrical field for different quantum states, normalized to the shotnoise level. Top left, squeezed vacuum state. Top right, coherent state. Bottom left, single photon state. Bottom right, Schrödinger's cat state.

For the case of optical homodyne tomography (see Sec.1.5.2), S can be two different objects, equivalent from the point of view of total information, but yielding different algorithms in practice. The first solution is to use the Wigner function $W(q, p)$ of the system which is the subject of the next paragraph. The second solution is to use the density matrix $\hat{\rho}$ as is explained in Sec.3.1.3. In the case of optical homodyne tomography, the data set $\{\vec{x}_i\}_i$ is nothing else than $\{x_i, \theta_i\}_i$ a set of angular resolved quadrature values, or in other words, an experimental measure of the marginal distribution of the electrical field of the quantum state $\hat{\rho}_0$, in the spatial mode of the local oscillator. Fig.3.1 shows examples of this marginal distribution for different quantum states.

3.1.2 The Radon transform

In 1917, Radon introduces the integral transform \mathcal{R} of two-dimensional functions integrated along straight lines and provides the formula for its inverse \mathcal{R}^{-1} [5]. Nowadays the Radon and inverse Radon transforms are ubiquitous in tomography and find applications in many different area of science. The Radon transform is as well applicable to optical homodyne tomography. First we

recall the definition of the observable operator \hat{x}_θ of an homodyne measurement,

$$\hat{x}_\theta = \hat{U}_\theta^\dagger \hat{x} \hat{U}_\theta = \hat{x} \cos \theta + \hat{p} \sin \theta, \quad (3.1.4)$$

where \hat{U}_θ is the rotation operator in phase space, or phase-shifting operator. The marginal distribution of the homodyne current $p(x, \theta)$ is distributed according to

$$|\langle x_\theta | \psi \rangle|^2 = \langle x | \hat{U}_\theta | \psi \rangle \langle \psi | \hat{U}_\theta^\dagger | x \rangle, \quad \text{or} \quad \text{tr} [|x_\theta\rangle \langle x_\theta| \hat{\rho}] = \langle x | \hat{U}_\theta \hat{\rho} \hat{U}_\theta^\dagger | x \rangle, \quad (3.1.5)$$

where $|x_\theta\rangle$ is the eigenvector of \hat{x}_θ . The Radon transform \mathcal{R} links the Wigner function $W(q, p)$ of the quantum state $|\psi\rangle$ and $p(x, \theta)$ the marginal distribution of the homodyne current with a projection of $W(q, p)$ onto a particular angle of observation θ [46]

$$\begin{aligned} p(x, \theta) &= \mathcal{R}(W) \\ &= \iint_{\mathbb{R}^2} W(q, p) \delta(x - q \cos \theta - p \sin \theta) dq dp \\ &= \int_{-\infty}^{+\infty} W(x \cos \theta - p \sin \theta, x \sin \theta + p \cos \theta) dp, \end{aligned} \quad (3.1.6)$$

where $W(q, p)$ is the Wigner function of $|\psi\rangle\langle\psi|$. There are different methods to prove this relation. A possibility is to prove the equality in the Fourier domain (see Sec.3.2.1). But the easiest solution has been already presented in Sec.1.3.1: starting from the definition of the Wigner function in Eq.(1.3.1) and then performing phase rotations and partial integrations directly in phase space, it is straightforward to obtain Eq.(3.1.6). Reciprocally, as is shown in [46], Eq.(3.1.6) is actually a possible definition of the Wigner function which can yield all its useful properties and characteristics. In essence the Radon transform is a projection from a higher dimensional space, the *feature space* which contains all the information of the physical object under studies, to a lower dimensional *image space*, the point of view for experimental measurements. In the case of optical homodyne tomography, the Radon transform simply states that the observable electrical field is nothing else but a shadow of the underlying Wigner function being looked at different quadrature phase angles θ .

3.1.3 The density matrix picture

Since The Wigner function $W(q, p)$ and the density matrix $\hat{\rho}$ are linked to each other through a linear bijection, it is also possible to formulate angular optical homodyne measurements directly with $\hat{\rho}$. If we recall Eq.(3.1.1) and in addition decompose the trace operation in Eq.(3.1.1) in the photon number basis, we obtain

$$p(x, \theta) = \sum_{n,m} \hat{\rho}_{nm} \langle m | x_\theta \rangle \langle x_\theta | n \rangle. \quad (3.1.7)$$

Using the expression of the photon number states wave-functions of Eq.(1.2.22) we obtain the complete decomposition of $p(x, \theta)$ as

$$p(x, \theta) = \sum_{n,m} \hat{\rho}_{nm} e^{i(m-n)\theta} \frac{H_n(x) H_m(x)}{\sqrt{\pi 2^{n+m} n! m!}} e^{-x^2}, \quad (3.1.8)$$

where we recall that $H_n(x)$ is the n-th order Hermite polynomial. If the measurement yields no phase information but only a measure of the phase averaged marginal distribution $\bar{p}(x)$ defined as

$$\bar{p}(x) = \frac{1}{2\pi} \int d\theta p(x, \theta), \quad (3.1.9)$$

using Eq.(3.1.8) we can express in this special case the optical homodyne tomography relation only with the diagonal elements of the density matrix

$$\bar{p}(x) = \sum_n \hat{\rho}_{nn} \frac{H_n(x)^2}{2^n n! \sqrt{\pi}} e^{-x^2}. \quad (3.1.10)$$

Equation (3.1.8) is the basis for the practical implementation of the maximum-likelihood tomography algorithm explained in Sec.3.3.2. Since it is also linear with respect to the density matrix $\hat{\rho}$, it is possible to instead inverse Eq.(3.1.8) and obtain a direct linear estimator of the density matrix coefficients $\hat{\rho}_{nm}$ of the form[40, 41]

$$\hat{\rho}_{nm} = \check{R}_{nm} (\{x_i, \theta_i\}_i) + \epsilon_{nm}, \quad (3.1.11)$$

where \check{R}_{nm} is an estimator for the $\hat{\rho}_{nm}$ component and ϵ_{nm} is the statistical random error. With similarity to the inverse Radon transform it turns out that this approach suffers severely from numerical implementation problems. Furthermore no mechanism guarantees the physicality of the full reconstructed density matrix.

3.1.4 Direct measurement

Notice that in theory it is actually possible to bypass these delicate numerical reconstruction operations and directly observe the Wigner function $W(q, p)$ with repeated measures of the parity operator $\hat{P} = e^{i\pi\hat{n}}$ where \hat{n} is the number operator. This measurement technique uses the link between the Wigner function value at point (q, p) and the expectation value of \hat{P} for the displaced density matrix $\hat{\rho}$

$$W(q, p) = \frac{2}{\pi} \text{tr} \left[\hat{D}(-\alpha) \hat{\rho} \hat{D}(\alpha) e^{i\pi\hat{n}} \right], \quad (3.1.12)$$

where \hat{D} is the displacement operator and $\alpha = (q + ip)/\sqrt{2}$ [185]. This technique has been first proposed for cavity quantum electrodynamics systems[47] and has been used in several experiments with flux qubits and strip cavities for the full measurement of the Wigner function[139, 169]. A close tomography technique has also been experimentally demonstrated in coupled systems of Rydberg atoms and radio-frequency light fields[70, 133, 134]. In these experiments, the state to be measured $\hat{\rho}$ is first displaced by the complex amplitude $\alpha = (q + ip)/\sqrt{2}$ before an averaged measure of the parity operator \hat{P} produces a direct reading of $W(q, p)$. Unfortunately parity detectors are highly non-linear detectors which can only be partially implemented in the optical regime. In practice it is possible to use transition edge sensors for this purpose, or for quantum states with only low photon number components quasi photon number resolving detectors like time-multiplexing single photon detectors [75] are sufficient to apply such non-linear measurement techniques. While most current quantum state tomography experiments are based on Gaussian optical homodyne tomography, the progress of photon counting technologies may allow in the near future for the more exotic non-linear tomography techniques to reach laboratories.

3.2 Linear inversion

Since the Radon transform of Eq.(3.1.6) is linear with the Wigner function $W(q, p)$, we know that there exists a way to inverse this relation and express the Wigner function $W(q, p)$ from the marginal distribution $p(x, \theta)$ with a linear operator we label \mathcal{R}^{-1}

$$\mathcal{R}^{-1}(W(q, p)) = p(x, \theta). \quad (3.2.1)$$

Such an inverse equations may only have sense as a relation on operators and not on numbers. In other words, although mathematically exact, technical difficulties in the numerical implementation of Eq.3.2.1 can arise with such linear inverse methods. Therefore practical approaches to linear inversion based tomography happen in two steps usually. First, the exact inverse formula is found mathematically. Second, an approximation of this relation is developed in a way relevant to numerical applications. In the next paragraph, we follow this approach for the inverse Radon transform and review the usual filtered back-projection algorithms for optical homodyne tomography. We show in Sec.3.2.2 that it is also possible to find a linear inversion relation in a way which is directly numerically applicable without approximations.

3.2.1 Inverse Radon transform

Expression

In his original paper, Radon mathematically inverses his transform with the back-projection \mathcal{B} of the derivative of the Hilbert transform \mathcal{H} of $p(x, \theta)$

$$W(q, p) = \frac{1}{2\pi} \mathcal{B} \left(\frac{\partial}{\partial y} \mathcal{H}(p(x, \theta))(y) \right). \quad (3.2.2)$$

The back-projection operator \mathcal{B} of a function $f(x, \theta)$ is the function $F(q, p)$ defined by

$$F(q, p) = \int_0^\pi f(q \cos \theta + p \sin \theta, \theta) d\theta. \quad (3.2.3)$$

The Hilbert transform \mathcal{H} of a function $f(t)$ is defined as the principal value of the convolution of $f(t)$ with $1/t$

$$\mathcal{H}(f)(u) = \frac{\mathcal{P}}{\pi} \int_{-\infty}^{+\infty} \frac{f(t)}{u - t} dt, \quad (3.2.4)$$

where \mathcal{P} is the principal-value operator. Expanding Eq. (3.2.2) we obtain the inversion formula

$$W(q, p) = -\frac{\mathcal{P}}{2\pi^2} \int_0^\pi \int_{-\infty}^{+\infty} \frac{p(x, \theta)}{(q \cos \theta + p \sin \theta - x)^2} dx d\theta. \quad (3.2.5)$$

The direct demonstration of this formula is mathematically delicate, and can be found for instance in Radon's article [5]. Although exact, this expression is nevertheless unusable with experimental data as the algebraic expression of $p(x, \theta)$ would be unknown and it would therefore be impossible to evaluate precisely the principal value of the integral in Eq.3.2.5. Furthermore, the $1/(q \cos \theta + p \sin \theta - x)^2$ term in Eq.(3.2.5) can lead to ill-defined values in the numerical integration of $p(x, \theta)$.

Numerically applicable formulation

The projection-slice theorem or Fourier slice theorem [10] gives another reverse path from $p(x, \theta)$ to $W(q, p)$ to work around the difficulties of the principal-value operator (see Fig.3.2). If $\tilde{p}(k, \theta)$ and $\tilde{W}(u, v)$ are, respectively, the one-dimensional and two-dimensional Fourier transforms of $p(x, \theta)$ and $W(q, p)$, then the projection-slice theorem states that

$$\tilde{p}(k, \theta) = \tilde{W}(k \cos \theta, k \sin \theta). \quad (3.2.6)$$

The projection slice theorem is a general relation which works in higher dimensions as well. To prove Eq.(3.2.6) one has to take the one dimensional Fourier transform of Eq.(3.1.6) with respect to the variable x . Simply computing the Fourier transform $\tilde{p}(k, \theta)$ from the measured data would

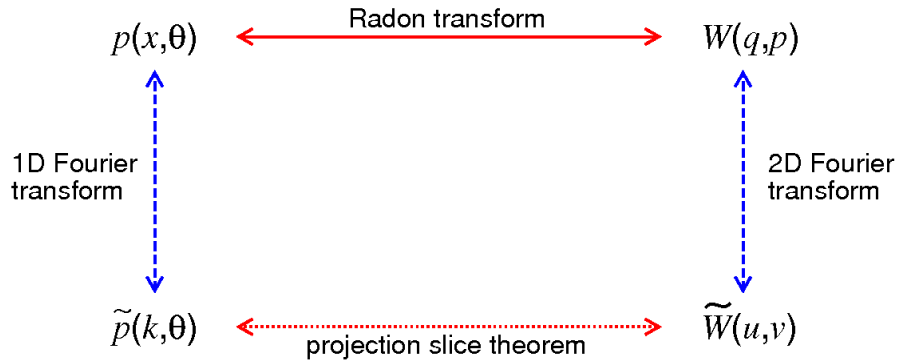


Figure 3.2: Different transforms for different paths from p to W .

seem like the most efficient way to obtain $W(q, p)$ after a second inverse Fourier transform, but Eq. (3.2.6) shows that it would be necessary to interpolate $\tilde{W}(u, v)$ in Fourier space to obtain $W(q, p)$, which leads to significant numerical difficulties [17]. To avoid this interpolation Eq. (3.2.6) can be used to replace $\tilde{W}(u, v)$ in the definition of the inverse Fourier transform of $W(q, p)$ to obtain the inversion formula,

$$W(q, p) = \frac{1}{2\pi} \int_0^\pi \int_{-\infty}^{+\infty} p(x, \theta) K(q \cos \theta + p \sin \theta - x) dx d\theta. \quad (3.2.7)$$

Here, the marginal distribution is convoluted with an integration kernel $K(x)$ and then back-projected into phase space, where $K(x)$ is defined as the inverse Fourier transform of $|k|$

$$K(x) = \frac{1}{2\pi} \int_{-\infty}^{+\infty} |k| e^{ikx} dk. \quad (3.2.8)$$

Implementation

To use Eq. (3.2.7) in practice it is necessary to regularize $K(x)$ and replace it with some numerical approximation, as the integral in Eq.(3.2.8) is divergent. This is possible with the use of a window function $g(k)$ such that the integral,

$$\frac{1}{2\pi} \int_{-\infty}^{+\infty} g(k) |k| e^{ikx} dk, \quad (3.2.9)$$

converges. The most common way to regularize Eq. (3.2.8) is to choose $g(k) = \mathbb{1}_{[-k_c, +k_c]}(k)$ and introduce a hard frequency cutoff parameter k_c so that

$$K(x) \approx \frac{1}{\pi x^2} (\cos(k_c x) + k_c x \sin(k_c x) - 1). \quad (3.2.10)$$

In practice, the choice of k_c affects how much high frequency components of the Wigner function will get reconstructed. If k_c is set too low the convolution in Eq .(3.2.7) will filter out the fine physical details of the Wigner function. If k_c is set too high, the convolution will introduce unphysical high frequency noise from the statistical errors in the measurement of $p(x, \theta)$. Choosing the right value of k_c is a trade off between these two regimes. Figure 3.3 shows the integration kernel $K(x)$ for different high frequency sensitivities. From Eqs.(3.2.6) and (3.2.7) it is also possible to insert other filter functions at different steps of the inversion to obtain modified algorithms with enhanced and more selective noise filtering properties. In any case the numerical implementation

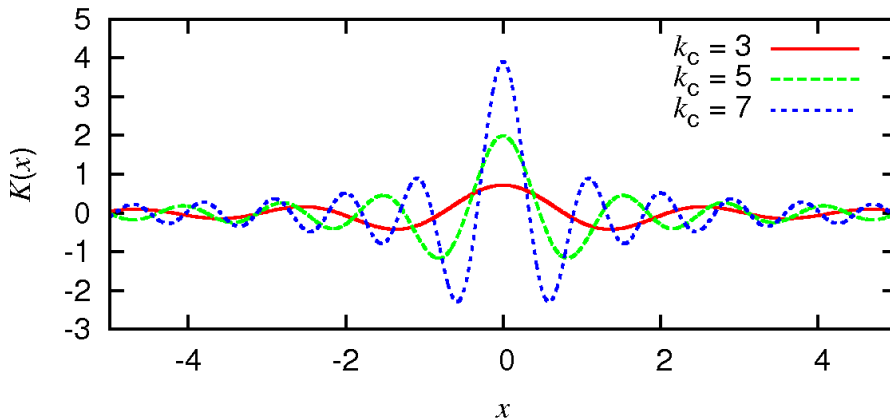


Figure 3.3: Regularized integration kernel $K(x)$ for different values of the cutoff k_c .

of Eq. (3.2.7) implicitly relies on deconvolution of the marginal distribution, an operation very sensitive to statistical noise.

Since the filtered back-projection algorithm is essentially a convolution, its execution speed is greatly reduced as the total size of numerical phase space used to reconstruct $W(q, p)$ increases. For every point (q, p) where the value of the Wigner function is computed, it is necessary to calculate the value of the kernel function and the integral over the quadrature and angle variables x and θ . There are several implementation techniques which can help to reduce the calculation cost. The kernel evaluation contains several transcendental function evaluations and additional multiplications and divisions which are costly in term of CPU cycles. We have found that look-up-value tables and pre-calculating $K(x, \theta)$ could yield speed up factors of an order of magnitude on typical Intel Core 2 machines. Because it is a linear algorithm, each value $W(q, p)$ can be calculated in parallel for every phase space point (q, p) and put together latter on. The computation can also be divided partitioning the experimental data points $\{x_i, \theta_i\}$ into subsets. The filtered back-projection algorithm is therefore straightforward to run on a multi-threaded machine and speed-up factors equal to the number of machine threads can be obtained easily with very good scalability. Although the Fourier convolution theorem might seem appropriate for another gain in execution speed, it is not straightforward to apply it to Eq.(3.2.7) since $p(x, \theta)$ cannot be sampled regularly by random valued experimental measurements[17].

3.2.2 Polynomial series expansion

As we stated in the introduction of this chapter, while the linear methods look inferior to the variational methods, most of their associated problems are only technical in nature and can in principle be solved. In this section we show that it is possible to use a linear reconstruction algorithm with better resilience to noise and better physical properties overall than the usual filtered back-projection method. The success of this approach lies in a systematic expansion of both the Wigner function $W(q, p)$ and the marginal distribution $p(x, \theta)$ in polar coordinates. This circular harmonic expansion technique has been applied in the past to other problems where the Radon transform plays a role in tomography [25, 101], and here we adapt it to the quantum framework of optical homodyne tomography.

To numerically perform optical homodyne tomography, it is necessary at some point to apply an approximation procedure from the infinite dimensional space which features the unknown physical state to a finite dimensional space used to describe the reconstructed state. In the filtered

back-projection algorithm, the discretization is achieved by direct evaluation of $W(x_i, p_i)$ on the set of points $\{(x_i, p_i)\}_i$ chosen to probe the phase space. Rather than this point-by-point reconstruction, a discretization of another space should help to solve the numerical issues encountered in the last section. Since we are dealing with objects behaving like probability distributions, the statistical moments of $p(x, \theta)$ and $W(q, p)$ might be a solution to the problem. In [100], Ourjoumtsev *et al.* describes such a technique where they parametrize the Wigner function of a photon subtracted squeezed vacuum with the second and fourth moments of the marginal distribution $p(x, \theta)$. Generalizing this approach for any quantum state to higher order moments requires the use of the moment generating function $\langle e^{\lambda x} \rangle$, where $\langle x \rangle$ is the expectation value of x with regards to $p(x, \theta)$. Superior to the moment generating function the characteristic function $\langle e^{i\lambda x} \rangle$ only needs the mean and variance to be defined to exist. This and the projection-slice theorem of Eq. (3.2.6) hint that Fourier space or a close space may be good candidates for an efficient discretization.

Derivation

We decompose our discretization procedure in two steps: (1) an angular harmonic decomposition with Fourier series; (2) a polynomial series expansion of the radial components. We express $W(q, p)$ in radial coordinates (r, ϕ) and notice that $W(r, \phi + 2\pi) = W(r, \phi)$. Therefore we write the radial part of $W(r, \phi)$ in terms of a Fourier series and we define the set of radial functions, or angular harmonic components $\{w_n(r)\}_n$ by

$$w_n(r) = \frac{1}{2\pi} \int_{-\pi}^{+\pi} W(r, \phi) e^{-in\phi} d\phi, \quad (3.2.11)$$

which allows us to write $W(r, \phi)$,

$$W(r, \phi) = \sum_{n=-\infty}^{\infty} w_n(r) e^{in\phi}, \quad (3.2.12)$$

with the symmetry relation $w_n(r) = w_{-n}^*(r)$. The 2D Fourier transform $\tilde{W}(u, v)$ of $W(q, p)$ is written in radial coordinates,

$$\tilde{W}(k, \theta) = \int_0^{+\infty} \int_{-\pi}^{+\pi} W(r, \phi) e^{-irk \cos(\theta - \phi)} r dr d\phi, \quad (3.2.13)$$

with the change of variables $k = \sqrt{u^2 + v^2}$ and $\theta = \arctan 2(v, u)$, where $\arctan 2$ takes into account the plane quadrant defined as

$$\arctan 2(v, u) = 2 \arctan \left(\frac{v}{\sqrt{u^2 + v^2} + v} \right). \quad (3.2.14)$$

$\tilde{W}(u, v)$ is related to the Weyl function $\chi(u, v) = \text{tr}(\hat{\rho} e^{-iv\hat{q} + iu\hat{p}})$ by a simple $\pi/2$ rotation,

$$\tilde{W}(u, v) = \chi(-v, u), \quad (3.2.15)$$

$$\tilde{W}(k, \theta) = \chi(k, \theta + \frac{\pi}{2}). \quad (3.2.16)$$

We can easily write \tilde{W} in polar coordinates in terms of the angular harmonic components $w_n(r)$ of $W(r, \phi)$,

$$\begin{aligned} \tilde{W}(k, \theta) &= \sum_{n=-\infty}^{\infty} \int_0^{+\infty} w_n(r) r dr \\ &\times \int_{-\pi}^{+\pi} e^{-irk \cos(\theta - \phi) + in\phi} d\phi. \end{aligned} \quad (3.2.17)$$

With a Jacobi-Anger expansion of $e^{iz \cos \phi}$ using Bessel functions J_n ,

$$e^{iz \cos \phi} = \sum_{n=-\infty}^{\infty} i^n J_n(z) e^{in\phi}, \quad (3.2.18)$$

it is possible to conduct the angular integration in Eq. (3.2.17) to obtain the expression,

$$\tilde{W}(k, \theta) = 2\pi \sum_{n=-\infty}^{\infty} (-i)^n e^{in\theta} \int_0^\infty w_n(r) J_n(kr) r dr. \quad (3.2.19)$$

Notice that $\int_0^\infty w_n(r) J_n(kr) r dr$ is the n^{th} order Hankel transform of $w_n(r)$. In the same fashion, since $p(x, \theta + 2\pi) = p(r, \theta)$ we decompose the marginal distribution as

$$p_\theta(x) = \sum_{n=-\infty}^{\infty} c_n(x) e^{in\theta}, \quad (3.2.20)$$

with the sets of radial functions $c_n(x)$ defined by

$$c_n(x) = \frac{1}{2\pi} \int_{-\pi}^{+\pi} p(x, \theta) e^{-in\theta} d\theta. \quad (3.2.21)$$

Using the projection-slice theorem of Eq.(3.2.6) and the orthogonality of $e^{in\theta}$ on $[-\pi, +\pi]$ we are able to write for every angular harmonic order n ,

$$\frac{i^n}{2\pi} \int_{-\infty}^{+\infty} c_n(x) e^{-ikx} dx = \int_0^\infty w_n(r) J_n(kr) r dr. \quad (3.2.22)$$

We have obtained a relation between, on one side the Fourier transform of the angular harmonics of $p(x, \theta)$, and on the other side, the Hankel transform of the angular harmonics of $W(r, \phi)$. If we inverse the Hankel transform with the orthogonality relation, or closure relation of Bessel functions,

$$\int_0^\infty k dk J_n(kr) J_n(kr') = \frac{1}{r} \delta(r - r'), \quad (3.2.23)$$

we finally obtain

$$w_n(r) = \frac{i^n}{2\pi} \int_0^\infty J_n(kr) k dk \int_{-\infty}^{+\infty} c_n(x) e^{-ikx} dx. \quad (3.2.24)$$

At that point it would be natural to convey some radial decomposition of $w_n(r)$ and $c_n(x)$. However, there is no simple way to achieve this. Looking at Eq.(3.2.24), we notice that the Fourier transform of $k J_n(k)$, or at least $J_n(k)$, should be involved in the process. The latter is written in terms of the Chebyshev's polynomials of the first kind T_n as

$$\int_{-\infty}^{+\infty} J_n(k) e^{-ikx} dk = \frac{2(-i)^n}{\sqrt{1-x^2}} T_n(x) \mathbb{1}_{[-1,+1]}(x). \quad (3.2.25)$$

Equation (3.2.25) hints at the use of polynomial series to achieve this radial decomposition. It is safe to assume for applications that the Wigner function will only take nonzero values from the origin up to a certain limit $L \geq r$. Since we are carrying the decomposition in polar coordinates what we are looking after is a polynomial family which is orthogonal on a disk of radius L . There are of course infinitely many such families but one which proves to be particularly adequate to the task is the set of Zernike polynomials $Z_s^n(r, \varphi) = R_s^n(r) e^{in\varphi}$ originally introduced for the study of optical aberrations in lenses and other circular optical systems [52]. The polynomials are defined

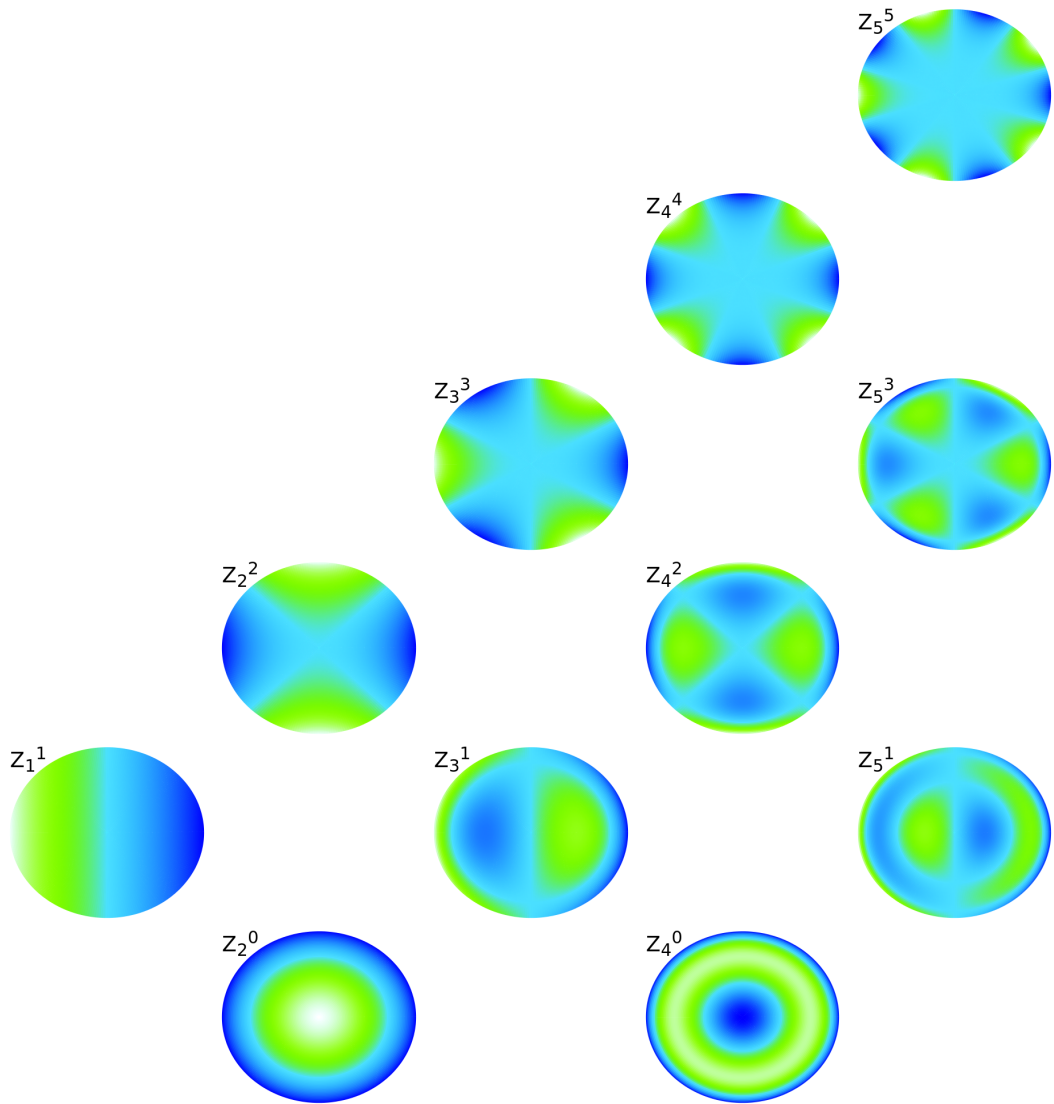


Figure 3.4: Real Zernike polynomials $Z_s^n(r, \theta) = R_s^n(r) \cos(n\theta)$ in the unit circle for $s \in [1 : 5]$ and $n \in [0, s]$.

for $s \geq |n| \geq 0$ and $s - |n|$ even. While the angular part gives straightforward orthogonality and fits with our previous approach using Fourier series, the radial components $R_s^{\pm n}$ defined for $t = |n| \geq 0$ by

$$R_s^{\pm n}(r) = \sum_{k=0}^{(s-t)/2} (-1)^k \frac{(s-k)!}{k! (\frac{s+t}{2} - k)! (\frac{s-t}{2} - k)!} r^{s-2k}, \quad (3.2.26)$$

are orthogonal on $[0, 1]$ with respect to the weight function r for all positive and negative orders n ,

$$\int_0^1 R_s^n(r) R_{s'}^n(r) r dr = \frac{1}{2(s+1)} \delta_s^{s'}. \quad (3.2.27)$$

Furthermore it turns out that the Radon transform of Zernike polynomials happens to have the simple expression,

$$\mathcal{R} \left(R_s^n(r) e^{in\phi} \right) = \frac{2}{s+1} \sqrt{1-x^2} U_s(x) e^{in\theta}, \quad (3.2.28)$$

where $U_s(x)$ are the Chebysheff's polynomials of the second kind [112, 16] (see also the last paragraph of this section for a proof of this relation). The critical aspect for tomography lies in the fact that $U_s(x)$ is again an orthogonal polynomial family on $[-1, 1]$ with respect to the weight function $\sqrt{1 - x^2}$. In other words by finding a family of orthogonal polynomials whose Radon transform element by element is yet another family of orthogonal polynomials, we have in some sense diagonalized the Radon transform. The inverse Radon transform can therefore be calculated without approximation and any technical difficulties associated with kernel functions or regularization immediately vanish. With the use of Eq.(3.2.27) we are eventually able to expand

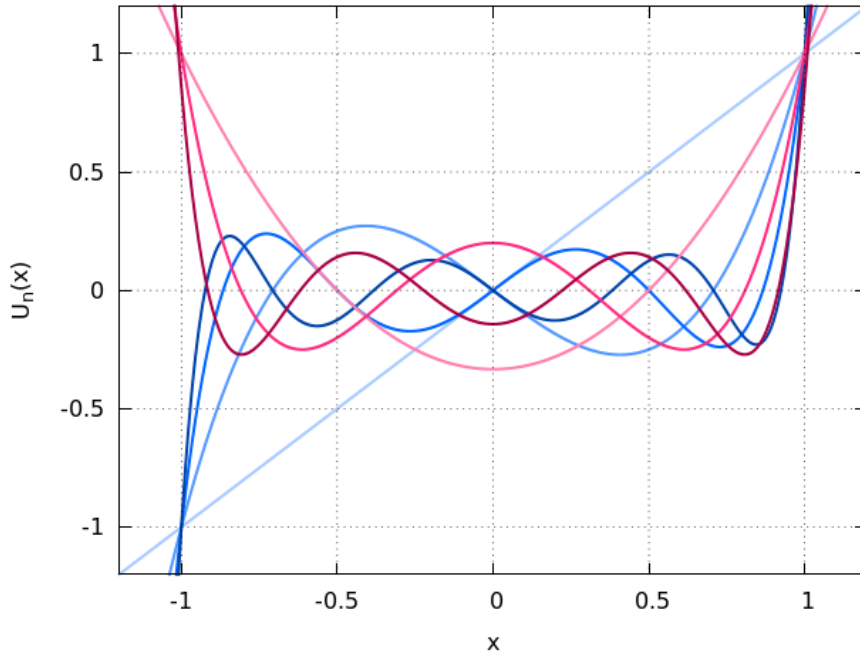


Figure 3.5: Chebysheff's polynomials of the second kind for $n \in [1, 7]$. Blue curves, $n = 1, 3, 5$ and 7 from lighter to darker tones. Red curves, $n = 2, 4$, and 6 from lighter to darker tones.

the angular harmonic functions $w_n(r)$ on the n^{th} order radial polynomials $R_s^n(r)$,

$$w_n(r) = \sum_{s=0}^{\infty} w_n^s R_s^n(r). \quad (3.2.29)$$

Given that $R_s^n(r)$ is non zero only when $s \geq |n| \geq 0$ and $s - |n|$ is even, we introduce the change of variable $s \rightarrow |n| + 2m$, re-index the sequence w_n^s and rewrite Eq.(3.2.29)

$$w_n(r) = \sum_{m=0}^{\infty} w_n^m R_{|n|+2m}^{|n|}(r). \quad (3.2.30)$$

Putting Eqs. (3.2.30) and (3.2.12) together we obtain the complete expansion of $W(r, \phi)$ inside the unit disk $D(0, 1)$,

$$W(r, \phi) = \sum_{n=-\infty}^{\infty} \sum_{m=0}^{\infty} w_n^m R_{|n|+2m}^{|n|}(r) e^{in\phi}. \quad (3.2.31)$$

Notice from Eq.(3.2.26) that $R_s^{+n}(r) = R_s^{-n}(r)$ which justifies the use of $R_{|n|+2m}^{|n|}$ although w_n^m are in general complex constants. Applying the relation (3.2.28) on Eq.(3.2.31), $p(x, \theta)$ is also

written in terms of the coefficients w_n^m as

$$p(x, \theta) = \sum_{n=-\infty}^{\infty} \sum_{m=0}^{\infty} \frac{2w_n^m}{|n| + 2m + 1} \sqrt{1 - x^2} U_{|n|+2m}(x) e^{in\theta}. \quad (3.2.32)$$

To justify the use of Zernike polynomials and prove Eq.(3.2.28), the relation[52]

$$\int_0^1 R_m^n(r) J_n(rk) r dr = (-1)^{(m-n)/2} \frac{J_{m+1}(k)}{k}, \quad (3.2.33)$$

between Zernike polynomials and Bessel functions is essential. If we recall Eq.(3.2.22), replace $w_n(r)$ by its expansion on $R_s^n(r)$ in Eq.(3.2.29) and cut the integration from $+\infty$ to unity, we obtain

$$\sum_{m=0}^{\infty} w_n^m (-1)^m \frac{J_{|n|+2m+1}(k)}{k} = \frac{i^{|n|}}{2\pi} \int_{-\infty}^{+\infty} c_n(x) e^{-ikx} dx. \quad (3.2.34)$$

To finally obtain the complete inversion of \mathcal{R} and the expansion of $c_n(x)$ as in Eq.(3.2.32), we only need to inverse the Fourier transform in Eq.(3.2.34) from the rhs to the lhs and use the Fourier transform of $J_s(k)/k$,

$$\int_{-\infty}^{+\infty} \frac{J_{s+1}(k)}{k} e^{ikx} dk = \frac{2i^s}{s+1} U_s(x) \sqrt{1-x^2} \mathbb{1}_{[-1,+1]}(x), \quad (3.2.35)$$

to obtain

$$c_n(x) = \sum_{m=0}^{\infty} \frac{w_n^m}{|n| + 2m + 1} U_{|n|+2m}(x) \sqrt{1-x^2} \mathbb{1}_{[-1,+1]}(x). \quad (3.2.36)$$

Notice that Eqs.(3.2.33) and (3.2.35) close the link between $U_s(x)$ and $R_m^n(r)$, the first two families of orthogonal functions used in the analysis, and the Bessel functions $J_n(k)$ orthogonal with respect to the weight function $1/k$,

$$\int_0^\infty J_s(k) J_t(k) \frac{dk}{k} = \frac{1}{2s} \delta_s^t. \quad (3.2.37)$$

In summary by identifying three families of orthogonal functions related together by the Radon transform \mathcal{R} and the Fourier transform \mathcal{F} , we have been able to find an expansion of the Wigner function $W(q, p)$ that allows to greatly simplify the technical difficulties of tomography with inverse Radon transform.

Implementation

The algorithm works in four steps: (1) choosing the size L of the reconstruction disk, (2) evaluating the coefficients w_n^m , (3) choosing the cutoffs N and M of the angular and radial series, and (4) calculating $W(r, \phi)$. Step 1 is necessary for the orthogonal relations given in Sec. II on $[0, 1]$ and $[-1, +1]$ to hold. In practice we have to normalize the marginal distribution $p(x, \theta) \rightarrow p(x/L, \theta)/L$ and the Wigner function $W(r, \phi) \rightarrow W(r/L, \phi)/L$. Step 2 is easily conducted by inverting the relation (3.2.32) with the orthogonal Chebyshev's polynomials $U_{|n|+2m}(x)$,

$$\begin{aligned} w_n^m &= \frac{|n| + 2m + 1}{2\pi^2} \int_{-\pi}^{+\pi} d\theta e^{-in\theta} \\ &\times \int_{-1}^{+1} dx \frac{p(x/L, \theta)}{L} U_{|n|+2m}(x). \end{aligned} \quad (3.2.38)$$

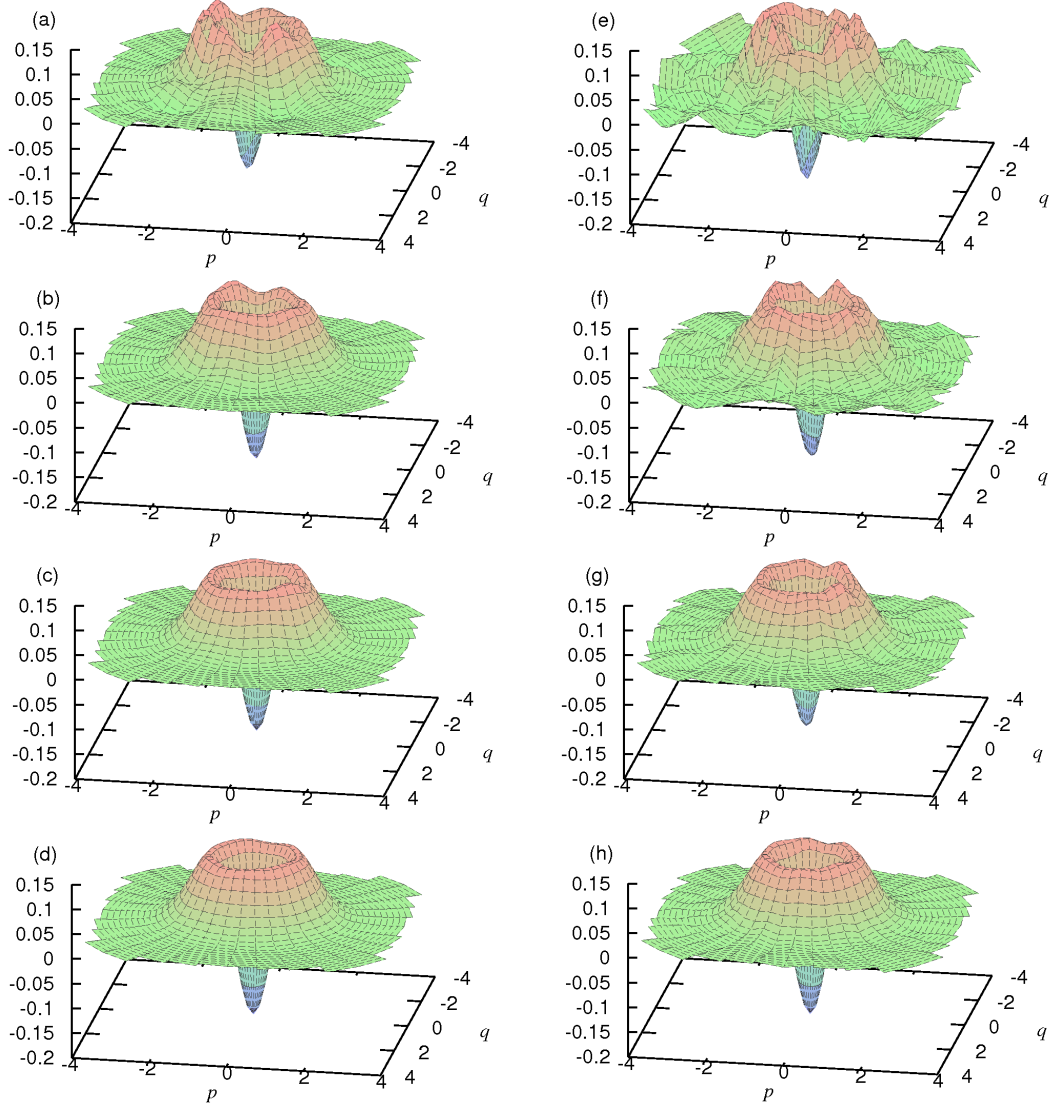


Figure 3.6: Comparison between polynomial series tomography (left panels: $N = 8, M = 30$) and filtered back-projection tomography (right panels: $k_c = 8.0$) for the state $\rho = 0.8|1\rangle\langle 1| + 0.2|0\rangle\langle 0|$. (a) $J = 5 \times 10^3$; (b) $J = 20 \times 10^3$; (c) $J = 80 \times 10^3$; (d) $J = 320 \times 10^3$; (e) $J = 5 \times 10^3$; (f) $J = 20 \times 10^3$; (g) $J = 80 \times 10^3$; (h) $J = 320 \times 10^3$. All data sets have been synthetically generated with rejection sampling.

The recurrence relation,

$$U_{s+1}(x) = 2xU_s(x) - U_{s-1}(x), \quad (3.2.39)$$

allows one to efficiently calculate $U_s(x)$ for any s and any x given $U_0(x) = 1$ and $U_1(x) = 2x$. After obtaining the coefficients w_n^m and choosing cutoff orders N and M , the Wigner function $W(r, \phi)$ is then approximated by the partial sums,

$$W'(r, \phi) = \sum_{n=-N}^N \sum_{m=0}^M w_n^m R_{|n|+2m}^{|n|} \left(\frac{r}{L}\right) e^{in\phi}/L, \quad (3.2.40)$$

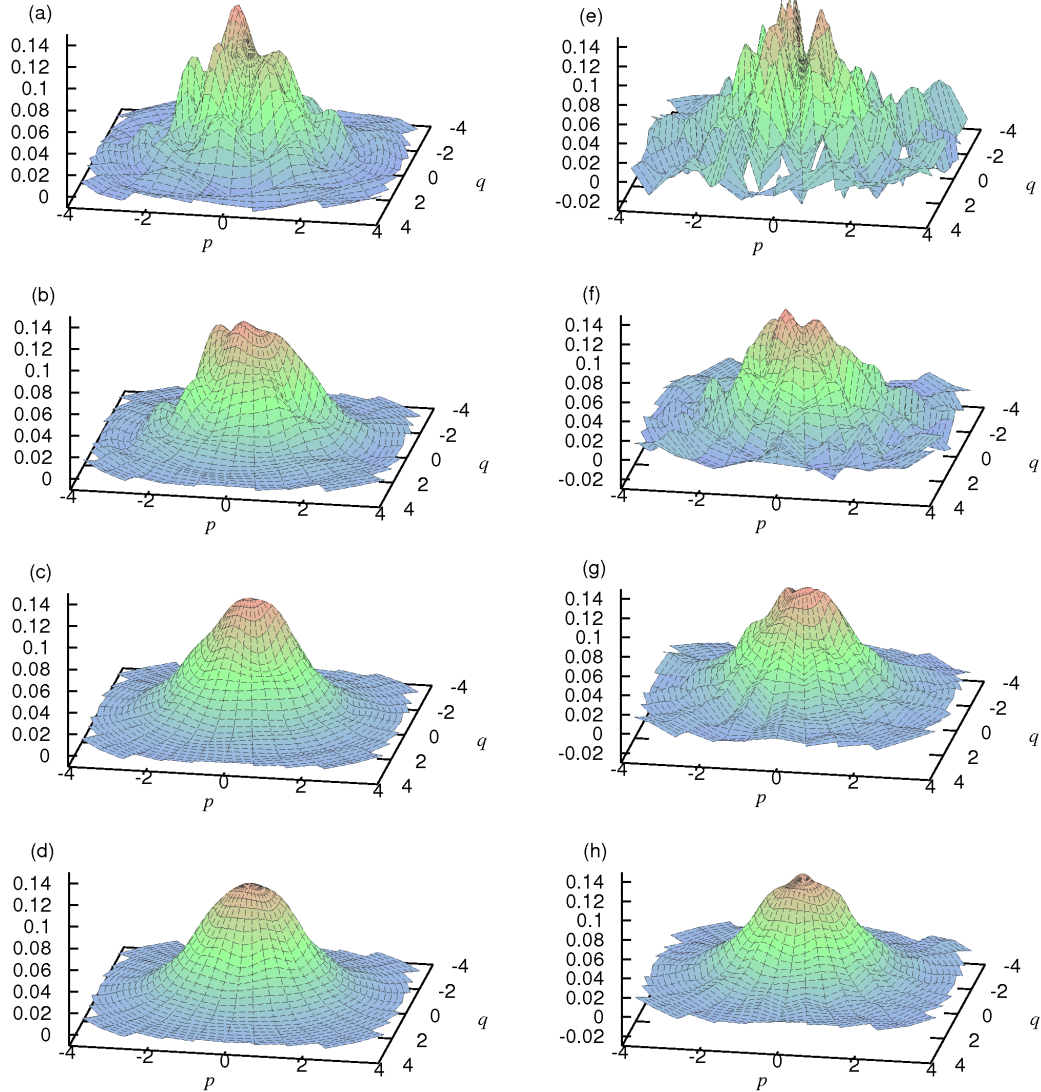


Figure 3.7: Comparison between polynomial series tomography (left panels: $N = 8, M = 30$) and filtered back-projection tomography (right panels: $k_c = 8.0$) for a thermal state of mean photon number $\langle \hat{n} \rangle = 1$. (a) $J = 5 \times 10^3$; (b) $J = 20 \times 10^3$; (c) $J = 80 \times 10^3$; (d) $J = 320 \times 10^3$; (e) $J = 5 \times 10^3$; (f) $J = 20 \times 10^3$; (g) $J = 80 \times 10^3$; (h) $J = 320 \times 10^3$. All data sets have been synthetically generated with rejection sampling.

Using the symmetry relation $w_{-n}^m = (w_n^m)^*$, we keep the real part of Eq.(3.2.40) and simplify the sum on n to

$$\begin{aligned} W'(r, \phi) &= \sum_{m=0}^M \sum_{n=0}^N R_{n+2m}^n \left(\frac{r}{L} \right) / L \\ &\quad \times (a_n^m \cos(n\phi) + b_n^m \sin(n\phi)). \end{aligned} \quad (3.2.41)$$

where we have defined $w_n^m = (a_n^m + ib_n^m)/2$ for $n \geq 1$ and $w_0^m = a_0^m$. Figures 3.6 and 3.7 show examples of reconstructed Wigner functions for a mixture of $|0\rangle$ and $|1\rangle$, and a thermal state respectively. In comparison to filtered back-projection tomography, polynomial series tomography

converges faster with fewer numbers of experimental points J . The reconstructed Wigner functions also show less visible artifacts and are overall smoother. To evaluate efficiently $R_n^m(r)$ we notice that $R_n^n(r) = r^{|n|}$ and then use the recurrence relation [29],

$$\begin{aligned} R_{n+2(m+1)}^n(r) &= \frac{n+2(m+1)}{(m+1)(n+m+1)} \times \left\{ \right. \\ &\left((n+2m+1)r^2 - \frac{(n+m)^2}{n+2m} - \frac{(m+1)^2}{n+2(m+1)} \right) R_{n+2m}^n(r) \right. \\ &\left. - m \frac{n+m}{n+2m} R_{n+2(m-1)}^n(r) \right\}. \end{aligned} \quad (3.2.42)$$

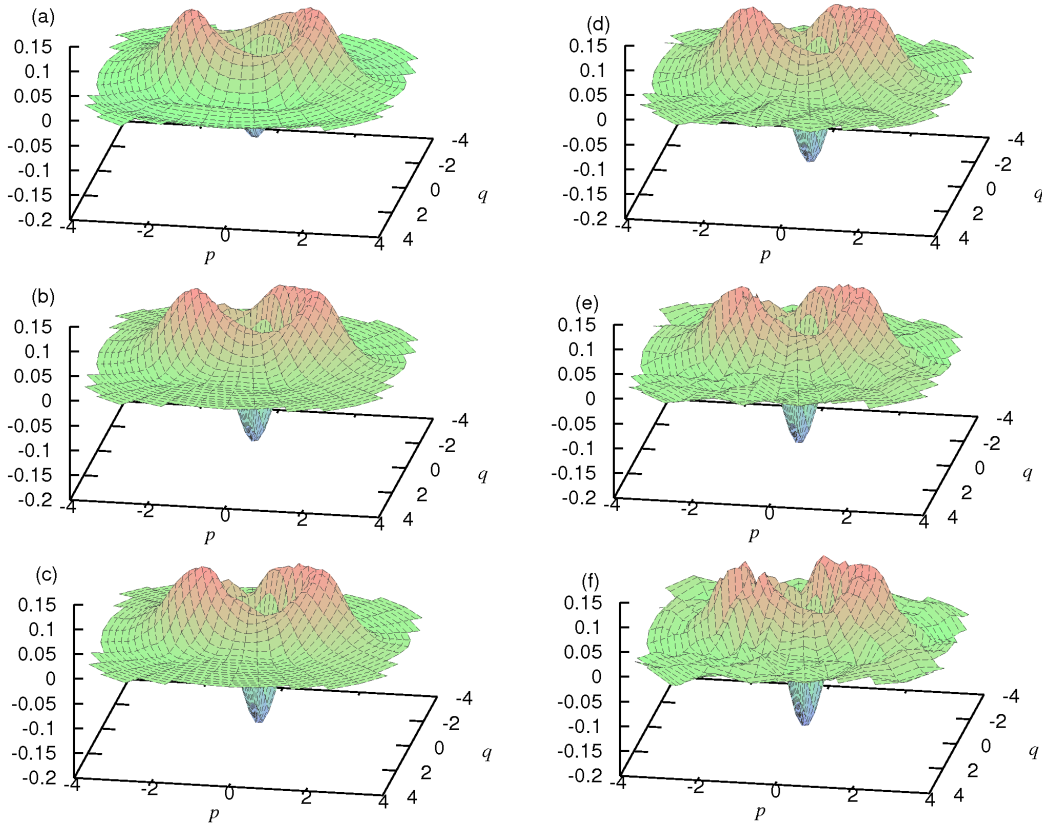


Figure 3.8: Effect of increased radial resolution on the stability of tomography of an experimentally measured photon subtracted squeezed vacuum (same data as in Ref. [167]). For all panels $J = 1 \times 10^5$. (a) Polynomial series tomography, $N = 8, M = 20$; (b) $M = 30$; (c) $M = 40$; (d) filtered back-projection tomography, $k_c = 7$; (e) $k_c = 9$; (f) $k_c = 11$.

Parameters influence on precision

In contrast to setting the value of k_c , the values of N and M have a real physical meaning. This is a major advantage of this method compared to the usual filtered back-projection algorithm. M will decide what will be the highest polynomial order of the radial features of W . Therefore it is equivalent to choosing the maximum photon number of the density matrix diagonal elements. N will set the resolution of the angular features of W , which decides how many off-diagonal

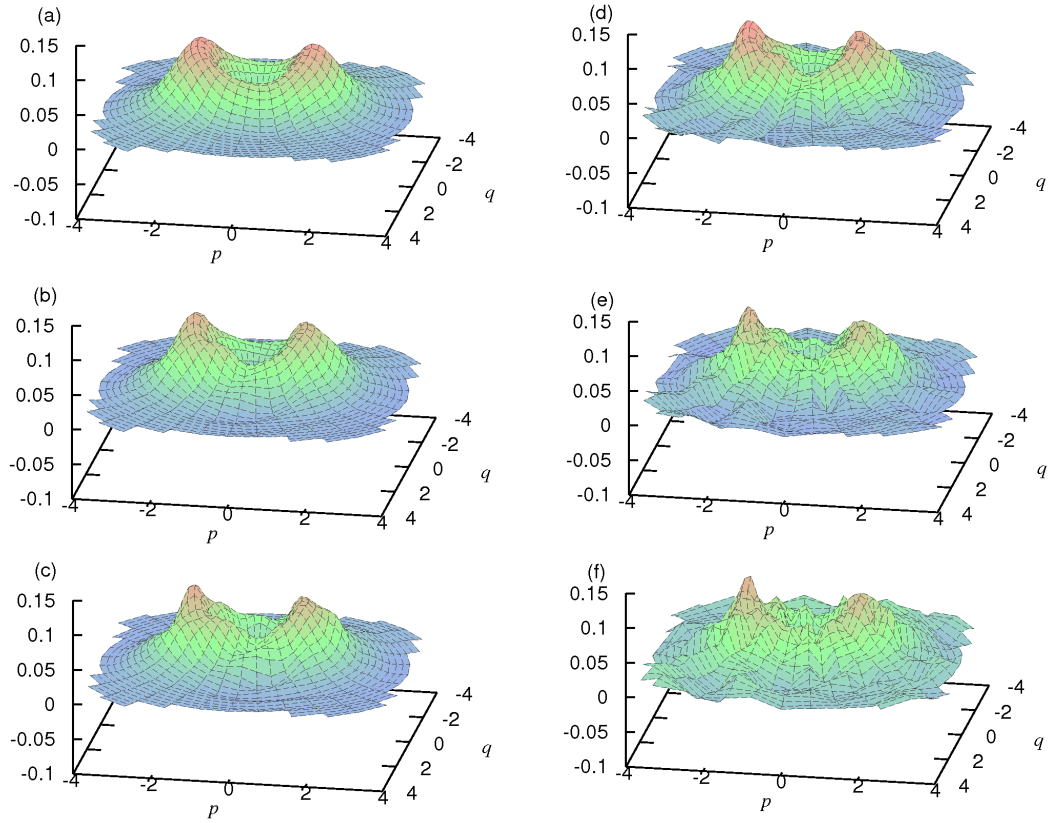


Figure 3.9: Effect of increased radial resolution on the stability of tomography of an experimentally measured photon subtracted squeezed vacuum (same data as in Ref. [167]). For all panels $J = 1 \times 10^5$. (a) Polynomial series tomography, $N = 8$, $M = 20$; (b) $M = 30$; (c) $M = 40$; (d) filtered back-projection tomography, $k_c = 7$; (e) $k_c = 9$; (f) $k_c = 11$.

components of the density matrix will be reconstructed. Furthermore it is easy to change N and M after computing the coefficients w_n^m . Figure 3.9 shows the effect of increasing M on the precision of polynomial series tomography. In comparison to filtered back-projection tomography when increasing the kernel sensitivity k_c , increasing the radial resolution M does not produce artifacts in the Wigner function. Figure 3.10 further shows the effect of increasing N and M on the precision of the tomography reconstruction of experimental data. While the angular components show quick convergence, the radial components require higher M values to be faithfully reconstructed. Figure 3.11 illustrates the advantage of polynomial series tomography in radial resolution for quantum states with a higher number of photons. Both M and k_c were set at values high enough to recover the original Schroedinger's cat state negativity at the origin of phase space. While the back-filtered projection shows numerical instability when k_c is set high, the Wigner function reconstructed by polynomial series tomography is smoother at the equivalent resolution.

Finally the value of R_{n+2m}^n in $r = 0$ will be non-zero only for $n = 0$, therefore we have the useful formula to evaluate the Wigner function at the origin of phase space,

$$W'(0, 0) = \sum_{m=0}^M (-1)^m a_0^m / L, \quad (3.2.43)$$

which is similar to the formulation of $W(0, 0)$ using the diagonal elements of the density matrix.

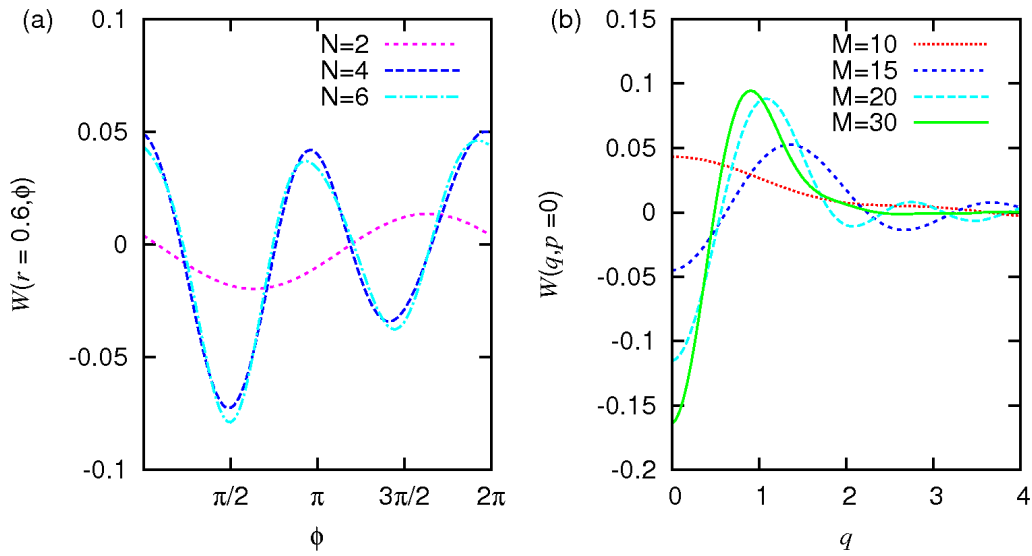


Figure 3.10: Effect of N and M on the convergence of polynomial series tomography. Same experimental data as in Fig. 3.9. (a) Circular cut at constant r and effect of N for $M = 32$, $J = 2 \times 10^5$. (b) Radial cut at constant ϕ and effect of M for $N = 10$, $J = 2 \times 10^5$.

3.3 Variational principles for tomography

3.3.1 Variational reconstruction principle

Variational principles provide a powerful approach to inverse problems. To the contrary of linear methods which only aims to mathematically inverse the statistical model used to predict the experimental results, reconstruction algorithms based on variational principle define the solution S_0 as the optimal value with respect to some figure of merit or metric. If the figure of merit is the functional $\mathcal{A}(S)$, the solution S_0 is expressed as

$$\mathcal{A}(S_0) = \max_{\{S\}} (\mathcal{A}(S)). \quad (3.3.1)$$

which usually takes the more practical form

$$0 = \left(\frac{\delta}{\delta S} \mathcal{A}(S) \right)_{S=S_0}. \quad (3.3.2)$$

It turns out that most linear inversion algorithms are actually special cases of variational estimator relatively to a distance in a metric space. If we approximate a function $f(x)$ onto a orthonormal basis of functions $\{\phi_n(x)\}_n$ in a metric space based on the integral scalar product

$$(f, g) = \int f(x)g(x)dx, \quad (3.3.3)$$

$f(x)$ is expressed as the linear combination $\check{f}(x)$

$$\check{f}(x) = \sum_n f_n \phi_n(x), \quad \text{with} \quad f_n = (f, \phi_n). \quad (3.3.4)$$

In a linear inversion algorithm, $f(x)$ would be reconstructed via the estimation of the coefficients f_n with Eq.(3.3.4). Therefore the distance between $f(x)$ and its estimation $\check{f}(x)$ would be

$$|f - \check{f}|^2 = (f, \check{f}) = \sum_n f_n \int f(x)\phi_n(x)dx, \quad (3.3.5)$$

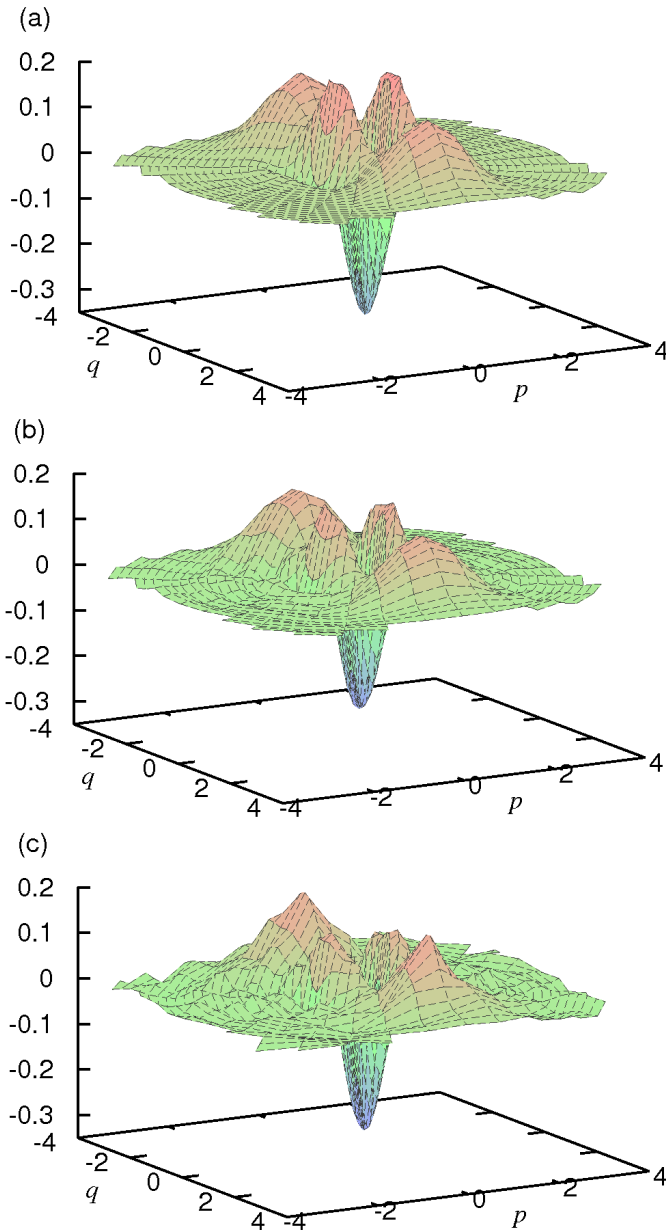


Figure 3.11: Effect of increased radial resolution on the stability of tomography of a Schroedinger's cat states with $\langle \hat{n} \rangle = 3$. For all panels $J = 4 \times 10^4$. (a) Original Wigner function; (b) polynomial series tomography, $N = 8$, $M = 46$; (c) filtered back-projection tomography, $k_c = 11$.

and is found to be simply expressed as the sum of the square of the coefficients f_n using the Pythagore's theorem

$$|f - \tilde{f}|^2 = \sum_n |f_n|^2. \quad (3.3.6)$$

This distance is actually minimal when the coefficients f_n are defined according to Eq.(3.3.4). Equivalently, linear inversion algorithms seek to minimize the linear least square distance between a target state and the estimated state with respect to the scalar product of the reconstruction space.

Maximum likelihood estimation

Maximum likelihood estimation defines the optimal state S_0 as the one which for a given measured data set $\{\vec{x}_i\}_i$ maximises the probability to observe this particular data set. In other words if the probability to observe $\{\vec{x}_i\}_i$ is written,

$$P(\{\vec{x}_i\}_{i \leq J}|S), \quad (3.3.7)$$

then the set of parameters S_0 which maximises P verifies

$$\left(\frac{\delta}{\delta S} P(\{\vec{x}_i\}_{i \leq J}|S) \right)_{S=S_0} = 0. \quad (3.3.8)$$

$P(\{\vec{x}_i\}_{I}|S)$ is also called the likelihood functional $\mathcal{L}(S, \{\vec{x}_i\}_{I})$. Under the identically and independently distributed (i.i.d) data hypothesis, it is usually easier to state the maximum likelihood principle with the log-likelihood functional $\log L(S)$:

$$0 = \frac{\delta}{\delta S} \log \mathcal{L}(S, \{\vec{x}_i\}_I) = \sum_i \left(\frac{\delta}{\delta S} p(\vec{x}_i|S) \right) / p(\vec{x}_i|S). \quad (3.3.9)$$

An underlying statistical model for the expression of $p(\vec{x}|S)$ is chosen and applied to the above differential equation. In some cases, it is possible to solve Eq.(3.3.9) and obtain a direct estimator $\check{S}(\{\vec{x}_i\}_i)$ of the optimal set of parameters S_0 . In most cases this is not possible and typically an iterative algorithm is constructed from a fixed point equation or eigen value relation derived from Eq.(3.3.9). Another popular iterative technique easily applicable to Eq.(3.3.9) is the Newton's method of roots approximation[125]. In practice maximum likelihood estimation works best with large set of experimental data and has desirable asymptotic properties. A well known case of maximum likelihood estimator which happens to be solvable is the linear least square method.

The maximum entropy principle

The maximum entropy principle is an estimation technique which seeks to maximise the unknown information in the experimental measurement. It could be argued it is physically the most relevant technique because it selects the state which minimises the knowledge obtained in the experimental measurement of $\{\vec{x}_i\}_{i \leq J}$. For this reason it is for instance the method of choice for analysis in thermodynamics at equilibrium. Let's imagine a system with N discrete possible states having each an experimental observation probability $p_n(S)$ with $0 < n \leq N$ parametrized by S . Then the entropy $\mathcal{H}(S)$ of the system is

$$\mathcal{H}(S) = - \sum_n p_n(S) \log p_n(S). \quad (3.3.10)$$

Let's assume we have an experimental value $\langle F \rangle$ of the mean of an observable F which takes the values F_n for every states n with probability p_n , so that

$$\langle F \rangle = \sum_n p_n(S) F_n. \quad (3.3.11)$$

With the constraint that the probabilities are normalized, the maximum entropy principle can be stated with Lagrange multipliers as the system of N differential equations

$$\frac{\partial}{\partial p_n} \left(\mathcal{H}(S) + \lambda_F \left(F - \sum_m p_m(S) F_m \right) + \lambda_0 \left(1 - \sum_m p_m(S) \right) \right) = 0. \quad (3.3.12)$$

The solutions $\{p_n\}$ to the above system are the one which satisfies the maximum entropy system while at the same time satisfying the constraint of the experimentally measured value of $\langle F \rangle$. They can be written in their canonical form as

$$p_n(\lambda_F) = \exp[-\lambda_F F_n] / \mathcal{Z}(\lambda_F), \quad (3.3.13)$$

using the partition function $\mathcal{Z}(\lambda_F)$ defined as

$$\mathcal{Z}(\lambda_F) = \sum_n p_n = \sum_n \exp[-\lambda_F F_n]. \quad (3.3.14)$$

There now remains only one free parameter which fully determines the underlying state of the system: λ_F . In other words $\lambda_F = S$. The value which satisfies the maximum entropy principle for a given experimental measurement of F is simply the one which solves the equation

$$\langle F \rangle = \sum_n F_n p_n(\lambda_F), \quad (3.3.15)$$

where $\langle F \rangle$ is the experimental measured value. For optical homodyne tomography, the experiment measurement is not a single value $\langle F \rangle$ but rather the set of J data points $\{x_i, \theta_i\}_{i \leq J}$. In this case, we have J Lagrange multipliers to determine with experimentally measured data. In effect, the maximum entropy principle reparametrizes the system in a lower dimensional space which matches in dimension the number of different measurements conducted. This lower dimensionality is achieved in a way which maximises the entropy. To the contrary of the maximum likelihood method, the maximum entropy estimation is therefore especially relevant and efficient when there is less information available from $\{\vec{x}_i\}_{i \leq J}$ than what is necessary to estimate without ambiguity and without any bias all the free parameters of the model. In practice it is generally not efficient to find the exact value of the Lagrange multipliers, because statistical noise in the experimental measurement may force the Lagrange multipliers to improbable values. Rather, it is usually more efficient to smooth out this statistical noise by relaxing the constraints on the Lagrange multipliers, for example with a weighted least square fitting procedure[149].

3.3.2 Density matrix maximum likelihood reconstruction

Expression of the likelihood

Application of the maximum likelihood principle to homodyne tomography is straightforward[45]. We use the Cholesky decomposition and write $\hat{\rho} = \sigma^\dagger \sigma$ where σ is a lower triangular matrix. This decomposition is allowed because $\hat{\rho}$ is positive definite and Hermitian. Therefore using this decomposition in the derivation will automatically satisfy the physical constraint that $\hat{\rho}$ be a Hermitian positive definite operator. We then express the likelihood functional $\mathcal{L}(\sigma)$ using results of Eq.(3.1.1)

$$\mathcal{L}(\sigma) = \prod_{i=1}^J \text{tr} \left[\sigma^\dagger \sigma |x_i, \theta_i\rangle \langle x_i, \theta_i| \right]. \quad (3.3.16)$$

and apply the maximum likelihood principle $\partial \log \mathcal{L} / \partial \sigma = 0$ with the constraint that the reconstructed density matrix be normalized

$$\frac{\partial}{\partial \sigma} \left(\log \mathcal{L}(\sigma) - \lambda \left(1 - \text{tr} (\sigma^\dagger \sigma) \right) \right) = 0, \quad (3.3.17)$$

where the Lagrange multiplier λ is yet an unknown parameter. Using the trace matrix derivative formula $\partial \text{tr}(AX) / \partial X = A^T$, Eq.(3.3.17) becomes

$$\sum_{i=1}^J \frac{1}{p(x_i, \theta_i)} |x_i, \theta_i\rangle \langle x_i, \theta_i| \sigma^\dagger = \lambda \sigma^\dagger. \quad (3.3.18)$$

To determine λ we multiply Eq.(3.3.18) on the right by σ and take the trace of both sides to obtain

$$\lambda = \sum_i^J \frac{1}{p(x_i, \theta_i)} \text{tr} [|x_i, \theta_i\rangle \langle x_i, \theta_i| \sigma^\dagger] = J, \quad (3.3.19)$$

which sets the parameter λ . We are left with the eigenvector equation

$$\frac{1}{J} \sum_{i=1}^J \frac{1}{p(x_i, \theta_i)} |x_i, \theta_i\rangle \langle x_i, \theta_i| \hat{\rho} = \hat{\rho}, \quad (3.3.20)$$

whose solution $\hat{\rho}_0$ is the density matrix which satisfies the maximum likelihood principle.

Iterative reconstruction

The iteration procedure towards $\hat{\rho}_0$ is now straightforward. We define the operator $\hat{R}(\hat{\rho})$ as

$$\hat{R}(\hat{\rho}) = \frac{1}{J} \sum_{i=1}^J \frac{1}{\text{tr}(\hat{\rho}|x_i, \theta_i\rangle \langle x_i, \theta_i|)} |x_i, \theta_i\rangle \langle x_i, \theta_i|, \quad (3.3.21)$$

and rewrite Eq.(3.3.20) as $\hat{R}(\hat{\rho})\hat{\rho} = \hat{\rho}$. Similarly if we derive $\log \mathcal{L}$ against σ^\dagger we have the symmetric relation $\hat{\rho}\hat{R}(\hat{\rho}) = \hat{\rho}$ and can therefore write

$$\hat{R}(\hat{\rho})\hat{\rho}\hat{R}(\hat{\rho}) = \hat{\rho}. \quad (3.3.22)$$

As was demonstrated in [87], it is possible to use the eigenvector equation (3.3.22) to craft an iterative algorithm yielding an approximation of $\hat{\rho}_0$. Starting from an initial guess state $\hat{\rho}^{(0)}$, we compute the operator $\hat{R}^{(0)} = \hat{R}(\hat{\rho}^{(0)})$ and iteratively define the matrix sequence $\{(\hat{\rho}^{(k)}, \hat{R}^{(k)})\}_k$ with the recurrence equation

$$\hat{\rho}^{(k+1)} = \hat{R}^{(k)}\hat{\rho}^{(k)}\hat{R}^{(k)}, \quad (3.3.23)$$

$$\hat{R}^{(k)} = \hat{R}(\hat{\rho}^{(k)}). \quad (3.3.24)$$

Mathematically this series is not always guaranteed to converge to $\hat{\rho}_0$ in the general case. The convergence depends on the experimental data set $\{x_i, \theta_i\}$ and the initial guess state $\hat{\rho}^{(0)}$ [87].

Implementation

The implementation of the maximum likelihood iterative reconstruction of the density matrix is less complex than its derivation. In practice the sequence $\{(\hat{\rho}^{(k)}, \hat{R}^{(k)})\}_k$ is calculated with Eq.(3.3.23) at every step k . The most practical approach for that is to use the photon number basis (also see Sec.3.1.3). With Eq.(3.1.8), it is immediate to calculate $\hat{R}^{(k)}$ at every rank k with the expression

$$\left(\hat{R}^{(k)} \right)_{nm} = \sum_i^J \frac{1}{p^{(k)}(x_i, \theta_i)} e^{i(m-n)\theta_i} \frac{H_n(x_i) H_m(x_i)}{\sqrt{\pi 2^{n+m} n! m!}} e^{-x_i^2}, \quad (3.3.25)$$

with $p^{(k)}(x_i, \theta_i)$ expressed using Eq.(3.1.8) and $\hat{\rho}^{(k)}$. The algorithm starts with a guess state $\hat{\rho}^{(0)}$, for example $\hat{\mathbb{I}}/\text{tr}[\hat{\mathbb{I}}]$, and then calculates iteratively the sequence $\{(\hat{\rho}^{(k)}, \hat{R}^{(k)})\}_k$ until a preselected rank k_{final} is reached or until a minimal error threshold is reached. For example using a distance metric $d(\hat{\rho}, \hat{\rho}')$ for density matrices, the algorithm can stop at rank k_ϵ when the condition

$$d(\hat{\rho}^{(k_\epsilon)}, \hat{\rho}^{(k_\epsilon-1)}) \leq \epsilon, \quad (3.3.26)$$

is satisfied (also see Fig.3.12). Several numerical optimizations are possible for good execution speeds. The Hermite polynomials should be calculated with the recurrence relation

$$H_{n+1}(x) = 2xH_n(x) - 2nH_{n-1}(x). \quad (3.3.27)$$

It is possible to speed up substantially the calculation of transcendental functions involved in Eq.(3.3.25) by calculating once at the start of the iteration all the values $\cos \theta_i$ and $\sin \theta_i$ for the data set $\{x_i, \theta_i\}_i$ and then using the iterative relations

$$\cos((k+1)\theta) = \cos(k\theta)\cos(\theta) - \sin(k\theta)\sin(\theta), \quad (3.3.28)$$

$$\sin((k+1)\theta) = \cos(k\theta)\sin(\theta) + \sin(k\theta)\cos(\theta). \quad (3.3.29)$$

$$(3.3.30)$$

Profiling reveals that in practice the expensive part of every iteration cycle isw the computation of the operator $\hat{R}^{(k)}$ and not the matrix product itself. $\hat{R}^{(k)}$ can be decomposed as a sum of projectors onto every experimental point (x_i, θ_i) by writing

$$\hat{R}^{(k)} = \sum \hat{R}_i^{(k)} \text{ with } \hat{R}_i^{(k)} = \frac{1}{N p^{(k)}(x_i, \theta_i)} |x_i, \theta_i\rangle \langle x_i, \theta_i|, \quad (3.3.31)$$

which helps with numerical calculations of $\hat{R}^{(k)}$. The individual projectors $\hat{R}_i^{(k)}$ can be evaluated concurrently on independently running machine threads. Notice also that the factor $\exp[-x_i]/\sqrt{\pi}$ in Eq.(3.3.25) appears on both the numerator and denominator and therefore vanishes.

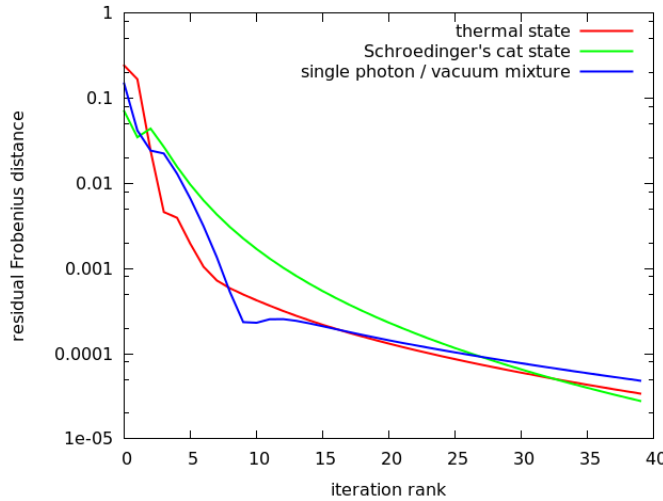


Figure 3.12: Convergence of the iterative maximum likelihood method with the number of iterative steps. On the vertical axis is plotted the Frobenius distance between two consecutive density matrix $\hat{\rho}^{(k)}$ and $\hat{\rho}^{(k-1)}$. The sampled states are a thermal state with average photon number $\langle \hat{n} \rangle = 1$, a mixture of single photon and vacuum $0.8|1\rangle\langle 1| + 0.2|0\rangle\langle 0|$ and an odd Schroedinger's cat states with $\alpha = 1$.

The convergence of the iterative procedure is in practice rather fast. Fig.3.13 shows how quickly the reconstructed state can stabilize around the convergence point. Unless the state to reconstruct is particularly complex, 15 to 20 iterations already yield precisely reconstructed quantum states. The size of the reconstruction space, that is the maximum photon number N_{\max} used when calculating $\hat{\rho}^{(k)}$ and $\hat{R}^{(k)}$, is surprisingly rather irrelevant, as long as it is sufficiently large.

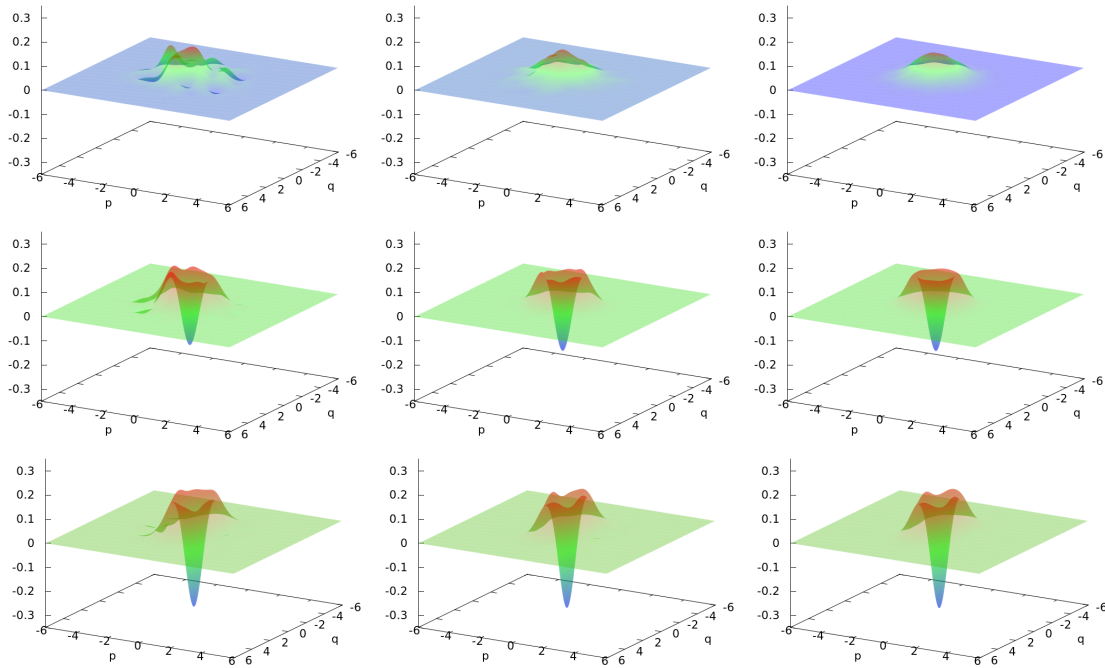


Figure 3.13: Convergence of the iterative maximum likelihood method with the number J of experimental data points as seen on the reconstructed Wigner functions. For every rows, from left to right, $J = 1000, 10000, 100000$. Top row, for a thermal state with average photon number $\langle \hat{n} \rangle = 1$. Middle row, for a mixture of single photon and vacuum $0.8|1\rangle\langle 1| + 0.2|0\rangle\langle 0|$. Bottom row, for an odd Schrödinger's cat states with $\alpha = 1$.

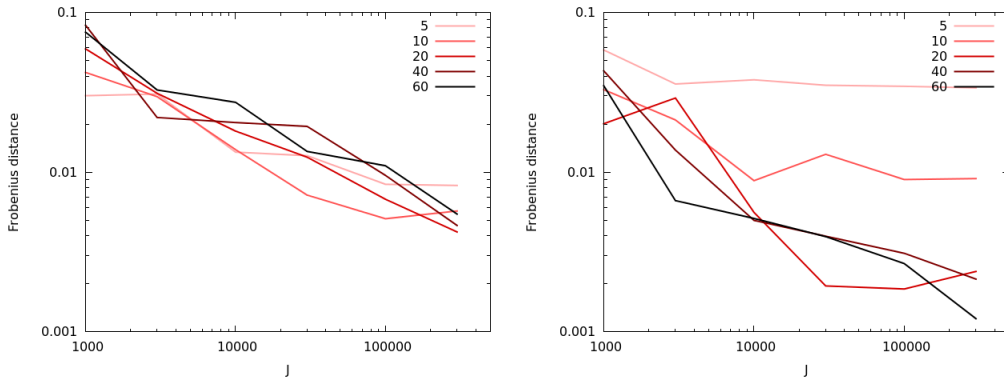


Figure 3.14: Convergence of the iterative maximum likelihood method with the number J of experimental data points, as seen on the Frobenius distance between the reconstructed density matrix and the target density matrix. Left, for a mixture of single photon and vacuum $0.8|1\rangle\langle 1| + 0.2|0\rangle\langle 0|$. Right, for an odd Schrödinger's cat states with $\alpha = 1$.

For example for "simple" non-Gaussian states such as small amplitude Schrödinger's cat state, it is not necessary to increase N_{\max} to levels much higher than twice the average photon numbers of the state. Gaussian states however do not quite follow this rules, since they have by definition "long tails" in the photon number basis. For non-zero coherent states and thermal states, the size of the reconstruction space may be significant to obtain relevant results. For example a low purity

thermal state quickly starts to populate higher photon number levels in non-negligible proportions. This hints that for Gaussian states the photon number basis may not be the ideal description. Of course as shows Figs.3.13 and 3.14 the number of experimental events J has an influence on the final reconstructed state. If the statistical properties of the data set are well defined, the higher J the more faithful a reconstructed state we can obtain.

3.3.3 Polynomial series maximum likelihood reconstruction

Applying the maximum likelihood reconstruction technique to the polynomial series decomposition of the Wigner function presented in Sec.3.2.2 is relatively easy. Thanks to Eq.(3.2.32), the expression of the log-likelihood functional $\mathcal{L}(\{w_n^m\})$ is straightforward

$$\log \mathcal{L}(\{w_n^m\}) = \sum_i^J \log \left(\vec{w} \cdot \vec{\phi}(x_i, \theta_i) \right), \quad (3.3.32)$$

where \vec{w} is a vector arrangement of the coefficients $\{w_n^m\}$ and $\vec{\phi}$ is defined so that the scalar product $\vec{w} \cdot \vec{\phi}(x_i, \theta_i)$ is equal to

$$\vec{w} \cdot \vec{\phi}(x_i, \theta_i) = \sum_{n=-\infty}^{\infty} \sum_{m=0}^{\infty} \frac{2w_n^m}{|n| + 2m + 1} \sqrt{1 - x_i^2} U_{|n|+2m}(x_i) e^{in\theta_i}. \quad (3.3.33)$$

There is no a-priori constraint or normalization on the set $\{w_n^m\}$ so the maximum likelihood principle simply reads

$$\partial_{\vec{w}} \log \mathcal{L}(\vec{w}) = \sum_i^J \frac{\vec{\phi}(x_i, \theta_i)}{\vec{\phi}(x_i, \theta_i) \cdot \vec{w}} = 0. \quad (3.3.34)$$

To solve this equation numerically we apply Newton's method. If a function f has a root \bar{x} so that $f(\bar{x}) = 0$, we can find a sequence $\{x_k\}_k$ whose limit is \bar{x} . We express $f(x_{k+1})$ from $f(x_k)$ with a first order linear approximation

$$f(x_{k+1}) = f(x_k + \Delta x_k) \approx f(x_k) + \Delta x_k f'(x_k), \quad (3.3.35)$$

where $x_{k+1} = x_k + \Delta x_k$ and $f'(x) = \partial f(x)/\partial x$. Asymptotically, we want the sequence $\{x_k\}_k$ to converge towards \bar{x} so we assume $f(x_{k+1}) \approx 0$ is negligible and then derive the iterative relation

$$x_{k+1} = x_k - f(x_k)/f'(x_k). \quad (3.3.36)$$

In the case of the polynomial series decomposition of the Wigner function, the sequence is a vector sequence $\{\vec{x}_k\}_k$, as well as $f \rightarrow \vec{f}$ is a vector function. The derivative $\partial f(x)/\partial x$ is replaced by a Jacobian matrix $J(x)$ defined by

$$(J(x))_{\alpha\beta} = \partial(\vec{f})_{\alpha}/\partial(\vec{x})_{\beta}, \quad (3.3.37)$$

so that Eq.(3.3.36) becomes

$$\vec{x}_{k+1} = \vec{x}_k - J(x_k)^{-1} \cdot \vec{f}(x_k). \quad (3.3.38)$$

The Jacobian matrix is actually the second order derivative of the log-likelihood functional with respect to \vec{w}

$$(J(\vec{w}))_{\alpha\beta} = \partial_{(\vec{w})_{\alpha}} \partial_{(\vec{w})_{\beta}} \log \mathcal{L} = - \sum_i^J \frac{\phi_{\alpha}(x_i, \theta_i) \phi_{\beta}(x_i, \theta_i)}{\left(\vec{\phi}(x_i, \theta_i) \cdot \vec{w} \right)^2}, \quad (3.3.39)$$

which can be easily calculated for every α and β from the log-likelihood functional $\mathcal{L}(\vec{w})$ of Eq.(3.3.32). From a starting state \vec{w}_0 , it is then straightforward to calculate the sequence $\{\vec{w}_k\}_k$ that approximate the solution \vec{w}_0 to the maximum likelihood principle of Eq.3.3.34 with the recurrence relation

$$\vec{w}_{k+1} = \vec{w}_k + (J(\vec{w}_k))^{-1} \cdot (\partial_{\vec{w}} \log \mathcal{L}(\vec{w}_k)). \quad (3.3.40)$$

The only difficulty to the numerical application of the above relation is the inversion of J . Since in our case J is a symmetric matrix, we can for example use the Cholesky decomposition and apply a pivot technique onto the resulting triangular matrix[125]. Implementation of this technique was not tested and do not report on its efficiency in this manuscript.

3.4 Faithfulness of reconstruction estimators

This section deals with the problem of error estimation in tomography reconstruction algorithms. If S is the underlying unknown parameter and \check{S} is an estimate of S , we would like to know the statistical properties of the error $\epsilon = S - \check{S}$. This problem belongs to the field of estimation theory, an important topic in applied mathematics and probability theory. We will only scratch the tip of the iceberg and try to qualitatively understand the statistical errors of the algorithms presented in Secs.3.2 and 3.3. We introduce simulation methods based on the Monte-Carlo techniques to probe the reconstruction errors of each algorithm. The objective is to obtain insights about how well inverse Radon transform and maximum likelihood reconstruction methods perform in practice and how do they compare to each other. In the first part of this section we look at linear inversion methods for which it is relatively easy to obtain a direct expression of the estimator of the variance σ of the reconstruction error. In the second part we look at the case of variational methods and the maximum likelihood principle. In the third part we introduce Monte-Carlo simulations to directly compare the filtered back projection and the polynomial series decomposition algorithms. Finally in the fourth part, we compare these two linear methods with the maximum likelihood reconstruction method by looking at distances between reconstructed states and the ideal target state using again Monte-Carlo simulations.

3.4.1 Error estimators for linear reconstruction method

We start with a quantitative comparison of the usual back-filtered tomography algorithm and our polynomial series decomposition algorithm presented before.

We give a consistent and quantitative method to estimate the reconstruction error and obtain confidence intervals when calculating the value of $W(q, p)$ with linear inversion methods. We call W' and W'' the reconstructed value of $W(q, p)$, respectively using our polynomial series decomposition algorithm with Eqs.(3.2.41), and using the usual back-filtered tomography algorithm with (3.2.7). We then call $\sigma_{W'}^2$ and $\sigma_{W''}^2$ the variance of the reconstruction errors assuming they are normally distributed for both cases. We also assume that there are only statistical errors and no systematic errors. Let's assume an optical homodyne measurement set consists of J experimental points $\{(x_j, \theta_j)\}_j$ independently and identically distributed according to the underlying marginal distribution $p(x, \theta)$. To begin with we give an estimator of $\sigma_{W''}^2(q, p)$ for the usual filtered back-projection method using formula (3.2.7). To calculate the value of W at point (q, p) , $p(x, \theta)$ will be replaced either by a binned histogram made from the data set $\{(x_j, \theta_j)\}_j$, or by a sum of delta functions approximating $p(x, \theta)$

$$p(x, \theta) = \frac{1}{J} \sum_j \delta(x - x_j) \times \delta(\theta - \theta_j). \quad (3.4.1)$$

In the latter case, the swap of $p(x, \theta)$ for expression (3.4.1) in Eq.(3.2.7) leads to

$$W''(q, p) = \frac{1}{2\pi J} \sum_{j=1}^J K(q \cos \theta_j + p \sin \theta_j - x_j). \quad (3.4.2)$$

Since $p(x, \theta)$ is a valid probability distribution $W''(q, p)$ is nothing else than $\langle K(q \cos \theta + p \sin \theta - x) \rangle$ the expectation value of the kernel function. Therefore Eq.(3.4.2) can be regarded as a Monte-Carlo integral where the expectation value of the kernel function is calculated by randomly sampling K according to the distribution $p(x, \theta)$. In other words, the optical homodyne tomography with filtered back-projection is in effect an analogical Monte-Carlo integration where the homodyne measurement plays the part of the random number generator. In that familiar case the statistical properties of the reconstruction error are well known. First of all we are assured of the unbiased convergence of the sum in Eq.(3.4.2). The central limit theorem also states that the error will indeed converge to a Gaussian distribution of zero mean and whose standard deviation $\sigma_{W''}(q, p)$ for J experimental points is

$$\sigma_{W''}(q, p) = \sigma_K / \sqrt{J - 1}, \quad (3.4.3)$$

which exhibits a $1/\sqrt{J}$ rate of convergence, and where $\sigma_K = \sqrt{\langle K^2 \rangle - \langle K \rangle^2}/2\pi$. By using the approximations,

$$\langle K \rangle \approx \frac{1}{J} \sum_{j=0}^J K(q \cos \theta_j + p \sin \theta_j - x_j), \quad (3.4.4)$$

$$\langle K^2 \rangle \approx \frac{1}{J} \sum_{j=0}^J K^2(q \cos \theta_j + p \sin \theta_j - x_j), \quad (3.4.5)$$

we can actually estimate σ_K in a straightforward way easy to include in the implementation of Eq.(3.4.2).

The same reconstruction technique applied to the calculation of the coefficients $\{w_n^m\}$ yields from Eq.(3.2.38) the reconstruction sum,

$$w_n^m = \frac{|n| + 2m + 1}{2\pi^2} \sum_{j=1}^J U_{|n|+2m}(x_j/L) e^{-in\theta_j}/L. \quad (3.4.6)$$

As previously errors are Gaussian distributed for every coefficient w_n^m with a $1/\sqrt{J}$ rate of convergence. If a quantity Y is calculated through the measure of the variables $\{y_i\}_{i \leq I}$ with the formula,

$$Y = f(y_1, \dots, y_I), \quad (3.4.7)$$

then the variance σ_Y^2 of Y can be approximated by

$$\sigma_Y^2 = \sum_{i=1}^I \left((\partial_{y_i} f)^2 \sigma_{y_i}^2 + 2 \sum_{j>i} (\partial_{y_i} f) (\partial_{y_j} f) \sigma_{y_i y_j}^2 \right), \quad (3.4.8)$$

where $\sigma_{xy}^2 = \langle xy \rangle - \langle x \rangle \langle y \rangle$. Using Eq.(3.2.41) we can apply this formula to estimate the variance $\sigma_{W'}$ anywhere in phase space, but because of its simple formulation thanks to Eq.(3.2.43), we will only study it at the origin $(0, 0)$ of phase space:

$$\sigma_{W'}^2(0, 0) = \frac{1}{(J-1)L^2} \sum_{m=0}^M \left(\sigma_{a_0^m}^2 + 2 \sum_{k>m}^M (-1)^{m+k} \sigma_{a_0^m a_0^k}^2 \right). \quad (3.4.9)$$

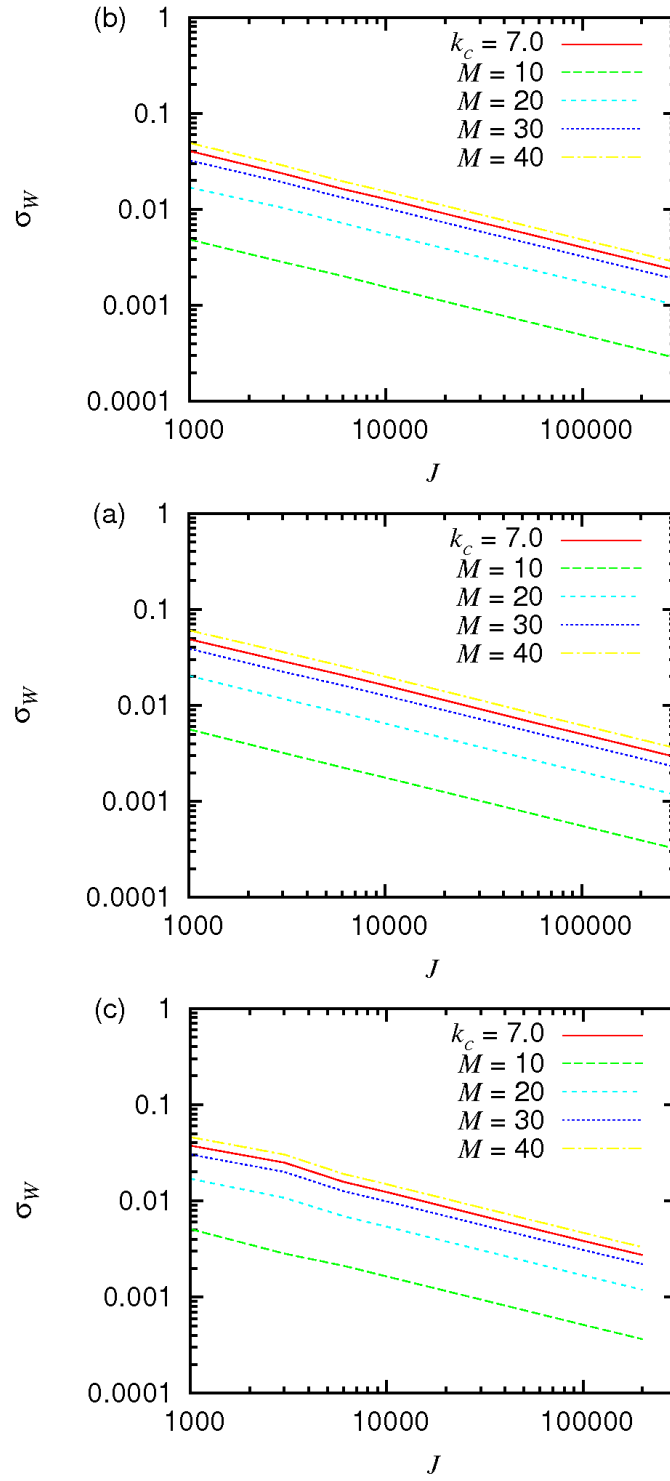


Figure 3.15: Estimation of $\sigma_W(0,0)$ with filtered back-projection tomography (plain line) and polynomial series tomography (dotted lines). (a) $\rho = 0.8|1\rangle\langle 1| + 0.2|0\rangle\langle 0|$; (b) thermal state with $\langle \hat{n} \rangle = 1$; (c) photon subtracted squeezed vacuum (same data as in Fig.3.9).

Notice that in this case the variance estimator formula of Eq.(3.4.8) is not an approximation anymore due to the linear combination nature of Eqs. (3.2.41) or (3.2.43). We can compute an estimate

of $\sigma_{a_0^m}$ when computing the coefficients w_n^m in the same way we did with Eqs. (3.4.4) and (3.4.5). Figure 3.15 shows estimation of the reconstruction errors for different states using Eq.(3.4.3) and (3.4.9). We have found that the value of k_c has very little influence on $\sigma_{W''}$ at the center of phase space. On the contrary M has a strong influence on $\sigma_{W'}(0, 0)$. However, as was shown in Figs.3.6, 3.7 and 3.9, far from the origin the polynomial series tomography algorithm shows less uncertainties. We also assumed the convergence error due to finite truncation N and M of the expansion

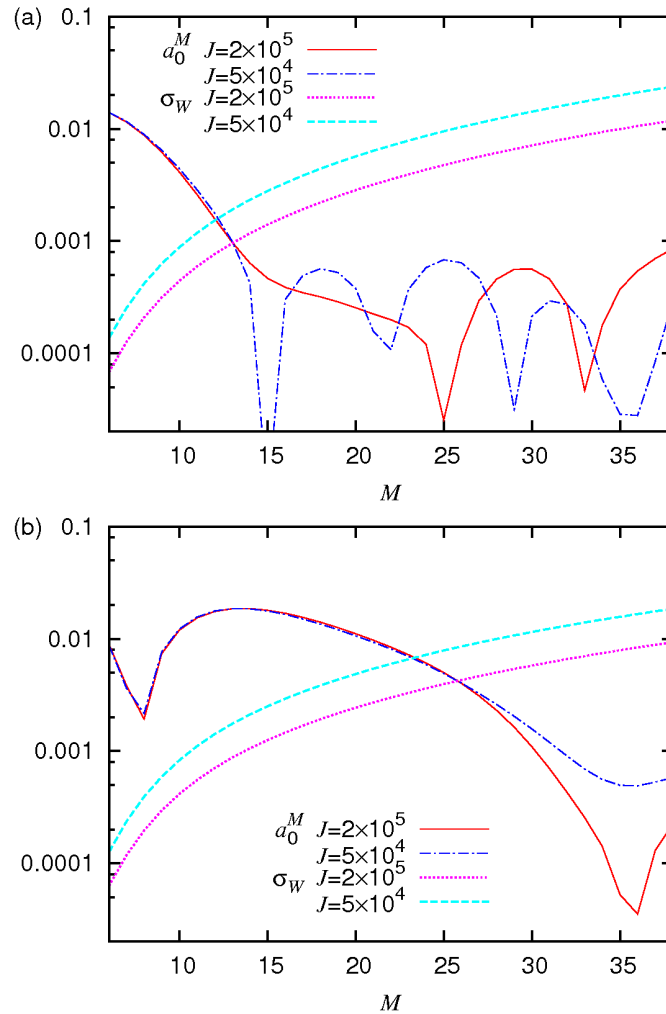


Figure 3.16: Effect of M on the convergence of $W'(0, 0)$ and the magnitude of $\sigma_{W'}(0, 0)$. (a) Thermal state with $\langle \hat{n} \rangle = 1$, rejection sampling. (b) Experimental photon subtracted squeezed vacuum state (same data as in Fig.3.9).

to be smaller than the statistical error itself. This can be checked in the algorithm by iteratively calculating $\sigma_{W'}^2(0, 0)$ for increasing values of M and stop when the magnitude of the M^{th} and last coefficient w_0^M is less than $\sigma_{W'}^2(0, 0)$ (see Fig. 3.16). This technique can be repeated independently for every point of phase space (q, p) , and different values of N and M can even be used for different points of phase space.

3.4.2 Maximum likelihood and the Cramer-Rao inequality

Fisher's information In practice, the maximum likelihood estimation algorithm has many statistical advantages. Because it is a variational algorithm, it can perform better than linear estimation methods with regards to noise. If the data set is statistically pure enough, the maximum likelihood algorithm is able to erase to some extent noise from the estimate $\tilde{S}(\{\vec{x}_i\}_i)$ and retrieve the original state from the statistics. The counterpart of this is that when the data set is statistically heavily mixed, the maximum likelihood algorithm yields poor results. In this situation it can also show trouble with convergences when iterative approximation techniques are involved. It is possible to quantify this behavior with the Fisher information functional $\mathcal{I}(S)$ which is defined as the variance of the first order derivative of the log-likelihood $\log \mathcal{L}$

$$\mathcal{I}(S) = E \left[\left(\frac{\delta}{\delta S} \log \mathcal{L}(S, \{x_i\}_i) \right)^2 \right], \quad (3.4.10)$$

$$\text{or equivalently } = -E \left[\frac{\delta^2}{\delta S^2} \log \mathcal{L}(S, \{x_i\}_i) \right], \quad (3.4.11)$$

where $E[\cdot]$ is the esperance with respect to the probability $\mathcal{L}(S, \{x_i\})$ of measuring the data set $\{x_i\}$ with parameter S . If S is a scalar, then the Fisher information $\mathcal{I}(S)$ is also a scalar. If S is a vector, $\mathcal{I}(S)$ is a covariance matrix. In our case S is the density matrix $\hat{\rho}$ and $\mathcal{I}(\hat{\rho})$ is therefore a 4th order tensor which reads exactly

$$(\mathcal{I}(\hat{\rho}))_{nm}^{n'm'} = E [(\partial_{\hat{\rho}_{nm}} \log \mathcal{L}(\hat{\rho})) (\partial_{\hat{\rho}_{n'm'}} \log \mathcal{L}(\hat{\rho}))]. \quad (3.4.12)$$

To calculate the Fisher's information from the above equation, we use a theorem which states that the Fisher's information of two independent event is the sum of the Fisher information of the two events. We can therefore evaluate the above esperance $E[\cdot]$ not on the data set itself, but on one arbitrary homodyne detection event (x, θ) so that Eq.(3.4.12) can be written

$$(\mathcal{I}(\hat{\rho}))_{nm}^{n'm'} = JE [\partial_{\hat{\rho}_{nm}} \log \text{tr} [\hat{\rho}|x_\theta\rangle\langle x_\theta|] \partial_{\hat{\rho}_{n'm'}} \log \text{tr} [\hat{\rho}|x_\theta\rangle\langle x_\theta|]], \quad (3.4.13)$$

$$= \frac{J}{2\pi} \int_{-\pi}^{+\pi} d\theta \int_{-\infty}^{+\infty} dx \frac{\langle n|x_\theta\rangle\langle x_\theta|m\rangle\langle n'|x_\theta\rangle\langle x_\theta|m'\rangle}{\text{tr} [\hat{\rho}|x_\theta\rangle\langle x_\theta|]^2}. \quad (3.4.14)$$

The Fisher information is a way of quantifying the amount of information that a single measurement x of the random observable variable X carries about an unknown parameter S upon which the probability of $p(x = X|S)$ depends. We know that the maximum likelihood estimation S_0 of S cancel asymptotically the first order derivative of $p(x = X|S)$ when $J \rightarrow \infty$. So looking at the variance of the first order derivative gives insight in which extent the estimate is accurate. In other word, while the maximum likelihood estimator seeks to find the parameter S_0 around which $\log \mathcal{L}(S)$ is stationary by cancelling the first order derivative, the Fisher's information looks with the second order derivative at how large changes ΔS to S are around this maximum stationary point. If the Fisher's information is high, then the maximum is stiff and a small change in S results in a large change to the log likelihood $\log \mathcal{L}(S)$. It becomes therefore easy to detect this large change to $\log \mathcal{L}(S)$ and to stay at the top of the maximum as the number of raw information J increases. In practice for this case an iterative method would converge faster and with more precision to the value S_0 . To the contrary if $\mathcal{I}(S)$ is small, an equivalently large change to S results into only a small change to $\log \mathcal{L}(S)$. The latter case happens if $\{\vec{x}_i\}_i$ is corrupted with statistical noise for example. Then $\mathcal{I}(S)$ decreases and the likelihood function $\mathcal{L}(S)$ is less peaked around S_0 which fragilises iterative approximation of S_0 .

Another difficulty in the maximum likelihood estimation algorithm is the inherent bias induced first by the particular data set $\{\vec{x}_i\}_i$ which is used to estimate S_0 , and second by the underlying

statistical model. For the former point, maximum likelihood estimation can be very sensible to small changes in data sets whose sizes are small. Usually, it is safe to apply this technique on data sets with redundant information compared to the number of degrees of freedom available in the statistical model. For the latter point, it is subtle but important to notice that the likelihood metric $\mathcal{L}(S)$ is arbitrary and depends entirely on the underlying statistical model used to calculate $p(\vec{x}|S)$. In other words, it is not possible to directly compare the maximum likelihood method with other estimation methods. It is not even possible to compare it with itself, using another parametrisation S' and another statistical model $p'(\vec{x}|S')$. In this case, the two Fisher information functionals $\mathcal{I}(S)$ and $\mathcal{I}'(S')$ are different for the same data set $\{\vec{x}_i\}_i$ and scales differently. It is however possible to express one from the other with the Jacobian-like transformation

$$\mathcal{I}(S) = \mathcal{I}'(S') \left(\frac{\delta S'}{\delta S} \right)^2, \quad (3.4.15)$$

if the parameter S' can be expressed from S . We understand from this transformation that for the same experimental data set, some parametrisation S_1 can perform better than some other parametrisation S_2 with respect to the amount of Fisher's information achievable. This fact proves that indeed maximum likelihood based method are inherently biased by the information about the system that the physicist implicitly puts in his statistical model.

Cramer-Rao inequality If a direct estimator \check{S} of S_0 the parameter which satisfies the maximum likelihood principle can be obtained then it is also possible to have a direct expression of the standard deviation of the error $\epsilon = S - \check{S}$. With an iterative algorithm, this is usually impossible. However, it is still possible to have some partial knowledge of the properties of ϵ with the quantity of Fisher's information \mathcal{I} and the Cramer-Rao inequality. The Cramer-Rao inequality states that for any unbiased estimator \check{S} of a parameter S , be it the maximum likelihood estimator or not, the variance of the estimator $\text{var}(\check{S})$ has a lower bound given in the scalar case by

$$\text{var}(\check{S}) = \langle \check{S}^2 \rangle - \langle \check{S} \rangle^2 \geq \frac{1}{J\mathcal{I}(S)}, \quad (3.4.16)$$

where J is the number of experimental events. The proof of the Cramer-Rao inequality relies on the Cauchy–Schwarz inequality and the adequate use of the definitions of the variance and the Fisher's information. If \check{S} is not a scalar but a vector, then $\text{var}(\check{S})$ is actually the covariance matrix of \check{S} defined as

$$(\text{var}(\check{S}))_{ij} = \langle (\check{S}_i - \langle \check{S}_i \rangle)(\check{S}_j - \langle \check{S}_j \rangle) \rangle. \quad (3.4.17)$$

This bound applies to all estimators but the maximum likelihood estimator is asymptotically the most efficient estimator with regards to the Cramer-Rao bound. Theoretically it reaches the minimal possible variance $1/\mathcal{I}$ when J tends toward infinity. In practice it is significantly more complex to evaluate the error with the maximum likelihood reconstruction of the density matrix $\hat{\rho}$. The main difficulty is the impossibility to know how far from the Cramer-Rao bound does the reconstruction algorithm perform. According to previous studies, it looks that in the case of optical homodyne tomography, the gap between the achievable error and the minimal error imposed by the Cramer-Rao inequality can be rather large[111].

3.4.3 Monte Carlo error simulation

Error simulation Independently from the estimators of the previous paragraph, we also use Monte Carlo simulations to generate synthetic data sets in order to evaluate the reconstruction errors [125]. This method is easily applied if we know precisely the underlying state $\hat{\rho}$. For

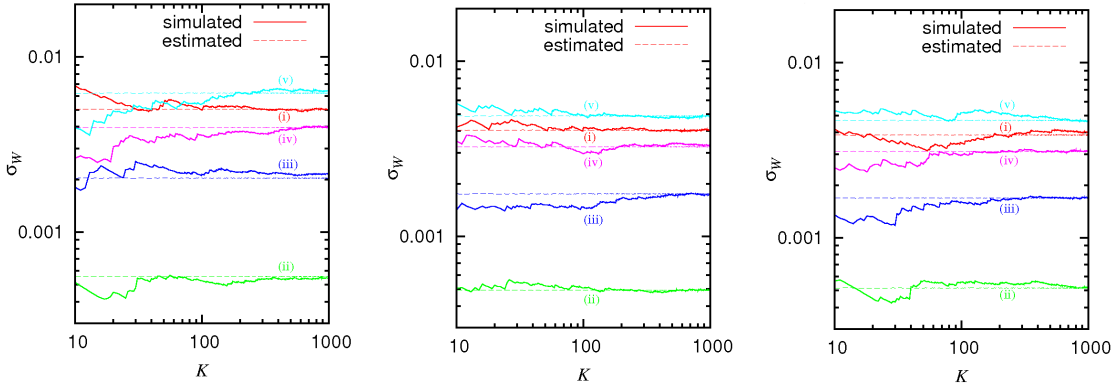


Figure 3.17: Comparison between Monte Carlo simulation and direct estimation of $\sigma_W(0,0)$. Black curves are the estimation of $\sigma_W(0,0)$ with Monte-Carlo simulation using K data sets. Dashed curves are the direct estimation of $\sigma_W(0,0)$ using Eqs. (3.4.3) and (3.4.9) for the K^{th} data set. Left, data sets of $J = 10^5$ points generated using rejection sampling for a thermal state of mean photon number $\langle n \rangle = 1$. Center, data sets of $J = 10^5$ points generated using rejection sampling for the state $0.8|1\rangle\langle 1| + 0.2|0\rangle\langle 0|$. Right, data sets of $J = 10^5$ points generated with bootstrapping resampling from the same experimental data as Fig. 3.9. (i) Filtered back-projection tomography with $k_c = 7$; (ii) polynomial series tomography with $M = 10$; (iii) $M = 20$; (iv) $M = 30$; (v) $M = 40$.

example, we can choose a known density matrix or Wigner function and calculate the associated marginal distribution $p(x, \theta)$. From this marginal distribution we generate K synthetic data sets of J points $\{(x_j, \theta_j)\}_j^{(k)}$. With the algorithm of our choice we repeat the tomography reconstruction and calculate a set of K Wigner function $\{W^{(k)}\}_k$. Finally for a given point of phase space (x_0, p_0) , we calculate the average value \bar{W}_0 of the set $\{W^{(k)}\}_k$:

$$\bar{W}_0 = \frac{1}{K} \sum_{k=1}^K W^{(k)}(x_0, p_0), \quad (3.4.18)$$

and obtain an estimate of the error $\sigma_{\bar{W}}$ at point (x_0, p_0) by

$$\sigma_{\bar{W}}^2 = \frac{1}{K} \sum_{k=1}^K \left(W^{(k)}(x_0, p_0) - \bar{W}_0 \right)^2. \quad (3.4.19)$$

Since it is a Monte Carlo based simulation, every quantity shows again a $1/\sqrt{K}$ convergence rate.

Rejection sampling To perform such Monte-Carlo simulations we use the rejection sampling technique to generate sequences of numbers $\{x_j, \theta_j\}_j$ distributed according to $p(x, \theta)$ [125]. In practice quasi-random number generators have most of the time uniform distribution and produce integers in $[0, 2^b - 1]$ where b is 32 or 64. When the algebraic expression of $p(x)$ where $x \in [a, b]$ is known it is possible to craft a formula to directly generate the desired sequence. For that we calculate the cumulative distribution function $F(x) = \int_a^x p(y)dy$, and then use its inverse $F^{-1}(x)$ to define the sequence

$$\{x_i\}_i = \{F^{-1}(y_i)\}_i \quad (3.4.20)$$

where the sequence of number $\{y_i\}_i$ is uniformly distributed in the interval $[0, 1]$. When $p(x)$ is unknown this technique is not valid and rejection sampling proves superior provided the fact we

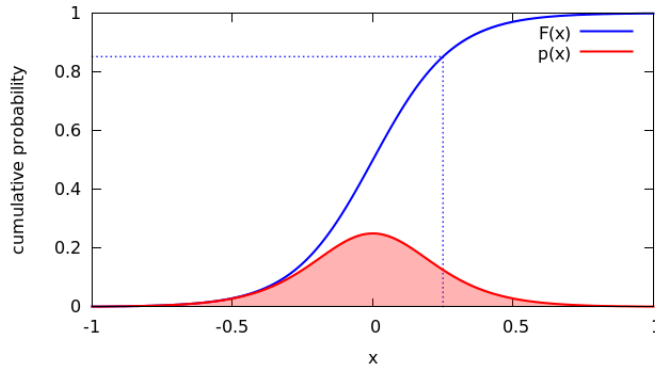


Figure 3.18: Illustration of the rejection sampling technique. Here $[a, b]$ is equal to $[-1, 1]$, $p(x) = 1/(1 + \exp[-\alpha x])(1 + \exp[+\alpha x])$, $F(x) = 1/(1 + \exp[-\alpha x])$ and $\alpha = 7$.

can estimate $p(x)$ for any valid x value. The algorithm consists to sample uniformly the square area $[a, b] \times [0, 1]$ and generate sequences of pair of numbers $\{(x_i, y_i)\}_i$. We then reject any pair (x_j, y_j) if

$$p(x_j) > y_j, \quad (3.4.21)$$

which is equivalent to selecting the pairs of number falling into the red area under the $p(x)$ curve in Fig.3.18. The remaining pairs in the sequence are therefore distributed according to $p(x)$. To increase the yield, it is possible to sample the y variable in the the interval $[0, \max_x(p(x))]$ instead.

Resampling Performing Monte-Carlo simulations with experimental data is a little harder, as we can sample the unknown distribution $p(x, \theta)$ only once. We therefore need a technique to generate the synthetic data sets after the experimental measurement. A possible approach is to consider the experimental data set $\{x_i, \theta_i\}$ as the best representation of the underlying distribution $p(x, \theta)$. The idea is to replace the unknown underlying state $\hat{\rho}$ with an estimate using the experimental data collected about $\hat{\rho}$. The assumption is that is if this experimental data is sufficiently large and well-defined, any $\hat{\rho}_{\text{data}}$ estimated from the data should be close enough to $\hat{\rho}$ to show similar properties. Using $\{x_i, \theta_i\}$ we can for example reconstruct a first Wigner function or density matrix with one tomography algorithm and then use the reconstructed object to estimate $p(x, \theta)$ and generate synthetic data sets for Monte-Carlo simulations[125]. Another technique is to use $\{x_i, \theta_i\}_{i \leq J}$ itself as a pool of possible experimental sequences with the bootstrapping resampling method [38]. In the bootstrap approach, we choose randomly and independently J' events in the data set $\{x_i, \theta_i\}_{i \leq J}$. The bootstrap resampling techniques works well together with Monte-Carlo estimation, especially if the size J of original data set is much larger than the resampled sets with size J' . Possible declinations of the bootstrap resampling techniques includes non-independent selections where for example one event of the original data set can only be selected once in a resampled sequence. In any case resampling is an easy technique to implement and in the next paragraph we estimate the reconstruction error of experimental data sets with the bootstrapping resampling method. The results of both the bootstrap technique and the direct sampling technique are illustrated in Fig. 3.17 and overall there is a good agreement between the estimated values of Monte Carlo simulations and the predicted value of $\sigma_W(0, 0)$ using Eq.(3.4.3) or (3.4.9).

3.4.4 Fidelity and distance to target state

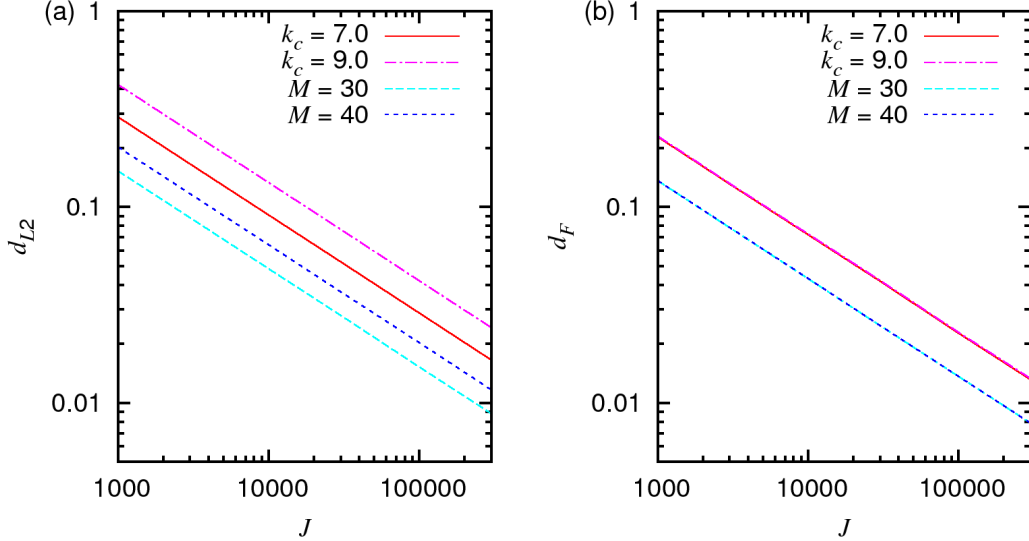


Figure 3.19: Estimation of the distance between the target thermal state of mean photon number $\langle \hat{n} \rangle = 1$ and reconstructed quantum states averaged over 1000 samples of J data points for different tomography settings. (a) L_2 distance $\langle d_{L2}(W_{\text{target}}, W_{\text{tomo}}) \rangle$. (b) Frobenius distance $\langle d_F(\hat{\rho}_{\text{target}}, \hat{\rho}_{\text{tomo}}) \rangle$.

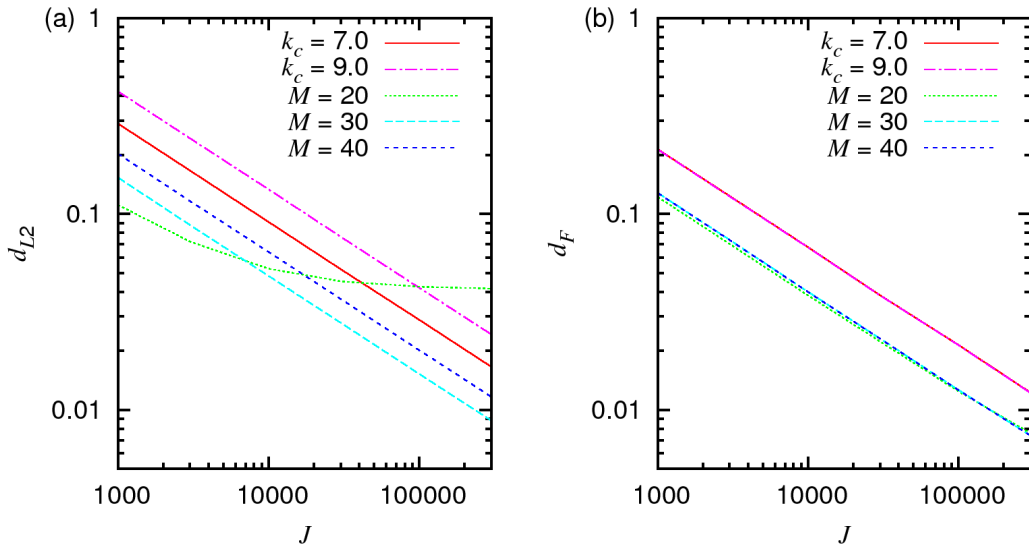


Figure 3.20: Estimation of the distance between the target state $0.8|1\rangle\langle 1| + 0.2|0\rangle\langle 0|$ and reconstructed quantum states averaged over 1000 samples of J data points for different tomography settings. (a) L_2 distance $\langle d_{L2}(W_{\text{target}}, W_{\text{tomo}}) \rangle$. (b) Frobenius distance $\langle d_F(\hat{\rho}_{\text{target}}, \hat{\rho}_{\text{tomo}}) \rangle$.

Comparison of linear inversion algorithms To conclude this comparative study of polynomial series expansion and filtered back-projection-based tomography, we numerically estimate the dis-

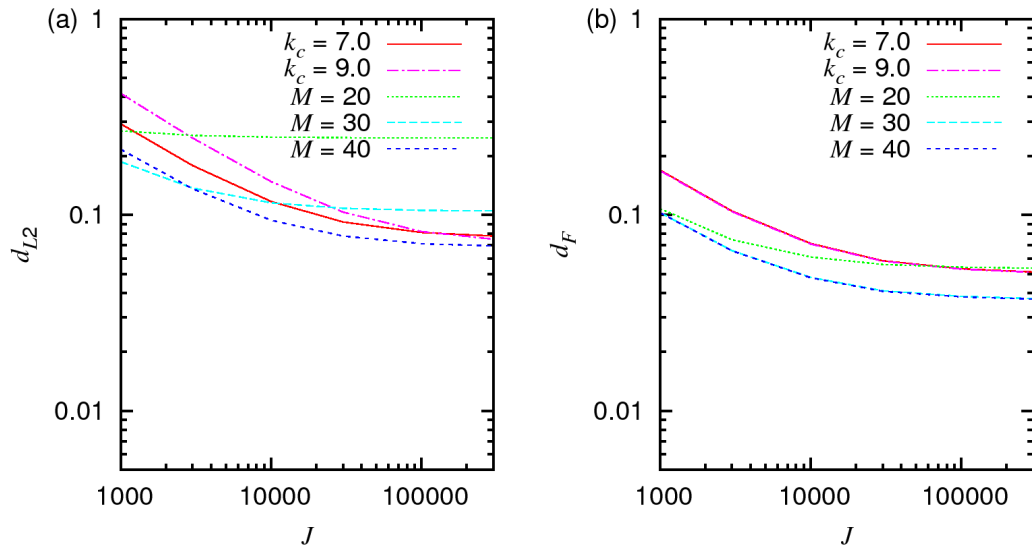


Figure 3.21: Estimation of the distance between the target odd Schrödinger's cat state $\propto |\alpha\rangle - |-\alpha\rangle$ with $\langle \hat{n} \rangle = 3$ and reconstructed quantum states averaged over 1000 samples of J data points for different tomography settings. (a) L_2 distance $\langle d_{L2}(W_{\text{target}}, W_{\text{tomo}}) \rangle$. (b) Frobenius distance $\langle d_F(\hat{\rho}_{\text{target}}, \hat{\rho}_{\text{tomo}}) \rangle$.

tance between some original target quantum state and reconstructed states using both algorithms. For this purpose we will consider one distance for the Wigner function and one distance for the density matrix. We use the L_2 Euclidian distance $d_{L2}(\cdot, \cdot)$ for the Wigner function defined by

$$d_{L2}(W_A, W_B) = \left(\int \int dx dp |W_A(x, p) - W_B(x, p)|^2 \right)^{1/2}, \quad (3.4.22)$$

and define a distance $d_F(\cdot, \cdot)$ for density matrices as

$$d_F(\hat{\rho}_A, \hat{\rho}_B) = \|\hat{\rho}_A - \hat{\rho}_B\|_F, \quad (3.4.23)$$

where $\|\cdot\|_F$ is the Frobenius norm defined by

$$\|A\|_F = \sqrt{\text{tr}(A^* A)} = \left(\sum_{i,j} |A_{ij}|^2 \right)^{1/2}. \quad (3.4.24)$$

First we choose a target state and derive its exact Wigner function W_{target} and density matrix $\hat{\rho}_{\text{target}}$. We then evaluate the distances from the target state according to Eqs. (3.4.22) and (3.4.23) using as before Monte Carlo sampling techniques. Rather than averaging a reconstructed state over many simulated data sets, we average the distance computed over many reconstructed states and estimate the numbers:

$$\langle d_{L2}(W_{\text{target}}, W_{\text{tomo}}) \rangle \text{ and } \langle d_F(\hat{\rho}_{\text{target}}, \hat{\rho}_{\text{tomo}}) \rangle, \quad (3.4.25)$$

where the averaging is conducted over synthetic measurement data. Numerical simulation results are shown in Figs. 3.19–3.21 for, respectively, a thermal state with $\langle \hat{n} \rangle = 1$, a mixture of vacuum and one-photon state $0.8|1\rangle\langle 1| + 0.2|0\rangle\langle 0|$, and an odd Schrödinger's cat state with $\langle \hat{n} \rangle = 3$. In agreement with the previous results on tomography uncertainties, we observe that polynomial series expansion tomography performs better than filtered back-projection for these two first cases.

In the case of the Schroedinger's cat state $\propto |\alpha\rangle - |-\alpha\rangle$, both distances behave differently for higher J and tend to reach a precision limit which depends on the tomography algorithm and settings. Although the exact cause of this saturation is unknown, we believe it is due to the significantly more complex structure of the Schroedinger's cat state. According to our simulations, it seems to depend only on the radial and angular precision settings, more precisely on parameters M , N , and k_c . In this case again, polynomial series expansion proves to reach a higher precision level than filtered back-projection for a relevant range of tomography settings. To conclude this paragraph, it is interesting to notice that in the case of the $d_{L2}(.,.)$ distance there is an intrinsic limitation on the precision of polynomial series expansion tomography due to the circular geometry of the reconstruction space [73]. This could be the reason for the saturation phenomenon visible in Fig. 3.21.

More precisely, polynomial series tomography is superior with fewer experimental data points and when higher radial resolution is needed for higher photon number states. These results are confirmed when looking at the distance between a chosen target state and states reconstructed with both tomography techniques. Furthermore this technique exploits the projection slice theorem directly and therefore is faster than convolution based filtered back-projection.

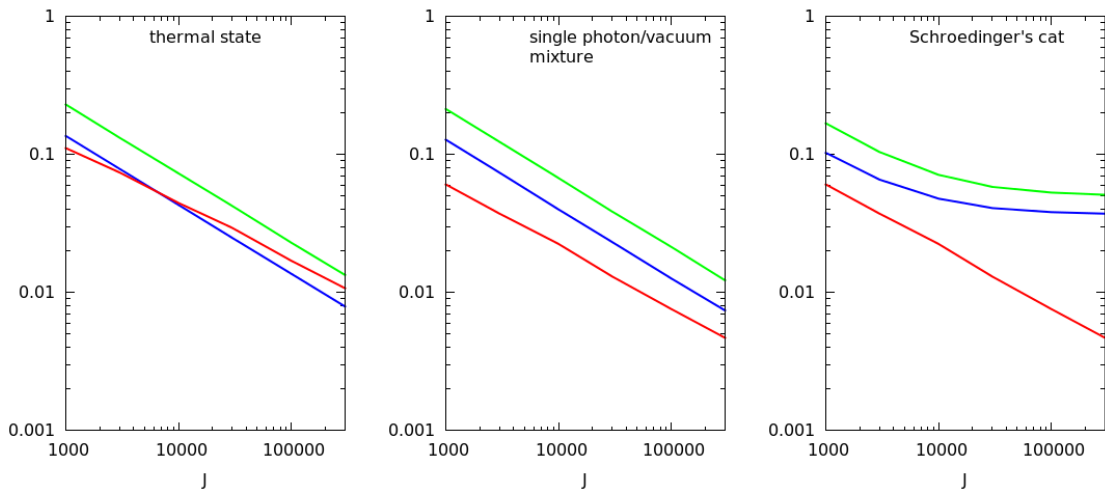


Figure 3.22: Comparison of the expected Frobenius distance between the reconstructed state and the target state for different tomography algorithms and different quantum states. Left, thermal state with $\langle \hat{n} \rangle = 1$. Center, mixture $0.8|1\rangle\langle 1| + 0.2|0\rangle\langle 0|$. Right, odd Schrödinger's cat state with amplitude $\alpha = 1$. Red trace, maximum likelihood estimation after 25 iterations with n_{\max} equals to 15 photons. Blue trace, polynomial series algorithm with $L = 10$, $N = 8$ and $M = 40$. Green trace, filtered back-projection with $k_c = 9.0$.

Comparison with the maximum likelihood reconstruction algorithm Until now we have not been able to directly compare the maximum likelihood reconstruction of the density matrix with methods based on the inverse Radon transform. Because the Cramer-Rao inequality only gives lower bounds, and due to the challenge of obtaining trustable variance estimates σ^2 of the reconstruction error for the iterative maximum likelihood algorithm presented in Sec. 3.3.2, this direct comparison is difficult. A possibility would be to restrict ourselves to the diagonal elements $\hat{\rho}_{nn}$ of the density matrix and use the formula

$$W(0, 0) = \frac{1}{\pi} \sum_n (-1)^{-n} \hat{\rho}_{nn}. \quad (3.4.26)$$

With an approach similar to the one we used with the polynomial series decomposition algorithm in Eq.(3.4.8), we could apply the Cramer-Rao inequality to obtain a lower bound on every variance parameters $\sigma_{nm}^{\hat{\rho}}$ defined as

$$\sigma_{nm}^{\hat{\rho}} = \langle (\hat{\rho}_{nn} - \langle \hat{\rho}_{nn} \rangle) \times (\hat{\rho}_{mm} - \langle \hat{\rho}_{mm} \rangle) \rangle. \quad (3.4.27)$$

However, it does not guarantee in any way that an actual reconstruction of the density matrix would achieve the Cramer-Rao bound. Rather, we continue to use the Frobenius distance and study the two families of reconstruction techniques with additional Monte-Carlo simulations. Fig.3.22 shows comparisons with the results of the previous paragraph of the iterative maximum likelihood reconstruction algorithm implemented as it is explained in Sec.3.3.2. We notice that in the case of a thermal state, the polynomial series reconstruction performs better than the maximum likelihood reconstruction above $J \approx 10000$. Furthermore, the slope of the distance does not follow the $1/\sqrt{J}$ rate of convergence and has a slower pace of convergence. Intuitively we understand this is as a consequence of the lower purity of the thermal state. In a context of low statistical purity, the expression of $\text{tr}[\hat{\rho}|x, \theta\rangle\langle x, \theta|]$ is inherently less precise. To confirm this fact we look at the case of a teleported single photon state. We derive the expression of the density matrix of a single photon state $|1\rangle$ after teleportation with ERR correlation r using for example the transfer operator[57, 67]. The output teleported state is further thermalized as the amount of correlation r decreases, and its purity is further reduced. As is shown in Fig.3.23, as the purity of the target teleported state decreases the maximum likelihood method performs worse and worse. Furthermore, the rate of convergence also falls further away from the theoretical rate $1/\sqrt{J}$ as the purity decreases. We checked in these simulations that the number of iterations or the size of the reconstructed density matrix had no influence on the results. It is important to notice that since the Cramer-Rao inequalities implies a $1/\sqrt{J}$ rate of convergence for an efficient estimator, the graphs of Figs.3.22 and 3.23 shows that there are situations where the maximum likelihood reconstruction algorithm fails to achieve the Cramer-Rao bound. Unfortunately we were not able to analyse further this phenomenon and better understand in which cases this effect happens.

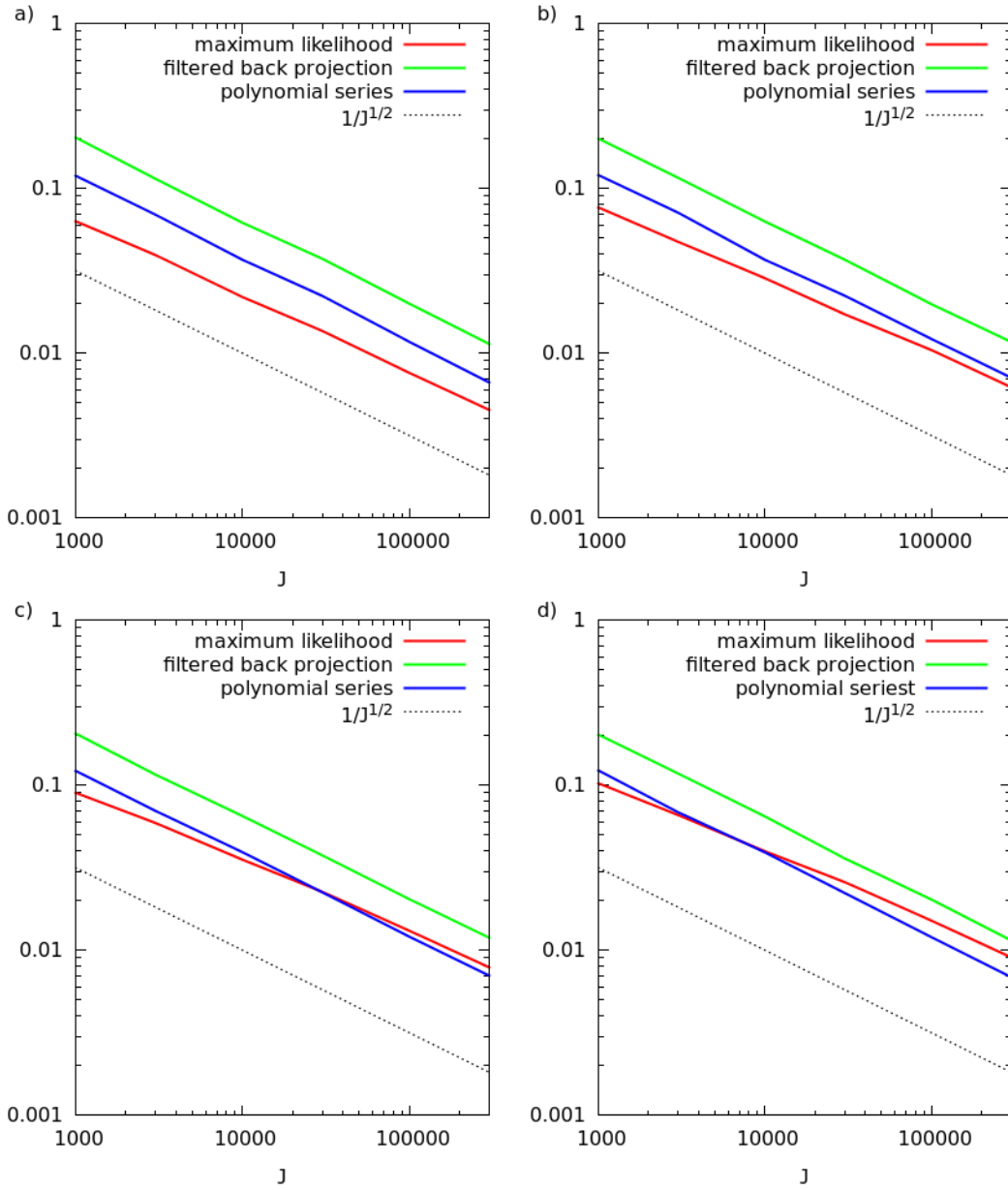


Figure 3.23: Comparison of the expected Frobenius distance between the reconstructed state and the target state for different tomography algorithms. The state used for simulation is a teleported single photon state with varying degree of EPR correlations. a), with 9 dB. b), with 6 dB. c), with 3 dB. d), with 1 dB. Red trace, maximum likelihood estimation after 25 iterations with n_{\max} equals to 15 photons. Blue trace, polynomial series algorithm with $L = 10$, $N = 8$ and $M = 40$. Green trace, filtered back-projection with $k_c = 9.0$.

Chapter 4

Broadband Quantum Teleportation

We present in this chapter our research on continuous variable quantum teleportation of non-Gaussian states of light. This experiment has three main noticeable aspects. First, the use of a non-Gaussian non-classical state as an input state for a continuous variable quantum circuit (see Chap.2 for details about this input quantum state). Although Gaussian states teleportation has been amply studied until now, due to the complex nature of non-Gaussian states and especially mixed non-Gaussian states, only few experimental and theoretical results exist for this case. Second, to accommodate with the transient nature of the input state used, the teleporter apparatus operates on a broad range of frequencies, in contrast with typical continuous variable experiments which only manipulate narrow sidebands of light. Third, the quality of teleportation is high enough that the output teleported state is also a non-classical state with a negative Wigner function.

In Sec.4.1, we present the minimal theory necessary to understand continuous variable quantum teleportation. We show how to extend this simple monomode theory to the wave-packet case. We also formally demonstrate the link between the Heisenberg and Schroedinger pictures models of teleportation, and show how it is possible to interpret the equations of teleportation as a thermalization process with a master equation formalism. In Sec.4.2, we present the experimental setup used to achieve quantum teleportation of non-Gaussian states and explain in details the elements added to the setup of non-Gaussian state generation found in Chap.2. We also present experimental results of vacuum state and non-Gaussian state teleportation, and derive a simple predictive model to understand quantitatively these experimental results. Finally in Sec.4.3, we introduce the technique of conditional teleportation as was proposed in [160] and derive a model relevant to our experimental parameters. We present and analyse experimental results of conditional teleportation which demonstrate improvement of the teleportation of non-classical features of the Wigner function in the conditional regime.

4.1 Theory of continuous variable teleportation

We implement in our optical setup the teleportation scheme proposed in [49] and experimentally demonstrated for the time in [51]. This continuous variable teleportation circuit is derived from the former continuous variable formulation of quantum teleportation in [39], itself adapted from the original qubit teleportation proposal [35]. In this section we want first analyse the mechanism of teleportation and gain a good understanding of it. Second, we want to obtain a predictive model that we can compare to experimental results. In this section we only develop the necessary tools to establish such a model which is finalized in Sec.4.2.4. Third, we want to precisely establish the limit between the quantum and the classical regimes.

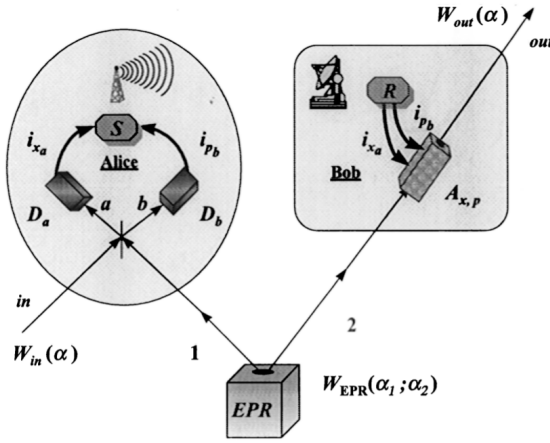


Figure 4.1: The continuous variable teleportation protocol as proposed in [49].

4.1.1 Criterion of success

Deciding on the success of continuous variable teleportation is a non-trivial problem as it is closely related to the kind of input states and entanglement used, as well as the specific protocol or quantum circuit that teleportation is actually used for. As we explain in this paragraph, the discussion on success or failure of quantum teleportation can only be a case by case study.

Gaussian fidelity

For the case of Gaussian input states and regardless of the protocol, the fidelity $F = \langle \psi_{in} | \hat{\rho}_{out} | \psi_{in} \rangle$ is the usual figure of merit to quantify the quality of teleportation. When more general non-Gaussian mixed states are used as input states, F loses much of its meaning as a figure of the quality of the teleportation process. Nevertheless, as a benchmark figure F is still useful for a vacuum input state. Historically, the fidelity was the first figure of merit used to try and define the limit between the classical and quantum regimes. In [55] it is shown that a fidelity higher than $1/2$ cannot be achieved with classical operations alone, but requires some form of entanglement and squeezing. It was shown later that the $F = 1/2$ threshold is not sufficient to assure that the output state of teleportation is the best copy of the state[66]. It was then additionally argued that the no-cloning limit $F = 2/3$ would be the true quantum threshold when considering applications of teleportation to communication algorithms. Relations between teleportation and optimal cloning was further investigated in [83]. On the contrary, [64] established that $F = 1/2$ is the relevant threshold for violation of the Bell's inequality, and that this fidelity threshold holds some meaning on the boundary between quantum and classical operations. Even in the simple case of pure Gaussian input states, finding an unambiguous criterion to decide on successfulness of teleportation is not a trivial problem. As with the interpretation of the Wigner function (see Sec.2.1.1), the meaning, properties and implied hypothesis of a given criterion should not be overlooked when evaluating the quality of a given teleportation apparatus.

Negativity teleportation and the no-cloning limit

While Gaussian states can be fully characterized by their first and second moments, which allow figures like the fidelity to have a useful meaning to some extent, such an approach fails with non-Gaussian states. Because non-classicality itself is an ambiguous property for continuous variable systems with infinite-dimensional Hilbert spaces, it is even more complex to decide on a relevant

criterion of success for continuous variable teleportation of non-classical quantum states. It is possible to define non-Gaussianity measures to quantify the non-Gaussianity of a quantum state[114, 138]. However, it is not clear what link there is, if any, between on the one hand such criteria solely based on the geometric shape of the Wigner function, and on the other hand the separation between classical and non-classical states. Therefore, when applied to continuous variable teleportation, it is not possible to define a precise threshold between classical and quantum operations with such measures.

In a striking similitude with the 2-dimensional qubit teleportation case, the most general condition for successful teleportation of non-Gaussian non-classical states may be the necessary but not sufficient $2/3$ threshold on fidelity [81]. We consider the input and output states of a teleportation process and look at W_{in} and W_{out} their respective Wigner functions. In the Braunstein-Kimble scheme described in [49], the teleportation operation can be expressed in phase space as the following convolution

$$W_{\text{out}} = W_{\text{in}} \circ G_{e^{-r}}, \quad (4.1.1)$$

with r the Einstein-Podolsky-Rosen (EPR) correlation parameter and $G_\alpha(q, p)$ a normalized Gaussian of standard deviation α (with $\hbar = 1$). In this case, teleportation of nonclassical features such as negativity has been shown to require at least 3 dB of squeezing [58, 81], or equivalently a vacuum fidelity of $F \geq 2/3$, which is also called the no-cloning limit [66]. More precisely, if we recall the discussion on Gaussian filtering of the Wigner function in Sec.1.3.3 and identifying Eq.(4.1.1) with Eq.(1.3.39), we see that for W_{out} to keep any negativity present in W_{in} through the teleportation process, it would require that

$$e^{-r} \geq 1/\sqrt{2} \rightarrow r \geq \ln \sqrt{2}, \quad (4.1.2)$$

or in other words that the EPR correlations are at least 3 dB. In practice, 3 dB is a lower bound for unity gain teleportation of negativity of any pure or mixed state. To observe some negativity after teleportation of a pure state, 3 dB plus an infinitesimal amount of squeezing is sufficient. However for mixed states this is not the case. We would like to have a model that predicts better the success or failure of negativity teleportation in the case of mixed non-Gaussian non-classical states more relevant to our experimental conditions. In the general case, this is too broad a problem to handle as teleportation is known to be input dependent: Eq.(4.1.1) would have to be applied on a case by case basis for any input state W_{in} to find a specific threshold value r for the successful teleportation of negativity.

In the remaining of this chapter, we again adopt as a criterion of success the transfer of negative features of the Wigner function. Provided W_{in} is itself a negative Wigner function, we decide that teleportation is successful when W_{out} also includes some negativity. Having for W_{in} a precise algebraic expression including the relevant experimental parameters, we want to know what are the requirements on these parameters and on the teleportation process for successful retrieval of negativity in W_{out} . In [160], the theoretical work closest to our experimental conditions, teleportation success is investigated for the case of a mixture of vacuum $|0\rangle$ and one photon $|1\rangle$ as an input state. However, the presence of squeezing in our input state and other experimental complications need to be taken into account to find the precise success threshold.

4.1.2 Heisenberg picture

We start our analysis of teleportation with the Heisenberg picture monomode equations. Continuous variable teleportation equations in the Heisenberg picture have been derived in [59]. For the treatment of quantum teleportation and quantum information with continuous variable in the Heisenberg picture, [91] is another very complete reference. We follow the 3-steps protocol of [49] which Fig.4.2 is an illustration of. First, a Gaussian 2-mode EPR entanglement resource is

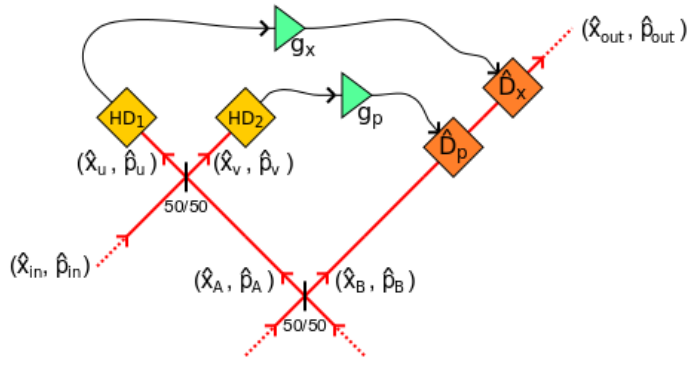


Figure 4.2: Protocol for continuous variable teleportation with operator modes naming convention of this chapter.

generated and distributed to Alice and Bob who then share an entangled 2-mode quantum channel. Second, Alice performs a joint measurement of her unknown input state in mode $(\hat{x}_{in}, \hat{p}_{in})$ and her entangled mode (\hat{x}_A, \hat{p}_A) . For that, she measures with two homodyne detectors the commuting relative position operator $\hat{x}_u = (\hat{x}_{in} - \hat{x}_A)/\sqrt{2}$ and total impulsion operator $\hat{p}_v = (\hat{p}_{in} + \hat{p}_A)/\sqrt{2}$. Third, she sends the results (\bar{x}_u, \bar{p}_v) to Bob which performs the displacement operation $\hat{D}((\bar{x}_u + i\bar{p}_v)/\sqrt{2})$ on his entangled mode (\hat{x}_B, \hat{p}_B) .

Two-mode squeezed vacuum state

Both squeezers inputs are two independent modes $(\hat{x}_1^{(0)}, \hat{p}_1^{(0)})$ and $(\hat{x}_2^{(0)}, \hat{p}_2^{(0)})$ in the vacuum state. If both squeezers produce an equal amount of squeezing and antisqueezing quantified by the parameter r , the 2-mode entangled state at the exit ports of the half beam-splitter is written for the position quadrature

$$\begin{pmatrix} \hat{x}_A \\ \hat{x}_B \end{pmatrix} = \frac{1}{\sqrt{2}} \begin{pmatrix} 1 & 1 \\ 1 & -1 \end{pmatrix} \begin{pmatrix} e^{+r} & \\ & e^{-r} \end{pmatrix} \begin{pmatrix} \hat{x}_1^{(0)} \\ \hat{x}_2^{(0)} \end{pmatrix}, \quad (4.1.3)$$

and for the momentum quadrature

$$\begin{pmatrix} \hat{p}_A \\ \hat{p}_B \end{pmatrix} = \frac{1}{\sqrt{2}} \begin{pmatrix} 1 & 1 \\ 1 & -1 \end{pmatrix} \begin{pmatrix} e^{-r} & \\ & e^{+r} \end{pmatrix} \begin{pmatrix} \hat{p}_1^{(0)} \\ \hat{p}_2^{(0)} \end{pmatrix}, \quad (4.1.4)$$

where A and B are respectively Alice and Bob entangled modes. This two-mode entangled state verifies the correlation properties of an EPR state[8], that is, vanishing relative position and total momentum at the same time in the limit of an infinite amount of squeezing $r \rightarrow \infty$

$$\hat{x}_A - \hat{x}_B = \sqrt{2}e^{-r}\hat{x}_2^{(0)}, \text{ and } \hat{p}_A + \hat{p}_B = \sqrt{2}e^{-r}\hat{p}_1^{(0)}. \quad (4.1.5)$$

Expressed in power, this takes the form

$$\langle \hat{x}_A^2 \rangle - \langle \hat{x}_B^2 \rangle = \langle \hat{p}_A^2 \rangle + \langle \hat{p}_B^2 \rangle = e^{-2r}, \quad (4.1.6)$$

$$\langle \hat{x}_A^2 \rangle + \langle \hat{x}_B^2 \rangle = \langle \hat{p}_A^2 \rangle - \langle \hat{p}_B^2 \rangle = e^{+2r}. \quad (4.1.7)$$

This 2-mode state is also called a *two-mode squeezed vacuum state*. It is completely specified by its Gaussian correlation matrix $\Gamma(r)$ written

$$\Gamma(r) = \begin{pmatrix} \cosh(2r) & -\sinh(2r) \\ -\sinh(2r) & \cosh(2r) \end{pmatrix}. \quad (4.1.8)$$

We notice that $\det(\Gamma) = 1$ and $\Gamma^{-1}(r) = \Gamma(-r)$. The two-mode squeezed vacuum state is the necessary quantum resource for teleportation. Here, we have showed that it can be obtained with two type-I squeezers and a half-beam splitter, but a type-II squeezer with a polarization beam-splitter can also produce this state. Experimentally, the former solution usually yields more pure entanglement.

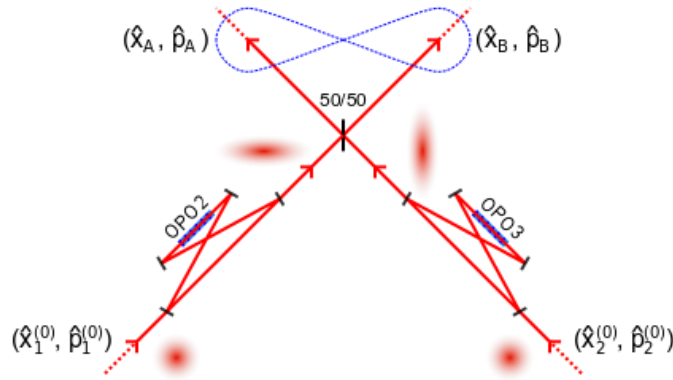


Figure 4.3: Setup with two optical parametric oscillators for the generation of a 2-mode EPR entangled state.

It is also possible to design teleportation protocols based on non-Gaussian entanglement resources. In [113], it is shown that a non-Gaussian entanglement resource tuned for a specific input state, Gaussian or non-Gaussian, can perform better than the usual EPR Gaussian entanglement for the purpose of teleportation. In contrary, the tuned non-Gaussian entanglement resource will perform worse for other input states. In [62] and [71], similar ideas of non-Gaussian entanglement teleportation based on the non-Gaussian distillation of an EPR state are proposed. However, in the laboratory Gaussian entangled states based on squeezing resources are much easier to produce and are virtually the only type of entanglement used for practical quantum information processing circuits. Furthermore, with unknown input states EPR Gaussian entanglement allows for the most universal algorithms with respect to performances.

Monomode teleportation

Alice and Bob both own one mode of the EPR entangled state presented above. Alice measurement basis are the two modes u and v defined by

$$\begin{pmatrix} \hat{x}_u \\ \hat{x}_v \end{pmatrix} = \frac{1}{\sqrt{2}} \begin{pmatrix} 1 & -1 \\ 1 & 1 \end{pmatrix} \begin{pmatrix} \hat{x}_{\text{in}} \\ \hat{x}_A \end{pmatrix}, \text{ and } \begin{pmatrix} \hat{p}_u \\ \hat{p}_v \end{pmatrix} = \frac{1}{\sqrt{2}} \begin{pmatrix} 1 & -1 \\ 1 & 1 \end{pmatrix} \begin{pmatrix} \hat{p}_{\text{in}} \\ \hat{p}_A \end{pmatrix}. \quad (4.1.9)$$

Alice can precisely measure at the same time only two operators whose commutator is zero, and we assume that she uses the basis (\hat{x}_u, \hat{p}_v) . When Alice obtains a measurement results (\bar{x}_u, \bar{p}_v) ,

Bob's entangled half is partially projected onto

$$\hat{x}_B = \hat{x}_{\text{in}} - \sqrt{2}e^{-r}\hat{x}_2^{(0)} - \sqrt{2}\bar{x}_u, \quad (4.1.10)$$

$$\hat{p}_B = \hat{p}_{\text{in}} + \sqrt{2}e^{-r}\hat{p}_1^{(0)} - \sqrt{2}\bar{p}_v. \quad (4.1.11)$$

Alice sends her results (\bar{x}_u, \bar{p}_v) to Bob, who applies the displacement operation $(+g\bar{x}_u, +g\bar{p}_v)$ to his mode (\hat{x}_B, \hat{p}_B) where g is the teleportation gain. We assume for simplicity that this gain coefficient is the same for both quadrature channels. His final output displaced state $(\hat{x}_{\text{out}}, \hat{p}_{\text{out}})$ is now written

$$\hat{x}_{\text{out}} = g\hat{x}_{\text{in}} - \frac{g+1}{2}\sqrt{2}e^{-r}\hat{x}_2^{(0)} - \frac{g-1}{2}\sqrt{2}e^{+r}\hat{x}_1^{(0)}, \quad (4.1.12)$$

$$\hat{p}_{\text{out}} = g\hat{p}_{\text{in}} + \frac{g+1}{2}\sqrt{2}e^{-r}\hat{p}_1^{(0)} + \frac{g-1}{2}\sqrt{2}e^{+r}\hat{p}_2^{(0)}. \quad (4.1.13)$$

In the case of unity gain $g = 1$, the contribution of antisqueezing $\sqrt{2}e^{+r}\hat{v}$ is strictly cancelled at the output and $(\hat{x}_{\text{out}}, \hat{p}_{\text{out}})$ becomes

$$\hat{x}_{\text{out}} = \hat{x}_{\text{in}} - \sqrt{2}e^{-r}\hat{x}_2^{(0)}, \quad (4.1.14)$$

$$\hat{p}_{\text{out}} = \hat{p}_{\text{in}} + \sqrt{2}e^{-r}\hat{p}_1^{(0)}. \quad (4.1.15)$$

In the limit of infinite EPR correlations $r \rightarrow \infty$, the output mode strictly equals the input mode. Recent work has shown that, given the precise nature of the input state and amount of anticorrelation in the teleportation quantum channel, there actually exists strategies in the non-unity gain regime which outperform unity-gain teleportation[160]. Especially, it is possible to surpass the 3 dB threshold for negativity teleportation by finely tuning the gain g . However, unless extremely pure entanglement is used, typical experimental antisqueezing imposes virtually unity gain operation in this kind of scenario. Furthermore, as the amount of gain tuning is input state dependent, the optimized teleportation setup losses its universal characteristic with respect to the input channel. In our experiment, due to the excess antisqueezing of our EPR resource, we always perform teleportation in the unity gain regime.

4.1.3 Phase space picture

For the unity gain regime, the continuous variable teleportation equations Eqs.(4.1.41) and (4.1.42) take in the Wigner formalism the very simple expression of Eq.(4.1.1)

$$W_{\text{out}} = W_{\text{in}} \circ G_{e^{-r}}, \quad (4.1.16)$$

with r the same EPR correlation coefficients. Eq.(4.1.16) is the most straightforward tool to develop a model of teleportation applicable to our experimental results. However, it is inconvenient to use to understand the wave-packet regime which can be better analysed in the Heisenberg picture. Therefore it is helpful to understand the equivalence between Eqs.(4.1.41) and (4.1.16). The aim of this paragraph is to rigorously prove this equivalence. For that purpose, we use the characteristic function $\chi(\alpha)$

$$\chi(\alpha) = \text{tr}(\hat{\rho}\hat{D}_\alpha) = \langle \hat{D}_\alpha \rangle, \quad (4.1.17)$$

related to the density matrix $\hat{\rho}$ by the Weyl expansion $\hat{\rho} = \int d\alpha \chi(\alpha)\hat{D}_{-\alpha}$, where \hat{D}_α is the displacement operator. If we write $\alpha = (u + iv)/\sqrt{2}$, we recall that χ and W are related by the following Fourier transform:

$$W(x, p) = \frac{1}{4\pi^2} \int \int du dv \chi(u, v) e^{ivx - iup}. \quad (4.1.18)$$

We consider the unitary transformation $\hat{x} \rightarrow \hat{x}' = \hat{x} - \sqrt{2}\gamma\hat{v}_x$ with an auxiliary mode (\hat{v}_x, \hat{v}_p) having commutators $[\hat{x}, \hat{v}_x] = [\hat{p}, \hat{v}_x] = 0$ and $[\hat{v}_x, \hat{v}_p] = i$. This mode transformation is our Heisenberg picture ersatz for teleportation. In Eq.(4.1.17), the displacement operator \hat{D}_α is changed to

$$\hat{D}_\alpha \rightarrow \hat{D}'_\alpha = \hat{D}_\alpha \otimes \hat{D}_{\alpha'}^{\hat{v}} = \hat{D}_\alpha \otimes e^{+i\sqrt{2}u\gamma\hat{v}_p}, \quad (4.1.19)$$

with \hat{D}^v a displacement operator acting on mode \hat{v} and $\alpha' = (-\sqrt{2}\gamma \times u + i \times 0)/\sqrt{2}$. To express the new characteristic function χ' , we have to evaluate the trace of \hat{D}^v taken on the vacuum state for mode (\hat{v}_x, \hat{v}_p) :

$$\text{tr}(|0\rangle\langle 0|\hat{D}_{\alpha'}^v) = \langle 0|\hat{D}_{\alpha'}^v|0\rangle = e^{-|\alpha'|^2/2}. \quad (4.1.20)$$

This lead for $\chi'(u, v)$ to the expression

$$\chi'(u, v) = \chi(u, v)e^{-\gamma^2 u^2/2}. \quad (4.1.21)$$

With the Fourier relationship of Eq.(4.1.18) between χ and W , the previous expression Eq.(4.1.21) translates into a Gaussian convolution similar to Eq.(4.1.1). In this case, we obtain the following semi-convolution on variable x'

$$W'(x, p) = \frac{1}{\sqrt{2\pi\gamma}} \int dx' W(x', p) e^{-(x-x')^2/2\gamma^2}. \quad (4.1.22)$$

Also adding the transformation $\hat{p} \rightarrow \hat{p}' = \hat{p} + \sqrt{2}\gamma\hat{v}_p$, we would finally obtain Eq.(4.1.1) provided we define γ as equal to $\exp[-r]$. Of course, it is possible to directly derive Eq.(4.1.16) in the phase space formalism, as was demonstrated for instance with the Wigner function in [82]. Similarly, using the characteristic function only, the Fourier equivalent of Eq.(4.1.16)

$$\chi_{\text{out}}(u, v) = \chi_{\text{in}}(u, v) G_{e+r}(u, v), \quad (4.1.23)$$

is derived in [96].

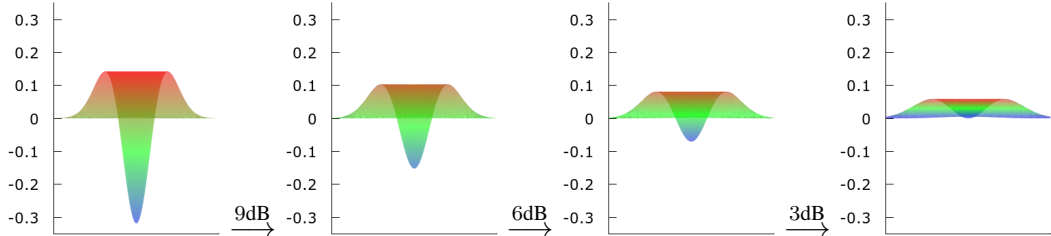


Figure 4.4: Effect of teleportation for different values of r on the Wigner function of a single photon state. From left to right, r equals successively ∞ , 1.037 (9 dB), 0.69 (6 dB) and finally 0.345 (3 dB).

4.1.4 Noise model

In this section, we try to better understand the effect of classical sources of noise on the teleportation process. In the laboratory it is a challenge to insulate the classical channel and Bob displacement operation from all external noise sources. As we see in Sec.4.1.5, this problem gets even worse in the wave-packet regime where the teleportation happens over a broad range of frequencies which offers as many opportunities for noise leakage. We first introduce a noise model based on the quantum Langevin equation and show that external Gaussian noise cannot be distinguished from teleportation induced thermalization. We then reinterpret this model with a master equation on the density matrix $\hat{\rho}$.

Quantum Langevin equation

Equations (4.1.41) look similar to quantum Langevin equations, where the terms $\sqrt{2}e^{-r}\hat{x}_2^{(0)}$ and $\sqrt{2}e^{-r}\hat{p}_1^{(0)}$ are nothing else than thermalization terms. We would intuitively add the effect of any classical source of noise directly in Eqs.(4.1.41) by writing

$$\hat{x}_{\text{out}} = \hat{x}_{\text{in}} - \sqrt{2}e^{-r}\hat{x}_2^{(0)} - \sqrt{2}\mathcal{N}_x \hat{y}, \quad (4.1.24)$$

$$\hat{p}_{\text{out}} = \hat{p}_{\text{in}} + \sqrt{2}e^{-r}\hat{p}_1^{(0)} + \sqrt{2}\mathcal{N}_p \hat{z}, \quad (4.1.25)$$

where we have introduced two new auxiliary and independent vacuum modes \hat{y} and \hat{z} . \mathcal{N}_x and \mathcal{N}_p describe the amplitude of noise normalized to the shotnoise level and added at the output of teleportation on top of the effect of finite squeezing. This noise can arise independently for both quadratures from imperfect electronics in the classical channel, for example. The most natural case is for noise to be uncorrelated with quadrature angle and we can assume $\mathcal{N}_x = \mathcal{N}_p = \mathcal{N}$ to be the average noise amplitude. We remember that all auxiliary modes appearing in the Heisenberg picture teleportation equations are traced out on the vacuum state and are uncorrelated. Therefore it would be natural to redefine a correlation parameter r' modified by the amount of noise with the simple relation

$$e^{-r} \rightarrow e^{-r'} = e^{-r} + \mathcal{N}, \quad (4.1.26)$$

so that Eqs.(4.1.24) could be eventually written as Eqs.(4.1.41). However, this approach is wrong and the correlation parameter r' cannot be redefined in amplitude but should be redefined in power by writing

$$e^{-2r} \rightarrow e^{-2r'} = e^{-2r} + \mathcal{N}^2. \quad (4.1.27)$$

In essence, the transformation of Eq.(4.1.24) has to be understood as two successive and independent Gaussian teleportation processes happening in series. The meaning of the renormalization procedure of Eq.(4.1.27) is therefore to find a single Gaussian process which is equivalent to the two successive processes introduced above. This simplification is made possible by the fact that the convolution of a Gaussian with another Gaussian is yet a third Gaussian, whom Eq.(4.1.27) is a simple statement of. It is possible to justify Eq.(4.1.27) rigorously by using the link between the Heisenberg picture equations (4.1.41) and the original phase space formulation of Eq.(4.1.1) as done in Sec.4.1.3. If we reproduce the derivation of Sec.4.1.3 on the transformations $\hat{x}_{\text{in}} \rightarrow \hat{x}_{\text{out}} = \hat{x}_{\text{in}} - \sqrt{2}e^{-r}\hat{v}_x - \sqrt{2}\mathcal{N}_x \hat{y}$, instead of Eq.(4.1.21) the final expression of $\chi'(u, v)$ would read

$$\chi'(u, v) = \chi(u, v)e^{-(\gamma^2 + \mathcal{N}^2)u^2/2}, \quad (4.1.28)$$

which therefore justifies to redefine the correlation parameter r in power and not in amplitude as

$$r \rightarrow r' = r - \ln \sqrt{1 + \mathcal{N}^2 e^{2r}}. \quad (4.1.29)$$

The key point in this renormalization procedure is to notice that modes \hat{x}_{out} and \hat{x}_{in} are evaluated on the same input state while modes $\hat{x}_2^{(0)}$ and \hat{y} are evaluated on two independent vacuum states introduced for the ease of use of the Heisenberg picture. This point is made subtle by the fact that the Heisenberg notation used in Eqs.(4.1.24) are not exactly rigorous but should actually include beam-splitter like operators $\hat{B}_1, \hat{B}_2, \dots$ for the precise introduction of the auxiliary modes \hat{x}_{out} and \hat{x}_{in} . To the contrary, the same procedure conducted in the Schrödinger picture while cumbersome would yield unambiguously to Eq.(4.1.27).

With the assumptions of the presence of an uncorrelated Gaussian noise term N uniformly spread over both quadratures \hat{x}_{out} and \hat{x}_{in} , we see that it is impossible to distinguish the thermalization induced by on the one hand a finite amount of EPR correlation parameter $r \neq \infty$ and on the other hand by a non-zero amount of noise $\mathcal{N} \neq 0$. We notice that if the amount of noise \mathcal{N} is

high, it is possible that r' becomes negative (see Fig.4.5), which simply means that after factoring in the effect of \mathcal{N} , quantum teleportation would perform worse than classical teleportation with $r = 0$ and $\mathcal{N} = 0$. When estimating the true experimental value of r , this effect needs to be taken into account. Especially if $\mathcal{N} \neq 0$, an estimation of r based on teleportation results cannot agree with an estimation of r based on the direct measurement of EPR correlations.

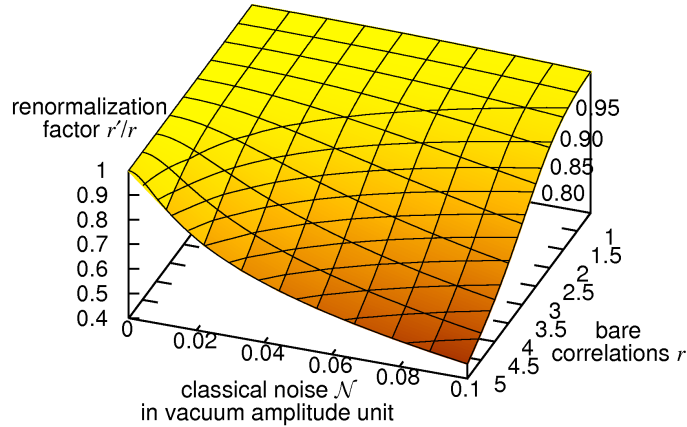


Figure 4.5: Influence of the noise amplitude \mathcal{N} on the ratio of r' and r .

Master equation

We now justify an interpretation of the teleportation mechanism as a differential equation. We look for a master equation describing the effect of teleportation on the density matrix $\hat{\rho}$ and follow a methodology similar to the one shown in Sec.1.3.4. We start by fully detailing Eq. (4.1.1) with input W and output W' :

$$W'(x, p) = \frac{1}{2\pi\sigma^2} \int \int dx' dp' W(x', p') e^{-\frac{(x-x')^2+(p-p')^2}{2\sigma^2}}. \quad (4.1.30)$$

We now assume that $\sigma \rightarrow \sigma(t)$ has a time dependence. We express the first derivative of W' with respect to time t ,

$$\begin{aligned} \frac{d}{dt} W'(x, p) &= \frac{1}{2\sigma(t)} \left(4 \frac{d}{dt} \sigma(t) - W'(x, p) \right. \\ &\quad \left. + \int \int dx' dp' W(x', p') ((x-x')^2 + (p-p')^2) G_{\sigma(t)}(x-x', p-p') \right) \end{aligned} \quad (4.1.31)$$

and the second derivative of W' with respect to position x

$$\partial_x^2 W'(x, p) = -\frac{1}{\sigma^2} W'(x, p) + \frac{1}{\sigma^4} \int \int \frac{dx' dp'}{2\pi\sigma^2} (x-x')^2 W(x', p') e^{-\frac{(x-x')^2+(p-p')^2}{2\sigma^2}}. \quad (4.1.32)$$

Combining Eqs.(4.1.31) and (4.1.32) we find the following differential equation for $W'_{(x,p;t)}$,

$$\frac{d}{dt} W'(x, p; t) = \frac{1}{2} (\partial_t \sigma^2(t)) \Delta W'(x, p; t), \quad (4.1.33)$$

where $\Delta = \partial_x^2 + \partial_p^2$. We choose σ to be $\sigma(t) = \sqrt{2\kappa't}$ with κ' a constant decay rate, so that Eq. (4.1.33) simplifies itself to a pure diffusion equation,

$$\frac{d}{dt} W'(x, p; t) = \kappa' \Delta W'(x, p; t). \quad (4.1.34)$$

Then, by using correspondence rules between the phase space formalism and the density matrix formalism[84], we find from Eq. (4.1.34) the following master equation for $\hat{\rho}$:

$$\frac{d}{dt}\hat{\rho} = \kappa' \left(2\hat{a}^\dagger \hat{\rho} \hat{a} + 2\hat{a} \hat{\rho} \hat{a}^\dagger - \hat{a}^\dagger \hat{a} \hat{\rho} - \hat{a} \hat{\rho} \hat{a}^\dagger - \hat{\rho} \hat{a}^\dagger \hat{a} - \hat{\rho} \hat{a} \hat{a}^\dagger \right), \quad (4.1.35)$$

which can be equivalently written as

$$\frac{d}{dt}\hat{\rho} = L[\hat{\rho}], \quad L[\hat{\rho}] = \kappa'[\hat{a}^\dagger, [\hat{\rho}, \hat{a}]] + \kappa'[\hat{a}, [\hat{\rho}, \hat{a}^\dagger]]. \quad (4.1.36)$$

The master equation (4.1.35) is the well-known damping process for the harmonic oscillator.

4.1.5 Wave packet teleportation

In contrast to the many quantum teleportation experiments conducted to date for narrow sidebands of light, our setup operates over a wide frequency bandwidth as required by the nature of our input state. Since its generation relies on the detection of a single photon and the induced projection, a Schroedinger's cat state made via photon-subtraction is a short wave-packet of light. A phenomenological picture to think about these wave-packets is to consider them as the closed boxes containing the macroscopic superposition states as in the original idea of Schroedinger. This requires Alice and Bob to teleport every frequency component of these “box-like” wave-packets for faithful teleportation to occur. In this way, Alice and Bob do not need to actually teleport the Schroedinger's cat states directly but merely the potential boxes containing them. Consequently Alice and Bob do not need to know when a detection event occurs but rather are only concerned with continuous and faithful “box” wave-packet teleportation, whichever state lies in the box. As a matter of fact Alice and Bob actually teleport most of the time a squeezed vacuum state $\hat{S}(s)|0\rangle$. In essence our teleporter is a time-resolved apparatus that deconstructs the input wave-packets into a stream of infinitely small time bins and reconstructs them at the output, within the extent of what we refer to as the teleportation bandwidth.

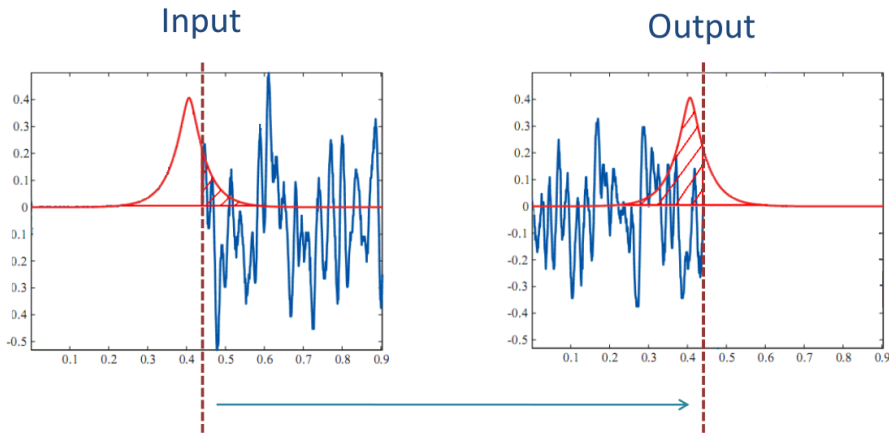


Figure 4.6: Illustration of the teleportation of wave-packets in successive time slices.

The aim of this section is to identify the effect of this teleportation bandwidth on the monomode expression of teleportation, in Eq(4.1.41) for the Heisenberg picture and in Eq(4.1.16) for the Wigner formalism. To our knowledge, there are actually very few results relevant to the case of multimode teleportation. In [153], multimode teleportation of a quantum field is investigated from the point of view of temporal fluctuations using the photon correlations function $g^{(2)}(\tau)$. In [59],

it is shown how to adapt the single-mode teleportation protocol of [49] to teleportation of a multi-mode field with finite teleportation bandwidth. Both these works attack the problem of multi-mode teleportation from the Heisenberg picture and additional considerations are required to handle the case of non-Gaussian nonclassical input states.

Which wave-packet mode ?

The APD triggered non-Gaussian state has been shown in Chap.2 to have complex multimode properties. On one hand, the OPO output beam is a continuous wave with a specific squeezing spectrum, while, on the other hand, the APD triggers that herald a non-Gaussian state happen at precisely defined times. Intuitively one expects that a given APD trigger induces non-Gaussian statistics in the immediate time vicinity of the trigger event to the extent of the OPO bandwidth. When the number of triggering events increases as R and s increase and more photons end up in the trigger channel, more complex time interference phenomena arise on the signal mode between neighboring photon subtracted wave packets[121]. Fortunately, in the specific regime of our experiment and in the limit of small s and small R , a simple two modes picture allows one to efficiently describe the input state and capture most of its experimental properties [97]. It involves two effective wave-packet modes, \hat{A}_{sig} for the signal mode and \hat{A}_{trig} for the trigger mode, defined by

$$\hat{A}_i = \int f_i(\omega) \hat{a}_\omega d\omega, \quad (4.1.37)$$

with $i \in \{\text{sig}, \text{trig}\}$. Preserving the commutators $[\hat{A}_i, \hat{A}_i^\dagger] = 1$ requires $\int |f_i(\omega)|^2 d\omega = 1$. While the exact form of $f_{\text{trig}}(\omega)$ is not really relevant, since the APD detection time is typically much shorter than any other time scale in these continuous wave experiments, $f_{\text{sig}}(\omega)$ will describe the temporal characteristic of the heralded non-Gaussian state. This function will be defined by the OPO bandwidth, as well as the possible filtering cavities used on the trigger channel (see Secs.2.2 and 2.3). In our case, for small s and R and wide filtering cavities, it can be taken as

$$f_{\text{sig}}(\omega) = \gamma/\pi[\gamma^2 + (\omega_0 - \omega)^2], \quad (4.1.38)$$

with γ the OPO decay rate including intra-cavity losses and ω_0 the light beam carrier frequency. In short, an APD heralded state behaves as a traveling wave packet of light with non-Gaussian characteristics. Using the definition of \hat{A}_{sig} in Eq. (4.1.37), we use a pure monomode model for the input state that we write as

$$|\psi\rangle = e^{-s(\hat{A}^{\dagger 2} - \hat{A}^2)/2} \hat{A}^\dagger |0\rangle. \quad (4.1.39)$$

As we recall, this expression is still an approximation of reality in the sense that a true multimode description would require an extension of the broadband squeezing operator \hat{S}_ζ on a basis of adequately chosen orthogonal functions $\{\phi_n(\omega)\}$. In practice, once a signal mode $f_{\text{sig}} = \phi_0$ is chosen, the other modes $n \neq 0$ are traced out, which leads to mixing of the density matrix to the extent of the multimode entanglement present in \hat{S}_B between all modes n :

$$\hat{\rho}_B = \text{tr}_{n \neq 0} \left(\hat{A}_0 \hat{S}_\zeta |0\rangle \langle 0| \hat{S}_\zeta^\dagger \hat{A}_0^\dagger \right). \quad (4.1.40)$$

In the general case of a non constant function ζ , the expression (4.1.39) is nevertheless useful as it only neglects a small amount of entanglement between the different orthogonal modes n if s is small. As a result, we will use expressions (4.1.37) and (4.1.39) for our following analysis of multimode teleportation.

Multimode Heisenberg picture

To investigate how this multimode aspect translates quantitatively, we start with the unity gain regime in the Heisenberg picture. From Eqs.(4.1.41) and (4.1.42) we notice that the input modes $(\hat{x}_{\text{in}}, \hat{p}_{\text{in}})$ and output modes $(\hat{x}_{\text{out}}, \hat{p}_{\text{out}})$ can actually represent any frequency mode ω . We therefore rewrite the input to output modes relationship as

$$\hat{x}_{\text{out}}(\omega) = \hat{x}_{\text{in}}(\omega) - \sqrt{2}e^{-r(\omega)}\hat{x}_2^{(0)}(\omega), \quad (4.1.41)$$

$$\hat{p}_{\text{out}}(\omega) = \hat{p}_{\text{in}}(\omega) + \sqrt{2}e^{-r(\omega)}\hat{p}_1^{(0)}(\omega). \quad (4.1.42)$$

where we have introduced $r(\omega)$ the spectrum of EPR correlations resolved in frequency. We define in the same way as in Eq. (4.1.37) two new modes, the input \hat{A}_{in} and output \hat{A}_{out} wave-packet modes by

$$\hat{A}_{\text{in}} = \int f_{\text{sig}}(\omega)\hat{a}_{\text{in}}(\omega)d\omega, \quad \hat{A}_{\text{out}} = \int f_{\text{sig}}(\omega)\hat{a}_{\text{out}}(\omega)d\omega. \quad (4.1.43)$$

as well as the input and output wave-packet quadratures $(\hat{X}_{\text{in}}, \hat{P}_{\text{in}})$ and $(\hat{X}_{\text{out}}, \hat{P}_{\text{out}})$ relevant for wave-packet teleportation. We can directly rewrite the teleportation input/output relationships (4.1.41) and (4.1.42) in the form

$$\hat{X}_{\text{out}} = \hat{X}_{\text{in}} - \sqrt{2} \int f_{\text{sig}}(\omega)e^{-r(\omega)}\hat{x}_2^{(0)}(\omega)d\omega, \quad (4.1.44)$$

$$\hat{P}_{\text{out}} = \hat{P}_{\text{in}} + \sqrt{2} \int f_{\text{sig}}(\omega)e^{-r(\omega)}\hat{p}_1^{(0)}(\omega)d\omega. \quad (4.1.45)$$

It is important to notice that modes $\hat{x}_2^{(0)}(\omega)$ and $\hat{p}_1^{(0)}(\omega)$ are the input modes of the EPR OPOs and are therefore in the vacuum state over all frequencies ω .

Parameter renormalization

From the physical properties of the OPO cavities used for EPR squeezing generation it is possible to deduce the expression of $r(\omega)$ from the squeezing spectrum $S_-(\omega) = \langle \Delta^2 \hat{x}_{\text{sqd}}^\dagger(\omega) \Delta^2 \hat{x}_{\text{sqd}}(\omega) \rangle / \langle \Delta^2 \hat{x}_{\text{vac}} \rangle$. See, for example, Ref. [59] for details. We now define an effective broadband EPR parameter r_{eff} by

$$e^{-r_{\text{eff}}} = \int f_s(\omega)e^{-r(\omega)}d\omega = \int f_s(\omega)S_-(\omega)d\omega, \quad (4.1.46)$$

and therefore Eqs.(4.1.44) and (4.1.45) simplify themselves to

$$\hat{X}_{\text{out}} = \hat{X}_{\text{in}} - \sqrt{2}e^{-r_{\text{eff}}}\hat{x}_2^{(0)}(\omega), \quad \hat{P}_{\text{out}} = \hat{P}_{\text{in}} + \sqrt{2}e^{-r_{\text{eff}}}\hat{p}_1^{(0)}(\omega). \quad (4.1.47)$$

Since the auxiliary modes $\hat{x}_2^{(0)}(\omega)$ and $\hat{p}_1^{(0)}(\omega)$ are effectively traced out on the vacuum state at all frequencies and yields the same shotnoise amplitude, it is possible to take them outside of the frequency domain integrals to obtain the formulation (4.1.47). We notice that Eqs. (4.1.47) are written in the same way as Eqs. (4.1.12). Thanks to the linearity of transformation (4.1.12) and the linear model of input state (4.1.37) in the Heisenberg picture, multimode teleportation is equivalent to familiar single-mode teleportation, where an effective broadband EPR parameter r_{eff} has been defined to take into account the finite bandwidth of entanglement. In short, all the previous formulas of Sec.4.1.2 for unity-gain teleportation are readily usable with the simple change $r \rightarrow r_{\text{eff}}$ to account for the wave-packet regime.

We notice that in Eq.4.1.46 the renormalization procedure is made in amplitude, in contrast to Eq.4.1.27 where the renormalization procedure was in power. To understand this difference it is necessary to look at the precise multimode nature of broadband teleportation: to the contrary of

Eqs.(4.1.24) where there is only one input mode and one output mode, in the multimode teleportation equations (4.1.41) and (4.1.42), there are infinitely many independent input modes $\hat{x}_{\text{in}}(\omega)$ for every different frequencies ω and infinitely many independent output modes $\hat{x}_{\text{out}}(\omega)$. Therefore broadband teleportation is nothing else than many independent teleportation processes happening in parallel, while in the situation of Sec.4.1.4 we had to consider two series teleportation processes on the same mode. In short, the amplitude renormalization of Eq.4.1.46 is a natural consequence of the convenient way we have chosen to look at broadband teleportation from the point of view of the single effective wave-packet mode \hat{A}_0 defined with $f_{\text{sig}}(t)$. Once again, this difference is made ambiguous by the simplification implicitly introduced by the Heisenberg picture but in the Schrödinger picture this ambiguity would be immediately solved.

With regards to this discussion, it is also interesting to ask ourselves what would be changed if the wave-packet mode approximation of Eq.(4.1.39) had stop to be valid and if we had to consider a non-factorizable broadband squeezing operator \hat{S}_ζ . Actually thanks again to the independence of teleportation over the different frequency modes ω it turns out that for the analysis of teleportation nothing change with non-zero frequency entanglement in the input state. Stated another way, the fact that the input state features entanglement between its frequency components is transparent to the broadband teleporter apparatus because all frequency modes are teleported independently. In short with such entanglement in the input state the teleporter actually achieves massive entanglement swapping over the full teleportation bandwidth between every frequency components. If we would express this process using the wave-packet basis $\{\phi_n(\omega)\}_n$ this would again be valid. In practice if we have chosen in the first place to measure the input state as a single mode state and we have chosen to ignore the entanglement between frequency components of the input state, then this hypothesis is still valid for the output state whether entanglement swapping between higher order wave-packet modes happens or not in the broadband teleportation. To obtain an estimation of how well this entanglement swapping is performed, it is possible to define higher order effective EPR correlation parameters $r_{\text{eff}}^1, r_{\text{eff}}^2, \dots$ for the higher order wave-packet modes $\phi_1(\omega), \phi_2(\omega), \dots$ used in the decomposition of \hat{S}_ζ . This can be done by following the renormalization procedure of Eq.4.1.46 replacing $f_s(\omega)$ by the corresponding wave-packet mode function. With these higher effective EPR correlation parameters it is then possible to express how the full multimode composite input mode density matrix would be affected by broadband teleportation in the context of entanglement between frequencies or between wave-packet modes, that is in the context of a non block-diagonal input mode density matrix.

Non-unity gain regime

The case of non-unity gain multimode teleportation is much more complex and we conclude this section with a brief overview of the non-unity gain case. First we introduce the transfer functions $g_x(\omega)$ and $g_p(\omega)$, which represent the effects in the frequency domain of the classical channel. g_x and g_p are in general complex-valued functions verifying the Kramers-Kronig relations. We are now facing the problem that the output quadratures operators of teleportation will not be Hermitian operators anymore, in general. By taking an approach similar to Eq. (4.1.44), we obtain for the position quadrature

$$\begin{aligned} \hat{X}_{\text{out}}^{\text{nonunit}} &= \int f_s(\omega) g_x(\omega) \hat{x}_{\text{in}}(\omega) d\omega \\ &\quad - \frac{1}{\sqrt{2}} \left(e^{-r_{\text{eff}}} + \int f_s(\omega) g_x(\omega) e^{-r(\omega)} d\omega \right) \hat{x}_2^{(0)}(\omega) \\ &\quad + \frac{1}{\sqrt{2}} \left(e^{+r_{\text{eff}}} - \int f_s(\omega) g_x(\omega) e^{+r(\omega)} d\omega \right) \hat{x}_1^{(0)}(\omega). \end{aligned} \quad (4.1.48)$$

where $\hat{X}_{\text{out}}^{\text{nonunit}}$ is the output teleported mode in the non-unity gain regime. To simplify this expression we define the two complex numbers g_x^\pm :

$$g_x^\pm = \int f_s(\omega) g_x(\omega) e^{\pm(r(\omega)-r_{\text{eff}})} d\omega, \quad (4.1.49)$$

so that Eq. (4.1.48) also reads

$$\hat{X}_{\text{out}}^{\text{nonunit}} = \int f_s(\omega) g_x(\omega) \hat{x}_{\text{in}}(\omega) d\omega - \frac{1+g_x^-}{\sqrt{2}} e^{-r_{\text{eff}}} \hat{x}_2^{(0)}(\omega) + \frac{1-g_x^+}{\sqrt{2}} e^{+r_{\text{eff}}} \hat{x}_1^{(0)}(\omega), \quad (4.1.50)$$

with a similar expression for $\hat{P}_{\text{out}}^{\text{nonunit}}$. By further separating $\hat{X}_{\text{out}}^{\text{nonunit}}$ and $\hat{P}_{\text{out}}^{\text{nonunit}}$ in real and imaginary parts as done in [59], it is possible to obtain from this model observable results. Equations (4.1.50) and (4.1.49) show that the output modes will get contaminated by antisqueezing when $|g_x(\omega)|$ and $|g_p(\omega)|$ are different from 1. Furthermore, the expression $\int f_s(\omega) g_x(\omega) \hat{x}_{\text{in}}(\omega) d\omega$ hints that the wave-packet shape from input to output will get modified by the teleportation process. An interesting and practical situation is the case of pure linear delay $g_x(\omega) = g_p(\omega) = \exp[-i\omega \Delta t]$. If such a phase factor is added by the classical channel to the output modes, its full effect can be absorbed in \hat{x}_{in} and auxiliary modes \hat{v}_x, \hat{w}_x by using their Fourier transforms,

$$\hat{x}_{\text{in}}(\omega) \rightarrow \hat{x}_{\text{in}}(\omega) e^{-i\omega \Delta t} = \frac{1}{\sqrt{2\pi}} \int dt \hat{x}_{\text{in}}(t) e^{i\omega(t-\Delta t)},$$

so that $\hat{X}_{\text{out}}^{\text{nonunit}}$ is related to \hat{X}_{out} by a simple time translation

$$\hat{X}_{\text{out}}^{\text{nonunit}}(t) = \hat{X}_{\text{out}}(t + \Delta t). \quad (4.1.51)$$

As a matter of fact, this is exactly how the experimental teleportation setup used in [167] behaves, where an optical delay line is used to match the phase answer of the classical channel and cancel this Δt phase factor.

Effects of broadband noise spectrum

This multimode model of teleportation allows us to consider the case of broadband noise when $\mathcal{N} \rightarrow \mathcal{N}(\omega)$ contaminates the whole frequency range relevant for teleportation. In the same way that we had deduced Eqs.(4.1.47) from Eqs.(4.1.41) using the wave-packet operator (4.1.37), we define an effective noise level $\mathcal{N}_{\text{eff}} = \int f_s(\omega) \mathcal{N}(\omega) d\omega$ and write

$$\begin{aligned} \hat{X}_{\text{out}} &= \hat{X}_{\text{in}} - \sqrt{2} e^{-r_{\text{eff}}} \hat{v}_x - \sqrt{2} \mathcal{N}_{\text{eff}} \hat{y}_n, \\ \hat{P}_{\text{out}} &= \hat{P}_{\text{in}} + \sqrt{2} e^{-r_{\text{eff}}} \hat{w}_p + \sqrt{2} \mathcal{N}_{\text{eff}} \hat{z}_n, \end{aligned} \quad (4.1.52)$$

so that finally it is possible to take into account the effect of $\mathcal{N}(\omega)$ by redefining r_{eff} as in Eq.(4.1.29):

$$r_{\text{eff}} \rightarrow r'_{\text{eff}} = r_{\text{eff}} - \ln \sqrt{1 + \mathcal{N}_{\text{eff}}^2 e^{2r_{\text{eff}}}}. \quad (4.1.53)$$

A typical noise spectrum $\mathcal{N}(\omega)$ found experimentally would be through the leakage in the output teleported mode $(\hat{x}_{\text{out}}, \hat{p}_{\text{out}})$ of a sideband modulation signal used for example in phase locking feedback loops.

4.2 Experimental setup and results

Quantum teleportation was experimentally demonstrated for the first time in the qubit regime by Zeilinger *et al.*[42]. However, without possible measurement of the complete Bell's states basis, it could be argued that this demonstration was only partial. In the qubit regime, the difficulty of achieving complete Bell's states measurement is still a problem nowadays, and it is generally agreed upon that it is not possible to do so without delicate non-linear optics components. The first unconditional teleportation experiment was reported in [51] and performed in the continuous variable regime. It followed the Braunstein Kimble protocol presented in Sec.4.1 where the teleportation operation succeeds unconditionally of the input state. The price to pay for unconditional operations is the degradation of the output teleported state which is thermalized by the imperfect teleportation apparatus and finite amount of EPR correlations. In the original experiment reported in [51], a Gaussian fidelity of $F = 0.58$ was observed. From this first step, fidelities of $F = 0.61$ [80] and $F = 0.64$ [76] were later reported with similar continuous variable setups. [93] was the first report of a continuous variable teleportation with a fidelity above the no-cloning limit $2/3$. This experiment was then soon extended to the teleportation of a squeezed vacuum state with observation of an output state showing sub-Poisson photon statistics[92]. In [129], sequential chained teleportation of a coherent states was reported, and later in [128], parallel multimode teleportation of a squeezed vacuum state over a broad range of frequencies. More recently with the availability of higher squeezing resources [103, 126], very high level of fidelity could be obtained in the sideband continuous variable regime[147].

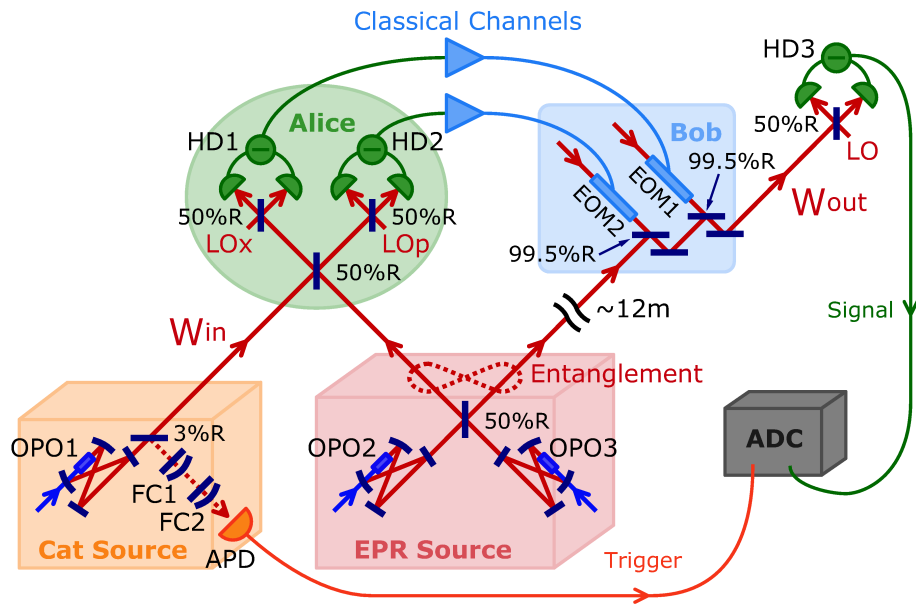


Figure 4.7: Overview of the experimental setup for broadband teleportation, showing the setup for generation of the non-Gaussian non-classical input state.

The step by step improvements achieved in these different teleportation experiments eventually allowed for the first successful and unconditional teleportation experiment with a non-Gaussian non-classical input state[167]. As we have explained before, the currently available experimental techniques used to produce non-Gaussian states force such an experiment to be performed outside of the sideband regime. Furthermore, to stay in the non-classical regime, non-Gaussian non-classical input states would have to be teleported with the recently achieved high fidelities to allow

for observation of non-classical features of the Wigner function at the output of the teleporter, for instance negativity. For breaking at the same time all these limitations, the experiment reported in [167] is indeed quite a step forward in the field on continuous variable information processing. It is one recent example, among other quantum mechanics experiments with different physical setups and different systems, that quantum information processing has recently achieved goals which were still thought absolutely out of reach even a few years ago. This section further focuses on the experimental setup of [167] and presents in more details experimental results shown in Secs.4.2.2 and 4.2.3. In addition, we apply the theoretical models of Sec.4.1 to analyse these experimental results in Sec.4.2.4.

4.2.1 Experimental setup

In general, our experimental setup is similar to the setups described in [147] and [167]. An overview of the teleportation setup is shown in Fig4.7 while details are available in Fig4.8. Appendix D contains a full schematic of the experimental table and of the optical setup, which includes the quantum teleportation setup. The teleporter apparatus itself is a direct implementation of the Braunstein-Kimble protocol and closely follows the setup of [147]. To make this former teleportation setup compatible with the wave-packet input state and to adapt it to run in the broadband regime, a number of careful additions are necessary. First, the teleportation setup is made compatible with the probe switching mechanisms presented in Sec.2.4.3 and necessary for phase feedback control. Additional digital circuitry are added in the different analogical feedback circuits so that the feedback loops are momentarily stopped when performing tomographic measurements. Also, the classical channels signals are turned on only in the measurement phase, and turned off in the control phase. To obtain the high enough fidelity that allows the teleportation of non-classical features of the Wigner function, the bandwidth requirements are stiff and needs to be met without failure. On one half of the teleporter, this implies wide enough bandwidth of squeezing for the two OPOs used in the generation of the EPR resource. On the other half of the teleporter, this implies high enough electronic bandwidth in Alice's homodyne detectors and in the classical channel.

EPR correlation generation and distribution

The 2-modes EPR entanglement resource is made with two type-I OPOs and one half beam-splitter. Both OPO2 and 3 are built with bow-tie cavities and PPKTP crystals. Compared to the bandwidth of OPO1 used for the generation of Schrödinger's cat states, OPOs with broader bandwidth are used for the EPR entanglement source. The output couplers of both OPOs have an intensity transmission coefficient of 15%. In addition the geometry of both cavities are smaller, with a cavity round-trip length of 30 mm only. For both OPOs, FWHM is 24 MHz and finesse is 41. For squeezed light generation, pump beam powers are 110 mW and 120 mW for OPO2 and 3 respectively. The different pump beam powers are a consequence of crystal individualities and different non-linear coefficients. Intra-cavity losses with pump beam injected are respectively 0.0035 and 0.0037. Pump beam powers are adjusted for optimal measurable squeezing purity.

To generate a stable 2-modes EPR state, five feedback loops are necessary for the control of the relative phases of the different light beams. Both cavities are controlled in length with two feedback circuits based on the Pound-Drever-Hall technique for resonance with the laser light[21]. Instead of using the probe beam, an auxiliary lock beam is injected inside the OPO in the counter-propagating mode and fully measured on the output mode. To minimize the effect of reflections, the lock beam is put in the TEM01 spatial mode. To compensate for the TEM01 frequency shift, the lock beam is first frequency shifted with AOMs. For OPOs 2 and 3, this frequency shift is achieved with a double pass AOM and then a single pass AOM for each lock beams. Once the cavity is at resonance, the 430nm pump beam is stabilized in phase by monitoring the parametric

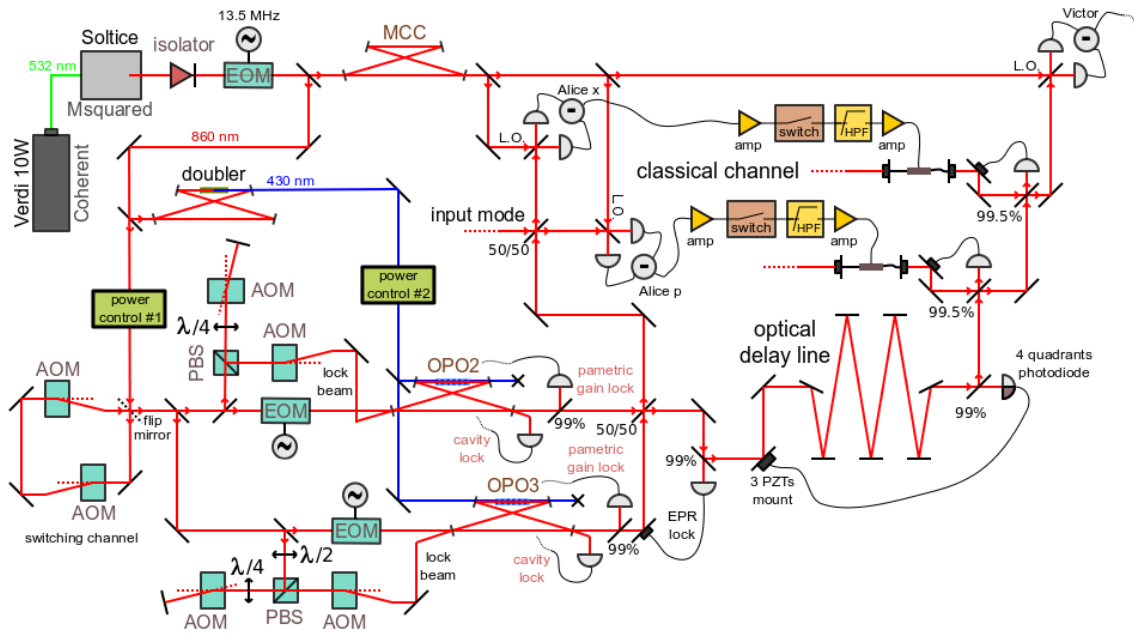


Figure 4.8: Details of the experimental setup for broadband teleportation, not showing the setup for generation of the non-Gaussian non-classical input state.

desamplification of the 860nm probe beam. More precisely, a phase modulated sideband on the probe beam is measured by a photodiode and a demodulation mixer circuit. The electrical signal after demodulation is proportional to the sideband intensity, which is minimal when the relative phase between the probe and pump beams allows for parametric desamplification of the probe beam. The feedback circuit then controls the phase of the pump beam with a PZT to stabilize the modulated sideband at minimum intensity. Finally, the two OPOs output beams are locked out of phase with a DC lock circuit. 1% of one of the two output modes after the beam-splitter is picked up and measured with a photodiode to generate an error signal and drive a PZT placed before the beam-splitter.

Classical channel

The classical channel consists of the electrical circuit used by Alice to send her measurement results to Bob, in addition with the phase modulation setup used by Bob to displace his entangled mode and produce the output teleported state. The electrical circuit contains a chain of amplifiers and filters, with an electrical switch in the middle to halt the displacement of the output state outside of the measurement phase. There are two channels for the two joint homodyne measurements of Alice. For teleportation to work on a broadband range of frequencies, every electronic stage in the classical channel needs a flat gain band as well as a linear phase delay. Only in that case will classical information received by Bob from Alice match in time and in magnitude the EPR correlations shared between them at every frequency. A nonlinear phase delay across the teleportation bandwidth would distort the wave-packet shape while a non-flat gain would result in excess noise at specific frequencies. This virtually forbids to use any complex analogical filters others than first or second order Bessel filters.

Bob performs his displacement operation by mixing two auxiliary coherent beams with his EPR beam on two 99.5/0.5 beam splitters to preserve strong quantum correlations. Each auxiliary beam is phase modulated according to Alice's results for the \hat{x} and \hat{p} quadratures. In our

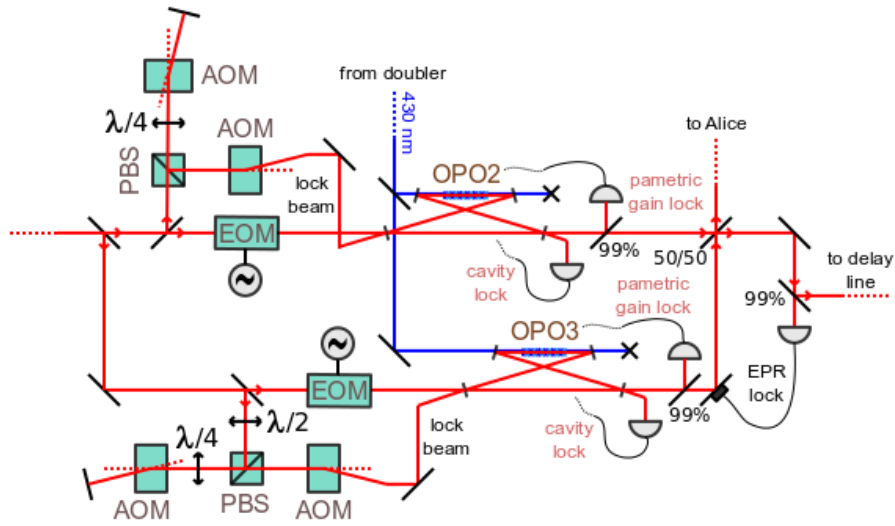


Figure 4.9: Experimental setup for the generation of a 2-mode EPR state.

wave-packet regime, using free space electro-optical modulators (EOMs) for phase modulation is virtually impossible. These modulators need a driving voltage in the range of 10V, and have a typical capacitance of 100nF. Over a 10MHz bandwidth, this requires 100 Watts of amplification with the additional requirement of a flat gain. To accommodate with the DC-10 MHz bandwidth of teleportation, we use instead for modulation of these auxiliary beams optical waveguide phase modulators based on Mach-Zehnder interferometers with a precise $50\ \Omega$ input impedance that allows for easy broadband operations. The disadvantage of such waveguide modulators is their natural tendency to easily pick-up any external noise and vibrations in the acoustic band. This introduce additional noise in the low frequency band.

Optical delay line

With the propagation delays of the different electrical amplification stages in the classical channel, the total delay induced is far from negligible. To compensate for the delay of this slower electrical classical channel, the optical path length of Bob's EPR beam is set at 12 m which allows synchronized overlap between classical information and EPR correlations owned by Bob at the output of the teleporter, both detrimental to the quality of teleportation. Due to its size, this optical delay line introduces significant spatial drifts on the output beam over time. Even with a good temperature control of the laboratory, the pointing stability of the output beam is typically shorter than one hour. To compensate for these drifts, we use a low frequency feedback loop made of a four-quadrant photodiode detector, an integrator circuit and a piezo-mounted mirror. The four-quadrant photodiode is wired to obtain the vertical and horizontal light intensity ratio on the photodiode. These two ratios are directly used as error signals in the feedback loop to control the angles of a mirror mounted on three PZTs. More details about this control system can be found in [166].

Setup calibration

The teleportation experiment is always run in the unity gain regime. For this to be true we need to calibrate the classical channel delay and amplification at every frequency of the teleportation bandwidth. In practice this is not possible with analogical circuitry and we only calibrate both channels at 2 MHz for amplitude and at 5 MHz for delay. Delays are simply adjusted with cables

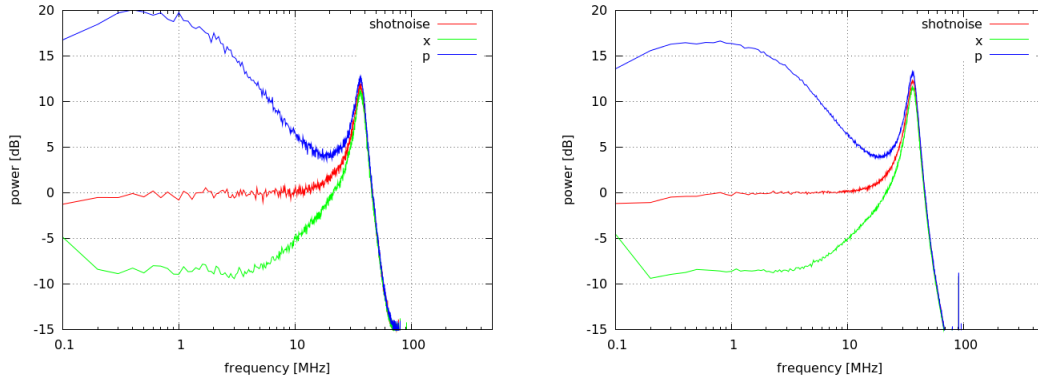


Figure 4.10: Experimental squeezing and antisqueezing power traces for OPOs 2 and 3. To measure these traces, the output modes from OPOs 2 and 3 were directly sent to an homodyne detector by replacing or removing the 50/50 beam-splitter mixing the 2 OPOs output modes and the 50/50 beam-splitter mixing Alice's entangled mode with the input state mode. With the DPO7000 oscilloscope (see Appendix B for details), direct records of the homodyne current are taken at a sampling rate of 1 GHz and then analysed with a Fourier transform to obtain the homodyne current power spectrum. The shotnoise of the vacuum state is first recorded and then used to calibrate the squeezed and antisqueezed quadratures measured afterwards. Left traces, OPO 2 output. Right traces, OPO 3 output. A 11KHz high-pass electrical filter is the cause of the attenuation of traces around DC. The resonance pic at 35MHz is an oscillation internal to the homodyne detector circuits (see [166] for details). Above 100 MHz, narrow resonance pics caused by aliasing and other digital artifacts are visible.

of different length added directly into the electrical chain. Amplitudes are adjusted with variable attenuators, in 0.1 dB steps.

The method for unity gain calibration is similar to the one reported in [147]. First, a sideband modulation is applied at either 2 or 5 MHz on one of the OPOs 2 and 3 probe beams. The sideband propagates to Alice's detectors and is measured and carried in the classical channel. It also propagates to Bob's displacement section and is displaced there. Then the third verification homodyne detectors is used to look at the sideband correction. For the unity gain regime to be achieved, the sideband needs to be completely cancelled by Bob, which can be monitored with a spectrum analyser. This allows to easily adjust the delay and the gain of the classical channels.

Experimental protocol

The general experimental protocol for the broadband teleportation of a photon subtracted squeezed vacuum state follows this order:

- Pre-alignment: all auxiliary locking beams and probe beams, OPOs pumping beams.
- Triggering channel: alignment and mode-matching between filtering cavities and the probe beam, alignment of the APD fiber coupler, confirmation of the dark count rate and total event count rate.
- Alice homodyne detectors: alignment of the visibility.
- Calibration of the classical channel.
- Final alignment of the OPO pumping beam and locking of the system.

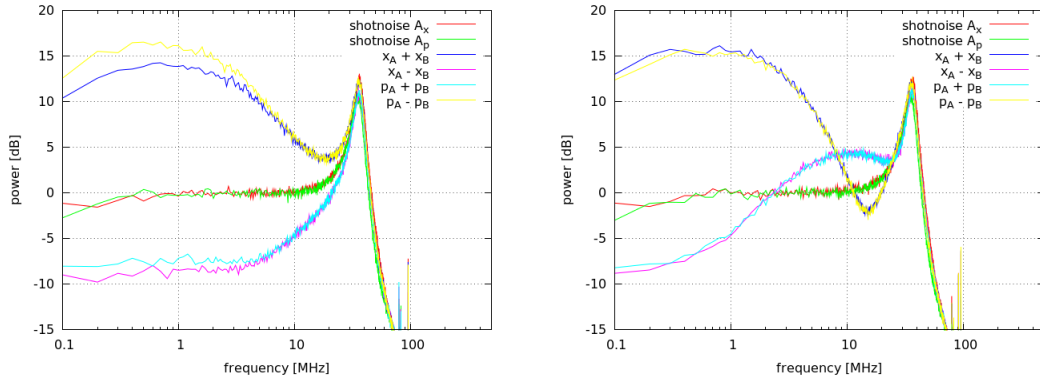


Figure 4.11: Experimental EPR correlation traces. To measure these traces, both output modes of the 50/50 beam-splitter mixing OPOs 2 and 3 output mode are directly and simultaneously measured with two homodyne detectors. To observe the EPR correlations it is necessary to look at the power spectrum of $\hat{x}_A - \hat{x}_B$ and $\hat{p}_A + \hat{p}_B$ at the same time. To calibrate this time reference, the auto-correlation function of $\int \langle (\hat{x}_A(t)\hat{x}_B(t - \Delta t))^2 \rangle dt$ of $\langle \hat{x}_A(t) - \hat{x}_B(t + \Delta t) \rangle$ is plotted first. The value of Δt for which the auto-correlation function is the minimum is the time reference of mode B relative to mode A . Once Δt is known, the EPR correlation and anticorrelation traces are obtained with the Fourier transforms of $\langle \hat{x}_A(t) - \hat{x}_B(t + \Delta t) \rangle$, $\langle \hat{p}_A(t) + \hat{p}_B(t + \Delta t) \rangle$ for correlations and $\langle \hat{x}_A(t) + \hat{x}_B(t + \Delta t) \rangle$, $\langle \hat{p}_A(t) - \hat{p}_B(t + \Delta t) \rangle$ for anticorrelations. If the time reference Δt is not well calibrated, the traces oscillate in the frequency domain according to how much phase shift does Δt translates into for every frequency value. The calibration of both homodyne detectors used to record modes A and B are done in the same way as when measuring OPO squeezing and antisqueezing (see Fig. 4.10). Left traces, correctly time calibrated EPR experimental traces. Right traces, incorrectly time calibrated EPR experimental traces. A 11KHz high-pass electrical filter is the cause of the attenuation of traces around DC. The resonance pic at 35MHz is an oscillation internal to the homodyne detector circuits (see [166] for details). Above 100 MHz, narrow resonance pics caused by aliasing and other digital artifacts are visible.

- Output homodyne detector: alignment of the visibility.
- Phase locking of the system.
- Pre-calibration of the time reference, confirmation of the presence of the heralded squeezed photon state with measure of $\langle U^2 \rangle(t)$.
- Tomography and measurement of the output Wigner function, with calibration of the shot-noise level before and after.

In the Braunstein-Kimble protocol, the teleportation happens theoretically in three steps. It is important to notice that in the continuous wave regime, this separation is virtually nonexistent. In practice, Alice never stops to do joint homodyne measurements, the classical channel never stops to send these results to Bob, and Bob never stops to apply a displacement operation to his output state. In other words the teleportation is therefore happening for every instant time which are as short as the teleportation bandwidth is large. Once the three OPOs are fed with blue light and once the different beams are phase controlled and locked together, the teleportation starts and quantum tomography of the output teleported mode can be performed.

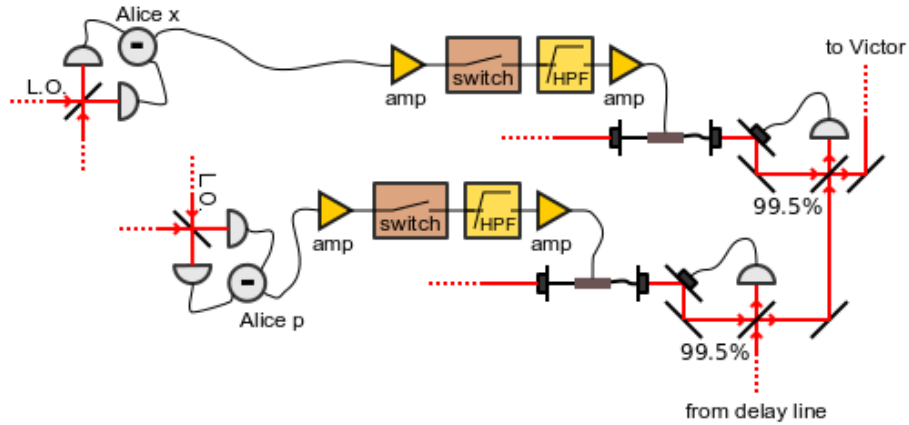


Figure 4.12: Classical channel experimental setup.

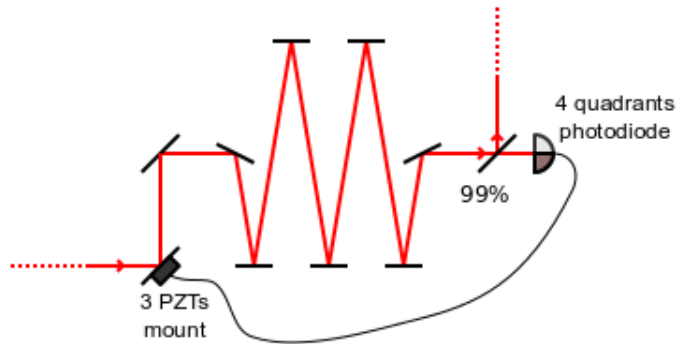
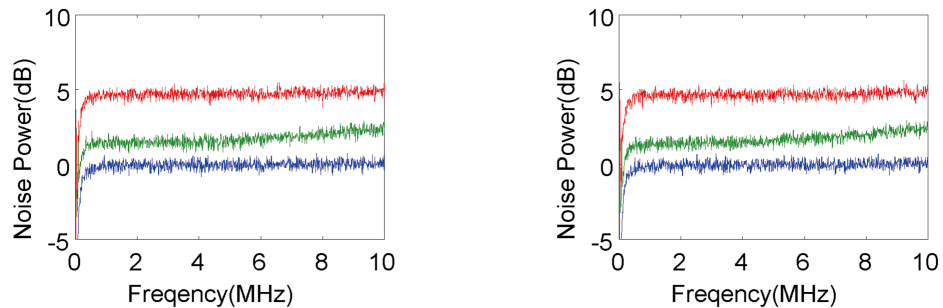


Figure 4.13: Diagram of the optical delay line setup and the pointing stabilization mechanism.

Figure 4.14: Power spectrum traces of the homodyne photocurrent for vacuum state broadband teleportation. Blue traces, shotnoise level. Green traces, quantum teleportation with $r \geq 0$. Red traces, classical teleportation with $r = 0$. Left, \hat{x}_{out} quadrature. Right, \hat{p}_{out} quadrature.

4.2.2 Vacuum state teleportation, experimental results

To benchmark our teleporter we first evaluate the fidelity F_{tele} of teleportation of the vacuum state $|0\rangle$, the coherent state of amplitude zero. At quantum optical frequencies where the mean thermal photon number is virtually 0 this is simply done by blocking the input port of the teleporter. The

teleported vacuum photocurrent is expected to have uniform Gaussian statistics with a variance $\sigma^2 = 1/2 + e^{-2r} (\hbar = 1)$ from which we can deduce teleportation fidelity $F_{\text{tele}} = 1/(1 + e^{-r})$. Fig.4.14 shows experimental measurements of the homodyne photocurrent of a vacuum state teleported with our apparatus for both quadratures \hat{x}_{out} and \hat{p}_{out} . The blue traces are the shot-noise limit, the noise spectrum of the input vacuum $|0\rangle$. It is recorded first and used to calibrate the homodyne detector. The red traces are the classical limit of teleportation obtained by turning off the entanglement between Alice and Bob ($r = 0$). We measure 4.8 dB of added noise above the shot-noise in agreement with the expected teleportation classical fidelity bound of 0.5. When Alice and Bob share entanglement the added noise drops to that shown by the green traces, 1.4 dB above the shot-noise at around 1 MHz and corresponding to a fidelity of 0.83. This is in agreement with the experimental figure of -6.9 dB that we observe when performing direct measure of the EPR correlations shared between Alice and Bob.

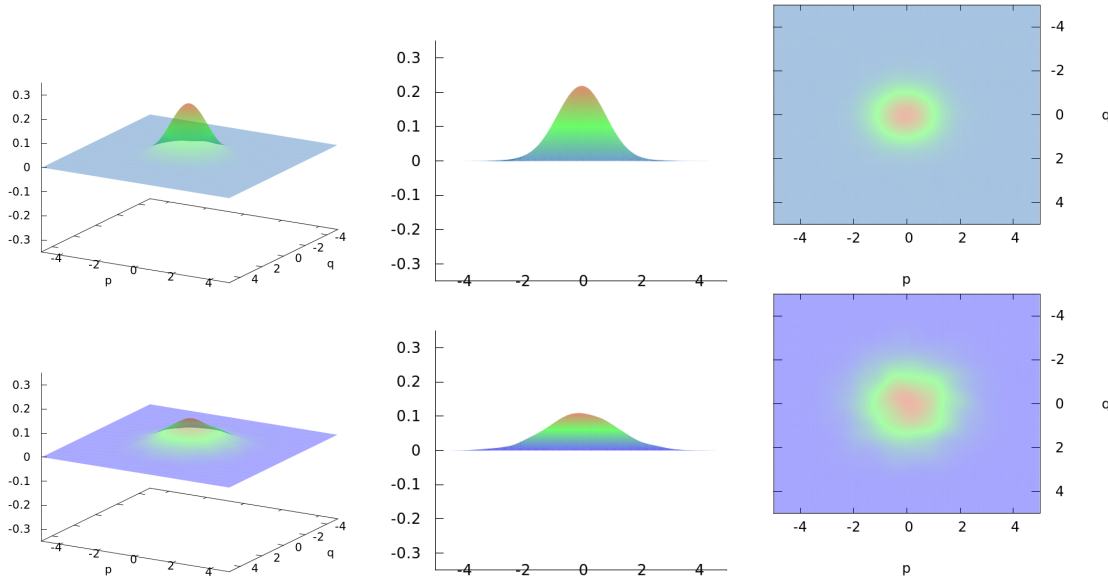


Figure 4.15: Reconstructed Wigner functions of an experimentally teleported vacuum state. Top row, broadband quantum teleportation of the vacuum state. Bottom row, broadband classical teleportation of the vacuum state.

The second step in our benchmark is to estimate the broadband EPR parameter r_{eff} , choosing one of two possible methods. A first method would consist of directly measuring spectra of the EPR correlations between Alice and Bob, such as those of Fig.4.11, and then using the mode function $\bar{f}(\omega)$ to obtain an estimation of r_{eff} . While this method automatically takes into account homodyne finite efficiency and phase errors, it does not probe any imperfections of the classical channel. A second method would consist of estimating r_{eff} with a measure of vacuum teleportation fidelity made through tomography of the temporal mode $\bar{f}(\omega)$. The benefit of this method is that the teleportation process is automatically taken into account as a whole. Furthermore, because we want to look at non-Gaussian state teleportation in phase-space and especially reconstruct the Wigner function of the output teleported state, this estimation method of r_{eff} the most relevant to our case. In the simple case of the vacuum state $|0\rangle$ as an input state, the teleportation fidelity and the EPR correlations parameter r are directly related by the relation

$$F_{\text{tele}} = 1/(1 + e^{-r}). \quad (4.2.1)$$

To measure the fidelity F_{tele} we first make a tomographic reconstruction of the teleported vac-

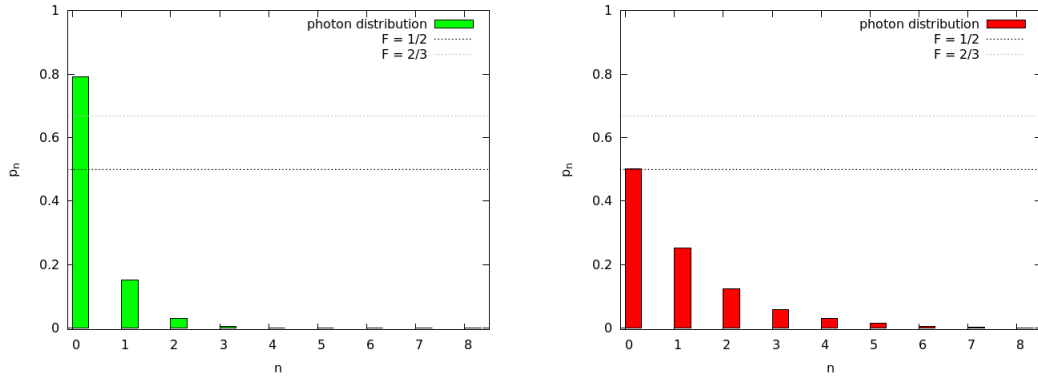


Figure 4.16: Photon number distribution of the experimentally teleported vacuum state. Photon statistics are directly extracted from the reconstructed density matrix obtained with the iterative maximum likelihood method. Left, quantum teleportation. Right, classical teleportation.

uum state. Figs.4.15 and 4.16 shows experimental results of the tomographic reconstruction of a teleported vacuum state, classical and quantum cases. To specifically estimate r_{eff} the effective broadband EPR correlation parameter, we consider the wave-packet vacuum state $|0\rangle_{f_s}$ defined by

$$|0\rangle_{f_s} = \int d\omega f_s(\omega) |0\rangle_\omega. \quad (4.2.2)$$

As before this is simply done by using the wave-packet projection function \bar{f} for analysis of the homodyne photocurrent. The fidelity $\langle 0 | \hat{\rho}_{\text{out}} | 0 \rangle$ can then be obtained immediately either by looking at the $\hat{\rho}_{00}$ component of the reconstructed density matrix or either by computing the overlap between the vacuum state and $W_{\text{out}}(q, p)$ with the integral

$$2\pi \int dq dp W_{\text{out}}(q, p) W_{|0\rangle}(q, p). \quad (4.2.3)$$

With this second tomography based method, our estimate of r_{eff} is 0.795.

4.2.3 non-Gaussian state teleportation, experimental results

To verify the success of Schroedinger's cat states teleportation we perform experimental quantum tomography of the output teleported states and look for negativity in the output Wigner function $W_{\text{out}}(q, p)$ (Fig.4.18). As the input did, the output marginal distributions exhibits the characteristic eye shape of photon-subtracted squeezed states, with a clear lack of detection events around the origin for any phase (see Fig.4.17). The output Wigner function W_{out} also retains the characteristic non-Gaussian shape as well as the negative dip ($W_{\text{out}}(0, 0) = -0.022 \pm 0.003$) of the input Wigner function W_{in} of Sec.2.4.5 to a lesser degree. The methods for quantum tomography and for the evaluation of the Schroedinger's cat state fidelity F_{cat} are performed as already explained in Sec.2.4.5. While the experimental input state has an average photon number $\langle \hat{n} \rangle$ equal to 1.22 ± 0.01 , for the output state $\langle \hat{n} \rangle$ is 1.33 ± 0.01 . The increase in the output state size is due to teleportation induced thermalization. After the teleportation we calculate that the fidelity F_{cat} of W_{out} is reduced from the initial value 0.750 ± 0.005 to 0.46 ± 0.01 of with the nearest Schroedinger's cat state having an amplitude $|\alpha_{\text{out}}|^2 = 0.66$. If W_{out} fidelity is calculated with $|\alpha_{\text{in}}|^2 = 0.98$ the amplitude of the nearest Schroedinger's cat state for the input state then $F_{\text{cat}} = 0.45 \pm 0.01$.

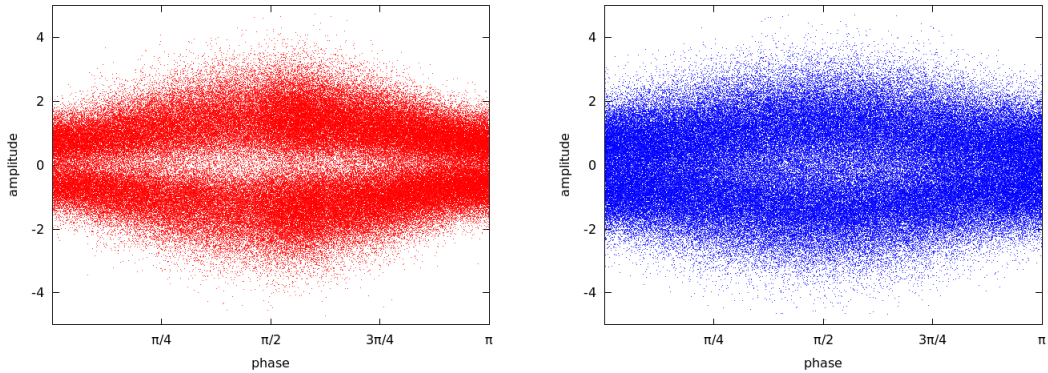


Figure 4.17: Marginal distribution of the electrical field of the experimentally generated photon subtracted squeezed vacuum state before and after quantum teleportation. Left, input state. Right, output state.

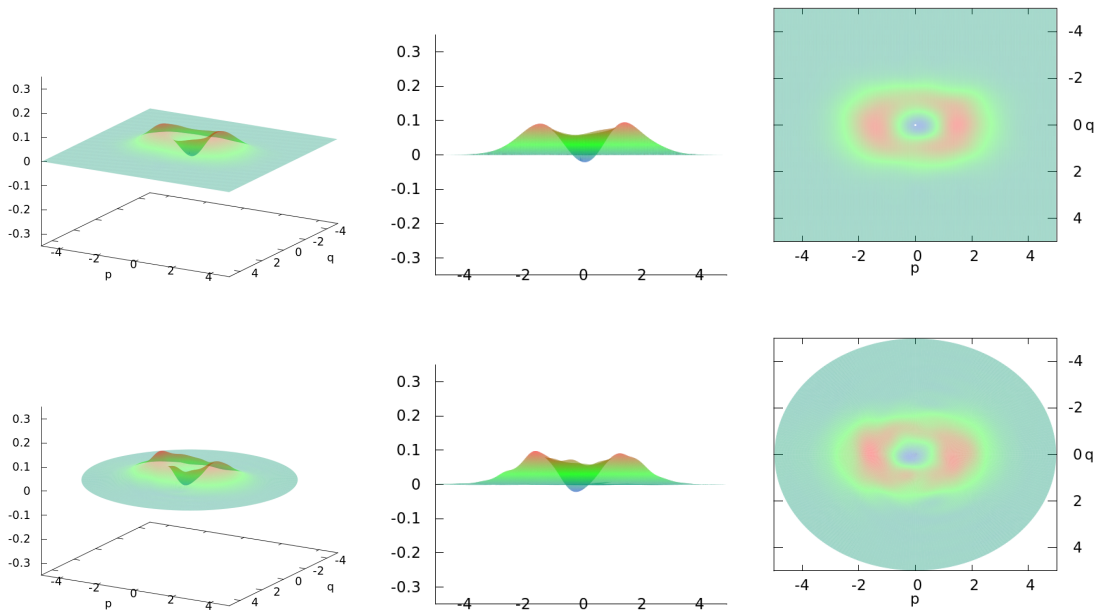


Figure 4.18: Reconstructed Wigner functions of the experimentally generated and teleported photon subtracted squeezed vacuum state. Top row, with the maximum likelihood iteration algorithm. Bottom row, with the polynomial series decomposition inverse Radon transform algorithm.

4.2.4 Model of non-Gaussian state teleportation

As we did in Sec.2.4.6, we develop here a phase-space model of teleportation to predict and explain the experimentally reconstructed Wigner functions of Fig.4.18. The degradation of the central negative dip and the full evolution of W_{in} towards W_{out} can be fully understood using Eq.(4.1.1) with the model of W_{in} developed in Sec.2.4.6 from which we start here. First we use the reference Wigner function not corrected for the APD dark count and optical losses. Applying teleportation

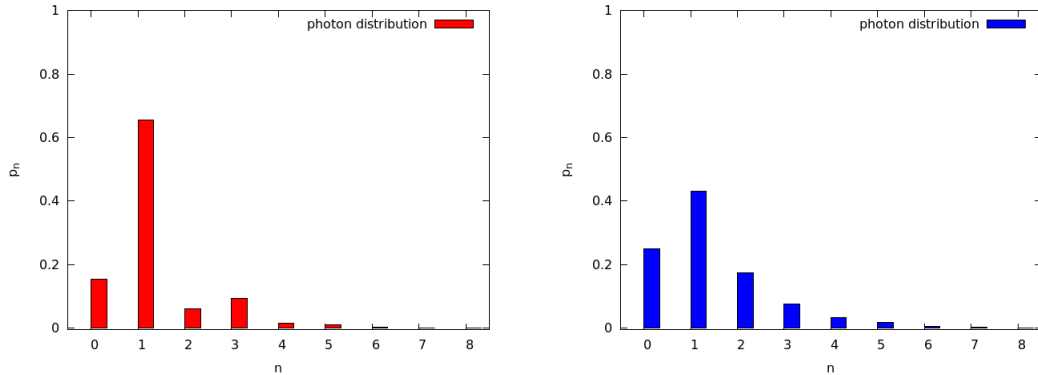


Figure 4.19: Photon number distribution of the experimentally generated photon subtracted squeezed vacuum state, before and after teleportation. Left, input state. Right, output state.

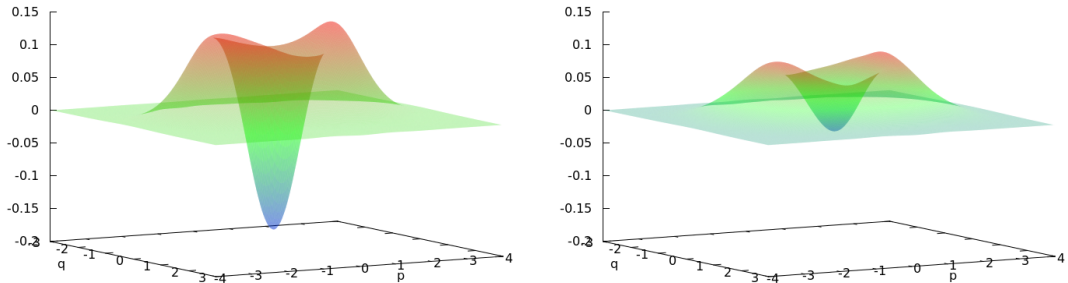


Figure 4.20: Wigner functions of the input and output states of broadband quantum teleportation. Left, input state. Right, output state.

equation (4.1.1) on Eq. (2.4.3), we find for the output negativity $W_{\text{ref out}}(0, 0)$

$$W_{\text{ref out}}(0, 0) = \frac{(2e^{-2r} + 1)(2e^{-2r} - 1)}{\pi \left((1 + 2e^{-2r}) + 8e^{-2r} \text{sh}^2(s) \right)^{3/2}}, \quad (4.2.4)$$

which indeed yields $W_{\text{ref out}}(0, 0) \leq 0$ for $r \geq \ln \sqrt{2}$ as expected (see Fig. 4.21). $W_{\text{ref out}}(0, 0)$ will become negative only if the parameter r is greater than $\ln \sqrt{2}$, equivalent to 3 dB of squeezing. We now use the model with optical losses but not yet corrected for the non-zero APD dark count. Using this model of imperfect input state we investigate negativity teleportation of W_{in} by concatenating Eqs. (2.4.4) and (4.1.1), the two successive Gaussian convolutions are reduced to one, while the phase space rescaling survives the teleportation. Eventually W_{out} happens to be written in the same form as W_{in} ,

$$W_{\text{out}}(x, p) = \frac{1}{\eta} (W_{\text{ref}} \circ G_{\lambda'}) \left(\frac{x}{\sqrt{\eta}}, \frac{p}{\sqrt{\eta}} \right), \quad (4.2.5)$$

where λ has been changed to $\lambda' = \sqrt{\lambda^2 + (e^{-r})^2 / \eta}$ in a way similar to classical amplifiers input/output SNR rules. We remark that besides the degradation of the input negativity $W_{\text{in}}(0, 0)$, the loss parameter $1 - \eta$ has also the effect of decreasing the effective correlation parameter r to $r' = r + \ln \sqrt{\eta} < r$. In practical terms, this means that both operations do not commute and losses at the input stage have more effect on the quality of the overall process than losses at the output

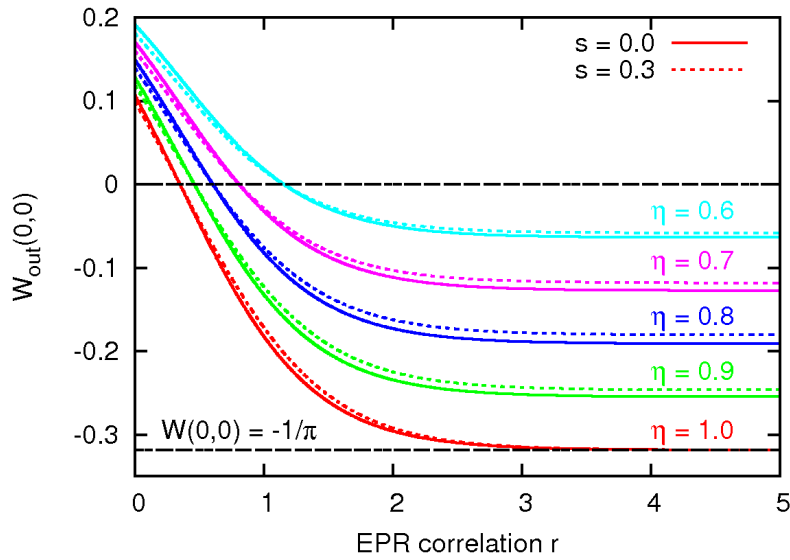


Figure 4.21: Output Wigner function negativity $W_{\text{in}}(0,0)$ as a function of r for different values of η and s . For a given η , different s curves cross the $W(0,0) = 0$ at the same $r(\eta)$.

stage. The output center negativity is now expressed as

$$W_{\text{out}}(0,0) = \frac{g_r(g_r - 2\eta)}{\pi (g_r^2 + 4\eta(g_r - \eta)\text{sh}^2(s))^{3/2}}, \quad (4.2.6)$$

with $g_r = 1 + 2e^{-2r}$ (plotted in Fig. 4.21). As expected for unity gain teleportation, the $W_{\text{out}}(0,0) = 0$ threshold is still independent of the squeezing parameter s and can be expressed as a function of the two parameters η and r alone by the simple relation (plotted in Fig. 4.22)

$$r = \ln \sqrt{2/(2\eta - 1)} \quad \text{at threshold.} \quad (4.2.7)$$

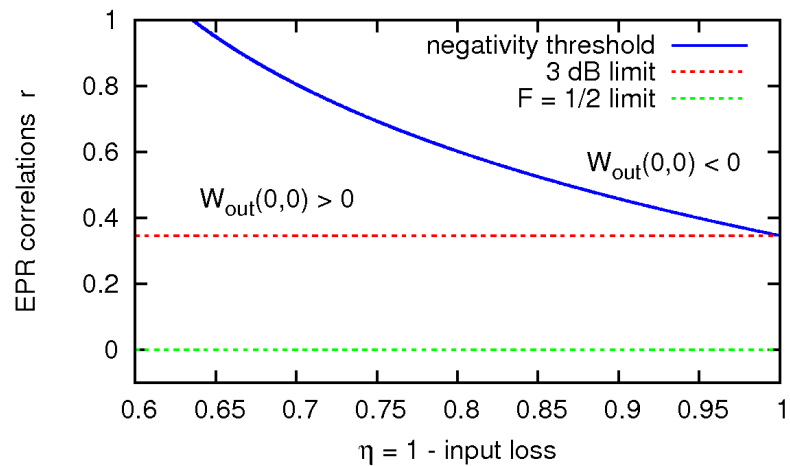


Figure 4.22: Negativity threshold as a function of r and η .

Finally, we take into account the non-zero APD dark count. Correcting for the effect of Eq.(2.4.7) in the output negativity equation (4.2.6) and negativity threshold equation (4.2.7) is just a matter of calculating how the Wigner function associated to $\hat{\rho}_{\text{false}}$, $W_{\text{false}}(x, p) = G_{1/\sqrt{2}}(e^s x, e^{-s} p)$, evolves in the teleportation process. We obtain for

$$W_{\text{out}}(0, 0) \rightarrow W_{\text{out}}(0, 0) + 2\epsilon\eta \frac{g_r + 2(g_r - \eta)\text{sh}^2(s)}{\pi (g_r^2 + 4\eta(g_r - 2\eta)\text{sh}^2(s))^{3/2}}, \quad (4.2.8)$$

for the corrected output negativity. The output negativity threshold corrected for ϵ is now expressed with the following quadratic equation:

$$0 = g_r^2 + 2b(\epsilon, s)\eta g_r - c(\epsilon, s)\eta^2, \quad (4.2.9)$$

with $b(\epsilon, s) = \epsilon(1 + 2\text{sh}^2(s)) - 1$ and $c(\epsilon, s) = 4\epsilon\text{sh}^2(s)$. Keeping the only physical solution in (4.2.9) the negativity teleportation threshold corrected for ϵ becomes

$$r = \ln \left(\frac{2}{\eta (\sqrt{b^2 + c} - b)} \right)^{1/2}. \quad (4.2.10)$$

which is plotted in Fig.4.23.

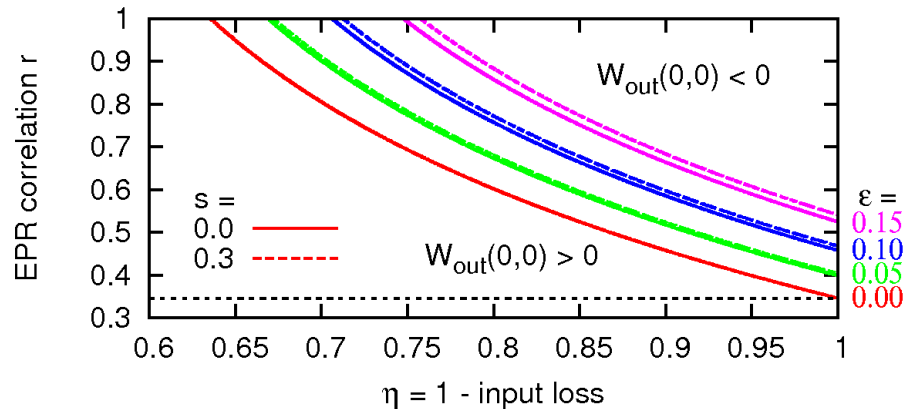


Figure 4.23: Influence of ϵ and s on the negativity threshold $W_{\text{out}}(0, 0) = 0$ at the output of teleportation.

Finally, we can check our prediction of W_{out} and particularly $W_{\text{out}}(0, 0)$ using Eq.(4.2.8) and all the known parameters estimated in Secs.2.4.6 and 4.2.2. Especially we assume the validity of the model of effective single-mode teleportation of wave-packet derived in Sec.4.1.5 and use the estimated value of r_{eff} in place of r . We start with the negativity and we obtain the value $W_{\text{out}}(0, 0) = -0.0243$, in agreement with the measured output negativity of -0.022 ± 0.003 of the experimental Wigner functions of Sec.4.2.3. Using the same technique as in Sec.2.4.6, we also check the overlap O' between the measured state and the predicted state and find a value of 0.988. The $L2$ distance between the two states is 0.04. Here again, the experimental results of teleportation are numerically in good agreement with our model of effective single-mode teleportation. Our approach to multimode teleportation in Sec.4.1.5 has the double benefit of intuitively picturing broadband operations in term of wave-packets, while at the same time allowing us to use

the usual results of single-mode teleportation with simple renormalization prescriptions. In summary, we have developed in this section a realistic yet simple model to account for the phase-space properties of the teleportation of photon subtracted squeezed vacuum states. With that model we have considered the effect of teleportation on these states and are able to predict the success of negativity teleportation. Together with the experimental results of Fig.4.18, we have demonstrated and analysed in details an experimental quantum teleporter able to teleport full wave-packets of light up to a bandwidth of 10 MHz while at the same time preserving the quantum characteristic of strongly non-classical superposition states, manifested in the negativity of the Wigner function. Although F_{cat} and $W(0,0)$ drop significantly in the teleportation process, there is no theoretical limitation besides available squeezing and stronger EPR correlations would achieve better fidelity and negativity transmission.

4.3 Conditional quantum teleportation

One of the great benefits of continuous variable quantum information processing is the possibility to design deterministic algorithms with 100% success rate. This is the case for instance with quantum teleportation but also with cluster state computation or most one-way computation algorithms. In the continuous variable case, both the generation of the necessary ancilla states and performing the actual quantum operation can be achieved deterministically. In the qubit world, although cluster states operations are deterministic, the generation of a qubit cluster state itself is not and relies on successful Bell's state measurements. Of course, the counterpart of the probabilistic operations is the ability to perform "perfect" operations when the protocol succeeds, while continuous variable circuits always add some minimal amount of noise to the output state due to finite available amount of squeezing, at least experimentally. However an optical qubit system is under the hood nothing else than a continuous variable system with restricted degrees of freedom. Therefore it is reasonable to believe that it should be possible to design continuous variable circuits with qubit-like properties. The central idea relies on the use of a measurement process inside the algorithm whose random result can be used to set up probabilistic operations. The measurement process can be tuned to design algorithms where the overall success rate is balanced with the overall quality of operation or a given figure of merit in particular. In other word, the conditional measurement can be used to give up on the deterministic output states in order to reduce the magnitude of errors in continuous variable circuits.

In the recent years, a number of proposals have started to look beyond deterministic operations for continuous variable quantum information. Cited earlier in this chapter, in [62] and [71] it was proposed to use photon-subtraction channels in addition to the standard 2-mode EPR channel for improved continuous variable quantum teleportation, which naturally leads to probabilistic operations conditioned to the detection of photons in these subtraction channels. With such measurement-induced probabilistic algorithms, it has been demonstrated that it is even possible to design circuits, such as noiseless amplifiers [164, 163, 158], with what appears to be unphysical properties [19]. These few examples are all based on the photon-subtraction protocol and therefore non-Gaussian measurements to perform the conditional operations. Photon detection is the usual way to perform conditional operation in quantum optics: a successful detection event reduces the quantum state of the system to a particular target state which is then used as an input or as an ancilla in a given quantum protocol. As we saw in Chap.2, these heralding techniques based on non-Gaussian measurements are nowadays routinely used to create a variety of non-Gaussian states. However, it is possible also to use Gaussian measurements such as optical homodyne measurements to design conditional algorithms. For example in [118], it is shown that a simple homodyne detector can be used to conditionally project a photon number state $|n\rangle$ onto a squeezed Schrödinger's cat state, whose experimental demonstration was reported in [123].

As was proposed in [160], conditional operations based only on Gaussian measurement can improve the quality of the output teleported state and the negativity beyond what is achievable with deterministic operations, in the context of non-classical state teleportation.

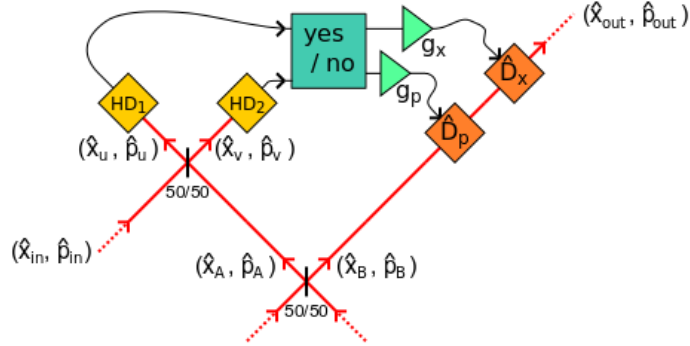


Figure 4.24: Overview of the conditional quantum teleportation protocol.

In this section, we present and experimentally demonstrate how to implement this conditional teleportation protocol to further enhance quantum teleportation of non-classical features of our input non-Gaussian state. Fig.4.24 shows the overview of the conditional teleportation experiment implemented on top of the experimental setup previously presented in Sec.4.2. In the Kimble-Braunstein teleportation protocol[49] on which our experimental setup is based, homodyne detection is used by Alice to perform joint quadrature measurements and can be used in principle for conditioning. The idea is therefore to use the measurement outcomes of both Alice's homodyne detector \bar{x}_u and \bar{p}_v and performs conditioning on this pair of numbers for every teleportation event independently: only when Alice's quadrature measurement results meet chosen requisite conditions that teleportation will be considered successful. The conditioning scheme of our experimental setup is based on a simple threshold mechanism: if Alice's homodyne measurement $\xi = (\bar{x}_u + i\bar{p}_v)/\sqrt{2}$ falls inside a circle of radius L , then the output teleported state is accepted; if not, the output teleported state is rejected (see Fig.4.25). The conditioning algorithm exploits the fact that a smaller and smaller measured value of ξ on Alice side means smaller and smaller displacements on Bob side. In other words, if for instance $\xi = 0$, Bob does not need to perform any displacement and the output teleported state is naturally found to be identical to the input state. Of course, the counterpart is that this particular event happens on average with probability 0. In short, conditional teleportation can be seen as an advanced technique of noise filtering where information at the output of the teleporter which is judged too noisy is removed from the final experimental data set. Furthermore it is based on Gaussian measurements only, and therefore easy to implement experimentally.

4.3.1 Theory of conditional operation

To start off we first investigate the mechanism of Gaussian conditional teleportation. Rather than following the derivation method proposed in [160] based on the transfer operator [57, 67], we have developed calculations purely based on the Wigner formalism and inspired from [82]. We want to calculate two figures: 1) the negativity $W_{\text{out}}(0, 0|L)$ of the Wigner function of the output teleported quantum state for a conditioning radius L at Alice's homodyne detectors; and 2) the probability of success of conditional teleportation $P(L)$ for a conditioning radius L . Again our input state is a photon subtracted squeezed vacuum state, as was shown in Chap.2. However for more simplicity in our analysis we only consider a mixture of a single photon state $|1\rangle$ and vacuum state $|0\rangle$ for

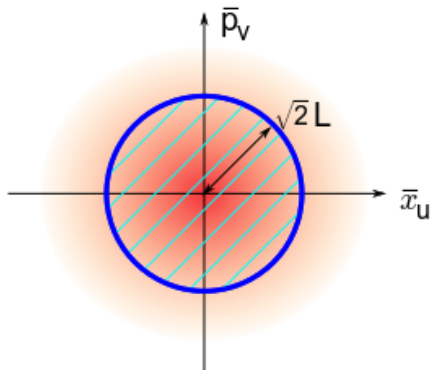


Figure 4.25: Acceptance area for Alice’s results (\bar{x}_u, \bar{p}_v) visualized in phase space. If for a single teleportation event the measured values of (\bar{x}_u, \bar{p}_v) falls outside of the blue circle, the output state is discarded.

the input state. This approach is justified by the low amount of squeezing of our experimental photon subtracted state: in practice it affects only slightly the prediction of the negativity value of the output teleported state. We also only consider unity gain conditional teleportation for further simplicity.

To the contrary of deterministic teleportation, there are additional experimental imperfections that need to be taken into account separately as they have different effects overall on the efficiency of conditional teleportation:

- We need to take into account the equivalent beam-splitter losses on the input state. If we assume an input density matrix of the form $(1 - e)|1\rangle\langle 1| + e|0\rangle\langle 0|$, we can simply fit the experimentally measured negativity $W_{\text{in}}(0, 0)$ to the expression $(2e - 1)/\pi$. Notice that in this simple case, e accounts for the equivalent optical losses $1 - \eta$ suffered by the $|1\rangle\langle 1|$ component as well as the APD dark count ϵ .
- We need to take into account the equivalent beam-splitter losses f suffered by the output teleported state due to the imperfect visibility of the verifying homodyne detector.
- Finally even in the unity gain regime we need to precisely consider the effect on conditional teleportation of any extra anti-squeezing present in the 2-mode EPR state. As with deterministic teleportation the contributions of extra anti-squeezing at Alice’s homodyne detectors is exactly cancelled at the output of teleportation by Bob’s teleportation, but extra anti-squeezing has nevertheless an influence on the probability of success $P(L)$ of conditional teleportation.

General formulation

For every teleportation event the value $\xi = (\bar{x}_u + i\bar{p}_v)/\sqrt{2}$ recorded by Alice is intrinsic to this event. In consequence the phase space formulation of teleportation of Eq.(4.1.1) is to be understood as an averaged phase space process over all possible measurement outcomes ξ happening with probabilities $p(\xi)$. To be able to calculate $W_{\text{out}}(0, 0|L)$ and $P(L)$ we have to uncover this averaging mechanism and use a more basic formulation of teleportation. For that purpose we base our analysis on the classical phase-space description of continuous variable teleportation proposed in [82]. Before Alice’s homodyne measurements and Bob’s displacement operations, the state of

the system can be described by the 3-mode states

$$W_{\text{in}}(\alpha)W_{\text{AB}}(\beta, \gamma), \quad (4.3.1)$$

where W_{in} is the 1-mode Wigner function of the input state and $W_{\text{AB}}(\beta, \gamma)$ is the 2-mode Wigner function of the 2-mode EPR state shared by Alice and Bob. We recall that W_{AB} is a Gaussian Wigner function completely determined by the Gaussian correlation matrix Γ given in Eq.(4.3.42). For every measurement outcome $\xi = (\bar{x}_u + i\bar{p}_v)/\sqrt{2}$ the action of Alice's homodyne measurements on the 3-mode Wigner function of Eq.(4.3.1) is equivalent to integrating variables α and β with the constraint that $\alpha + \beta^* = \xi$. Therefore before Bob's displacement operation Alice's measurements project the 3-mode Wigner function $W_{\text{in}}(\alpha)W_{\text{AB}}(\beta, \gamma)$ onto the conditional Wigner function $W(\gamma|\xi)$ written

$$W(\gamma|\xi) = \frac{1}{p(\xi)} \int_{\mathbb{R}^2} d^2\alpha \int_{\mathbb{R}^2} d^2\beta \delta(\alpha + \beta^* - \xi) W_{\text{in}}(\alpha)W_{\text{AB}}(\beta, \gamma), \quad (4.3.2)$$

where $p(\xi)$ is the probability for Alice to obtain the result ξ and which is simply expressed as the integral of $W(\gamma|\xi)$ on γ over \mathbb{R}^2

$$p(\xi) = \int_{\mathbb{R}^2} d^2\alpha \int_{\mathbb{R}^2} d^2\beta \int_{\mathbb{R}^2} d^2\gamma \delta(\alpha + \beta^* - \xi) W_{\text{in}}(\alpha)W_{\text{AB}}(\beta, \gamma). \quad (4.3.3)$$

After Alice's measurements Bob performs the displacement operation $\gamma \rightarrow \gamma - \xi$ so that the final conditional output Wigner function $W_{\text{out}}(\gamma|\xi)$ is expressed for every ξ by

$$W_{\text{out}}(\gamma|\xi) = W(\gamma - \xi|\xi) = \frac{1}{p(\xi)} \int_{\mathbb{R}^2} d^2\alpha W_{\text{in}}(\alpha)W_{\text{AB}}(\xi^* - \alpha^*, \gamma - \xi). \quad (4.3.4)$$

In the case of deterministic quantum teleportation the output state $W_{\text{out}}(\gamma)$ is expressed as the following weighted average over all possible outcomes ξ

$$W_{\text{out}}(\gamma) = \int_{\mathbb{R}^2} d\xi p(\xi) W_{\text{out}}(\gamma|\xi) = \int_{\mathbb{R}^2} d^2\alpha \int_{\mathbb{R}^2} d^2\xi W_{\text{in}}(\alpha)W_{\text{AB}}(\xi^* - \alpha^*, \gamma - \xi). \quad (4.3.5)$$

From this last expression and after performing the integration on ξ which only involves W_{AB} , we obtain the usual phase space formula

$$W_{\text{out}}(\gamma) = \int_{\mathbb{R}^2} d^2\alpha W_{\text{in}}(\gamma - \alpha) G_{e^{-r}}(\alpha), \quad (4.3.6)$$

for teleportation. Using a formal mathematics software it is easy to carry on this integration to obtain Eq.(4.3.6). In conditional teleportation the output state $W_{\text{out}}(\gamma|\xi)$ is discarded from the final data set when ξ falls outside of the conditioning area $\Lambda = \{\xi \in \mathbb{C}, |\xi| \leq L\}$. A successful conditional teleportation event therefore happens with probability $P(L)$ expressed as the average of $p(\xi)$ over Λ

$$P(L) = \int_{\Lambda} d^2\xi p(\xi) = \int_{\Lambda} d^2\xi \int_{\mathbb{R}^2} d^2\alpha \int_{\mathbb{R}^2} d^2\gamma W_{\text{in}}(\alpha)W_{\text{AB}}(\xi^* - \alpha^*, \gamma). \quad (4.3.7)$$

To express the average output state $W_{\text{out}}(\gamma|\xi \in \Lambda) = W_{\text{out}}(\gamma|L)$ of conditional teleportation, we simply have to adjust Eq.4.3.5 so as to average ξ over Λ instead of \mathbb{R}^2 :

$$W_{\text{out}}^u(\gamma|L) = \int_{\Lambda} d\xi p(\xi) W_{\text{out}}(\gamma|\xi). \quad (4.3.8)$$

Notice that $W_{\text{out}}^u(\gamma|L)$ is not normalized and that the incomplete ξ integration over Λ imposes to normalize W_{out}^u by the factor

$$N(L) = \int_{\Lambda} d^2\xi \int_{\mathbb{R}^2} d^2\alpha \int_{\mathbb{R}^2} d^2\gamma W_{\text{in}}(\alpha) W_{\text{AB}}(\xi^* - \alpha^*, \gamma - \xi). \quad (4.3.9)$$

Applying the change of variable $\gamma \rightarrow \gamma + \xi$ in the above equation, we notice that this normalization factor $N(L)$ is actually equal to $P(L)$. Eventually, the normalized averaged output Wigner function $W_{\text{out}}(\gamma|L)$ after successful conditional teleportation reads

$$W_{\text{out}}(\gamma|L) = \frac{W_{\text{out}}^u(\gamma|L)}{N(L)} = \frac{1}{N(L)} \int_{\Lambda} d^2\xi \int_{\mathbb{R}^2} d^2\alpha W_{\text{in}}(\alpha) W_{\text{AB}}(\xi^* - \alpha^*, \gamma - \xi). \quad (4.3.10)$$

Eqs.(4.3.7) and (4.3.11) are the basis of our analysis of conditional teleportation in the next following paragraphs. We first apply these equations to the simple case of a single photon state. Then we progressively include the relevant experimental parameters such as optical losses and excess anti-squeezing into the calculation of $P(L)$ and $W_{\text{out}}(\gamma|L)$ in order to compare the prediction to experimental results.

$$W_{\text{out}}(\gamma|L) = \frac{W_{\text{out}}^u(\gamma|L)}{P(L)} = \frac{\int_{\Lambda} d^2\xi \int_{\mathbb{R}^2} d^2\alpha W_{\text{in}}(\alpha) W_{\text{AB}}(\xi^* - \alpha^*, \gamma - \xi)}{\int_{\Lambda} d^2\xi \int_{\mathbb{R}^2} d^2\alpha \int_{\mathbb{R}^2} d^2\gamma W_{\text{in}}(\alpha) W_{\text{AB}}(\xi^* - \alpha^*, \gamma)}. \quad (4.3.11)$$

Prolegomenon

In this paragraph we explain how to efficiently carry the calculations of $P(L)$ and $W_{\text{out}}(\gamma|L)$ from Eqs.(4.3.7) and (4.3.11). The difference between deterministic and conditional teleportation essentially lies in the integration range of the variable ξ . For conditional teleportation this range is not \mathbb{R}^2 but rather a finite interval, which makes the successive Gaussian integrations much harder to perform. The general methodology is to compute all integrations over \mathbb{R}^2 starting with Gaussian integrations and at the very end only compute the integration on variable ξ over Λ . We recall that our input non-Gaussian state produced with a single photon subtraction has a Wigner function of the form

$$W(x, p) = \frac{2}{\pi} \left(A_x x^2 + A_p p^2 - \frac{B}{2} \right) e^{-x^2/C_x - p^2/C_p}. \quad (4.3.12)$$

For simplicity we focus on the single photon state with rotational symmetry so that $A_x = A_p = A$ and $C_x = C_p = C$. All transformations of the input Wigner function considered in the following paragraphs, such as losses and teleportation, are Gaussian transformations and preserve the particular form of Eq.(4.3.12). Therefore in the analysis of conditional teleportation we recurrently encounter the following integral

$$W_{\Lambda}(A, B, C) = \int_{\Lambda} dx dp \frac{2}{\pi} \left(A(x^2 + p^2) - \frac{B}{2} \right) e^{-(x^2 + p^2)/C}, \quad (4.3.13)$$

which can be calculated in advance only once for a chosen conditioning set Λ . When $\Lambda = \{\xi \in \mathbb{C}, |\xi| \leq L\}$ is a disk of radius L centered on $(0, 0)$, we obtain

$$W_{\text{disk}}(A, B, C) = \int_0^{\sqrt{2}L} 2\pi r dr \frac{2}{\pi} (Ar^2 - B/2) e^{-r^2/C}, \quad (4.3.14)$$

$$= C \left((2AC - B)(1 - e^{-2L^2/C}) - 4AL^2 e^{-2L^2/C} \right). \quad (4.3.15)$$

If for example $\Lambda = \{\xi \in \mathbb{C}, |\bar{x}_u| \leq L, |\bar{p}_v| \leq L\}$ is a square of length $2L$ centered on $(0, 0)$, we obtain

$$W_{\text{square}}(A, B, C) = \int_{-L}^{+L} dp \int_{-L}^{+L} dx \frac{2}{\pi} (A(x^2 + p^2) - B/2) e^{-(x^2 + p^2)/C}, \quad (4.3.16)$$

$$= C \operatorname{erf}(L/\sqrt{C}) \left((2AC - B) \operatorname{erf}(L/\sqrt{C}) - 4AL\sqrt{C/\pi} e^{-L^2/C} \right), \quad (4.3.17)$$

where $\operatorname{erf}(x)$ is the Gaussian error function. We now simply have to restate every calculus with $W_\Lambda(A, B, C)$ and then calculate the three coefficients A, B and C to finally apply formula (4.3.14). We also recall that $W_{AB}(\beta, \gamma)$ can be expressed from the 2-mode EPR correlation matrix Γ as

$$W_{AB}(\beta, \gamma) = \frac{1}{\pi} \exp \left[- \begin{pmatrix} \beta \\ \gamma \end{pmatrix}^T \Gamma^{-1} \begin{pmatrix} \beta \\ \gamma \end{pmatrix} \right]. \quad (4.3.18)$$

As we tinker with the expression of $W_{AB}(\beta, \gamma)$ when dealing with optical losses on the output teleported mode, we define in addition the function

$$G_{AB}(\alpha, \gamma, \xi) = W_{AB}(\xi^* - \alpha^*, \gamma - \xi), \quad (4.3.19)$$

which allows us to rewrite Eqs.(4.3.7) and (4.3.8) in the more convenient and general forms

$$P(L) = \int_{\Lambda} d^2\xi \int_{\mathbb{R}^2} d^2\alpha \int_{\mathbb{R}^2} d^2\gamma W_{\text{in}}(\alpha) G_{AB}(\alpha, \gamma + \xi, \xi), \quad (4.3.20)$$

$$W_{\text{out}}^u(\gamma|L) = \int_{\Lambda} d^2\xi \int_{\mathbb{R}^2} d^2\alpha W_{\text{in}}(\alpha) G_{AB}(\alpha, \gamma, \xi). \quad (4.3.21)$$

Appendix E contains tables summarizing the results of calculation of the coefficients A, B and C for the two above expressions used in the following paragraphs and different case studies.

Single photon case

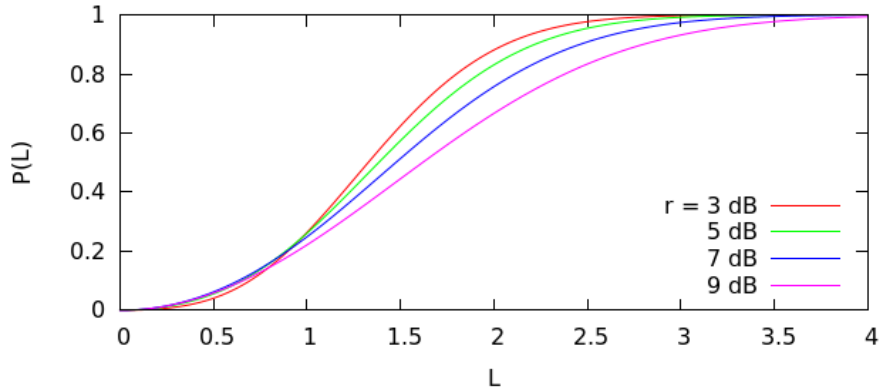


Figure 4.26: Evolution of the probability of success of conditional teleportation with L for a single photon input state and different values of r .

A single photon state as an input state to teleportation is the most simple case of non-Gaussian state conditional teleportation. To start off we compute the probability of success $p(\xi)$ for every ξ from Eq.(4.3.7) with $W_{\text{in}}(x, p) = 2(x^2 + p^2 - 1/2) \exp(-x^2 - p^2)/\pi$ and obtain as expected

$$p(\xi) = \frac{2}{\pi} (A(x^2 + p^2) - B/2) e^{-(x^2 + p^2)/C}, \quad (4.3.22)$$

with

$$A = 1/C^3, \quad B = (1-a)/C^2, \quad C = 1+a, \quad (4.3.23)$$

where $a = \cosh(2r)$ and r is as usual the amount of EPR correlation. Using Eq.(4.3.15) we immediately obtain the expression of $P(L)$ as

$$P(L) = 1 - \left(1 + \left(\frac{2L}{1+a}\right)^2\right) e^{-2L^2/(1+a)}, \quad (4.3.24)$$

which is plotted in Fig.4.30 for different values of r . We now turn to $W_{\text{out}}(\gamma|L)$ and for simplicity only evaluate it at $\gamma = 0$ the center of phase space. We calculate the non-normalized output negativity $W_{\text{out}}(0|\xi)$ for every ξ and obtain from Eq.(4.3.5) the expression

$$W_{\text{out}}^u(0|\xi) = \frac{1}{p(\xi)} \frac{2}{\pi} (A(x^2 + p^2) - B/2) e^{-(x^2 + p^2)/C}, \quad (4.3.25)$$

with

$$\begin{aligned} A &= +(a-b)^2/\pi D^3, & C &= D/(1+2(a-b)), \\ B &= -(1-a)/\pi D^2, & D &= 1+a. \end{aligned} \quad (4.3.26)$$

where $b = \sinh(2r)$. We can finally obtain an explicit expression of $W_{\text{out}}(\gamma|L)$, which is plotted in Fig.4.30 for different values of r . We observe that when r is high, although deterministic teleportation only achieves moderate output negativity, conditional teleportation is able to bring the output state close to perfection. For 9 dB of EPR correlations, a success rate set around 10% allows to bring the output negativity around -0.3 close to the $-1/\pi \approx -0.318$ absolute maximum. When r is lower, the effect of conditional teleportation is still clearly visible but manifests itself at lower success rates. To obtain eventually equivalent levels of output negativity for lower r values the data set has to be purified much more.

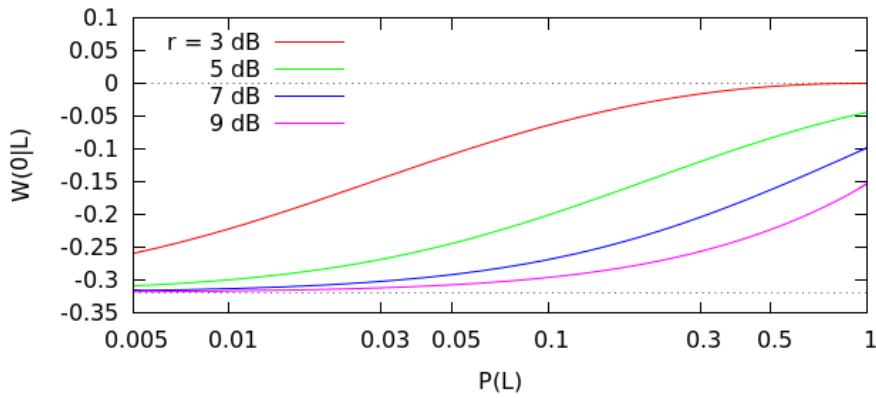


Figure 4.27: Improvement to $W(0, 0)$ and evolution of the negativity with the probability of success of conditional teleportation for a single photon input state. The plotted curve is the parametric curve ($x = P(L)$, $y = W_{\text{out}}(0|L)$) with L as the curvilinear abscissa.

Optical losses on the input state

Including the effect of optical losses for a single photon input state is relatively easy. The Wigner function of a single photon state which has suffered $1 - \epsilon$ of equivalent beam-splitter losses can be

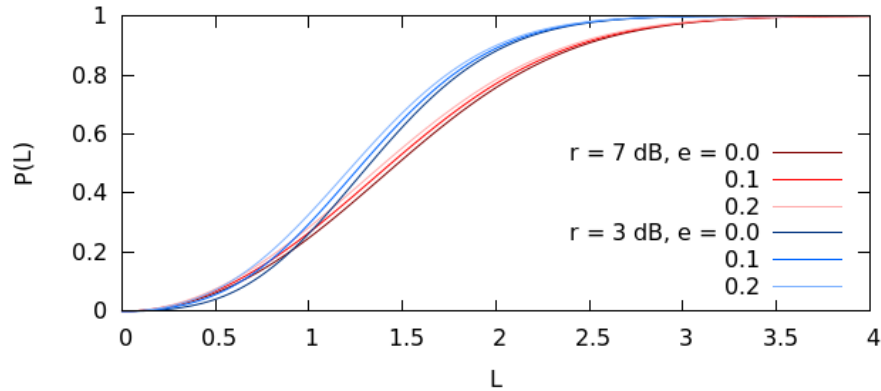


Figure 4.28: Evolution of the probability of success of conditional teleportation with L for a mixture of single photon and vacuum state and different values of r .

written as the mixture

$$W(x, p) = (1 - e)W^{|1\rangle}(x, p) + eW^{|0\rangle}(x, p). \quad (4.3.27)$$

The two formula (4.3.20) and (4.3.21) for conditional teleportation are linear with respect to the input Wigner function W_{in} we only need to compute $P(L)$ and $W_{\text{out}}(0|L)$ for the vacuum state Wigner function $\exp[-x^2 - p^2]/\pi$. We can then apply the above linear combination to include the effect of optical losses on the input state. With the same methodology as before we obtain for $p(\xi)$ the expression $W_{\Lambda}(A, B, C)$ with

$$A = 0, \quad B = -1/C, \quad C = 1 + a, \quad (4.3.28)$$

which yields

$$P(L) = 1 - e^{-2L^2/(1+a)}, \quad (4.3.29)$$

for $|0\rangle\langle 0|$. For $W_{\text{out}}(0|\xi)$, we have

$$\begin{aligned} A &= 0, & C &= D/(1 + 2(a - b)), \\ B &= -1/\pi D, & D &= 1 + a. \end{aligned} \quad (4.3.30)$$

The curves for $P(L)$ and $W_{\text{out}}(0|L)$ corrected for equivalent optical losses $1 - e$ are shown respectively in Figs.4.30 and 4.30 for different values of r . Looking at the former we notice that the presence of a vacuum component in the input state has almost no influence on $P(L)$. Quite to the contrary, Fig.4.30 shows that the vacuum component input has a strong influence on the maximally obtainable output negativity with conditional teleportation. However this should not be a surprise as it just means that conditional teleportation cannot retrieve negativity beyond the limit imposed by the input state itself. In the following paragraph, we now calculate $P(L)$ and $W_{\text{out}}(0|L)$ separately for the $|1\rangle\langle 1|$ and $|0\rangle\langle 0|$ components of our input state. We also notice that starting from a positive output Wigner function at $P(L) = 1$, conditional teleportation can to some extent extract negativity from a thermalized state and bring it into the quantum domain.

Optical losses on the output states

Taking into account the effect of optical losses on the output teleported state proves to be harder. Notice that these optical losses have not link whatsoever with conditional teleportation. In particular the probability of success of teleportation remains unchanged. However it is necessary to

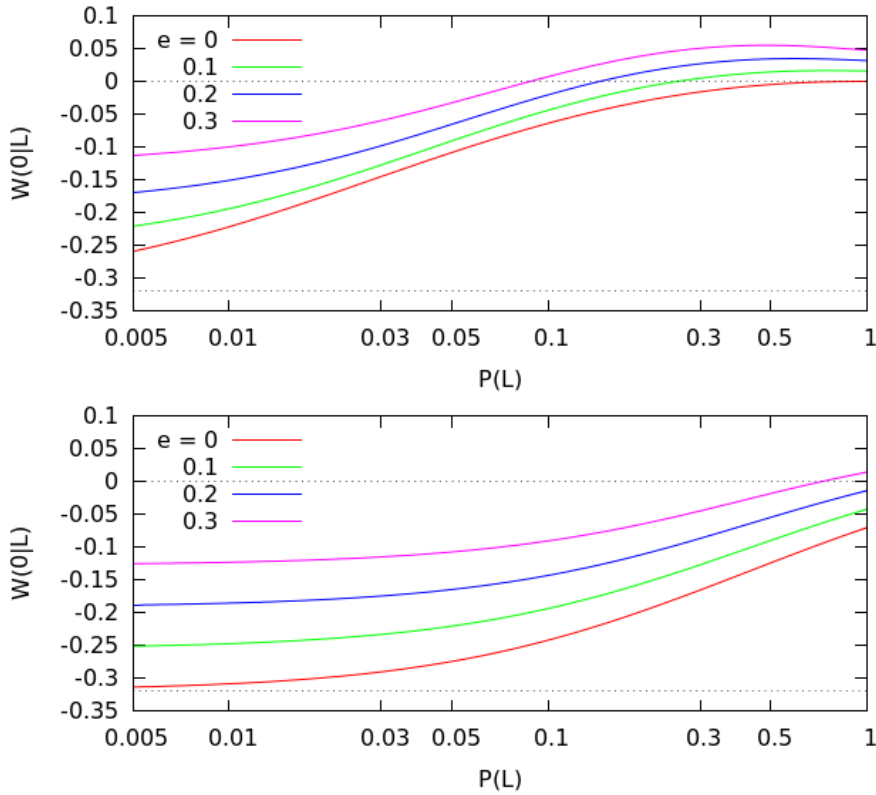


Figure 4.29: Improvement to $W(0, 0)$ and evolution of the negativity with the probability of success of conditional teleportation for a mixture of single photon and vacuum input state. Top, with 3 dB of EPR correlations. Bottom, with 6 dB of EPR correlations

include this effect to be able to properly fit the output teleported states measured with an imperfect homodyne detector setup. With deterministic teleportation we could previously ignore to some extent this effect and instead include it in the estimation of the parameter r . Furthermore since the output teleported state is thermalized by the teleportation process it cannot be written as a mixture of $|1\rangle$ and $|0\rangle$ states. Therefore the effect of additional optical losses has to be calculated with the phase space model presented in Sec. 1.3.4. We assume that the output Wigner function suffer equivalent beam-splitter losses f and apply the additional Gaussian convolution to the output Wigner function $W_{\text{out}} \rightarrow W'_{\text{out}}$

$$W'_{\text{out}}(\gamma'|\xi) = \frac{1}{1-f} (W_{\text{out}}(\gamma|\xi) \circ G_\lambda(\gamma))(\gamma'), \quad (4.3.31)$$

with $\lambda = \sqrt{f/2(1-f)}$. Combining the above equation with Eq.(4.3.11), we incorporate the additional Gaussian convolution into the expression of $G(\alpha, \gamma, \xi)$ and rewrite $W_{\text{out}}(0|\xi)$ in the same form as before

$$W_{\text{out}}(0|L) = \frac{1}{N(L)} \int_{\mathbb{R}^2} d^2\alpha W_{\text{in}}(\alpha) \int_{\Lambda} G_{\text{loss}}(\alpha, 0, \xi), \quad (4.3.32)$$

where G_{loss} is given by

$$\begin{aligned} G_{\text{loss}}(\alpha, \gamma, \xi) &= \frac{1}{1-f} \int d^2\gamma' G_\lambda(\gamma') G(\alpha, \gamma/\sqrt{1-f} - \gamma', \xi), \\ &= \frac{1}{1-f} \int d^2\gamma' G_\lambda(\gamma') W_{\text{AB}}(\xi^* - \alpha^*, \gamma/\sqrt{1-f} - \gamma' - \xi). \end{aligned} \quad (4.3.33)$$

We only need to evaluate the above integral at $\gamma = 0$ and we first recalculate the new Gaussian kernel $G_{\text{loss}}(\alpha, 0, \xi)$ by performing integrations on γ' and obtain the expression

$$G_{\text{loss}}(\alpha, \gamma, \xi) = \frac{1}{\pi^2 F_0} \exp \left[-\frac{2}{F_0} (F_1 |\xi - \alpha|^2 + F_2 |\xi|^2 + F_3 |\alpha|^2) \right], \quad (4.3.34)$$

where

$$\begin{aligned} F_0 &= 1 + f^2(a - 1), & F_1 &= f^2 + (a - b)(1 - f^2), \\ F_2 &= (a - b)(1 - f^2), & F_3 &= b(1 - f^2). \end{aligned} \quad (4.3.35)$$

We now perform the integration over α in Eq.(4.3.32) to recompute Eq.(4.3.11) again. We obtain the expression of the coefficients A, B, C

$$\begin{aligned} A &= F_1^2 / \pi D^3, & C &= F_0 D / ((F_0 + F_3)(F_1 + F_2) + F_1 F_2), \\ B &= (F_1 - F_0 + F_3) / \pi D^2, & D &= F_0 + F_1 + F_3, \end{aligned} \quad (4.3.36)$$

for the $|1\rangle\langle 1|$ single photon input component and

$$\begin{aligned} A &= 0, & C &= F_0 D / ((F_0 + F_3)(F_1 + F_2) + F_1 F_2), \\ B &= -1/\pi D, & D &= F_0 + F_1 + F_3, \end{aligned} \quad (4.3.37)$$

for the $|0\rangle\langle 0|$ vacuum state input component. Figs.4.30 show $W(0|L)$ plotted against the probability of success with additional optical losses on the output mode for a single photon $|1\rangle\langle 1|$ input state. Overall, the different curves look similar to the case of optical losses on the input state before teleportation. However, the effect of losses on the output mode are weaker overall. Again, we notice that conditional teleportation is able to pull outside of the classical regime a quantum state thermalized beyond the negativity threshold $W(0|L) = 0$.

Effect of extra anti-squeezing

In the laboratory it is impossible to create a pure 2-mode EPR state exactly described by the correlation matrix Γ of Eq.(4.3.42). If two non-pure squeezed vacuum states are mixed on a half beam-splitter to create a 2-mode EPR state, it is instead usually possible to rewrite the quadrature correlations and anti-correlations of Eq.(4.3.38) as

$$\langle \hat{x}_A^2 \rangle - \langle \hat{x}_B^2 \rangle = \langle \hat{p}_A^2 \rangle + \langle \hat{p}_B^2 \rangle = e^{-2r}, \quad (4.3.38)$$

$$\langle \hat{x}_A^2 \rangle + \langle \hat{x}_B^2 \rangle = \langle \hat{p}_A^2 \rangle - \langle \hat{p}_B^2 \rangle = e^{+2(r+z)}, \quad (4.3.39)$$

where z is the extra amount of anti-correlations, equivalently the extra anti-squeezing. For unity gain deterministic quantum teleportation, even when $z \neq 0$ the contribution of z to teleportation output noise is exactly cancelled. For conditional teleportation this is not the case anymore. Looking at Eqs.(4.1.9) we see that \hat{x}_u and \hat{p}_v are sensible to the amount of extra anti-squeezing z seen by Alice. Thus the parameter z has an influence on selection and rejection of teleportation events according to Alice's homodyne photocurrent results ξ . To take it into account, we simply have to adjust the expression of $\Gamma(r) \rightarrow \Gamma'(r, z)$ with the change

$$a(r) \rightarrow a'(r, z) = (e^{+2(r+z)} + e^{-2r}) / 2, \quad (4.3.40)$$

$$b(r) \rightarrow b'(r, z) = (e^{+2(r+z)} - e^{-2r}) / 2. \quad (4.3.41)$$

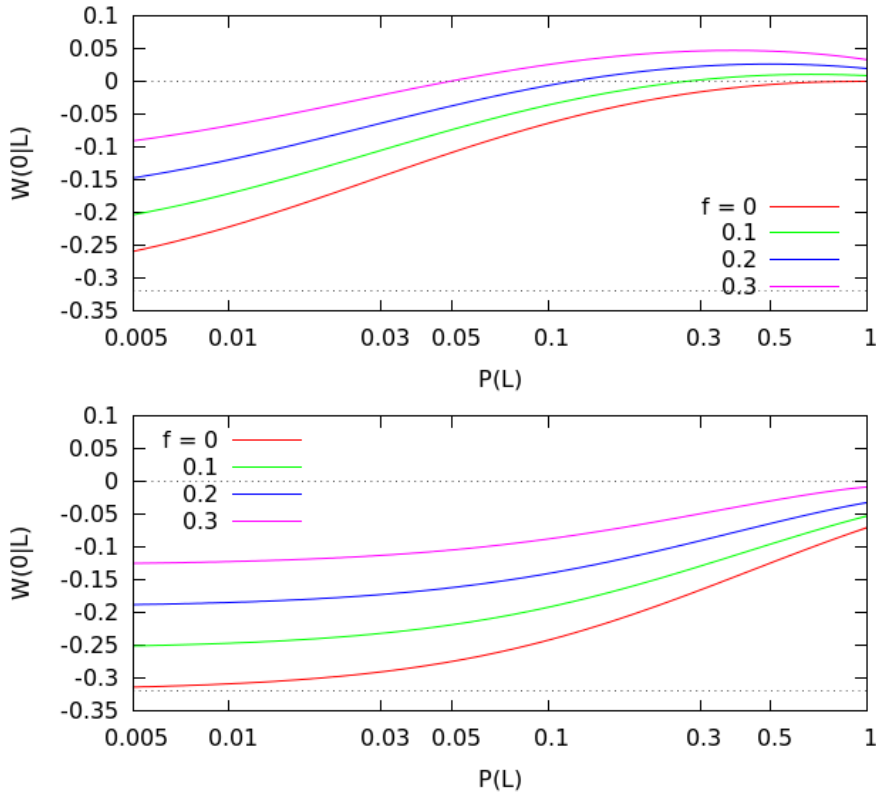


Figure 4.30: Improvement to $W(0, 0)$ with the probability of success of conditional teleportation with additional optical losses f on the output mode. Top, with 3 dB of EPR correlations. Bottom, with 6 dB of EPR correlations.

The determinant of $\Gamma'(r, z)$ is now $\det[\Gamma'] = \exp[2z]$ and we have for its inverse

$$(\Gamma')^{-1}(r, z) = \frac{\Gamma'(-r - z, z)}{\det[\Gamma'(r, z)]} = e^{-2z} \begin{pmatrix} a'(r, z) & +b'(r, z) & & \\ +b'(r, z) & a'(r, z) & -b'(r, z) & \\ & -b'(r, z) & a'(r, z) & a'(r, z) \end{pmatrix}. \quad (4.3.42)$$

From there on, we simply have to reevaluate previous integrals with this new correlation matrix and the corrected expression of the 2-mode EPR state

$$G'_{AB}(\alpha, \gamma, \xi) = \frac{1}{\pi} \exp \left[- \left(\begin{array}{c} \beta \\ \gamma \end{array} \right)^T (\Gamma')^{-1} \left(\begin{array}{c} \beta \\ \gamma \end{array} \right) \right]. \quad (4.3.43)$$

Excluding the effect of optical losses on the output mode for now the probability of success $P(L)$ is expressed with coefficients A, B and C exactly similar to Eqs.(4.3.23) and (4.3.28) for respectively a single photon input state and a vacuum state input state, provided $a(r)$ is changed to $a'(r, z)$. The non-normalized output negativity $W_{\text{out}}^u(0|L)$ is written with $W_\Lambda(A, B, C)$ using the corrected coefficients A, B and C given by

$$\begin{aligned} A &= +(a' - b')^2 / \pi D^3, & C &= D / (1 + 2(a' - b')), \\ B &= +(a' - e^{2z}) / \pi D^2, & D &= a' + e^{2z}, \end{aligned} \quad (4.3.44)$$

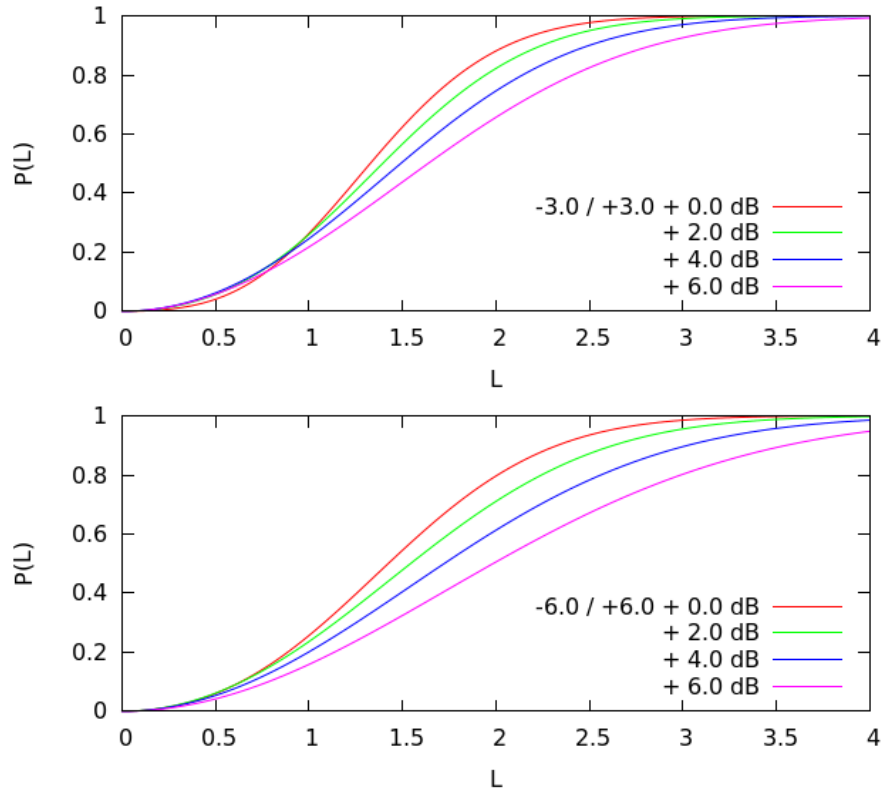


Figure 4.31: Effect of extra anti-squeezing on the evolution of the probability of success of conditional teleportation for a single photon input state. Top, with 3 dB of EPR correlations and +0,+2,+4,+6 dB of extra anti-squeezing. Bottom, with 6 dB of EPR correlations and +0,+2,+4,+6 dB of extra anti-squeezing.

for the $|1\rangle\langle 1|$ single photon input component and

$$\begin{aligned} A &= 0, & C &= D/(1 + 2(a' - b')), \\ B &= -1/\pi D, & D &= a' + e^{2z}, \end{aligned} \quad (4.3.45)$$

for the $|0\rangle\langle 0|$ vacuum state input component. In practice, conditional teleportation is very sensible to the amount of extra anti-squeezing. Looking at Figs.4.31, we notice that additional anti-squeezing reduce the probability of success. Anti-squeezing adds additional noise to the value of ξ which tends to make it fall more often outside of Λ on average. Fig.4.32 show that an extra amount of anti-squeezing quickly limits the efficiency of conditional teleportation. In practice, the noise added by anti-squeezing blinds the conditional teleportation process which cannot filter anymore the teleportation added noise efficiently.

Finally, we include the effect of additional optical losses on the output state on top of extra anti-squeezing. We repeat the procedure of the previous paragraph with the new expression of the correlation matrix $\Gamma'(r, z)$. The corrected expression of $G'_{\text{loss}}(\alpha, \gamma, \xi)$ is similar to Eq.(4.3.34) with the coefficients F'_0, F'_1, F'_2 and F'_3 now written

$$\begin{aligned} F'_0 &= e^{2z} + f^2(a' - e^{2z}), & F'_1 &= f^2 + (a' - b')(1 - f^2), \\ F'_2 &= (a' - b')(1 - f^2), & F'_3 &= b'(1 - f^2), \end{aligned} \quad (4.3.46)$$

with F'_0 being the only different coefficient compared to Eqs.(4.3.35). The algebraic expression of $G_{\text{loss}}(\alpha, \gamma, \xi)$ being unchanged with respect to those four coefficients we can directly deduce the

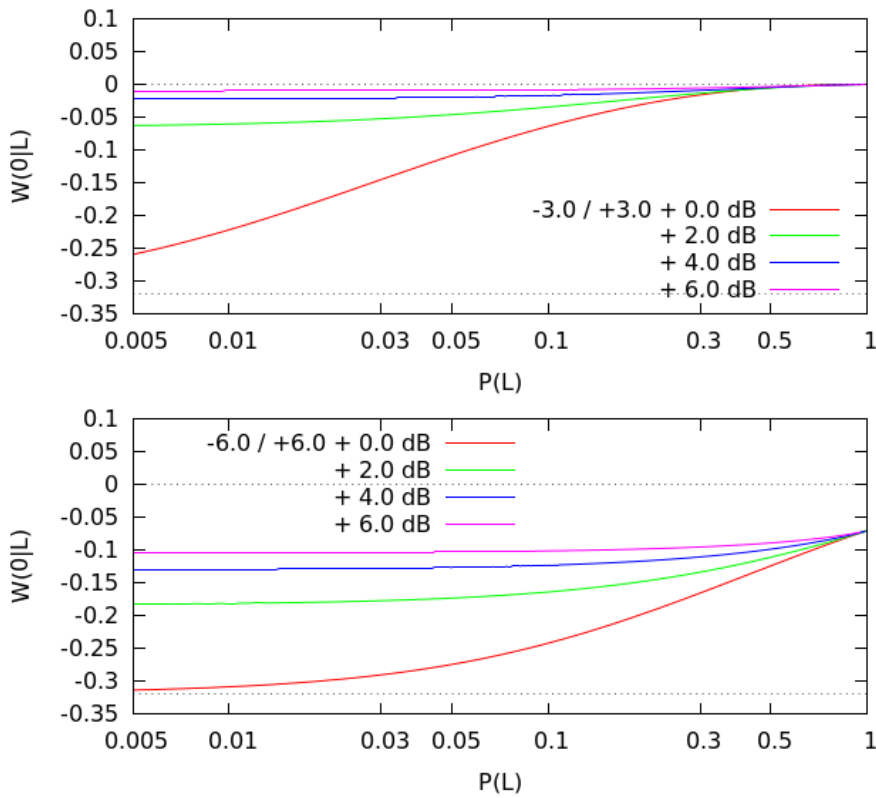


Figure 4.32: Effect of extra anti-squeezing on the improvement to $W(0,0)$ and evolution of the negativity for a single photon $|1\rangle\langle 1|$ input state. Top, with 3 dB of EPR correlations and $+0,+2,+4,+6$ dB of extra anti-squeezing. Bottom, with 6 dB of EPR correlations and $+0,+2,+4,+6$ dB of extra anti-squeezing.

expression of $W_{\text{out}}^u(0|L)$ from Eqs(4.3.36) and (4.3.37) for respectively the $|1\rangle\langle 1|$ and $|0\rangle\langle 0|$ input components.

4.3.2 Experimental Conditional Teleportation

Experimental setup The experimental setup for conditional teleportation is based on the setup for non-classical non-Gaussian states teleportation shown previously. In addition to all previously described systems a second analog to digital converter (PXI-5152[176]) is used to record Alice's \hat{x}_u and \hat{p}_v homodyne detector currents. The updated setup is shown in Fig.4.33. Instead of directly recording the output of Alice's homodyne detectors, the second ADC actually records voltage signals taken from the classical channel amplification chains. Appendix B shows in Fig.B.4 the electrical configuration of this second ADC. The second ADC is triggered by the same APD signal used to trigger the first ADC.

Homodyne detectors calibration It is necessary to carry two additional calibration procedures for both Alice's \hat{x}_u and \hat{p}_v homodyne detectors. The amplitude calibration is done in the same way as with the output state recording homodyne detector: signal modes are physically blocked off and 20000 measurements of the vacuum state are performed using FPGA generated random triggers to obtain a reading of the shotnoise level with the three homodyne detectors. The mean variance of these shotnoise traces allow to properly scale the respective homodyne photocurrent time series.

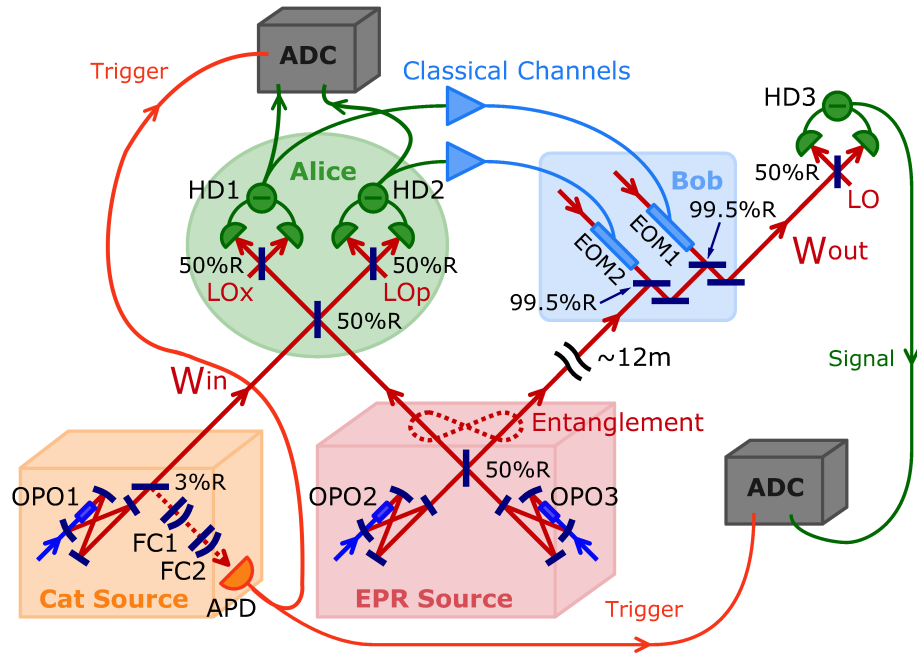


Figure 4.33: Overview of the experimental setup for conditional quantum teleportation featuring the additional analog-to-digital converter.

Because Alice's homodyne detectors are measuring the input non-classical wave-packet in front of the classical channel, there is a significant lag between the instant the wave-packet is seen right before teleportation at Alice's homodyne detectors and the instant the wave-packet is eventually measured after teleportation by the final homodyne detector. As this time lag drifts as much as the classical channel do it is necessary to independently calibrate Alice's homodyne detectors' reference time with respect to the APD. The same time calibration technique previously explained in Sec.2.3.4 is used again for both \hat{x}_u and \hat{p}_v homodyne detectors. In practice, this is done by blocking Alice's half of the 2-mode EPR resource and splitting the input non-classical wave-packet into two at the input half-beam splitter. The same wave-packet can then be directly measured by both homodyne detectors. Despite the non-classical state signal being reduced by 3 dB due to the splitting, the signature of the photon subtracted state is still clearly visible and can be used for time calibration. To the contrary of the output mode homodyne detector, it is not possible to finely tune the time calibration of \hat{x}_u and \hat{p}_v with tomography and maximisation of the negativity. This time calibration process is therefore a delicate procedure in the case of conditional teleportation.

ADCs control and synchronization The multithreaded architecture used for the control and automation of measurements presented in Sec.2.4.4 easily allows to run both ADCs in parallel. The details of this multithreaded architecture are shown in Fig.C.3 of Appendix C. In addition, although the data bandwidth requirement is doubled for conditional teleportation, data acquisition can be performed without any slowdown thanks to the fast DMA memory readout of the ADCs. Both ADCs are set at the same 1 GHz sampling rate speed. Vertical precision is set at 0.2 mV for a total dynamic range of 0.4 mV with 8 bits of precision. Inputs impedance values are set to $1 \text{ M}\Omega$ for all channels and are DC coupled.

It is important to note that the synchronization of both ADCs is automatically achieved with

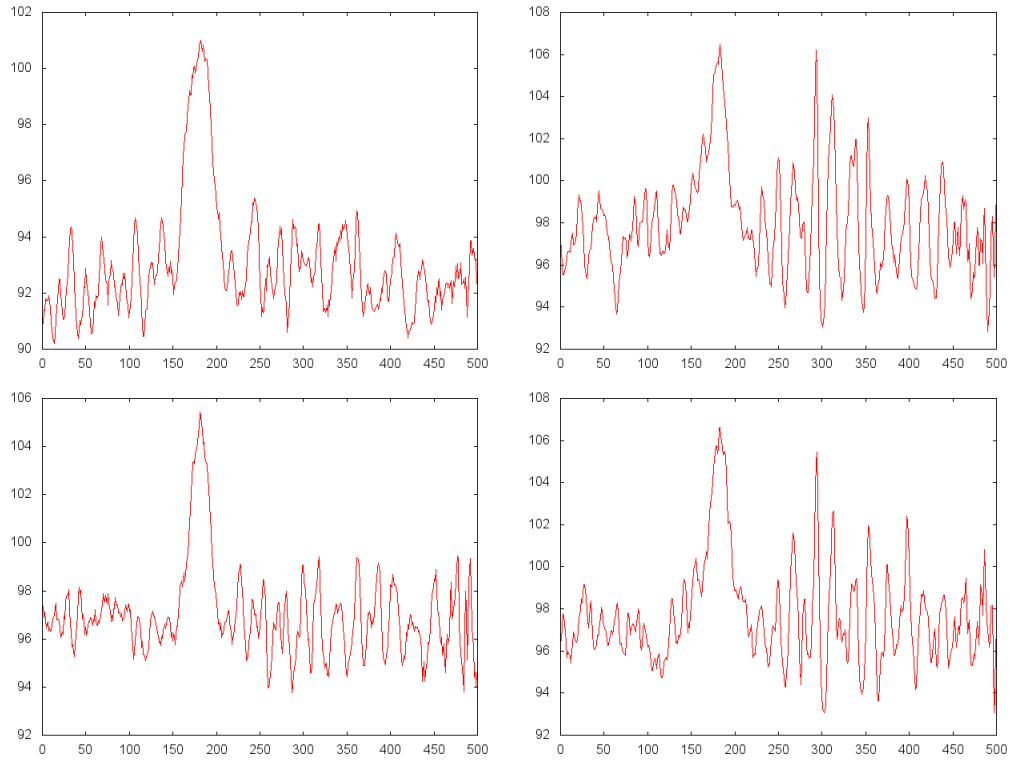


Figure 4.34: Example of experimental traces for Alice’s homodyne detectors time calibration. Point-by-point ensemble average $\langle x^2(t) \rangle$ of the quadrature photocurrent for two different experimental sessions. Top traces: first session. Bottom traces: second session. Left traces: \hat{x}_u . Right traces: \hat{p}_v . The traces for the \hat{p}_v quadrature show a ringing noise caused by the APD triggers. This noise cancelled by the mode projection function $\bar{f}(t)$ used to extract single-mode quadrature values from the homodyne photocurrent time series.

the APD trigger and the external triggers circuits controlled by the FPGA (see Fig.B.2 in Appendix B.). In practice to ensure that both ADCs record exactly the same sequences of events, the control script first turns off the APD triggers using the FPGA and starts the acquisition on both ADCs. Then a short settlement time is waited by the control script to guarantee that both ADCs are ready to acquire data and are waiting for input triggers. Finally the control script turns back on the APD triggers using the FPGA and the data acquisition automatically starts for both ADCs starting from the same first APD trigger which are not desirable for our application.

This implicit synchronization method is by far the simplest to implement. Other methods of synchronization are possible but make the data acquisition procedure more complex and less efficient in term of measurement time. It is for example possible to ask both ADCs to record individual time stamps for every triggers with a microsecond precision. Comparing the time stamps information in a post-acquisition data analysis allows to guarantee the synchronization of both ADCs records. Another technique would be to externally trigger only one ADC and program the second ADC to receive software triggers from the first APD triggered ADC. This technique is reliable for event synchronization but induces larger time jitters for every events between both ADCs time series.

Measurement and data acquisition Excluding the final calibration and measurement process the experimental protocol and alignment procedure is the same as previously explained. Since we can record the three relevant homodyne photocurrents at the same time, we do not need to perform "online" conditional teleportation. Rather we can simply perform usual deterministic teleportation as was described in the previous section and in addition to it records \hat{x}_u and \hat{p}_v photocurrents for every APD triggers. Then only later in the "offline" data analysis stage, we can look at the output teleported state for different radius L of the conditioning area. This technique allows for more consistent data analysis, because conditional negativity $W(0|L)$ can be evaluated for different values of L with the same experimental sets of data.

To be able to experimentally probe the efficiency of the conditional teleportation process at low success rates with good statistical precision, we need to acquire significantly more experimental data than for usual deterministic quantum teleportation. For one data acquisition session, we measure 400000 teleportation events in total. This longer total measurement time can pose problems with the stability of the setup, especially with phase control feedback loop which are more likely to lose their locking points as the measurement time increases. To mitigate this problem, we cut one total acquisition in 8 slices of 50000 events each and reset all feedback loops between acquisitions. All other values being equal, 400000 total events is barely sufficient when looking at conditional teleportation at the 1% success rate mark. Unfortunately, trying to acquire more events results in experimental data set plagued with experimental drifts. Paradoxically, larger experimental data sets contain more statistical uncertainties beyond a certain experimental measurement time.

4.3.3 Experimental results

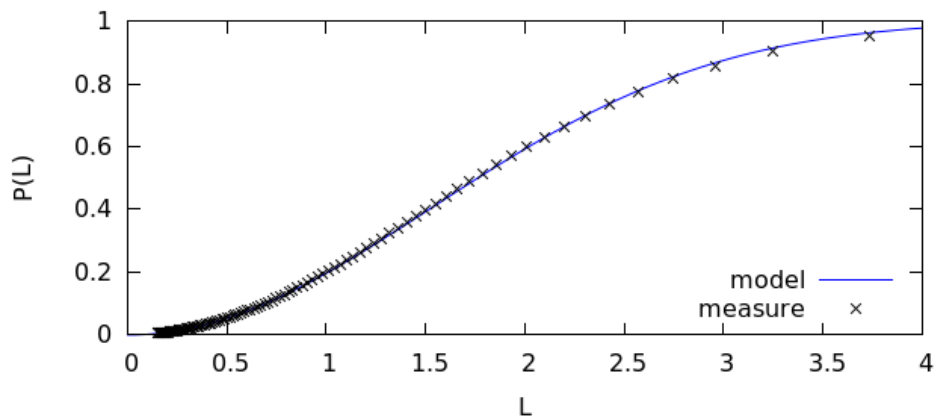


Figure 4.35: Experimental probability of success of teleportation and its evolution with the value of L . The experimental curve is fitted with the models developed in the previous section.

To estimate the conditional output negativity $W_{\text{out}}(0, 0|L)$ from experimental data we employ the following procedure. We start with the finite set of quadruplets of numbers $S(J) = \{x_i, \theta_i, \bar{x}_i, \bar{p}_i\}_{i \leq J}$ where J is the total number of experimental events, x_i and θ_i the usual quadrature and phase values at the output teleported mode homodyne detector, and \bar{x}_i and \bar{p}_i are the quadrature values at Alice's \hat{x}_u and \hat{p}_v homodyne detectors for the same trigger event. To obtain the three values x_i , \bar{x}_i and \bar{p}_i , the same mode projection function $\bar{f}(t)$ as before is used on the raw homodyne photocurrent time series, with different time calibration parameters for x_i on the one hand and for \bar{x}_i and \bar{p}_i on the other hand. In addition, Alice's homodyne photocurrents are DC filtered to remove any bias in the mean voltage values. Once the set of quadruplets

$S(J) = \{x_i, \theta_i, \bar{x}_i, \bar{p}_i\}_{i \leq J}$ is obtained it is sorted according to the metric $\bar{x}_i^2 + \bar{p}_i^2$ into the sequence

$$S_\sigma(J) = \{x_{\sigma(i)}, \theta_{\sigma(i)}, \bar{x}_{\sigma(i)}, \bar{p}_{\sigma(i)}\}_{i \leq J}, \quad (4.3.47)$$

where $\sigma(i)$ is the permutation function which guarantees that for any $i < j$

$$\bar{x}_{\sigma(i)}^2 + \bar{p}_{\sigma(i)}^2 \leq \bar{x}_{\sigma(j)}^2 + \bar{p}_{\sigma(j)}^2. \quad (4.3.48)$$

From the sequence of sorted experimental data point $S_\sigma(J)$ we can easily compute the parametric curve ($x = L, y = P(L)$) for the probability of success of conditional teleportation. We simply discard events by looking at successive sub-sequences $S_\sigma(J')$ for $J' < J$ and estimate L and $P(L)$ with

$$L = (\bar{x}_{\sigma(J')}^2 + \bar{p}_{\sigma(J')}^2) / 2, \quad (4.3.49)$$

$$P(L) = J'/J. \quad (4.3.50)$$

Fig.4.35 shows experimental results of the evolution of the probability of success of conditional teleportation $P(L)$ with the value of the parameter L . The experimental curve is fitted with the models developed in Sec.4.3.1 with 6.7 dB of EPR correlations, 4.1 dB of extra anti-correlations, and 20% of optical intensity loss on the input mode. Overall the theory fits well and is in good agreement with the experimental results. In addition, for all the different data acquisition sessions, the results are very similar and consistent between themselves. Therefore we only present one set of data for $P(L)$ in this paragraph.

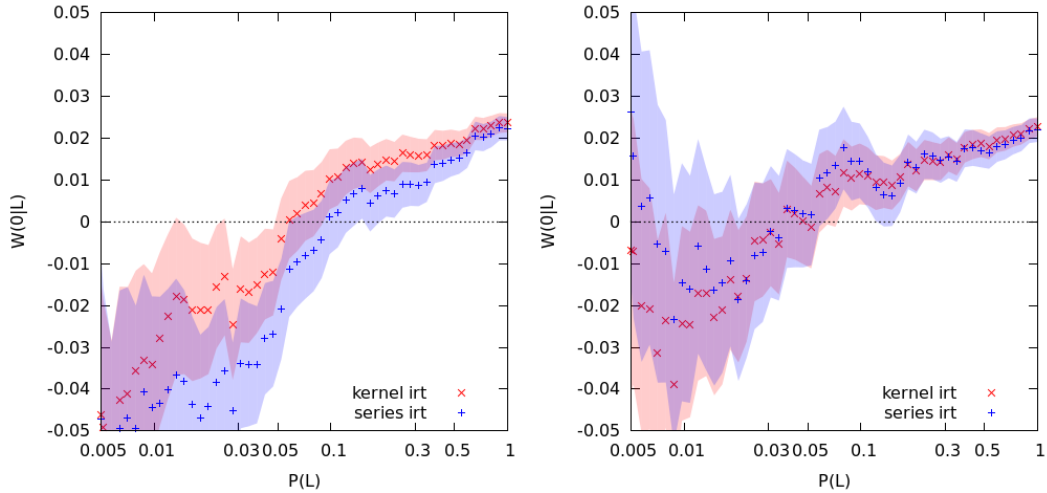


Figure 4.36: Improvement of negativity $W(0|L)$ with the probability of success $P(L)$, for experimental data sets #1 (left) and #2 (right). The negativity is independently estimated with the filtered back-projection algorithm (red traces) and the polynomial series decomposition algorithm (blue traces). Error bars are plotted with the estimators presented in Sec.3.4.1. $P(L) = 1$ corresponds to an experimental data set made of 400000 data points.

The output negativity $W_{\text{out}}(0|L)$ is estimated using the inverse Radon transform with the detection events satisfying the condition $\bar{x}_u^2 + \bar{p}_u^2 \leq 2L^2$. This is again done by calculating $W_{\text{out}}(0|L)$ on successive sub-sequences $S_\sigma(J')$. For an homogenous estimation of $W_{\text{out}}(0|L)$ in logarithmic scale over the axis $P(L)$, we employ the sequence of J' values defined by $\{J'_{(n)} = \rho^n\}_n$ with for example $\rho = 0.9$. We use both the polynomial series decomposition algorithm with $L = 10.0$,

$M = 30$ and the filtered back-projection kernel algorithm with $k_c = 7.0$ for the practical estimation of $W_{\text{out}}(0|L)$ (see Sec.3.2). Compared to the maximum likelihood iterative reconstruction of the density matrix there are two benefits. First, we have in both case a simple and direct estimate of the statistical error in the estimation of $W_{\text{out}}(0|L)$. Second, we are guaranteed that there is no ensemble effect of any kind when using linear methods. A third practical advantage is the greater speed of computation using the linear methods.

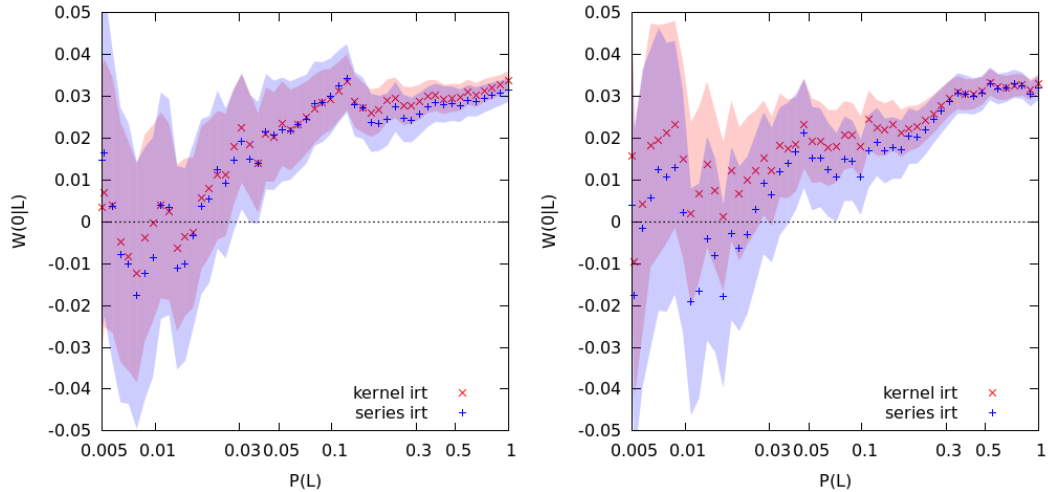


Figure 4.37: Improvement of negativity $W(0|L)$ with the probability of success $P(L)$, for experimental data sets #3 (left) and #4 (right). The negativity is independently estimated with the filtered back-projection algorithm (red traces) and the polynomial series decomposition algorithm (blue traces). Error bars are plotted with the estimators presented in Sec.3.4.1. $P(L) = 1$ corresponds to an experimental data set made of 400000 data points.

Figs.4.36, 4.37 and 4.38 show the evolution of the negativity $W_{\text{out}}(0|L)$ with the probability of success of conditional teleportation for different sets of experimental data points. Rather than plotting $W(0|L)$ against the value of the conditioning radius L which has an arbitrary scale, we plot the parametric curve ($x = P(L)$, $y = W(0|L)$) which tells how much conditioning it takes to obtain a target gain in output negativity. Six experimental data sets are shown in three different pairs, with varying degree of success of conditional teleportation:

- The data sets #1 and #2 shown in Fig.4.36 are the ones where the effect of conditional teleportation is the most clearly visible. In this case it can be said that the experiment is a success. Starting from a raw output state which is measured to have a positive reconstructed Wigner function, we see that conditional teleportation can extract the underlying non-classical features of the quantum state by removing enough noisy experimental points. In Sec.4.3.1 we saw that this situation corresponds to the presence of optical losses on the input or output modes of teleportation.
- With data sets #3 and #4 the effect of conditional teleportation is still clearly visible but not as strong. Unfortunately, the effect is not strong enough to recover the non-classical features of the input non-Gaussian state and observe negativity in the Wigner function. However, the $W_{\text{out}}(0|L) = 0$ threshold can still be reached eventually.
- Data sets #5 and #6 are examples of measurement sessions where conditional teleportation has almost no effect. Several explanations are possible but we suspect that for this particular

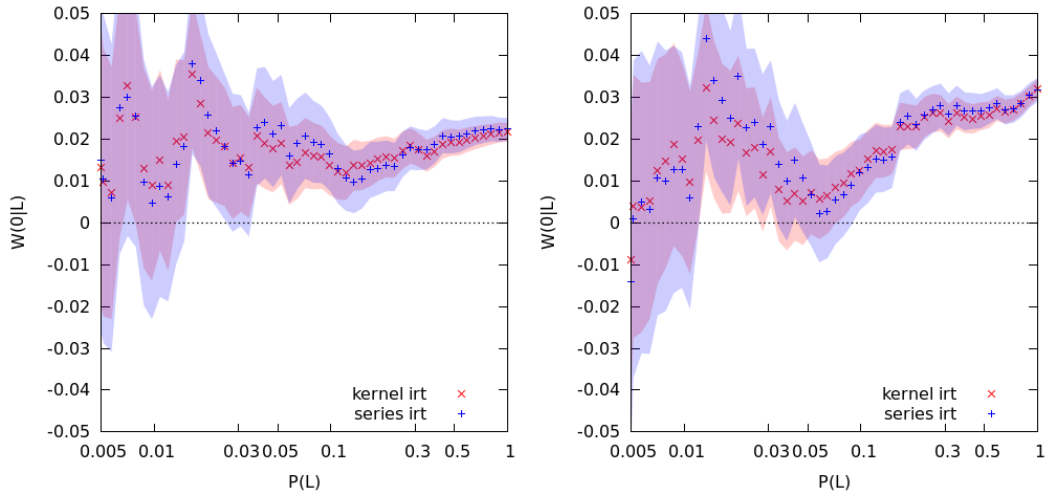


Figure 4.38: Improvement of negativity $W(0|L)$ with the probability of success $P(L)$, for experimental data sets #5 (left) and #6 (right). The negativity is independently estimated with the filtered back-projection algorithm (red traces) and the polynomial series decomposition algorithm (blue traces). Error bars are plotted with the estimators presented in Sec.3.4.1. $P(L) = 1$ corresponds to an experimental data set made of 400000 data points.

measurements the EPR correlation level was much lower than usual, which resulted in the complete thermalization of the output teleported state.

In Figs.4.39 and 4.39 we show reconstructed Wigner functions for the experimental data sets #1 and #2 for three different values of L that yields 1, 0.1 and 0.01 for $P(L)$. Looking at the central negative dip, we see a clear improvement in both cases with conditional teleportation. The purity of the conditionally teleported quantum state is also found to increase with conditional teleportation. The following table summarizes this increases in purity:

	data set #1		data set #2	
$P(L)$	series	maxlik	series	maxlik
1.0	0.27	0.29	0.31	0.33
0.1	0.28	0.31	0.33	0.35
0.01	0.29	0.32	0.36	0.37

Although we have developed a complete model of conditional teleportation in Sec.4.3.1, we found out it was not possible to fit the experimental results efficiently. Fig.4.41 shows an attempt to fit the curves of data set #2 with our model. Overall, the experiment is found not to perform as well as expected by the model. There are several possible reasons for this discrepancy. According to our analysis procedure to obtain estimates of $W_{\text{out}}(0|L)$ and $P(L)$, we can safely discard normalization and scaling problems. The first possible explanation are related to limitations in the

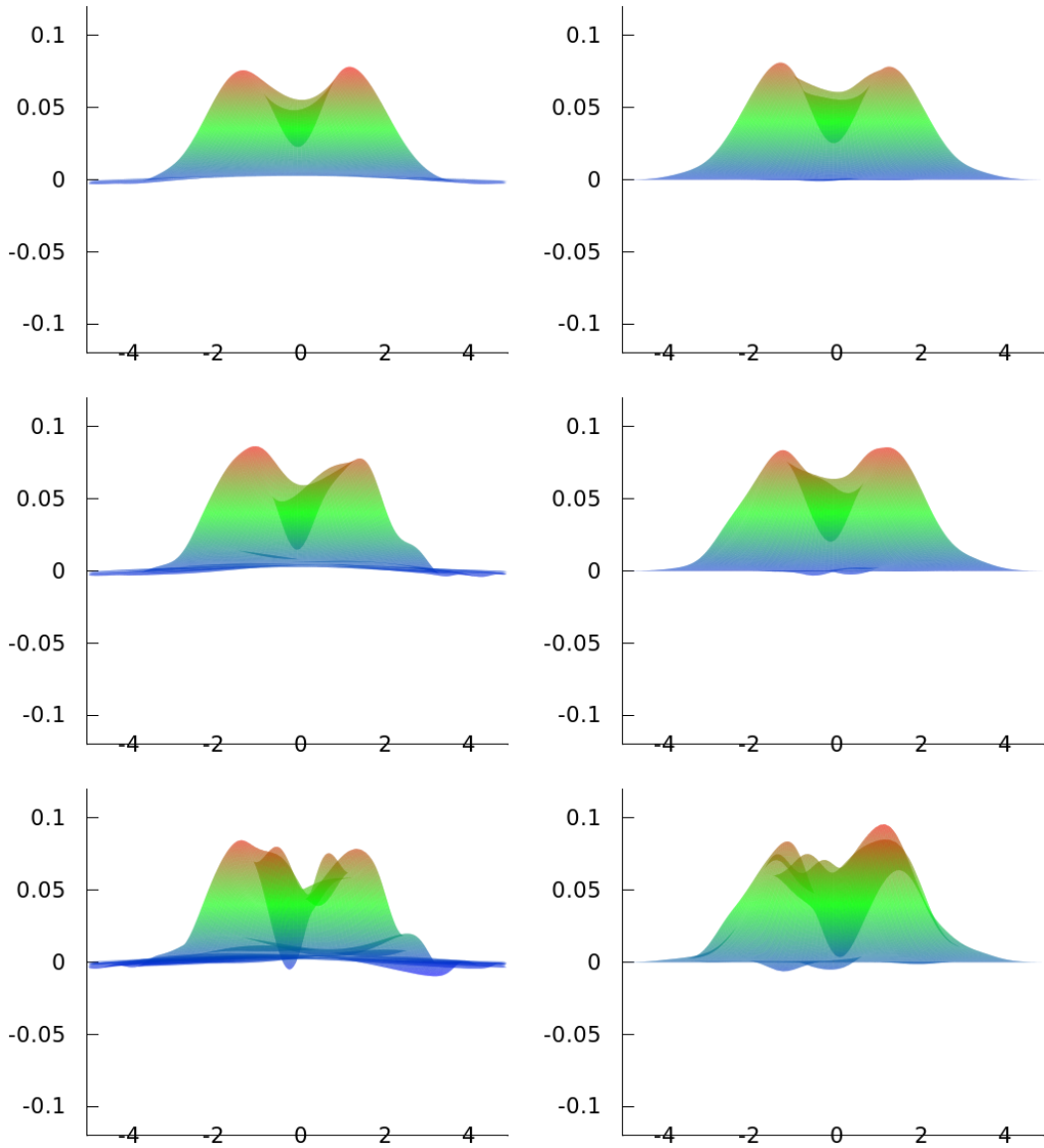


Figure 4.39: Effect of conditional teleportation on the Wigner function for experimental data set #1. On the left, Wigner functions reconstructed with the polynomial series decomposition algorithm. On the right, Wigner functions reconstructed with the maximum likelihood iteration algorithm. Top row, $P(L) = 1.0$, 400000 experimental data points. Middle row, $P(L) = 0.1$, 40000 experimental data points. Bottom row, $P(L) = 0.01$, 4000 experimental data points.

model itself. We recall that we omitted to take squeezing into account for instance. However given the fact that our state is only weakly squeezed we think it should not have such an influence on the behavior of $W_{\text{out}}(0|L)$. Another possibility is the underestimation of external uncorrelated noise added by Bob's displacement operation in the teleportation operation. In practice such noise cannot be seen by Alice's homodyne detector and thus it is not possible to filter it with conditional teleportation. This could explain why the experimental curves seem to lag behind the model in term of improvement to $W_{\text{out}}(0|L)$ for equal values of $P(L)$. In deterministic teleportation it was possible to ignore this subtle point and instead use a single effective EPR correlation parameter r_{eff} taking into account these additional uncorrelated noise sources. Finally, our model is a pure

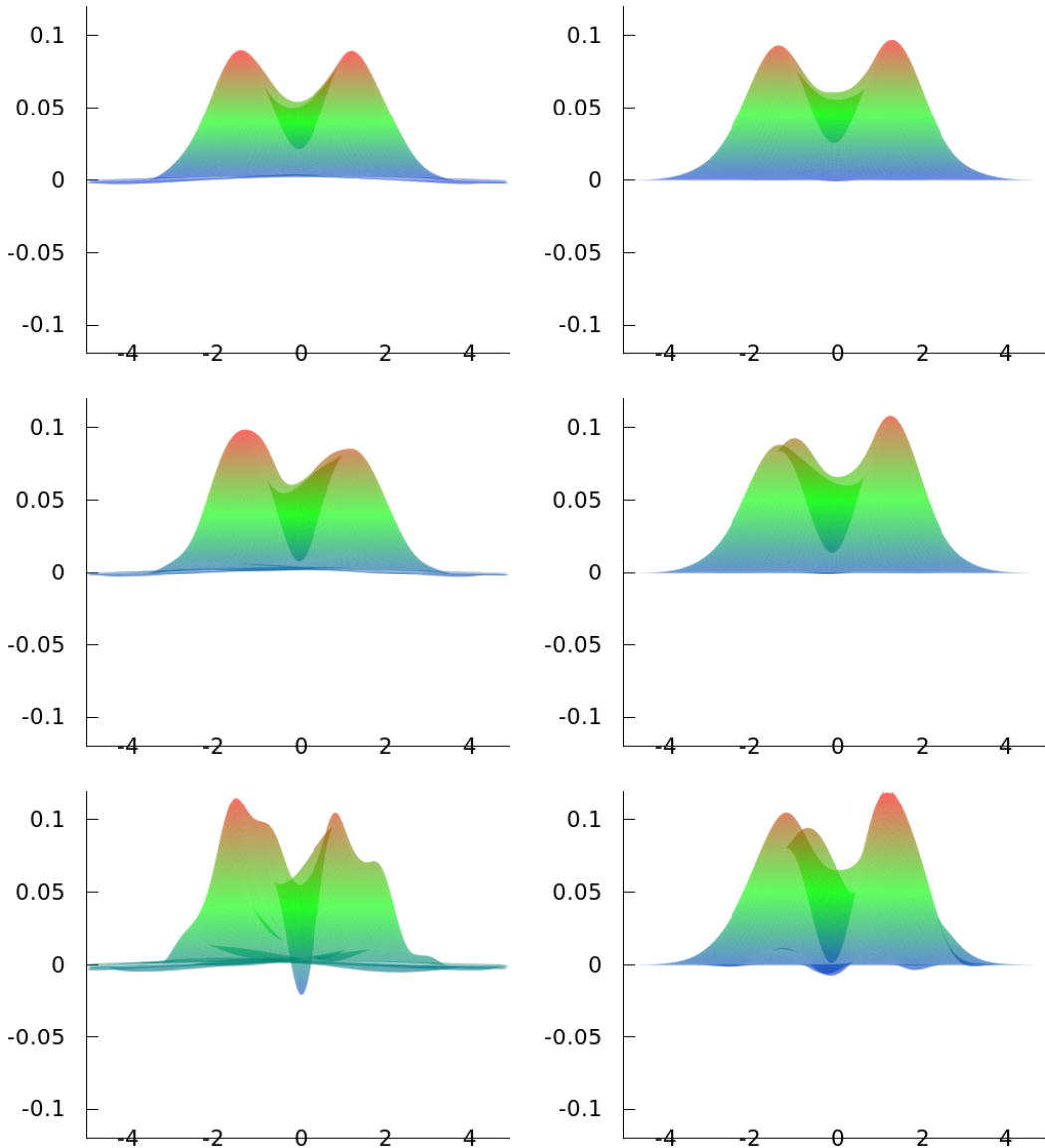


Figure 4.40: Effect of conditional teleportation on the Wigner function for experimental data set #2. On the left, Wigner functions reconstructed with the polynomial series decomposition algorithm. On the right, Wigner functions reconstructed with the maximum likelihood iteration algorithm. Top row, $P(L) = 1.0$, 400000 experimental data points. Middle row, $P(L) = 0.1$, 40000 experimental data points. Bottom row, $P(L) = 0.01$, 4000 experimental data points.

monomode model which ignore the complex multimode properties of broadband teleportation and puts itself after the mode projection of the homodyne photocurrent times series with $\bar{f}(t)$. Besides the approximation of single mode teleportation, it is possible that some specific noise in some particular frequency range lowers the efficiency of conditional teleportation filtering. With regards to these issues, we believe it may be possible to refine the analysis procedure in order to extract more information from the photocurrent time series of Alice's \hat{x}_u and \hat{p}_v homodyne detectors. Despite these problems, our experimental results clearly demonstrate the effect of the conditional teleportation protocol and its ability to induce improvement in the negativity of the output Wigner function. Especially, we have observed that conditional teleportation can pull out negativity from

a state which appears to be a state with a positive Wigner function when measured with additional optical losses or insufficient detection efficiency.

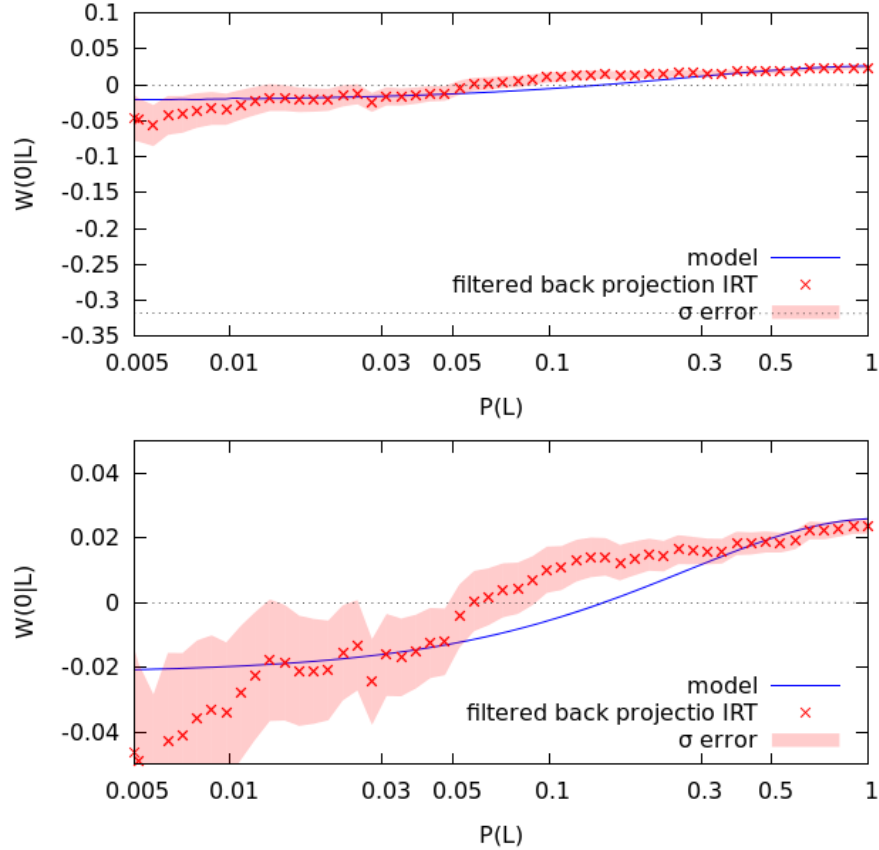


Figure 4.41: Effect of conditional teleportation on $W_{\text{out}}(0|L)$, model against experimental results for the data set #2. The model curve is traced with 3.8 dB of EPR correlations, 5.8 dB of anti-correlations, 0.2 intensity losses on the input mode and 0.04 intensity losses on the output mode.

Conclusion:

4.4 Summary

In this thesis manuscript we have presented the main results of three years of research on quantum teleportation of non-Gaussian non-classical quantum states of light. Besides the technical aspects of this experiment and the main experimental results, we have also presented in details several theoretical questions and demonstrated several results in the context of our experimental studies. Overall, the work presented in this manuscript has been of several nature, including experimental results, featuring measurement and automation implementation and engineering, developing theoretical analysis and numerical algorithms. As much as we could we have tried to keep an appropriate balance between these subjects despite their variety. As a conclusion we first review these experimental and theoretical results chapter after chapter.

In chapter 2 We have presented the photon subtraction protocol and its experimental implementation. We have presented and analysed in details our experimental results of generation of non-classical quantum states and we have shown that we could closely approximating small amplitude Schroedinger's cat states. Our experimental results have demonstrated the reliable generation of highly non-classical quantum states of light with the experimental observation of strong negativity values and high purity of the reconstructed Wigner functions. As far as we know, this particular experimental setup remains until now unmatched in term of negativity and purity for generation of optical Schroedinger's cat states. Furthermore we have also developed a complete phase space model of our photon subtracted states matching the experimental results and including the relevant experimental parameters for the regime in which we operate. In addition in our theoretical analysis we have shown how a multimode model was necessary to take precisely the wave-packet nature of these states and their temporal characteristic into account in the homodyne measurement process and the tomography of the Wigner function.

In chapter 3 We have presented our work and results on quantum tomography and reconstruction algorithms of the Wigner function. We have first given the basis of the usual filtered back-projection algorithm and explained the main reason for its weak performances against statistical noise. We have also introduced the projection-slice theorem and the relation between phase space, Fourier space and the marginal distribution. We then have shown that it is possible to link three families of orthogonal functions between these three spaces to decompose $p(x, \theta)$ the marginal distribution, $W(q, p)$ the Wigner function, and their Fourier transforms. We have shown that the Radon transform preserves the orthogonality of these families and therefore takes an especially simple form in this framework. In other word we have shown and demonstrated a new technique for optical homodyne tomography based on polynomial series expansion of the Wigner function. We have explained and applied to experimental and simulated data the most straightforward implementation of that technique with a direct linear estimation of the coefficients of the polynomial series expansion. We have presented the reconstruction methods based on variational principles

such as the maximum likelihood reconstruction method, and have explained how these techniques could be also applied to the polynomial series expansion of the Wigner function. Finally we have provided estimators of the statistical reconstruction errors and shown that it performs better than filtered back-projection tomography with respect to reconstruction artifacts and statistical errors. We have also shown that it can perform better than maximum likelihood iterative reconstruction of the density matrix in the context of low purity quantum states.

In chapter 4 We have presented our theoretical work and experimental results on quantum teleportation of non-classical wave packets of light. We have shown in details our experimental setups and shown experimental results of broadband teleportation for Gaussian input states and non-Gaussian input states. Especially, the reconstructed Wigner functions of the latter after teleportation show negative areas and therefore demonstrate the success of quantum teleportation of non-classical features of the input state. We have shown that in this broadband regime a careful multimode model of both the non-classical input state and the broadband teleportation apparatus were necessary to understand the exact behavior of the experimental apparatus and predict precisely the value of the negativity and the shape of the Wigner function at the output of the teleporter.

In addition, we have introduced the idea of Gaussian conditional teleportation to balance a continuous variable teleportation apparatus between determinism and a lower amount of errors. We have shown experimentally that a simple conditioning done with Alice's measurements can be used to increase the negativity and the purity of the output teleported quantum state. We have also shown that it is possible to predict with good accuracy the probability of success of conditional teleportation, and with correct behavior the evolution of negativity at the output of the teleporter when using conditional teleportation.

Concluding remarks On the experimental side, we were able to bring the previous generation of continuous wave continuous variable experiments to a new level. The teleportation of non-classical state in a broadband regime is a new state-of-the-art reference in this domain. On the one side, we found that the broadband regime for wave-packet teleportation was much more challenging than the sideband regime, requiring additional care. Experimentally, it implies a number of additional components, such as fast optical switches, complex measurements and control triggering, feedback control circuits with switchable operations. The electronics requirements are more than all the hardest to meet. Developing fast wideband amplifiers and filters with in addition uniform gain characteristic is very hard. Due to the design notes commanding minimal latency and high bandwidth, such circuits had in addition to be made fully analogical. On the other side, the successful teleportation of non-classical features of the Wigner function is a straightforward task. Once the broadband electronics have been constructed up to specification, the switching apparatus and optical setup tuned, and the sources of noise tamed, success or failure is essentially a matter of how much squeezing is available. To reach the required parameters for negativity teleportation, only higher purity and higher squeezed light is necessary. Our theoretical analysis has showed that with good quality non-Gaussian input states, these required parameters are somewhat reasonable, at least experimentally achievable, with squeezing values under the 8 dB mark. Finally at the occasion of increasing the efficiency of the experimental setup further, quite a lot of work has been done on the systematic automation of control and measurements for this experiment.

On the theoretical side, we have shown several interesting results around the subject of multimode teleportation. We have developed an efficient yet simple framework to model the properties of multimode continuous variable teleportation. Although this work is tied to a specific class of non-Gaussian states, it is natural to ask if a similar approach can handle more general non-Gaussian states. As it is known that any Wigner function can be approximated by successive displacements

and photon subtractions, it is in principle possible to describe any non-Gaussian states in a systematic way that would be compatible with the Gaussian convolutions needed in our model. A second and harder issue would be to identify criteria more robust than negativity to decide on the success of teleportation and Gaussian operations in general in the context of non-Gaussian non-classical input states. Although quantum teleportation is in some sense an aging discovery by today standards, we believe there are still some interesting questions to answer.

We have proposed a simple multimode model for single photon subtracted squeezed vacuum states. Although a number of theoretical results already exists for this family of states, most of them are blind to certain experimental conditions, or need some substantial adaptation to be applied to realistic scenarios, essentially due to the complex multimode properties of these states. Our model was specifically developed for the purpose of analysing our experimental setup, and we have therefore carefully taken into account these issues. We have achieved the development of a complete rigorous model starting from the multimode expression of the squeezing operator and APD measurement operator and ending at the single mode expression of the mode projected homodyne photocurrent. Especially we have shown that a rigorous multimode model for a quantum state does not make sense without also a multimode model for the measurement operation.

In both teleportation and photon subtraction cases, we notice that the weak point of previous analysis is in the efficient treatment and consideration, if any, of multimode quantum optics. As future quantum optics experiments will rely more and more on the application of the photon subtraction method, which implies in some way or another complex multimode properties, we believe that significant progress will be achieved in the near future to adapt a number of existing theories and proposals to the relevant experimental context. Furthermore, the complex multimode properties of light have been already used as an asset to create interesting states (see for example [143]) and we believe that more experiments using these features to generate more complex quantum states will also appear in the near future.

On the tomography side, since the maximum likelihood technique was applied to the reconstruction of the density matrix[87], it was widely accepted as the method of choice for optimal tomography of a single quantum mode, and thought superior to the inverse Radon transform. We have proved that it is not necessarily the case and that linear methods are also relevant according to the situation and the statistical properties of the quantum state to reconstruct. As we explained in Chap.3, Sec.3.3.3, it would be interesting to apply variational methods to the polynomial series reconstruction method we have introduced to diagonalise the Radon and inverse Radon transforms. Also, we think that better criteria for the distinction between classical and non-classical states are needed, a question which is inherently linked with quantum tomography. One possible objective would be to have a simple test criterion which from an experimental set of quadrature values could without any ambiguity detect the non-Gaussian character and high enough purity for the presence of negativity in the Wigner function without reconstructing it. We therefore believe in the likely existence of unexplored possibilities for quantum tomography of a single quantum mode.

Finally, it is interesting to ask ourselves if conditional teleportation is simply an algorithm based on post-selection and therefore not really relevant to any application, or if conditional teleportation can be applied and be used to genuinely provide better teleported states. In the current state of knowledge this question is certainly still open and cannot be fully answered. However, we will emphasize three facts that defend the latter opinion:

- Firstly, the selection process is done for every individual input state independently from all the other experimental events. Furthermore, we have been especially careful to use a linear quantum tomography algorithm which guarantees that all experimental events are treated equally as independent events. Therefore, it is safe to assume that the improvement of negativity at the output of the teleporter is free from any ensemble effect.

- Secondly, in the case that the teleported output state right after teleportation is not anymore a classical state, conditional teleportation cannot be used to bring back negativity into the Wigner function. This is consistent with the fact that it is only a classical operation not involving any non-classical operations.
- Thirdly, we notice that there are some quantum circuit situations where conditional teleportation is useful in a straightforward way. For example, if a non-Gaussian state generated with optical means has to be teleported with additional noise into a quantum memory, conditional teleportation can be used to genuinely improve the state inside the quantum memory for a second stage demonstration.

In conclusion, conditional teleportation can be seen as an advanced technique of noise filtering where information at the output of the teleporter which is judged too noisy is progressively removed from the final experimental data set.

Appendix A

FPGA digital program and circuitry

This appendix presents the complete digital circuit of the PXI-7833 FPGA[175] used in the experimental setup, shown here in the Labview FPGA graphical language. For more information about Labview FPGA programing, online ressources are available at [178]. For more information about the electrical diagram around the FPGA I/O pins, see Appendix B.

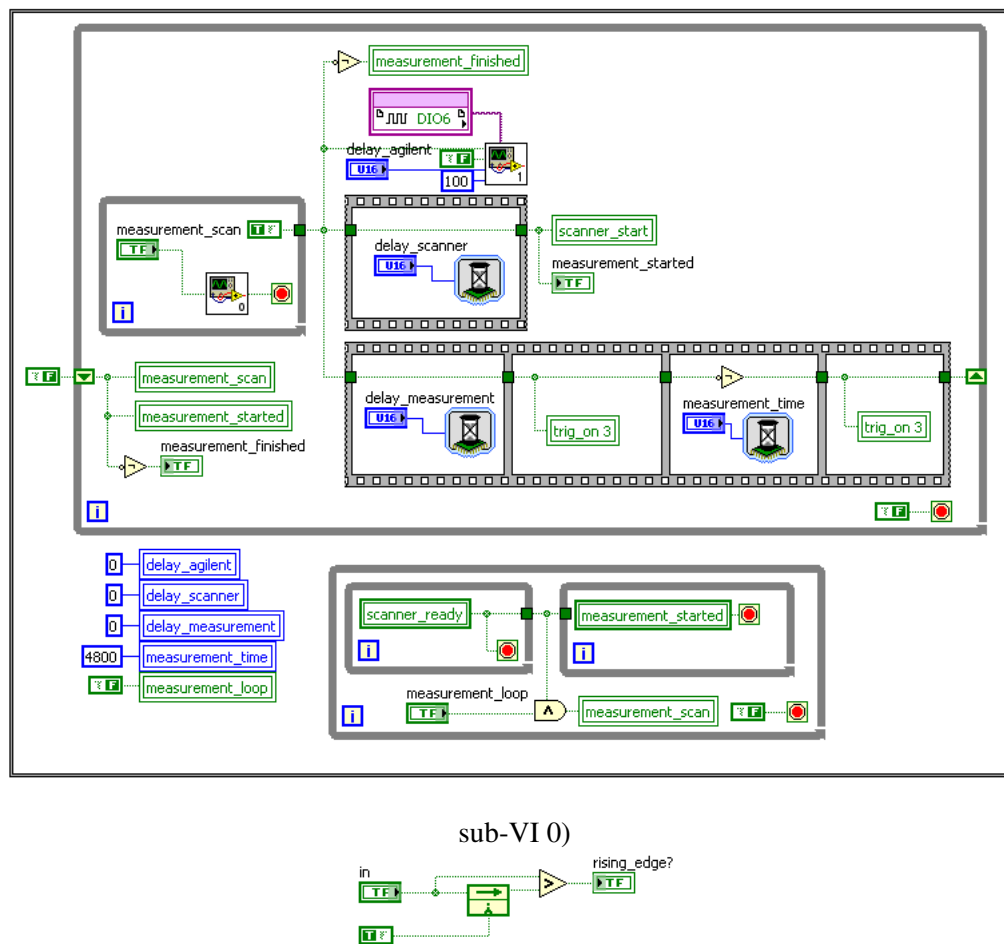


Figure A.1: Top, circuit for synchronisation and looping of local oscillator phase scanning sequences (see Fig.A.3), locking triggers (see Fig.A.2), and time gating of the APD triggers (see Fig.B.2). Bottom, sub-VI 0) circuit for detection of rising digital edge.

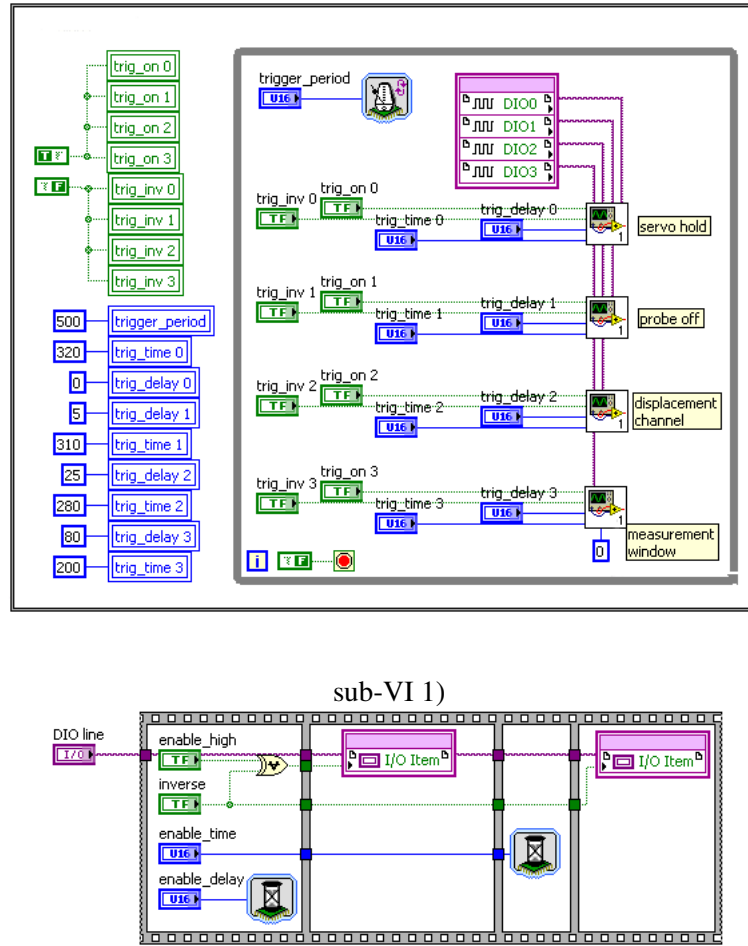


Figure A.2: Top, circuit for triggers generation and synchronisation. Bottom, sub-VI 1) circuit for generation of a single square wave period.

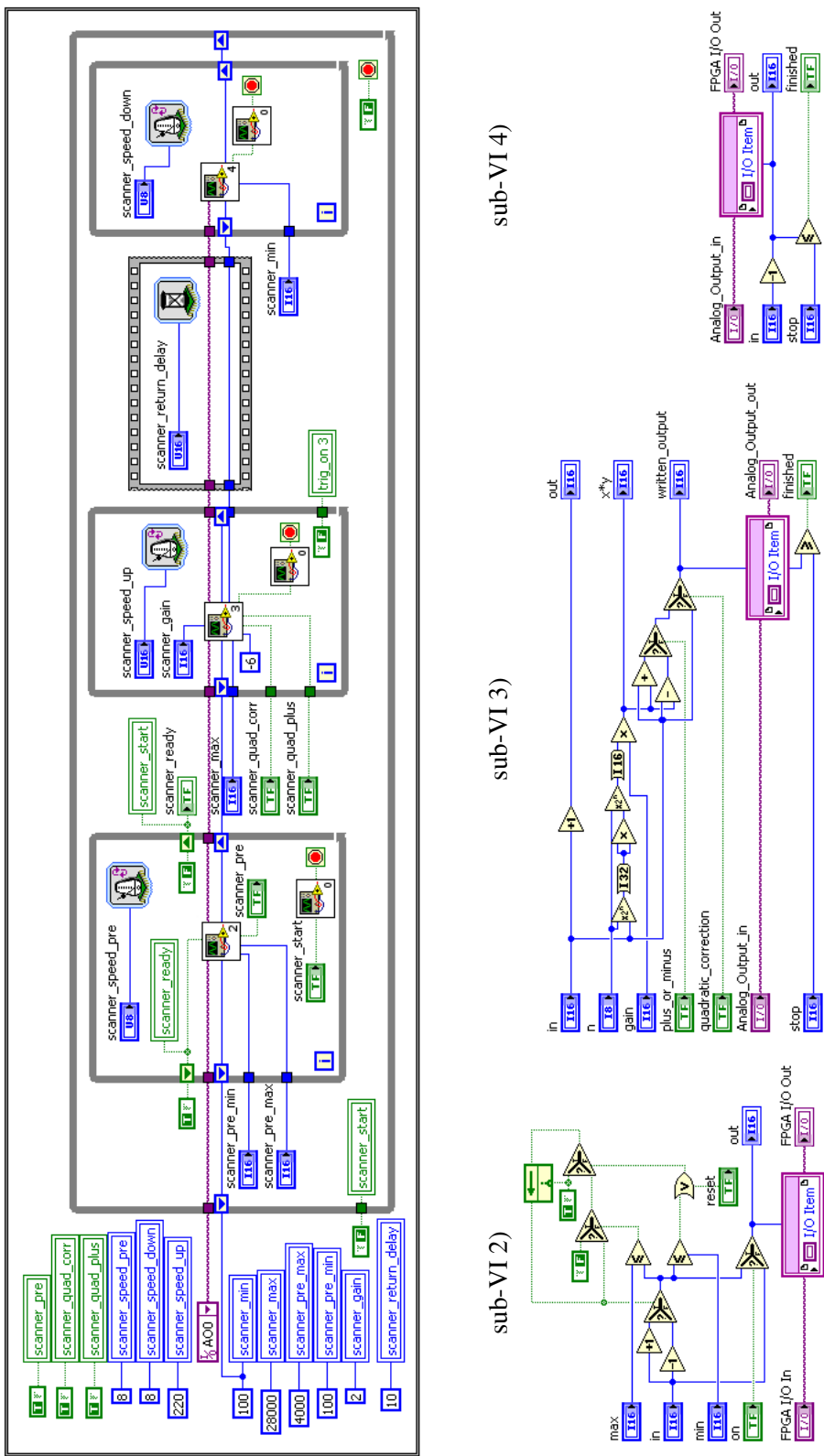


Figure A.3: Top, circuit for generation of the analogical voltage ramp applied to the PZT and used for scanning the local oscillator phase. Bottom left, sub-VI 2) triangle wave generator with programmable amplitude and offset values. Bottom center, sub-VI 3) linear ramp generator with harmonic correction. Bottom right, sub-VI 4) linear ramp generator.

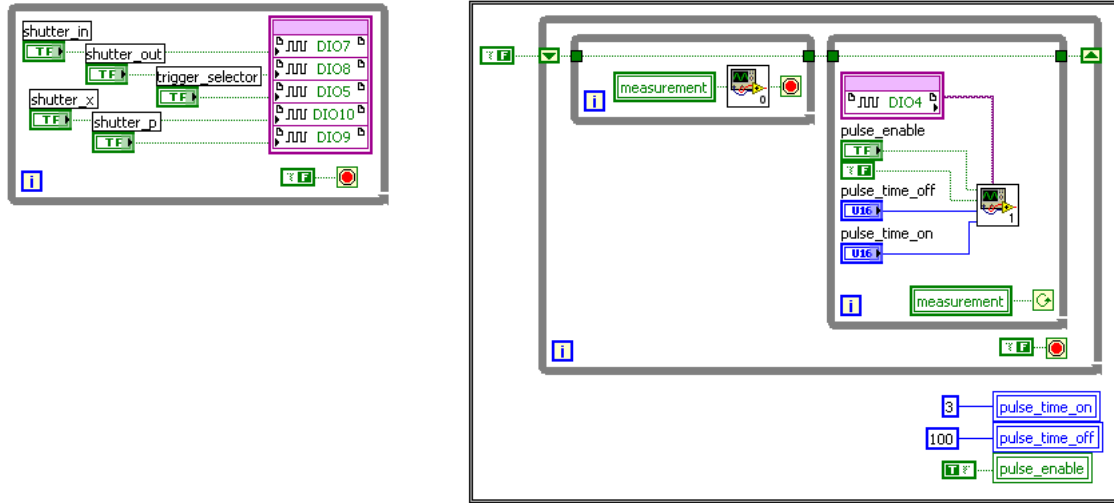


Figure A.4: Left, circuit for the direct control of mechanical shutters. Right, circuit for generation of fake APD triggers used in various measurement protocols of the vacuum state of light.

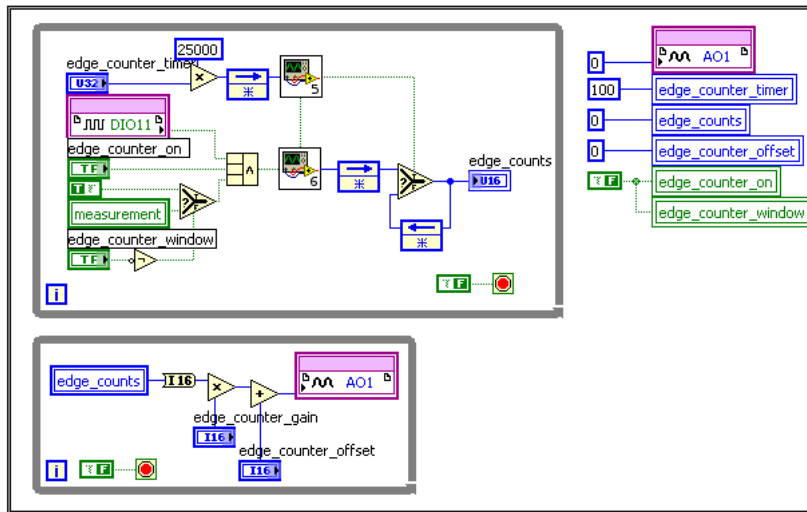


Figure A.5: Top, circuit for counting of the rate of APD triggers over length-programmable intervals of time. Bottom left, sub-VI 5) self-reset counter. Bottom right, sub-VI 6) rising digital edges counter with external synchronous reset.

Appendix B

Control and automation setup

This appendix shows the complete connections of the different digital triggers, analogical signals and hardware equipments used in the measurement and the alignment phases. For more information about the programing of the FPGA chip, see Appendix A. For more information about the general programing architecture and driver software interface, see Appendix C.

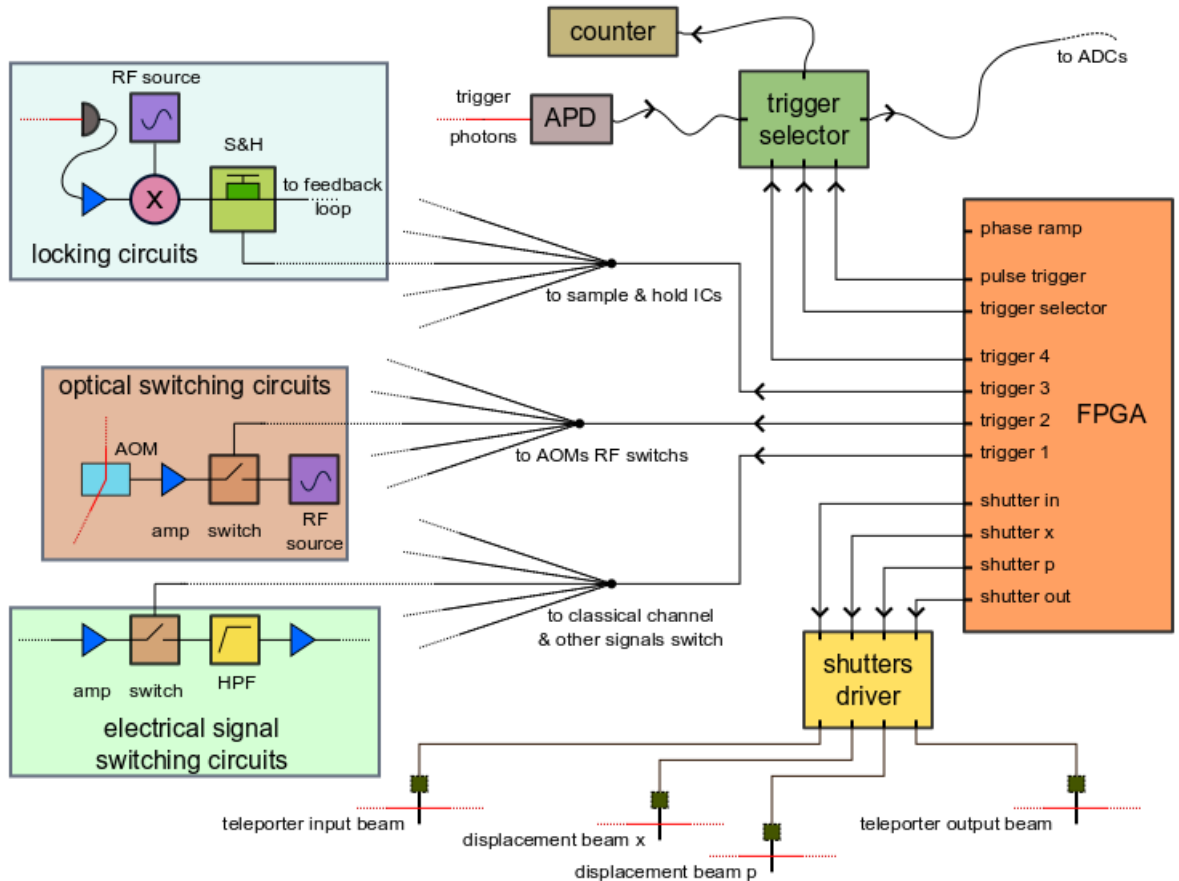


Figure B.1: External connection of FPGA generated signals. For details on ADC connection, see Fig.B.4. Fig.B.2 shows details on the digital circuit of the external trigger selector. Details on the analogical locking, optical switching and electrical signal switching circuits can be found in [166].

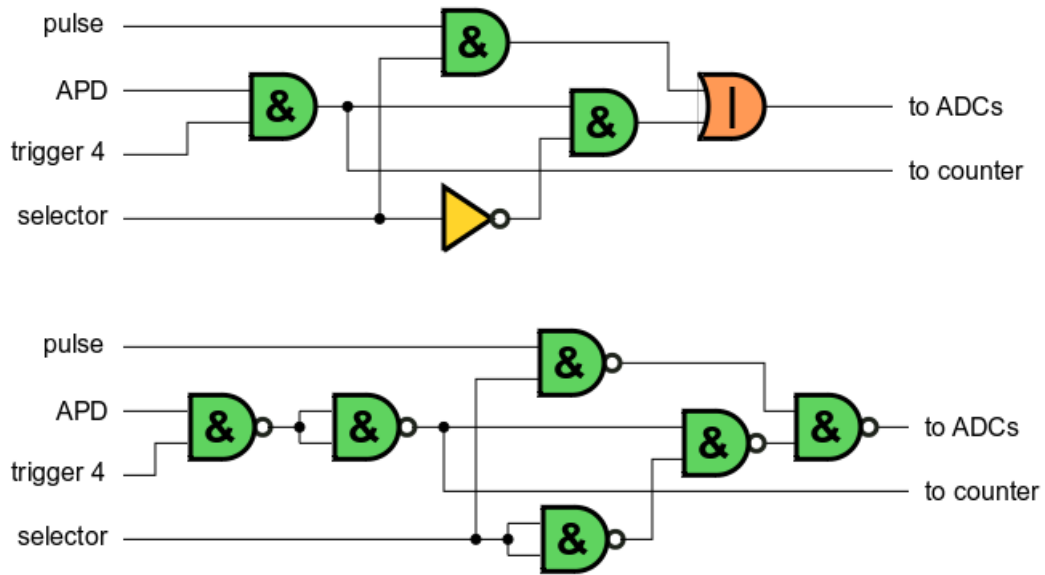


Figure B.2: Top, logical function realized by the external trigger selector circuit. Bottom, implementation with NAND gates only, using the logical rule $X \cdot Y = X + \bar{Y}$. The electric implementation uses regular digital ICs from the 74HC00xx logic family. The external implementation of the trigger selector circuit outside of the FPGA is necessary because the FPGA clock cycles and the APD triggers are asynchronous. Therefore if the digital I/Os of the FPGA are used to implement this circuit, the 40MHz FPGA clock would induce a very large 25ns jitter on the output trigger.

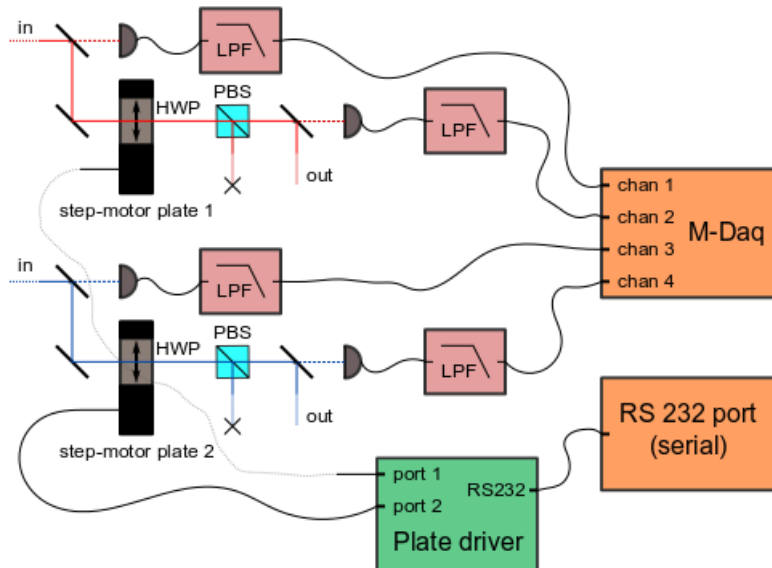


Figure B.3: Laser beam intensity power control system. HWP: half-wave plate. LPF: low-pass filter. PBS: polarization beam-splitter. The front photodiodes are used to check for the presence of the laser light and hold the feedback circuit when there is no incoming light. A plate driver circuit receives the commands sent on the serial port from the computer and translates them in electrical signals to drive the step motors of the two plate rotators.

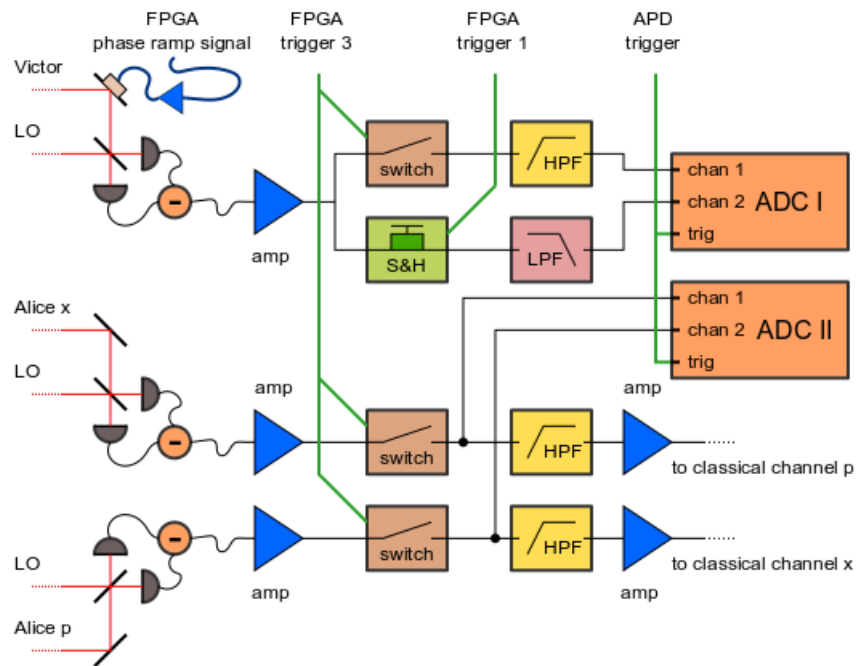


Figure B.4: Acquisition and measurement of the homodyne photocurrent. The setup is shown in the conditional teleportation configuration. Two PXI-5152 digitizers[176] are used in parallel to record the photocurrents of the three homodyne detector(see Appendix C). The first digitizer is used to record the quadrature and phase of a single homodyne detector, either Victor's detector when teleportation is performed, or either Alice's \hat{p} detector when the input state is measured. The second digitizer is used in the conditional teleportation experiment to record Alice's \hat{x} and \hat{p} detectors. These digitizers can be run either at 2 GHz on 1 input channel or at 1 GHz on 2 channels. They have a total internal memory of 64 Mbytes.



Appendix C

Control and drivers software interface

This appendix gives additional and further details on the general software architecture and programming techniques used in the control and automation of the experimental setup. The programs are written in the Ruby[181] and C programming languages. GCC is used for the compilation of all C programs[170]. The architecture is made of several smaller Ruby modules which can be run and used independently (See Fig.C.1). The different Ruby modules make heavy use of Ruby special features as a language, such as blocks and anonymous functions, reflection and dynamic programming, unified object architecture and message passing. This allows for a dramatic reduction in the total size of the program and an improvement in the modification and maintenance of the whole software programs. We use several Ruby extensions, also called gems, for specific purposes. The two main ones are the FFI gem for the direct interfacing with C libraries[171], and the EventMachine gem for the scalable asynchronous architecture and the TCP/IP connection facilities[173].

In total, the programs for the control of the experimental setup only are made of 4501 non-blank non-commentary lines of Ruby code divided over 66 files and 5483 lines of C code over 37 files. The analysis and tomography programs take in addition 2899 lines of Ruby over 57 files and 6156 lines of C over 74 files. It is not possible to explain these programs in details. In consequences we only list the main different modules and describe their operational logic in this appendix.

The client process is run every time a measurement on the experiment is started. It first loads the necessary modules, then configures the different hardware equipments, establishes a connection with the server process, and starts the measurement. When the measurement runs the main thread of the client process is blocked until the required amount of data points are recorded. In parallel to the measurement, the client process also runs a first background thread to copy the data from the measuring ADC to the computer RAM, and a second background thread to save the data put into the RAM to the hard-drive (see Fig.C.4). For practical and safety reasons, the hard-drive is a network attached storage device with 4 hard-drives in a RAID configuration, for a total capacity of 750 Go. For good control of the different threads run in the client process, the multithreading architecture is based on an event-driven reactor pattern using the EventMachine Ruby Gem[173]. The Ruby interpreter is the standard Ruby 1.9 YARV interpreter[181].

The server process runs the modules which are necessary for the everyday control of the optical setup outside of measurement sessions. In practice the server process is run without interruption and is restarted every few months only. It includes the power control and FPGA modules. For good long term memory stability, the server program is run by the JRuby interpreter, based on Java[172]. This allows for easy access to all Java libraries, and we use the Java RS232 serial port, Swing, and AWT APIs. The server process also runs the Ruby console for direct online tinkering of

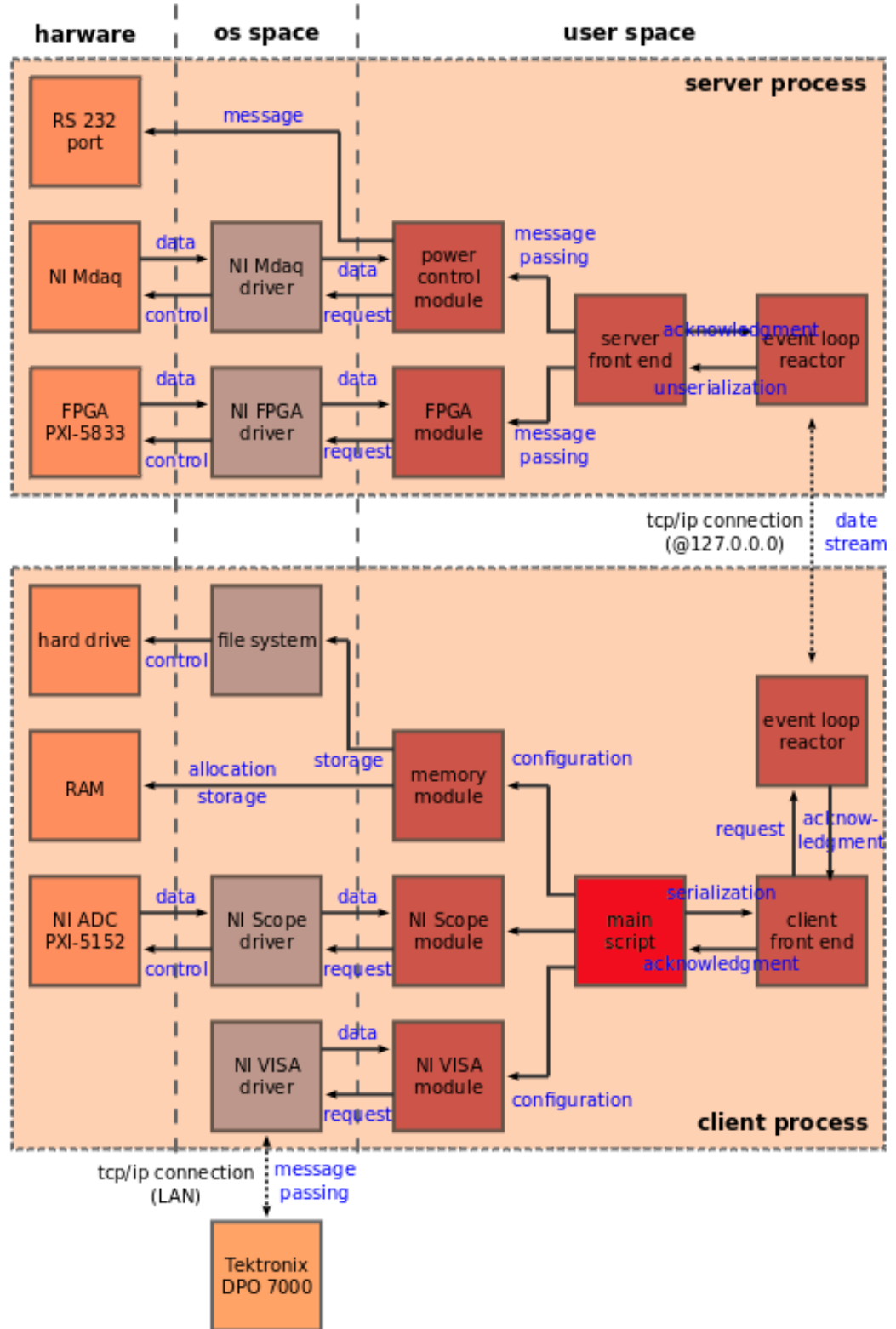


Figure C.1: General organization of the different software modules inside the client and server processes.

the programs while they are running. The server process is multithreaded with the EventMachine Ruby gem[173]. Thanks to Java, the threads are real machine threads which runs in parallel.

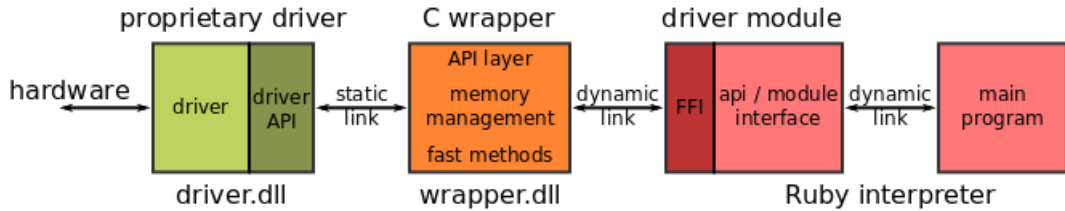


Figure C.2: Proprietary driver API interface architecture.

Driver interface modules architecture Most hardware devices which can be programmatically controlled have an external API which allows to interface with the device drivers. With the API it is usually possible to precisely configure the device and tune it for a specific purpose. It is standard for such APIs to be implemented in the C language which is one of the most portable programming languages available and is especially relevant for system software engineering and low level programming tasks. To easily interface to the driver from the Ruby interpreter, we use the FFI Gem[171], where FFI stands for Foreign Function Interface. The FFI gem is able to send OS system calls to load native libraries and activate functions inside them. On Windows the native libraries take the form of .dll files. The strategy is to write a thin C layer to wrap around the device API, use only the necessary functions of the API, and manage the memory resources inside the C layer. Then a Ruby module can use the FFI gem to load this C layer and indirectly control the API. The C layer can also sports low-level functions with high execution speed. The general architecture of this design is shown in Fig.C.2. With it, it is possible to easily abstract away and hide the details of any API and build on top of the device driver a clean Ruby module.

Client/server module is used to allow remote activation of the FPGA and power control modules run in the server process from the client process. It captures message request from the client, serializes them and sends them on the network. The request is then executed by the server, which sends back an acknowledgement. To assure synchronicity, the client control flow is blocked until the acknowledgement from the server is received (see Fig.C.3).

FPGA module is used to interface with the Labview FPGA driver from National Instrument[178]. Although the FPGA needs to be programmed with Labview, once a bitfile has been compiled, the driver can be used to load and control the FPGA outside of Labview.

NI-Scope module is used to interface with the Scope driver for high speed digitizers made by National Instrument[184]. The module can configure and control an arbitrary number of digitizers in parallel. In the experimental setup, two PXI-5152 digitizers[176] are used in parallel.

Asynchronous data transfer The National Instrument digitizers are connected on the PCI or PXI bus of a computer and allow for Direct Memory Access. A DMA copy is directly handled by the memory controller ICs on the computer mother board and can therefore be executed in parallel to anything the CPU might be doing. It allows to reach very high bandwidth and data throughput without blocking the control flow of the CPU and is ideal for our experimental measurement purposes. Fig.C.4 shows how the DMA copy mechanism is used in the measurement process.

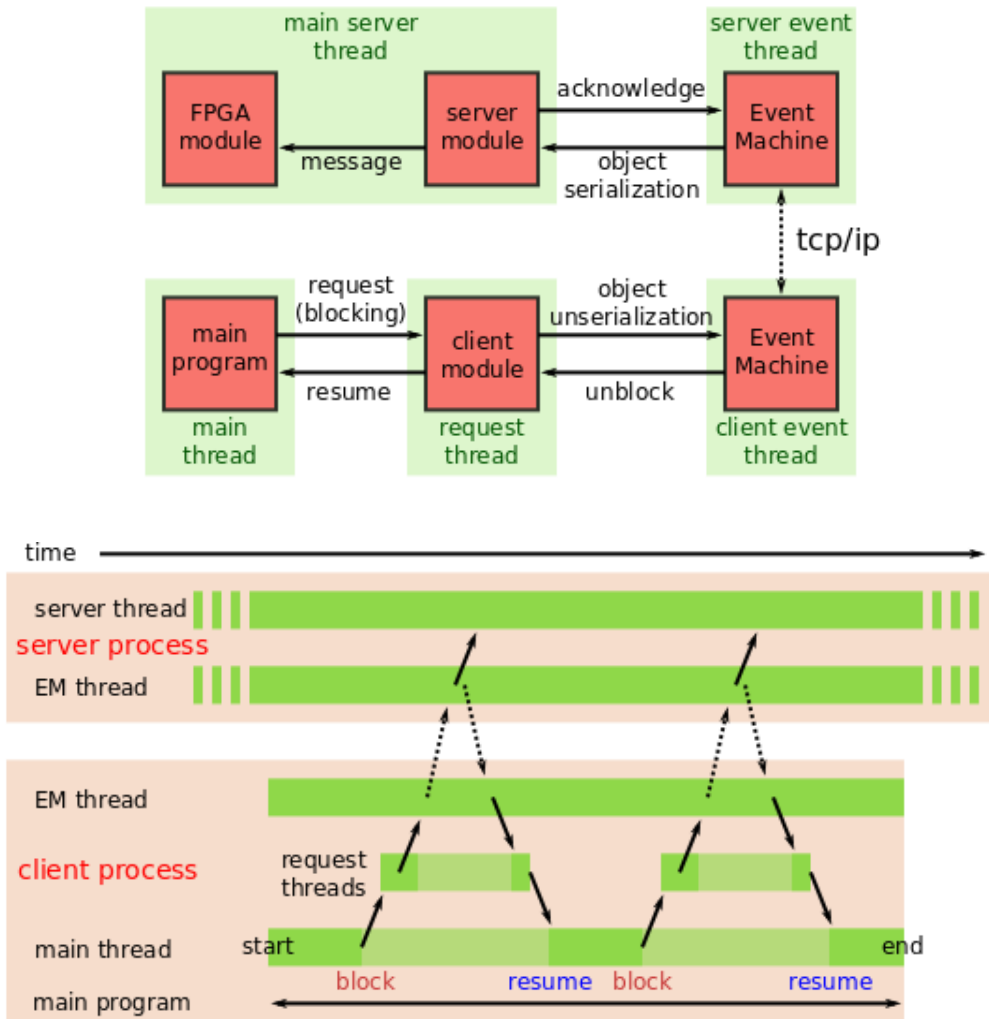


Figure C.3: Client/server architecture design. Top, logical organization of the modules and the communication between them. Bottom, thread model of communication. When the main program sends a remote request, a request thread is created and started and the main client thread blocks. Until the server receives and acknowledges the request, the request thread waits before completion. The main threads then unlocks and the control flow of the client process is resumed.

NI-VISA module VISA is a device independent message passing protocol to control electronic equipment used in measurement systems. It is supported by several constructors and allows to remotely control hardware equipment over the GPIB, USB or ethernet port. The NI-VISA module is an interface to the driver implementation of the VISA standards by National Instrument[179]. It is used to control a Textronix oscilloscope[183] over a TCP/IP connection. The oscilloscope is used to record FFT power spectrum of the photocurrent when the teleportation of the vacuum state is performed. The oscilloscope front memory and the VISA protocol are not fast enough for that setup to be used for tomography.

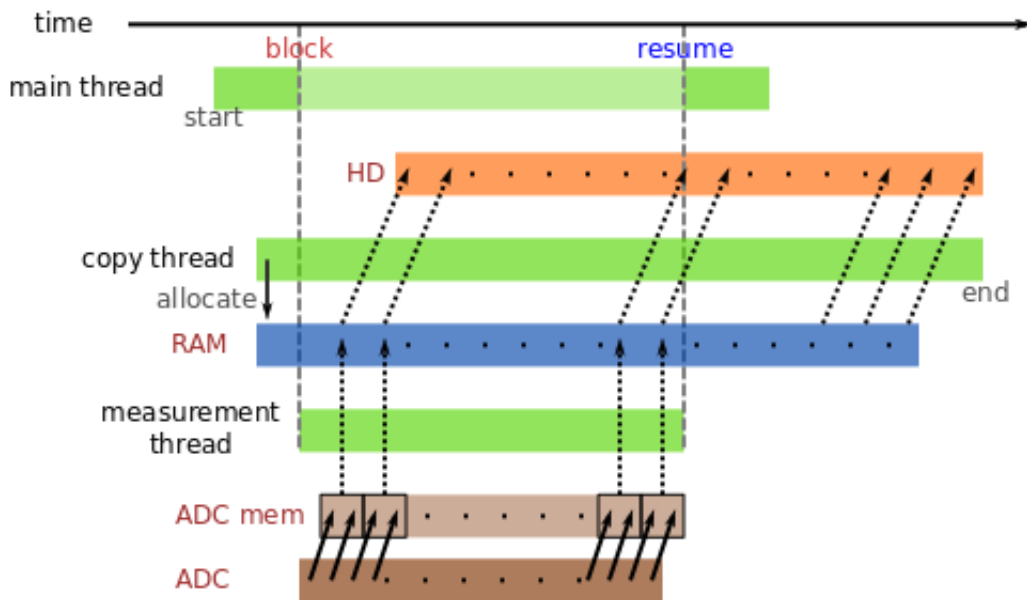
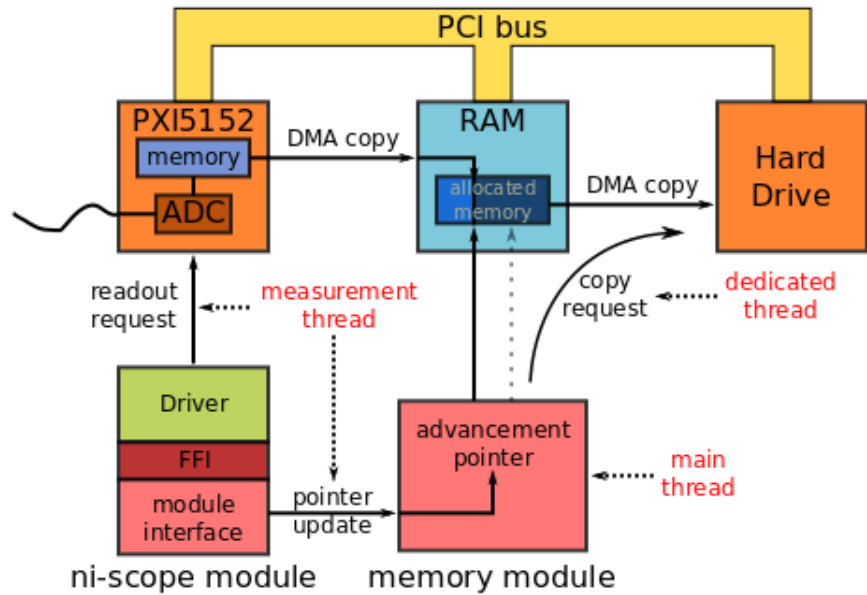


Figure C.4: Data transfer and data copying architecture. Top, logical organization of the modules and hardware elements. Bottom, thread model of data transfer. After the main program has configured the memory and NI-Scope modules, the measurement and copying threads start and the main threads is blocked. The ADC starts recording data immediately with every APD triggering event, and stock the data in its memory buffer. Every n data points, the buffer is cleared and the data is streamed to the RAM through a DMA copy. The data is then transferred again to the hard-drive. Since the memory buffer of the ADC is relatively small and the hard-drive relatively slow on data writing time, it is not possible to directly copy its content to the hard-drive for long measurement sessions. The measurement and copy threads are synchronised respectively with the DMA copy of data from the ADC memory to the RAM, and from the RAM to the hard drive. An advancement pointer prevents the copy thread to advance beyond the measurement thread and allow for synchronisation of both threads.

Appendix D

Optical setup

This appendix gives additional details on the optical setup in the form of a complete schematic of the experimental table and the optical setup. The detailed schematics of Fig.2.13 in Chap.2 and Fig.4.8 in Chap.4 roughly follow the layout of the actual setup as it is shown in Fig.D.1 and scaled accordingly.

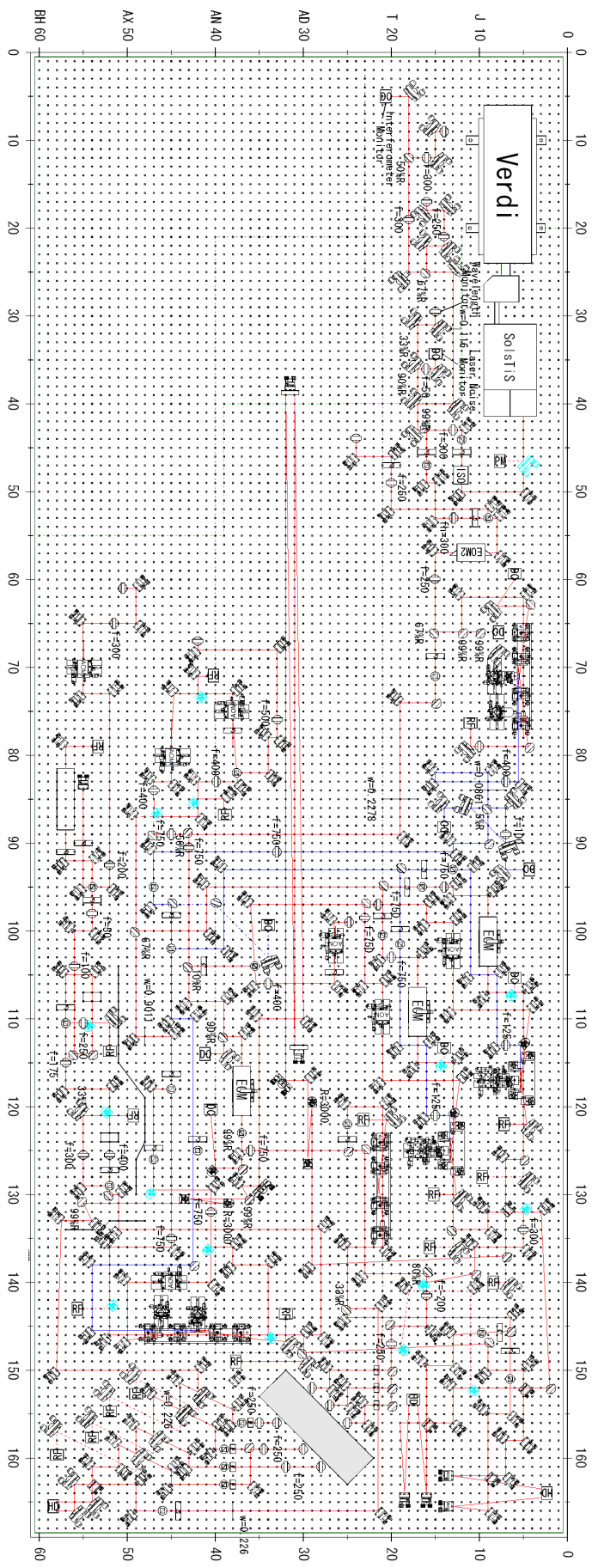


Figure D.1: Detailed schematic of the optical table.

Appendix E

Conditional teleportation theory summary

This appendix contains summarizing tables relative to the theoretical description of conditional teleportation found in Sec.4.3.1. The tables are put together by pair for the $|1\rangle\langle 1|$ and $|0\rangle\langle 0|$ input state components, and organized with respect to consideration or not of extra anti-squeezing and additional optical losses on the output teleported mode. We also remind the integral equations which yields the coefficients A , B and C for every cases.

General expressions

$$a(r) = \cosh(2r), \quad (\text{E.1.1})$$

$$b(r) = \sinh(2r), \quad (\text{E.1.2})$$

$$a'(r, z) = (e^{2r+2z} + e^{-2z})/2, \quad (\text{E.1.3})$$

$$b'(r, z) = (e^{2r+2z} - e^{-2z})/2, \quad (\text{E.1.4})$$

$$W_{AB}(\beta, \gamma) = \frac{1}{\pi} \exp \left[-2 \begin{pmatrix} \beta \\ \gamma \end{pmatrix}^T \Gamma^{-1} \begin{pmatrix} \beta \\ \gamma \end{pmatrix} \right], \quad (\text{E.1.5})$$

$$G'_\lambda(\gamma) = \frac{1}{2\pi(1-f)} e^{-2\frac{1-f}{f}|\gamma|^2}, \quad (\text{E.1.6})$$

$$G_{\text{loss}}(\alpha, \gamma, \xi) = \frac{1}{1-f} \int d^2\gamma' G_\lambda(\gamma') W_{AB}(\xi^* - \alpha^*, \frac{\gamma}{\sqrt{1-f}} - \gamma' - \xi), \quad (\text{E.1.7})$$

$$= \frac{1}{\pi^2 F_0} \exp \left[-\frac{2}{F_0} \left(F_1 \left| \xi - \alpha - \frac{\gamma}{\sqrt{1-f}} \right|^2 \right. \right. \quad (\text{E.1.8})$$

$$\left. \left. + F_2 \left| \xi - \frac{\gamma}{\sqrt{1-f}} \right|^2 + F_3 |\alpha|^2 \right) \right]. \quad (\text{E.1.9})$$

Partial integration on a disk

$$W_{\text{disk}}(A, B, C) = \int_0^{\sqrt{2}L} 2\pi r dr \frac{2}{\pi} (Ar^2 - B/2) e^{-r^2/C}, \quad (\text{E.1.10})$$

$$= C \left((2AC - B)(1 - e^{-2L^2/C}) - 4AL^2 e^{-2L^2/C} \right). \quad (\text{E.1.11})$$

$$\quad (\text{E.1.12})$$

Ideal teleportation

$$P(L) = \int_{\Lambda} d^2\xi \int_{\mathbb{R}^2} d^2\alpha \int_{\mathbb{R}^2} d^2\gamma W_{\text{in}}(\alpha) W_{AB}(\xi^* - \alpha^*, \gamma), \quad (\text{E.2.13})$$

$$W_{\text{out}}^u(0|L) = \int_{\Lambda} d^2\xi \int_{\mathbb{R}^2} d^2\alpha W_{\text{in}}(\alpha) W_{AB}(\xi^* - \alpha^*, -\xi). \quad (\text{E.2.14})$$

$ 1\rangle\langle 1 $	A	B	C	D
$P(L)$	$1/C^3$	$(1-a)/C^2$	$(1+a)$	
$W_{\text{out}}^u(0 L)$	$(a-b)^2/\pi D^3$	$(a-1)/\pi D^2$	$D/(1+2(a-b))$	$(1+a)$
$ 0\rangle\langle 0 $	A	B	C	D
$P(L)$	0	$-1/C$	$(1+a)$	
$W_{\text{out}}^u(0 L)$	0	$-1/\pi D$	$D/(1+2(a-b))$	$(1+a)$

Teleportation with additional optical losses

$$P(L) = \int_{\Lambda} d^2\xi \int_{\mathbb{R}^2} d^2\alpha \int_{\mathbb{R}^2} d^2\gamma W_{\text{in}}(\alpha) W_{AB}(\xi^* - \alpha^*, \gamma), \quad (\text{E.3.15})$$

$$W_{\text{out}}^u(0|L) = \int_{\Lambda} d^2\xi \int_{\mathbb{R}^2} d^2\alpha W_{\text{in}}(\alpha) G_{\text{loss}}(\alpha, 0, \xi). \quad (\text{E.3.16})$$

F_0	$1 + f(a-1)$	F_2	$(a-b)(1-f^2)$
F_1	$f^2 + F_2$	F_3	$b(1-f^2)$

$ 1\rangle\langle 1 $	A	B	C	D
$P(L)$	$1/C^3$	$(1-a)/C^2$		$(1+a)$
$W_{\text{out}}^u(0 L)$	$\frac{F_1^2}{\pi D^3}$	$\frac{(F_1-F_0+F_3)}{\pi D^2}$	$\frac{F_0 D}{(F_0+F_3)(F_1+F_2)+F_1 F_2}$	$F_0 + F_1 + F_3$
$ 0\rangle\langle 0 $	A	B	C	D
$P(L)$	0	$-1/C$		$(1+a)$
$W_{\text{out}}^u(0 L)$	0	$-1/\pi D$	$\frac{F_0 D}{(F_0+f_3)(F_1+F_2)+F_1 F_2}$	$F_0 + F_1 + F_3$

Teleportation with extra anti-squeezing

$$P(L) = \int_{\Lambda} d^2\xi \int_{\mathbb{R}^2} d^2\alpha \int_{\mathbb{R}^2} d^2\gamma W_{\text{in}}(\alpha) W'_{AB}(\xi^* - \alpha^*, \gamma), \quad (\text{E.4.17})$$

$$W_{\text{out}}^u(0|L) = \int_{\Lambda} d^2\xi \int_{\mathbb{R}^2} d^2\alpha W_{\text{in}}(\alpha) W'_{AB}(\xi^* - \alpha^*, -\xi). \quad (\text{E.4.18})$$

$ 1\rangle\langle 1 $	A	B	C	D
$P(L)$	$1/C^3$	$(1-a')/C^2$		$(1+a')$
$W_{\text{out}}^u(0 L)$	$(a'-b')^2/\pi D^3$	$(a'-e^{2z})/\pi D^2$	$D/(1+2(a'-b'))$	$(a'+e^{2z})$
$ 0\rangle\langle 0 $	A	B	C	D
$P(L)$	0	$-1/C$		$(1+a')$
$W_{\text{out}}^u(0 L)$	0	$-1/\pi D$	$D/(1+2(a'-b'))$	$(a'+e^{2z})$

Teleportation with extra-antisqueezing and additional output losses

$$P(L) = \int_{\Lambda} d^2\xi \int_{\mathbb{R}^2} d^2\alpha \int_{\mathbb{R}^2} d^2\gamma W_{\text{in}}(\alpha) W'_{AB}(\xi^* - \alpha^*, \gamma), \quad (\text{E.5.19})$$

$$W_{\text{out}}^u(0|L) = \int_{\Lambda} d^2\xi \int_{\mathbb{R}^2} d^2\alpha W_{\text{in}}(\alpha) G'_{\text{loss}}(\alpha, 0, \xi). \quad (\text{E.5.20})$$

F'_0	$e^{2z} + f(a' - e^{2z})$	F'_2	$(a' - b')(1 - f^2)$
F'_1	$f^2 + F'_2$	F'_3	$b'(1 - f^2)$

$ 1\rangle\langle 1 $	A	B	C	D
$P(L)$	$1/C^3$	$(1 - a')/C^2$		$(1 + a')$
$W_{\text{out}}^u(0 L)$	$\frac{(F'_1)^2}{\pi D^3}$	$\frac{F'_1 - F'_0 + F'_3}{\pi D^2}$	$\frac{F'_0 D}{(F'_0 + F'_3)(F'_1 + F'_2) + F'_1 F'_2}$	$F'_0 + F'_1 + F'_3$
$ 0\rangle\langle 0 $	A	B	C	D
$P(L)$	0	$-1/C$		$(1 + a')$
$W_{\text{out}}^u(0 L)$	0	$-1/\pi D$	$\frac{F'_0 D}{(F'_0 + F'_3)(F'_1 + F'_2) + F'_1 F'_2}$	$F'_0 + F'_1 + F'_3$

Bibliography

- [1] M. Planck. “On the Law of Distribution of Energy in the Normal Spectrum[Über das Gesetz der Energieverteilung im Normalspektrum]”. In: *Annalen der Physik* 4 (1901), p. 553.
- [2] A. Einstein. “On a Heuristic Viewpoint Concerning the Production and Transformation of Light [Über einen die Erzeugung und Verwandlung des Lichtes betreffenden heuristischen Gesichtspunkt]”. In: *Annalen der Physik* 17 (1905), p. 132.
- [3] M. V. Berry. “Quantal Phase Factors Accompanying Adiabatic Changes”. In: *Proc. R. Soc. Lond. A* 392 (1907), pp. 45–47.
- [4] E. Schmidt. “Zur Theorie der linearen und nicht linearen Integralgleichungen”. In: *Math. Ann.* 63 (1907), p. 4339.
- [5] J. Radon. “Berichte der Sachsischen Akademie der Wissenschaft **69**, 262 (1917)[J.Radon (by P. C. Parks), IEEE Transactions on medical imaging MI-5, 170(1986)]”. In: *Akademie der Wissenschaft* 69 (1917), p. 262.
- [6] A. H. Compton. “A Quantum Theory of the Scattering of X-Rays by Light Elements”. In: *Phys. Rev.* 21 (1923), p. 483.
- [7] E. Wigner. “On the Quantum Correction For Thermodynamic Equilibrium”. In: *Phys. Rev.* 40 (1932), pp. 749–759.
- [8] A. Einstein, B. Podolsky, and N. Rosen. “Can quantum-mechanical description of physical reality be considered complete?” In: *Phys. Rev.* 47 (1935), pp. 777–780.
- [9] C. E. Shannon. “A Mathematical Theory of Communication”. In: *Bell System Technical Journal* 27 (1948), p. 379.
- [10] R. N. Bracewell. “Strip integration in Radio astronomy”. In: *Phys. Rev. Lett.* 9 (1956), p. 198.
- [11] R. Hanbury Brown and R. Q. Twiss. “Correlation between Photons in two Coherent Beams of Light”. In: *Nature* 177 (1956), p. 27.
- [12] A.M. Gleason. In: *J. Math. Mech.* 6 (1957), p. 885.
- [13] T. H. Maiman. “Stimulated Optical Radiation in Ruby”. In: *Nature* 187 (1960), p. 493.
- [14] P. A. Franken et al. “Generation of Optical Harmonics”. In: *Phys. Rev. Lett.* 7 (1961), p. 118.
- [15] R. L. Hudson. “When is the Wigner quasi-probability density non-negative?” In: *Rep. Math. Phys.* 6 (1974), p. 1849.
- [16] E. Zeitzer. “The reconstruction of objects from their projections.” In: *Optik* 39 (1974), pp. 396–415.

- [17] I. Paul R. Hingorani H. Stark J. W. Woods. “An investigation of computerized tomography by direct fourier inversion and optimum interpolation”. In: *IEEE Trans, Biomed. Eng.* 28 (1981), pp. 496–505.
- [18] A. Aspect, J. Dalibard, and G. Roger. “Experimental Test of Bell’s Inequalities using Time-Varying Analyzers”. In: *Phys. Rev. Lett.* 49 (1982), p. 1804.
- [19] C. Caves. “Quantum limits on noise in linear amplifiers”. In: *Phys. Rev. D* 26 (1982), p. 1817.
- [20] R. Feynman. “Simulating physics with computers”. In: *Internat. J. Theoret. Phys.* 21 (1982), 467–488.
- [21] R. W. P. Drever et al. “Laser phase and frequency stabilization using an optical resonator”. In: *App. Phys. B: Photophys. Laser Chem.* 31 (1983), p. 97.
- [22] M. J. Collett and C. W. Gardiner. “Squeezing of intracavity and traveling-wave light fields produced in parametric amplification”. In: *Phys. Rev. A* 30 (1984), p. 1386.
- [23] D. Deutsch. “Quantum theory, the Church–Turing principle and the universal quantum computer”. In: *Proceedings of the Royal Society of London, A* 400 (1985), p. 97.
- [24] R. E. Slusher et al. “Observation of squeezed states generated by four-wave mixing in an optical cavity”. In: *Phys. Rev. Lett.* 55 (1985), p. 2409.
- [25] W. G. Hawkins and H. H. Barrett. “A numerically stable circular harmonic reconstruction algorithm”. In: *SIAM J. Numer. Anal.* (1986).
- [26] L-A. Wu et al. “Generation of Squeezed States by Parametric Down Conversion”. In: *Phys. Rev. Lett.* 57 (1986), p. 2520.
- [27] R. E. Slusher et al. “Pulsed Squeezed Light”. In: *Phys. Rev. Lett.* 59 (1987), p. 2566.
- [28] C. Cohen-Tannoudji, J. Dupont-Roc, and G. Grynberg. *Photons and Atoms. Introduction to Quantum Electrodynamics*. Wiley-VCH, Berlin, 1989.
- [29] A. Prata and W. V. T. Rusch. “Algorithm for computation of Zernike polynomials”. In: *Appl. Opt.* 28 (1989), pp. 749–754.
- [30] K. Vogel and H. Risken. “Determination of quasiprobability distributions in terms of probability distributions for the rotated quadrature phase”. In: *Phys. Rev. Lett.* 40 (1989), p. 2847.
- [31] P. D. Drummond and M. D. Reid. “Correlations in nondegenerate parametric oscillation. II. Below threshold results”. In: *Phys. Rev. A* 41 (1990), p. 3930.
- [32] S. Song, C. M. Caves, and B. Yurke. “Generation of superpositions of classically distinguishable quantum states from optical back-action evasion”. In: *Phys. Rev. A* 41 (1990), p. 5261.
- [33] B. Yurke, W. Schleich, and D. F. Walls. “Quantum superpositions generated by quantum nondemolition measurements”. In: *Phys. Rev. A* 42 (1990), p. 1703.
- [34] C. Zhu and C. Caves. “Photocount distributions for continuous-wave squeezed light”. In: *Phys. Rev. A* 42 (1990), p. 6794.
- [35] C. H. Bennett et al. “Teleporting an unknown quantum state via dual classical and Einstein-Podolsky-Rosen Channels”. In: *Phys. Rev. Letts* 70 (1993), p. 1895.
- [36] D. T. Smithey et al. “Measurement of the Wigner distribution and the density matrix of a light mode using optical homodyne tomography, Application to squeezed states and the vacuum”. In: *Phys. Rev. Lett.* 70 (1993), p. 1244.

- [37] M. Ban. “Quasicontinuous measurements of photon number”. In: *Phys. Rev. A* 49 (1994), p. 5078.
- [38] B. Efron and R. J. Tibshirani. *An Introduction to the Bootstrap*. Chapman & Hall/CRC, New York, 1994.
- [39] L. Vaidman. “Teleportation fo quantum states”. In: *Phys. Rev. A* 49 (1994), p. 1473.
- [40] G. M. D’Ariano, U. Leonhardt, and H. Paul. “Homodyne detection of the density matrix of the radiation field”. In: *Phys. Rev. A* 52 (1995), p. 1801.
- [41] U. Leonhardt and M. G. Raymer. “Observation of Moving Wave Packets Reveals Their Quantum State”. In: *Phys. Rev. Lett.* 76 (1996), p. 1985.
- [42] D. Bouwmeester et al. “Experimental quantum teleportation”. In: *Nature* 390 (1997), p. 575.
- [43] M. Dakna et al. “Generating Schrödinger-cat-like states by means of conditional measurements on a beam splitter”. In: *Phys. Rev. A* 55 (1997), p. 3184.
- [44] L. K. Grover. “Quantum mechanics helps in searching for a needle in a haystack”. In: *Phys. Rev. Lett.* 78 (1997), 325–328.
- [45] Z. Hradil. “Quantum state estimation”. In: *Phys. Rev. A* 55 (1997), R1561.
- [46] U. Leonhardt. *Measuring the Quantum State of Light, 2nd edition*. Cambridge University Press, Cambridge, Uk, 1997.
- [47] L. G. Lutterbach and L. Davidovich. “Method for Direct Measurement of the Wigner Function in Cavity QED and Ion Traps”. In: *Phys. Rev. Lett.* 78 (1997), p. 2547.
- [48] P. W. Shor. “Polynomial-time algorithms for prime factorization and discrete logarithms on a quantum computer”. In: *SIAM J. Comput.* 27 (1997), 1484–1509.
- [49] S. L. Braunstein and H. J. Kimble. “Teleportation of Continuous Quantum Variables”. In: *Phys. Rev. Lett.* 80 (1998), p. 869.
- [50] B. Cabrera et al. “Detection of single infrared, optical, and ultraviolet photons using superconducting transition edge sensors”. In: *App. Phys. Lett.* 73 (1998), p. 735.
- [51] A. Furusawa et al. “Unconditional Quantum Teleportation”. In: *Science*. 282 (1998), p. 706.
- [52] M. Born and E. Wolf. *Principles of Optics*. Cambridge University Press, Cambridge, 1999.
- [53] S. Lloyd and S. L. Braunstein. “Quantum Computation over Continuous Variables”. In: *Phys. Rev. Lett.* 82 (1999), p. 1784.
- [54] D. A. Shaddock, M. B. Gray, and D. E. McClelland. “Frequency locking a laser to an optical cavity by use of spatial mode interference”. In: *Opt. Lett.* 24 (1999), p. 1499.
- [55] S. L. Braunstein, C. A. Fuchs, and H. J. Kimble. “Criteria for continuous-variable quantum teleportation”. In: *J. Mod. Opt* 47 (2000), p. 267.
- [56] P. C. D. Hobbs. *Building Electro-Optical Systems: Making It All Work, 1st Edition*. Wiley-Interscience, Berlin, 2000.
- [57] H. F. Hofmann et al. “Fidelity and information in the quantum teleportation of continuous variables”. In: *Phys. Rev. A* 62 (2000), p. 062304.
- [58] J. Lee, M. S. Kim, and H. Jeong. “Transfer of nonclassical features in quantum teleportation via a mixed quantum channel”. In: *Phys. Rev. A* 62 (2000), p. 032305.
- [59] P. van Loock, S. L. Braunstein, and H. J. Kimble. “Broadband teleportation”. In: *Phys. Rev. A* 62 (2000), p. 022309.

- [60] R. Loudon. *The Quantum Theory of Light*. Oxford University Press, USA, 2000.
- [61] Y. J. Lu and Z. Y. Ou. “Optical parametric oscillator far below threshold: Experiment versus theory”. In: *Phys. Rev. A* 62 (2000), p. 033804.
- [62] T. Opatrný, G. Kurizki, and D.-G. Welsch. “Improvement on teleportation of continuous variables by photon subtraction via conditional measurement”. In: *Phys. Rev. A* 61 (2000), p. 032302.
- [63] W. Vogel. “Nonclassical States: An Observable Criterion”. In: *Phys. Rev. Lett.* 84 (2000), pp. 749–759.
- [64] S. L. Braunstein et al. “Quantum versus classical domains for teleportation with continuous variables”. In: *Phys. Rev. A* 64 (2001), p. 022321.
- [65] G. N. Gol’tsman et al. “Picosecond superconducting single-photon optical detector”. In: *App. Phys. Lett.* 79 (2001), p. 705.
- [66] F. Grosshans and P. Grangier. “Quantum cloning and teleportation criteria for continuous quantum variables”. In: *Phys. Rev. A* 64 (2001), 010301(R).
- [67] H. F. Hofmann et al. “Information losses in continuous-variable quantum teleportation”. In: *Phys. Rev. A* 64 (2001), 040310 (R).
- [68] A. I. Lvovsky et al. “Quantum State Reconstruction of the Single-Photon Fock State”. In: *Phys. Rev. Lett.* 87 (2001), p. 05.
- [69] W. P. Schleich. *Quantum Optics in Phase Space*. Wiley-VCH, Berlin, 2001.
- [70] P. Bertet et al. “Direct Measurement of the Wigner Function of a One-Photon Fock State in a Cavity”. In: *Phys. Rev. Lett.* 89 (2002), p. 200402.
- [71] P. T. Cochrane, T. C. Ralph, and G. J. Milburn. “Teleportation improvement by conditional measurements on the two-mode squeezed vacuum”. In: *Phys. Rev. A* 65 (2002), p. 062306.
- [72] G. Drobny and V. Buzek. “Reconstruction of motional states of neutral atoms via maximum entropy principle”. In: *Phys. Rev. A* 65 (2002), p. 053410.
- [73] S. X. Liao M. Pawlak. “On the Recovery of a Function on a Circular Domain”. In: *IEEE Trans. Info. Theory* 48 (2002), pp. 2736–2753.
- [74] C. Schori, J. L. Sørensen, and E. S. Polzik. “Narrow-band frequency tunable light source of continuous quadrature entanglement”. In: *Phys. Rev. A* 66 (2002), p. 033802.
- [75] D. Achilles et al. “Fiber-assisted detection with photon number resolution”. In: *Opt. Lett.* 28 (2003), p. 2387.
- [76] W. P. Bowen et al. “Experimental investigation of continuous-variable quantum teleportation”. In: *Phys. Rev. A* 67 (2003), p. 032302.
- [77] P. Busch. “Quantum States and Generalized Observables: A Simple Proof of Gleason’s Theorem”. In: *Phys. Rev. Lett.* 91 (2003), p. 120403.
- [78] Y. J. Lu, R. L. Campbell, and Z. Y. Ou. “Mode-locked two-photon states”. In: *Phys. Rev. Lett.* 91 (2003), p. 163602.
- [79] T. C. Ralph et al. “Quantum computation with optical coherent states”. In: *Phys. Rev. A* 68 (2003), p. 042319.
- [80] T. C. Zhang et al. “Quantum teleportation of light beams”. In: *Phys. Rev. A* 67 (2003), p. 033802.
- [81] M. Ban. “Phase-space approach to continuous variable quantum teleportation”. In: *Phys. Rev. A* 69 (2004), p. 054304.

- [82] C. M. Caves and K. Wódkiewicz. “Classical Phase-Space Descriptions of Continuous-Variable Teleportation”. In: *Phys. Rev. Lett.* 93 (2004), p. 040506.
- [83] P. T. Cochrane, T. C. Ralph, and A. Doli/'nska. “Optimal cloning for finite distributions of coherent states”. In: *Phys. Rev. A* 69 (2004), p. 042313.
- [84] C. W. Gardiner and P. Zoller. *Quantum Noise*. Springer, New York, 2004.
- [85] A. Kenfack and K. Zyczkowski. “Negativity of the Wigner function as an indicator of non-classicality”. In: *J. Opt. B: Quantum Semiclass. Opt.* 6 (2004), p. 396.
- [86] A. P. Lund et al. “Conditional production of superpositions of coherent states with inefficient photon detection”. In: *Phys. Rev. A* 70 (2004), 020101(R).
- [87] A. I. Lvovsky. “Iterative maximum-likelihood reconstruction in quantum homodyne tomography”. In: *J. Opt. B: Quantum Semiclass. Opt.* 6 (2004), S55.
- [88] A. Wallraff et al. “Strong coupling of a single photon to a superconducting qubit using circuit quantum electrodynamics”. In: *Nature* 431 (2004), p. 162.
- [89] J. Wenger, R. Tualle-Brouri, and P. Grangier. “Non-Gaussian Statistics from Individual Pulses of Squeezed Light”. In: *Phys. Rev. Lett.* 92 (2004), p. 153601.
- [90] H. Jeong and T. C. Ralph. “Production of superpositions of coherent states in traveling optical fields with inefficient photon detection”. In: *Phys. Rev. A* 72 (2005), p. 013801.
- [91] P. van Loock and S. L. Braunstein. “Quantum information with continuous variables”. In: *Phys. Rev. A* 77 (2005), p. 513.
- [92] N. Takei et al. “Experimental demonstration of quantum teleportation of a squeezed state”. In: *Phys. Rev. A* 72 (2005), p. 042304.
- [93] N. Takei et al. “High-Fidelity Teleportation beyond the No-Cloning Limit and Entanglement Swapping for Continuous Variables”. In: *Phys. Rev. Lett.* 94 (2005), p. 220502.
- [94] A. Zavatta, S. Viciani, and M. Bellini. “Single-photon excitation of a coherent state: Catching the elementary step of stimulated light emission”. In: *Phys. Rev. A* 72 (2005), p. 023820.
- [95] A. E. Dunlop et al. “Generation of a frequency comb of squeezing in an optical parametric oscillator”. In: *Phys. Rev. A* 73 (2006), p. 013817.
- [96] P. Marian and T. A. Marian. “Continuous-variable teleportation in the characteristic-function description”. In: *Phys. Rev. A* 74 (2006), p. 042306.
- [97] K. Mølmer. “Non-Gaussian states from continuous-wave Gaussian light sources”. In: *Phys. Rev. A* 73 (2006), p. 063804.
- [98] J. S. Neergaard-Nielsen et al. “Generation of a Superposition of Odd Photon Number States for Quantum Information Networks”. In: *Phys. Rev. Lett.* 97 (2006), p. 083604.
- [99] A. Ourjoumtsev, R. Tualle-Brouri, and P. Grangier. “Quantum Homodyne Tomography of a Two-Photon Fock State”. In: *Phys. Rev. Lett.* 96 (2006), p. 213601.
- [100] A. Ourjoumtsev et al. “Generating Optical Schroedinger Kittens for Quantum Information Processing”. In: *Science* 312 (2006), p. 83.
- [101] N. C. Rouze, V. C. Soon, and G. D. Hutchins. “On the connection between the Zernike moments and Radon transform of an image”. In: *Phys. Rev. Lett.* 27 (2006), pp. 636–642.
- [102] M. Sasaki and S. Suzuki. “Multimode theory of measurement-induced non-Gaussian operation on wideband squeezed light: analytical formula”. In: *Phys. Rev. A* 73 (2006), p. 043807.

- [103] S. Suzuki et al. “7 dB quadrature squeezing at 860 nm with periodically poled KTiOPO4”. In: *App. Phys. Lett.* 89 (2006), p. 0611106.
- [104] S. Suzuki et al. “Analysis on generation schemes of Schrödinger cat-like states under experimental imperfections”. In: *Opt. Comm.* 259 (2006), p. 758.
- [105] S. Suzuki et al. “Practical purification scheme for decohered coherent-state superpositions via partial homodyne detection”. In: *Phys. Rev. Lett.* 73 (2006), p. 042304.
- [106] G. J. de Valcárcel et al. “Multimode squeezing of frequency combs”. In: *Phys. Rev. A* 74 (2006), 061801(R).
- [107] E. Waks, E. Diamanti, and Y. Yamamoto. “Generation of photon number states”. In: *New J. Phys.* 8 (2006), p. 06.
- [108] A. Zavatta, S. Viciani, and M. Bellini. “Tomographic reconstruction of the single-photon Fock state by high-frequency homodyne detection”. In: *Phys. Rev. A* 70 (2006), p. 053821.
- [109] J. Appel et al. “Electronic Noise in Optical Homodyne Tomography”. In: *Phys. Rev. A* 75 (2007), p. 035802.
- [110] A. Biswas and G. S. Agarwal. “Nonclassicality and decoherence of photon-subtracted squeezed states”. In: *Phys. Rev. A* 75 (2007), p. 032104.
- [111] N. J. Cerf, G. Leuchs, and E. S. Polzik (eds.) *Quantum Information with Continuous Variables of Atoms and Light, chap. 21*. Imperial College Press, Cambridge, 2007.
- [112] S. R. Deans. *The Radon Transform and Some of Its Applications*. Dover Publications, New York, 2007.
- [113] F. Dell’Anno et al. “Continuous-variable quantum teleportation with non-Gaussian resources”. In: *Phys. Rev. A* 76 (2007), p. 022301.
- [114] M. G. Genoni, M. G. A. Paris, and K. Banaszek. “Measure of the non-Gaussian character of a quantum state”. In: *Phys. Rev. A* 76 (2007), p. 042327.
- [115] R. J. Glauber. *Quantum Theory of Optical Coherence*. Wiley-VCH, Berlin, 2007.
- [116] S. Gleyzes et al. “Quantum jumps of light recording the birth and death of a photon in a cavity”. In: *Nature* 446 (2007), p. 297.
- [117] A. A. Houck et al. “Generating single microwave photons in a circuit”. In: *Nature* 449 (2007), p. 328.
- [118] A. M. Lance et al. “Quantum-state engineering with continuous-variable postselection”. In: *Phys. Rev. A* 041801(R) (2007), p. 73.
- [119] J. S. Neergaard-Nielsen et al. “High purity bright single photon source”. In: *Opt. Express* 15 (2007), p. 7940.
- [120] A. E. Nielsen and K. Mølmer. “Conditional generation of path-entangled optical $|N, O\rangle + |0, N\rangle$ states”. In: *Phys. Rev. A* 75 (2007), p. 063803.
- [121] A. E. Nielsen and K. Mølmer. “Photon number states generated from a continuous-wave light source”. In: *Phys. Rev. A* 75 (2007), p. 043801.
- [122] A. E. Nielsen and K. Mølmer. “Single-photon-state generation from a continuous-wave nondegenerate optical parametric oscillator”. In: *Phys. Rev. A* 75 (2007), p. 023806.
- [123] A. Ourjoumtsev et al. “Generation of optical Schroedinger cats from photon number states”. In: *Nature* 448 (2007), p. 784.
- [124] A. Ourjoumtsev et al. “Increasing Entanglement between Gaussian States by Coherent Photon Subtraction”. In: *Phys. Rev. Lett.* 98 (2007), p. 030502.

- [125] W. H. Press et al. *Numerical Recipes, The Art of Scientific Computing, 3rd Edition*. Cambridge University Press, Cambridge, 2007.
- [126] Y. Takeno et al. “Observation of -9dB quadrature squeezing with improvement of phase stability in homodyne measurement”. In: *Optics Express* 15 (2007), p. 4312.
- [127] K. Wakui et al. “Photon subtracted squeezed states generated with periodically poled KTiOPO₄”. In: *Opt. Express* 15 (2007), p. 3568.
- [128] H. Yonezawa, S. L. Braunstein, and A. Furusawa. “Experimental Demonstration of Quantum Teleportation of Broadband Squeezing”. In: *Phys. Rev. Letts* 99 (2007), p. 110503.
- [129] H. Yonezawa, A. Furusawa, and P. van Loock. “Sequential quantum teleportation of optical coherent states”. In: *Phys. Rev. A* 76 (2007), p. 032305.
- [130] J. Yoshikawa et al. “Demonstration of deterministic and high fidelity squeezing of quantum information”. In: *Phys. Rev. A* 76 (2007), 060301(R).
- [131] K.-I. Yoshino, T. Aoki, and A. Furusawa. “Generation of continuous-wave broadband entangled beams using periodically poled lithium niobate waveguides”. In: *App. Phys. Lett.* 90 (2007), p. 041111.
- [132] J. Bernu et al. “Freezing Coherent Field Growth in a Cavity by the Quantum Zeno Effect”. In: *Phys. Rev. Lett.* 101 (2008), p. 180402.
- [133] M. Brune et al. “Process Tomography of Field Damping and Measurement of Fock State Lifetimes by Quantum Nondemolition Photon Counting in a Cavity”. In: *Phys. Rev. Lett.* 201 (2008), p. 240402.
- [134] S. Deléglise et al. “Reconstruction of non-classical cavity field states with snapshots of their decoherence”. In: *Nature* 455 (2008), p. 510.
- [135] A. Divochiy et al. “Superconducting nanowire photon-number-resolving detector at telecommunication wavelengths”. In: *Nat. Phot.* 2 (2008), p. 320.
- [136] M. Hofheinz et al. “Generation of Fock states in a superconducting quantum circuit”. In: *Nature* 454 (2008), p. 310.
- [137] M. Hofheinz et al. “Synthesizing arbitrary quantum states in a superconducting resonator”. In: *Nature* 459 (2008), p. 546.
- [138] J. S. Ivan, M. S. Kumar, and R. Simon. “A measure of non-Gaussianity for quantum states”. In: *quant-ph/0812.2800* (2008).
- [139] N. Katz et al. “Reversal of the Weak Measurement of a Quantum State in a Superconducting Phase Qubit”. In: *Phys. Rev. Lett* 101 (2008), p. 200401.
- [140] A. E. Lita, A. J. Miller, and S. W. Nam. “Counting near-infrared single-photons with 95% efficiency”. In: *Opt. Exp.* 16 (2008), p. 705.
- [141] A. P. Lund, T. C. Ralph, and H. L. Haselgrove. “Fault-Tolerant Linear Optical Quantum Computing with Small-Amplitude Coherent States”. In: *Phys. Rev. Lett.* 100 (2008), p. 030503.
- [142] J. S. Neergaard-Nielsen. “Generation of single photons and Schroedinger kitten states of light”. PhD thesis. Niels Bohr Institute, 2008.
- [143] H. Takahashi et al. “Generation of Large-Amplitude Coherent-State Superposition via Ancilla-Assisted Photon Subtraction”. In: *Phys. Rev. Lett.* 101 (2008), p. 233605.
- [144] M. Takeoka, H. Takahashi, and M. Sasaki. “Large-amplitude coherent-state superposition generated by a time-separated two-photon subtraction from a continuous-wave squeezed vacuum”. In: *Phys. Rev. A* 77 (2008), p. 062315.

- [145] J. D. Thompson et al. “Strong dispersive coupling of a high-finesse cavity to a micromechanical membrane”. In: *Nature* 452 (2008), p. 72.
- [146] H. Vahlbruch et al. “Observation of squeezed light with 10-dB quantum-noise reduction”. In: *Phys. Rev. Lett.* 100 (2008), p. 033602.
- [147] M. Yukawa, H. Benichi, and A. Furusawa. “Teleportation of Non-Classical Wave-Packets of light”. In: *Phys. Rev. A* 77 (2008), p. 022314.
- [148] E. A. Daulera et al. “Photon-number-resolution with sub-30-ps timing using multi-element superconducting nanowire single photon detectors”. In: *J. Mod. Opt* 56 (2009), p. 364.
- [149] S. Deleglise. “Reconstruction complète d’états non-classiques du champ en électrodynamique quantique en cavité”. PhD thesis. Université Pierre et Marie Curie, 2009.
- [150] I. Dotenko et al. “Quantum feedback by discrete quantum nondemolition measurements: Towards on-demand generation of photon-number states”. In: *Phys. Rev. A* 80 (2009), p. 013805.
- [151] J. Fiurášek. “Single-photon excitation of a coherent state: Catching the elementary step of stimulated light emission”. In: *Phys. Rev. A* 80 (2009), p. 053822.
- [152] R. H. Hadfield. “single-photon detectors for optical quantum information applications”. In: *Nature Phot.* 3 (2009), p. 696.
- [153] C. Noh et al. “Quantum Teleportation of the Temporal Fluctuations of Light”. In: *Phys. Rev. Lett.* 102 (2009), p. 230501.
- [154] A. Ourjoumtsev et al. “Preparation of non-local superpositions of quasi-classical light states”. In: *Nature Phys.* 05 (2009), p. 189.
- [155] H. Takahashi. “二光子検出による非ガウス状態の生成と連続量量子エンタングルメント蒸留に関する研究 (Two photons subtraction and entanglement distillation experiments)”. PhD thesis. The University of Tokyo, 2009.
- [156] T. Takeno. “非ガウス型状態の時間領域量子テレポーテーションの研究 (Time resolved quantum teleportation of non-Gaussian states of light)”. PhD thesis. The University of Tokyo, 2009.
- [157] T. Eberle et al. “Quantum Enhancement of the Zero-Area Sagnac Interferometer Topology for Gravitational Wave Detection”. In: *Phys. Rev. Lett.* 104 (2010), p. 251102.
- [158] F. Ferreyrol et al. “Implementation of a Nondeterministic Optical Noiseless Amplifier”. In: *Phys. Rev. Lett.* 104 (2010), p. 123603.
- [159] T. Gerrits et al. “Generation of optical coherent-state superpositions by number-resolved photon subtraction from the squeezed vacuum”. In: *Phys. Rev. A* 82 (2010), 031802(R).
- [160] L. Mišta Jr, R. Filip, and A. Furusawa. “Continuous-variable teleportation of a negative Wigner function”. In: *Phys. Rev. A* 82 (2010), p. 012322.
- [161] J. M. Raimond et al. “Phase Space Tweezers for Tailoring Cavity Fields by Quantum Zeno Dynamics”. In: *Phys. Rev. Lett.* 105 (2010), p. 213601.
- [162] H. Takahashi et al. “Entanglement distillation from Gaussian input states”. In: *Nature Phot.* 4 (2010), p. 178.
- [163] G. Y. Xiang et al. “Heralded noiseless linear amplification and distillation of entanglement”. In: *Nat. Phot.* 4 (2010), p. 316.
- [164] A. Zavatta, J. Fiurášek, and M. Bellini. “A high-fidelity noiseless amplifier for quantum light states”. In: *Nat. Phot.* 5 (2010), p. 52.

- [165] T. Amri. “Comportement Quantique des Appareils de Mesure, illustrations en Optique Quantique”. PhD thesis. Université Pierre et Marie Curie, 2011.
- [166] N. Lee. “シュレーディンガーの猫状態の量子テレポーテーションの研究(Quantum teleportation of Schroedinger’s cat states of light)”. PhD thesis. The University of Tokyo, 2011.
- [167] N. Lee et al. “Teleportation of Nonclassical Wave Packets of light”. In: *Science* 332 (2011), pp. 330–333.
- [168] R. Ukai et al. “Demonstration of unconditional one-way quantum computations for continuous variables”. In: *Phys. Rev. Lett.* 106 (2011), p. 240504.
- [169] H. Wang et al. “Deterministic Entanglement of Photons in Two Superconducting Microwave Resonators”. In: *Phys. Rev. Lett.* 106 (2011), p. 060401.
- [170] <http://gcc.gnu.org/>. 2012.
- [171] <http://github.com/ffi/ffi>. 2012.
- [172] <http://jruby.org/>. 2012.
- [173] <http://rubyeventmachine.com/>. 2012.
- [174] <http://sine.ni.com/nips/cds/view/p/lang/en/nid/14125/>. 2012.
- [175] <http://sine.ni.com/nips/cds/view/p/lang/en/nid/202009>. 2012.
- [176] <http://sine.ni.com/nips/cds/view/p/lang/en/nid/203069>. 2012.
- [177] <http://www.minicircuits.com/homepage/homepage.html>. 2012.
- [178] <http://www.ni.com/fpga/>. 2012.
- [179] <http://www.ni.com/support/visasupp.htm>. 2012.
- [180] <http://www.perkinelmer.com/>. 2012.
- [181] <http://www.ruby-lang.org/>. 2012.
- [182] http://www.sigma-koki.com/index_sd.php?lang=en&smcd=C060205. 2012.
- [183] <http://www.tek.com/products/oscilloscopes/dpo7000/>. 2012.
- [184] <http://zone.ni.com/devzone/cda/tut/p/id/3382>. 2012.
- [185] In: () .